

**SUSTAINABLE MOBILITY
TECHNOLOGIES FOR ASSISTIVE
HEALTHCARE AND MONITORING**

YEOH WUI KEAT

(B. ENG (EEE) (Hons.), NTU)

**A THESIS SUBMITTED
FOR THE DEGREE OF DOCTOR OF PHILOSOPHY
DEPARTMENT OF ELECTRICAL AND COMPUTER ENGINEERING
NATIONAL UNIVERSITY OF SINGAPORE**

2016

DECLARATION

I hereby declare that the thesis is my original work and it has been written by me in its entirety. I have duly acknowledged all the sources of information which have been used in the thesis.

This thesis has also not been submitted for any degree in any university previously.

A handwritten signature in black ink, appearing to be 'Yeoh Wui Keat', is positioned above a horizontal line.

Yeoh Wui Keat

30-Jun-2016

Acknowledgments

First and foremost, I owe sincere gratitude to my supervisor, Prof. Tan Kok Kiong. He has been instrumental in guiding me in the right path whenever I seemed to deviate or lose focus in the research direction. This thesis could not be finished without his patient and careful guidance, constant support, and encouragement.

I shall extend my thanks to all my friends and colleagues at the Mechatronics & Automation Lab, for their companionship during my candidature at the National University of Singapore.

I would also like to thank my colleagues at Nanyang Polytechnic, especially Mr. Oh Tiong Keng, for the support and understanding throughout the years. I would not be able to do this without their continued backing and I am grateful for that. My sincere thanks to the management of Nanyang Polytechnic as well for providing me with the financial support over the course of my study.

Finally, special thanks to my family and friends for the abundance of love, support and encouragement over the years. Nothing would have been possible without them.

Contents

Acknowledgments	I
Contents	II
Summary	X
List of Tables	XII
List of Figures	XV
List of Symbols	XXVI
List of Abbreviations	XXXI
1 Introduction	1
1.1 Aging Population in Singapore	2
1.2 Senior Citizen and Assistive Healthcare Technology	4
1.3 Motivation	7
1.4 Problems Formulation	13
1.5 Thesis Contributions and Organization	16
2 Common Framework for Assistive Healthcare and Monitoring	22

2.1	Introduction	22
2.2	Proposed Framework	24
2.3	System Architecture Overview	27
2.3.1	System Architecture	27
2.3.2	Hardware Setup	28
2.4	Low Power 16/32-Bit Microcontroller Unit	29
2.5	Wireless Personal Area Network	30
2.6	Wireless Point-to-Point Simple Network	31
2.7	Thermal Infrared and Inertial Sensors	31
2.7.1	Infrared Thermopile Sensors Array	32
2.7.2	Passive Infrared Motion Sensor	32
2.7.3	Tri-axial Accelerometer based Motion Sensor	33
2.8	Contact Vibration Sensor with Analogue Front-end	34
2.9	Broadband Communication and Location based Service	34
2.10	Summary	35
3	Core Body Temperature Sensing: Re-visiting the Tympanic	
	Membrane Vicinity and Temperature Modeling	37
3.1	Introduction	37
3.2	Exploration Focal Points	44
3.2.1	Ethical Issue in Animal Testing	45
3.2.2	Temperature Uniformity in the TM Vicinity and Measure- ment Point Selection	45
3.2.3	ME Cavity as CBT Site	52

3.3	Re-visiting the TM Vicinity: Design of Experiments and Equip- ments	53
3.3.1	Temperature Probes	53
3.3.2	Heat Chamber and Probes Setup	54
3.3.3	Scientific Validity of the Primate Experiments	56
3.3.4	Experiment 1	58
3.3.5	Experiment 2	59
3.3.6	Experiment 3	59
3.4	Re-visiting the TM Vicinity: Results and Discussions	60
3.4.1	Temperature Uniformity in the TM Vicinity and Measure- ment Point Selection	61
3.4.2	ME Cavity as CBT Site	68
3.4.3	Other Observations	75
3.5	Modeling of Dynamics Between ME Cavity and TM Temperatures	77
3.5.1	ME Heat Balance Model	77
3.5.2	Graphical Representation of MEHB Model	81
3.5.3	Inference Procedures	82
3.5.4	Model Parameter Estimation	84
3.6	Model Verification: Experiment and Results	87
3.6.1	Setup and Procedures	87
3.6.2	Results and Discussions	88
3.7	Model Extensions to ES and RM CBT Sites	93
3.7.1	Critical Site Heat Balance (CSHB) Model	93
3.7.2	CSHB Model Verification and Discussion	95

3.8	Model Improvement with Gain-Scheduled Lookup Table	99
3.8.1	Gradient Detector	100
3.8.2	GS Lookup Table	101
3.8.3	Partitioning Procedure for Experiment Dataset	103
3.8.4	GS-CSHB Model Verification and Discussion	105
3.8.5	GS-CSHB Model Extensions to ME and RM CBT Sites .	109
3.9	Summary	113
4	Core Body Temperature Sensing: VitalMON, a Minimally In-	
	vasive System for Mobile Monitoring	115
4.1	Introduction	115
4.2	System Architecture	119
4.2.1	Operational Advantages	123
4.2.2	Operational Configurations	124
4.3	Hardware Design	126
4.3.1	P-VSM Hardware	127
4.3.2	GC Hardware	133
4.4	Thermal Infrared based TM Temperature Measurement with P-	
	VSM	134
4.4.1	Optical line-of-sight view of the TM for accurate temper-	
	ature measurement via thermal infrared emission	135
4.5	Feasibility Study of WTA for Measuring TM Temperature	142
4.6	User Data Privacy and Security Considerations	153
4.7	Ethical Issue	154
4.8	Summary	155

5	e-Care: A Non-Intrusive Activity Monitoring for the Elderly	156
5.1	Introduction	156
5.2	Problem Formulation and Proposed Solution	157
5.3	e-Care Operating Concept	160
5.3.1	e-Care Base Station	161
5.3.2	Thermal-Motion Sensor Module	163
5.3.3	PIR Door (PIRD) Sensor Module	164
5.3.4	Wireless Alert Switch and Wireless Alert Cancel Switch Modules	164
5.3.5	Deployment Modes	165
5.4	Feasibility Study on Posture Detection and Forehead Surface Tem- perature Measurement with TSA	166
5.4.1	Study Procedure and Setup	166
5.4.2	Results and Discussion	169
5.5	e-Care Trial, Result and Discussion	173
5.5.1	Parameter Setup for Base Station	173
5.5.2	Motion Inactivity Monitoring and Lying Down Posture Sensing	176
5.5.3	Forehead Surface Temperature Measurement	177
5.6	User Data Privacy and Security Considerations	177
5.7	Ethical Issue	180
5.8	Summary	180
6	pVoice: Assistive Device for a Class of Speech Impaired Elderly with Vocal Cord Paralysis	182

Contents

6.1	Introduction	182
6.2	Overview	185
6.3	DSP Voice Enhancement Algorithms	186
6.3.1	Noise Suppressor	187
6.3.2	Speech Detection and Voice Activation	191
6.3.3	Speech Enhancement	191
6.4	Tests and Results	195
6.4.1	Assessment of Amplification and Clarity	198
6.4.2	Assessment of Multi-tone Quality	204
6.5	User Data Privacy and Security Considerations	205
6.6	Ethical Issue	207
6.7	Summary	207
7	Conclusions	209
7.1	Main Contributions	210
7.2	Limitations and Suggestions for Future Work	212
7.2.1	VitalMON	213
7.2.2	e-Care	214
7.2.3	pVoice	215
7.3	Ethical Issues	216
7.4	Summary	217
	Bibliography	219
	Appendix A	236

Appendix B	242
B.1 WTA firmware design	242
B.1.1 <i>GetArrayTemperature()</i> - Infrared to temperature conver-	
sion and hot pixel location identification algorithm	245
B.1.2 <i>ConstructNewMask()</i> - <i>TM-MASK</i> adjustment algorithm	246
B.2 PDL/TM firmware design for CBT calculation	247
Appendix C	251
C.1 Hardware Design	251
C.1.1 e-Care Base Station	251
C.1.2 TMotion and PIRD Sensors Modules	253
C.1.3 AlertSW and AlertCL Modules	256
C.2 Firmware Design	258
C.2.1 Base Station	259
C.2.2 TMotion Sensor	262
C.2.3 PIRD Sensor	264
C.2.4 AlertSW and AlertCL	264
Appendix D	269
D.1 Audio System	269
D.2 Communication	270
D.3 Motion and Location Sensors	271
D.4 Digital Signal Processor	272
D.5 Indicators	272
D.6 User Interface	272
D.7 Power Control	272

Author's Publications	274
------------------------------	------------

Summary

This thesis focused on the development of technologies for assistive health care and monitoring, all pulled by real and significant clinical needs. Three collaborations with medical and health care practitioners resulted in the development of three prototypes. They all share similar requirements in scalability, mobility, form factor, power consumption and cost as they are all designed with uptake efficacy as an end objective. They all leverage on an appropriate synergy of constituent technologies in low power embedded systems, wireless communications networks, and sensing and instrumentation, and share a unified design architecture which allows these technologies to be integrated where appropriate. The thesis may thus be regarded as a collation of results enabling an advance in technology frontiers to allow novel health care applications, building on high power and cost efficiency, embedded and wireless sensing platforms.

The first work and prototype is a scalable human vital status information monitoring hardware and communication infrastructure to monitor the Core Body Temperature (CBT) of sports/military personnel performing strenuous physical activities. It is the outcome of a collaboration with Defense Science Organization to deal with the many cases of heat related injuries due to inadequate CBT monitoring. Precise knowledge of CBT during these exercise is critical to optimize performance and to prevent common heat related injuries. The prototype provides a complete CBT measurement solution to replace the current slow rectal thermometry and costly ingestible wireless pill thermometers in continuous CBT monitoring.

The second work and prototype is pulled by an aging demography in Singapore and consequent of collaboration/discussions with Southwest CDC (Community Development Council), Ministry of Health and Family Welfare, Housing Development Board (HDB) and LionsBefrienders, and other welfare communities. The prototype is designed for use by senior citizens to allow them to age in grace in their own homes as there is an increasing trend in the number of elderly staying by themselves. In an increasing number of unfortunate situations, elderly lost their lives in their own apartments without anyone knowing or due to help arrived too late. The challenges faced in the prescription of a solution go beyond technology, as the physiological dimension of these end users is critical to be addressed to determine how well the solutions can be adopted. The third work and prototype is a portable voice assistive device for human voice processing and enhancement to assist patient or senior citizen with mild to moderate speech dysfunction arising from vocal cord paralysis due to disease or advance aging. It resulted from a collaboration with the ENT Department of the National University Hospital. The prototype is intended to offer both augmentative and corrective speech functions to users with vocal cord paralysis who can still speak albeit poorly and who are difficult to be understood. It serves to improve vocal communication in the form of enhancing the clarity and loudness by processing throat vibrations signals sampled from a throat vibration sensor physically attached to the throat surface of the user.

The works resulted in six papers being written.

List of Tables

2.1	Summary of core building blocks used by VitalMON, e-Care and pVoice in accordance to the proposed AH framework.	28
3.1	Correlations and Bland-Altman Analyzes results for Experiment 3B.	74
3.2	Electrical-Thermal Analogy	81
3.3	MEHB Model Benchmarks for T_{me}	91
3.4	CSHB Model Benchmarks for T_{es}	98
3.5	CSHB Model Benchmarks for T_{rm}	98
3.6	Layout of GS Lookup Table	102
3.7	Number of subsets in T_{es} Experiment dataset and its corresponding MAE	105
3.8	GS-CSHB Model Benchmarks for T_{es}	107
3.9	GS-CSHB Model Benchmarks for T_{me}	112
3.10	GS-CSHB Model Benchmarks for T_{rm}	112
4.1	Volunteer 1 - TM temperature measured from WTA and Braun ThermoScan 5	149

4.2	Volunteer 2 - TM temperature measured from WTA and Braun ThermoScan 5	150
4.3	Volunteer 3 - TM temperature measured from WTA and Braun ThermoScan 5	151
4.4	Volunteer 4 - TM temperature measured from WTA and Braun ThermoScan 5	152
4.5	Volunteer 5 - TM temperature measured from WTA and Braun ThermoScan 5	153
5.1	Elderly person E1 - E2 Wakeup (WT), Sleep (ST), Inactivity (IT), Lying Position (LT) durations, TSA Temperature (TS) and Measured Temperature (MT).	175
5.2	Elderly person E3 - E4 Wakeup (WT), Sleep (ST), Inactivity (IT), Lying Position (LT) durations, TSA Temperature (TS) and Measured Temperature (MT).	175
5.3	Elderly person E1 - E4 Wakeup (WT_{th}), Sleep (ST_{th}), Inactiv- ity (IT_{th}), Lying Position (LT_{th}) and TSA Temperature(TS_{th}) threshold values.	176
5.4	Elderly person E1 - E2 Wakeup (WT), Sleep (ST), Inactivity (IT), Lying Position (LT) durations, and TSA Temperature(TS).	178
5.5	Elderly person E3 - E4 Wakeup (WT), Sleep (ST), Inactivity (IT), Lying Position (LT) durations, and TSA Temperature(TS).	179
6.1	Assessment of Amplification	203
6.2	Assessment of Clarity	203
6.3	Pronunciation Accuracy of Listened Speech	204

6.4	Assessment of Multi-tone Quality	205
-----	--	-----

List of Figures

1.1	Age pyramid of resident population in Singapore	3
1.2	Singapore's declining old-age support ratio	4
2.1	Assistive healthcare hardware framework.	36
3.1	TM temperature measurement pioneered by Benzinger.	41
3.2	TM of the right ear showing a temperature measurement spot at the lower anterior quarter (pointed by the arrow).	42
3.3	Temperature uniformity map of the left ear.	48
3.4	Temperature uniformity map of the left ear under face cooling.	48
3.5	Human Ear Model used in Finite Element Analysis.	50
3.6	FEA showing temperature uniformity	50
3.7	TM of the right ear with temperature measuring points labeled as A1, B1 and C1.	51
3.8	Clinical Temperature Probes supplied by Exacon Scientific A/S for use in Experiments 1 - 3.	54
3.9	Clinical TM Probe supplied by Exacon Scientific A/S retrofitted with a Keyence Reflective Fibre Unit for use in Experiment 1.	55
3.10	Custom heating chamber constructed for use in Experiments 2 - 3.	55

3.11 ES, RM and TM (left and right) temperature plots for primate body temperature measurement. Experiment results are split into two test scenarios for Experiment 2: (1) $X2$ - Full Body Hyperthermia, and (2) $Y2$ - Full Body Hyperthermia with Left Face Fanning.	61
3.12 Analytical results for Experiment 2 that illustrate the effects of full body hyperthermia + full body hyperthermia with left face fanning ($X2 + Y2$ test scenarios) on the left TM temperature. (A) Relationship between left TM temperature ($T_{tm,L}$) and ES temperature (T_{es}), and (B) the respective Bland-Altman plot. . .	64
3.13 Analytical results for Experiment 2 that illustrate the effects of full body hyperthermia + full body hyperthermia with left face fanning ($X2 + Y2$ test scenarios) on the right TM temperature. (A) Relationship between right TM temperature ($T_{tm,R}$) and ES temperature (T_{es}), and (B) the respective Bland-Altman plot. . .	64
3.14 Analytical results for Experiment 2 that illustrate the effects of full body hyperthermia ($X2$ test scenario) on the left TM temperature. (A) Relationship between left TM temperature ($T_{tm,L}$) and ES temperature (T_{es}), and (B) the respective Bland-Altman plot.	66

3.15	Analytical results for Experiment 2 that illustrate the effects of full body hyperthermia ($X2$ test scenario) on the right TM temperature. (A) Relationship between right TM temperature ($T_{tm,R}$) and ES temperature (T_{es}), and (B) the respective Bland-Altman plot.	66
3.16	Analytical results for Experiment 2 that illustrate the effects of full body hyperthermia with left face fanning ($Y2$ test scenario) on the left TM temperature. (A) Relationship between left TM temperature ($T_{tm,L}$) and ES temperature (T_{es}), and (B) the respective Bland-Altman plot.	67
3.17	Analytical results for Experiment 2 that illustrate the effects of full body hyperthermia with left face fanning ($Y2$ test scenario) on the right TM temperature. (A) Relationship between right TM temperature ($T_{tm,R}$) and ES temperature (T_{es}), and (B) the respective Bland-Altman plot.	67
3.18	Analytical results for Experiment 2 that illustrate the effects of full body hyperthermia + full body hyperthermia with left face fanning ($X2+Y2$ test scenarios) on RM and ES temperatures. (A) Relationship between RM temperature (T_{rm}) and ES temperature (T_{es}), and (B) the respective Bland-Altman plot.	68
3.19	T_{rm} , T_{me} and $T_{tm,R}$ vs. Time plots that depict behavior of each measurement site in Experiment 3A (No GA Disruption).	68

3.20	Analytical results for Experiment 3A that illustrate the effects of full body hyperthermia on the right TM temperature. (A) Relationship between right TM temperature ($T_{tm,R}$) and RM temperature (T_{rm}), and (B) the respective Bland-Altman plot.	69
3.21	Analytical results for Experiment 3A that illustrate the effects of full body hyperthermia on the left middle ear cavity temperature. (A) Relationship between left middle ear cavity temperature (T_{me}) and RM temperature (T_{rm}), and (B) the respective Bland-Altman plot.	70
3.22	T_{rm} , T_{me} and $T_{tm,R}$ vs. Time plots that depict behavior of each measurement site with GA being disrupted in Experiment 3B. .	71
3.23	Analytical results for Experiment 3B that illustrate the effects of full body hyperthermia with GA on the left middle ear cavity temperature. (A) Relationship between left middle ear cavity temperature (T_{me}) and esophageal temperature (T_{es}), and (B) the respective Bland-Altman plot.	72
3.24	Analytical results for Experiment 3B that illustrate the effects of full body hyperthermia with GA halted (for 15 minutes) on the left middle ear cavity temperature. (A) Relationship between left middle ear cavity temperature (T_{me}) and esophageal temperature (T_{es}), and (B) the respective Bland-Altman plot.	72

3.25	Analytical results for Experiment 3 <i>B</i> that illustrate the effects of full body hyperthermia with GA on the right TM temperature. (A) Relationship between right TM temperature ($T_{tm,R}$) and esophageal temperature (T_{es}), and (B) the respective Bland-Altman plot.	74
3.26	Analytical results for Experiment 3 <i>B</i> that illustrate the effects of full body hyperthermia with GA halted (for 15 minutes) on the right TM temperature. (A) Relationship between right TM temperature ($T_{tm,R}$) and esophageal temperature (T_{es}), and (B) the respective Bland-Altman plot.	75
3.27	Analytical results for Experiment 3 <i>B</i> that illustrate the effects of full body hyperthermia with GA on the RM temperature. (A) Relationship between RM temperature (T_{rm}) and esophageal temperature (T_{es}), and (B) the respective Bland-Altman plot.	75
3.28	Analytical results for Experiment 3 <i>B</i> that illustrate the effects of full body hyperthermia with GA halted (for 15 minutes) on the RM temperature. (A) Relationship between RM temperature (T_{rm}) and esophageal temperature (T_{es}), and (B) the respective Bland-Altman plot.	76
3.29	Graphical representation of the MEHB model.	82
3.30	Anatomy of a human ear with superimposed MEHB model in graphical form.	82
3.31	T_{es} , T_{rm} , T_{tm} and T_{mc} vs. Time plots from the Experiment.	88

3.32 Inference Errors associated with the inferred ME temperatures (T_{tm} , \hat{T}_{me} , \tilde{T}_{me} and \bar{T}_{me}) vs. Time plots using the <i>VERIFY</i> dataset.	91
3.33 Inferred \tilde{T}_{me} and \bar{T}_{me} , and measured T_{me} vs. Time plots using the <i>VERIFY</i> dataset.	93
3.34 Modified model (from MEHB) representing the TM-ES and TM- RM relationships.	94
3.35 Inferred \check{T}_{es} and Actual T_{es} vs. Time	96
3.36 Inferred \check{T}_{rm} and Actual T_{rm} vs. Time	96
3.37 Inference Errors showing the various Inferred Esophageal Tem- peratures vs. Time plots using the <i>VERIFY</i> dataset.	97
3.38 Inference Errors showing the various Inferred RM Temperatures vs. Time plots using the <i>VERIFY</i> dataset.	97
3.39 Comparison of Inference Errors for ME Cavity, Esophagus and Rectum Temperatures vs. Time plots using the <i>VERIFY</i> dataset.	99
3.40 Proposed GS-CSHB Functional Block Diagram	100
3.41 Inference Errors showing the various Inferred Esophageal Tem- peratures vs. Time plots using the <i>VERIFY</i> dataset.	108
3.42 Inferred \bar{T}_{es} and Actual T_{es} vs. Time (using GS-CSHB Model) .	108
3.43 Inferred \check{T}_{me} and Actual T_{me} vs. Time (using GS-CSHB Model)	111
3.44 Inferred \bar{T}_{rm} and Actual T_{rm} vs. Time (using GS-CSHB Model)	111
3.45 Inference Errors showing the GS-CSHB Inferred ME Temperature vs. Time plots using the <i>VERIFY</i> dataset.	112
3.46 Inference Errors showing the GS-CSHB Inferred RM Tempera- tures vs. Time plots using the <i>VERIFY</i> dataset.	112

4.1	P-VSM functional block diagram.	122
4.2	GC functional block diagram.	122
4.3	VitalMON in small group deployment at a localized area.	125
4.4	VitalMON in multiple groups deployments (local and pervasive categories).	126
4.5	VitalMON in multiple groups deployments under the pervasive category.	127
4.6	WTA block diagram.	128
4.7	(a) Conceptual design and fitting of a WTA for ordinary military personnel, and (b) Actual WTA prototype with a clinical ear speculum.	130
4.8	TSA Thermal Pixel Configuration.	130
4.9	TSA embedded in disposable plastic speculum with 10° effective FOV forming the WTA module prototype.	132
4.10	PDL/TM: (a) Block diagram (b) Prototype	133
4.11	GC: (a) DC block diagram (b) GC prototype	134
4.12	Clinical speculum with distal end exposed to the TM within an automatically straightened ear canal.	138
4.13	Short length speculum with distal end partially exposed to the TM within an un-straightened ear canal.	139
4.14	Short length speculum with distal end exposed to the TM within a straightened ear canal.	141
4.15	WTA prototype tightly fitted into an ear canal.	142

4.16	Constructed thermal image at the view from a speculum of Volunteer 1 (Thermal data at time t).	144
4.17	Constructed thermal image at the view from a speculum of Volunteer 2 (Thermal data at time t).	144
4.18	Constructed thermal image at the view from a speculum of Volunteer 3 (Thermal data at time t).	144
4.19	Constructed thermal image at the view from a speculum of Volunteer 4 (Thermal data at time t).	145
4.20	Constructed thermal image at the view from a speculum of Volunteer 5 (Thermal data at time t).	145
4.21	View of 8 TM thermal images from a speculum attached to an ear, each image was recorded at 1h interval for Volunteer 1: (a) without head cooling), (b) with head cooling.	148
4.22	View of 8 TM thermal images from a speculum attached to an ear, each image was recorded at 1h interval for Volunteer 2: (a) without head cooling), (b) with head cooling.	149
4.23	View of 8 TM thermal images from a speculum attached to an ear, each image was recorded at 1h interval for Volunteer 3: (a) without head cooling), (b) with head cooling.	150
4.24	View of 8 TM thermal images from a speculum attached to an ear, each image was recorded at 1h interval for Volunteer 4: (a) without head cooling), (b) with head cooling.	151

4.25	View of 8 TM thermal images from a speculum attached to an ear, each image was recorded at 1h interval for Volunteer 5: (a) without head cooling), (b) with head cooling.	152
5.1	e-Care system in Simple Mode for a lone elderly person with 2 caregivers.	166
5.2	e-Care system (Simple Mode) deployed in a studio apartment. . .	167
5.3	e-Care systems (Infrastructure Mode) deployed in multiple studio apartments and central managed by an organization.	168
5.4	Experiment Setup - Simple Human Posture Detection with TSA	168
5.5	Thermal image of Volunteer 1	171
5.6	Thermal image of Volunteer 2	171
5.7	Thermal image of Volunteer 3	171
5.8	Thermal image of Volunteer 4	172
5.9	Thermal image of Volunteer 5	172
5.10	Thermal image of Volunteer 1 lying down	172
5.11	Thermal image of Volunteer 2 lying down	172
5.12	Thermal image of Volunteer 3 lying down	172
5.13	Thermal image of Volunteer 4 lying down	172
5.14	Thermal image of Volunteer 5 lying down	172
6.1	pVoice Main Working Principle	185
6.2	pVoice Main Functional Block Diagram	186
6.3	pVoice DSP Functional Blocks	187
6.4	FXLMS Algorithm for pVoice	189
6.5	Unfiltered and filtered clean speech signals plots	190

6.6	Unfiltered and filtered contaminated speech signals plots	190
6.7	pVoice Digital Equalizer Implementation	192
6.8	pVoice LPC Filter Implementation	195
6.9	pVoice prototype with an attached Throat Microphone	196
6.10	pVoice prototype worn by a user	196
6.11	Spectrogram - Reference Speech Signal	199
6.12	Spectrogram - UVCP (Raw)	199
6.13	Spectrogram - UVCP (Enhanced, $\alpha = 0.28$)	199
6.14	Spectrogram - UVCP (Enhanced, $\alpha = 0.32$)	200
6.15	Spectrogram - UVCP (Enhanced, $\alpha = 0.34$)	200
6.16	Spectrogram - UVCP (Enhanced, $\alpha = 0.36$)	200
6.17	Spectrogram - TMP (Raw)	201
6.18	Spectrogram - TMP (Enhanced, $\alpha = 0.28$)	201
6.19	Spectrogram - TMP (Enhanced, $\alpha = 0.32$)	201
6.20	Spectrogram - TMP (Enhanced, $\alpha = 0.34$)	202
6.21	Spectrogram - TMP (Enhanced, $\alpha = 0.36$)	202
B1	WTA firmware operational states.	243
B2	Pseudo-code for <i>MeasureTemperature()</i> state.	244
B3	Summary of processes for pixels masking, pixels conversion to temperatures and computational algorithm to determine maxi- mum TM temperature.	248
B4	<i>TM-MASKs</i> from possible hot pixel locations.	249
B5	Summary of processes for PDL/TM firmware.	250
C1	e-Care Base Station System Block Diagram	251

List of Figures

C2	e-Care Base Station Hardware	253
C3	e-Care TMotion System Block Diagram	254
C4	e-Care TMotion Sensor Hardware	255
C5	e-Care PIRD System Block Diagram	256
C6	e-Care PIRD Sensor Hardware	256
C7	e-Care AlertSW/AlertCL System Block Diagram	257
C8	e-Care AlertSW/AlertCL Hardware	258
C9	Base Station firmware represented in a top-level state diagram. .	266
C10	Thermal-Motion sensor module firmware represented in a top- level state diagram.	267
C11	PIR Door sensor module firmware represented in a simple state diagram.	268
C12	AlertSW/AlertCL module firmware represented in a simple state diagram.	268
D1	pVoice Hardware Block Diagram	269

List of Symbols

α	Formant enhancement control coefficient
α_{de-amp}	De-emphasize filter gain coefficient
$\alpha_{pre-amp}$	Pre-emphasize filter gain coefficient
\bar{T}_{es}	ES temperature estimated using GS-CSHB model
\bar{T}_{me}	ME cavity temperature estimated using MEHB model (without radiant term)
\bar{T}_{rm}	RM temperature estimated using GS-MEHB model
\check{T}_{es}	ES temperature estimated using CSHB model
\check{T}_{me}	ME Cavity temperature estimated using GS-CSHB model
\check{T}_{rm}	RM temperature estimated using CSHB model
ϵ_{rt}	Surface emissivity constant of the ME cavity
$\hat{a}(p)$	Modified LP coefficients with improved vocal characteristics
$\hat{f}_a(p)$	Modified LSF with improved vocal characteristics
\hat{S}	FIR filter estimates of S

List of Symbols

\hat{T}_{es}	ES temperature estimated using a static model
\hat{T}_{me}	ME cavity temperature estimated using a static model
\hat{T}_{rm}	RM temperature estimated using a static model
$\hat{v}(n)$	Re-synthesized improved speech signal
$\hat{z}(n)$	Excitation signal (or residual speech signal) extracted from $z_p(n)$ after LPC filtering
λ_m	Maximum eigenvalue of matrix $[r_0(n)r_0^T(n)]$
μ	Convergence constant (weight) affecting $w(n)$ update
\tilde{T}_{es}	ES temperature estimated using MEHB model
\tilde{T}_{me}	ME cavity temperature estimated using MEHB model
\tilde{T}_{rm}	RM temperature estimated using MEHB model
$a(p)$	LP coefficients
A_{me}	Effective surface area of the ME cavity
A_{tm}	Effective surface area of the TM
C_b	Rate of convective heat exchange per unit area
C_{me}	Heat storage element for ME cavity
D_b	Rate of conductive heat exchange per unit area
E_b	Rate of evaporative heat exchange per unit area
$f_a(p)$	Original LSF

List of Symbols

h_{ca}	Convective heat transfer coefficient for heat transfer from TM to AM
h_{ct}	Lumped convective and conductive heat transfer coefficient for the heat transfer from an effective area A_{me} of the ME cavity to the TM.
h_{ra}	T_{tm} and T_{am} dependent coefficient
h_{rt}	T_{me} and T_{tm} dependent coefficient
L	Filter length of W
M_b	Rate of metabolic energy expenditure per unit area
P	Order of LPC filter
p	Probability in support of a null hypothesis
Q_b	Rate of change of the heat content of that point in terms of heat flow rate per unit area (heat flux)
q_{am}	Heat flow rate from the TM to the ambient environment
r	Pearson correlation coefficient
$r(n)$	Discrete-time noise reference signal
R_b	Rate of radiant heat exchange per unit area
S	Transfer function for ANC secondary path effect
t	Time
T_{am}	Ambient room temperature
T_{ch}	Temperature of the heating chamber

List of Symbols

T_{es}	Temperature of the Esophagus
T_{me}	Temperature of the Middle Ear cavity
T_{pa}	Temperature of the Pulmonary Artery
T_{rm}	Temperature of the Rectum
$T_{tm,L}$	Temperature of the Tympanic Membrane (Left Side)
$T_{tm,R}$	Temperature of the Tympanic Membrane (Right Side)
T_{tm}	Temperature of the Tympanic Membrane
$v(n)$	Filtered speech signal after applying de-emphasize filter on $\hat{v}(n)$
W	Adaptive FIR filter
$w(n)$	Coefficients vector for W
W_b	Rate of external work per unit area
$x(n)$	Discrete-time sample speech-induced vibrations signal
$x(t)$	Continuous-time speech-induced vibrations signal
$y(n)$	True voice activity (speech) discrete-time signal
$z(n)$	Equalized voice activity (speech) discrete-time signal
$z_p(n)$	pre-emphasized signal of $z(n)$
$z_j(n)$	Individual FIR bandpass filter of a equalizer, where $j = 1, 2, 3, \dots$
Δ_{am}	TM - AM Radiant heat transfer term
Δ_{tm}	ME - TM Radiant heat transfer term

List of Symbols

ϵ_{ra} TM surface emissivity constant

σ Stefan-Boltzmann constant

List of Abbreviations

Community Development Council (CDC)

Housing Development Board (HDB)

Core body temperature (CBT)

Assistive healthcare (AH)

Electro-cardiogram (ECG)

Microelectromechanical systems (MEMS)

Global positioning system (GPS)

Epileptic crises (EC)

Electroencephalogram (EEG)

Electromyography (EMG)

Electrodermal activity (EDA)

Passive infrared (PIR)

Global System for Mobile Communications (GSM)

Microcontroller unit (MCU)

Defense Science Organization (DSO)

Thermopile sensors array (TSA)

Severe acute respiratory syndrome (SARS)

Ear Nose and Throat (ENT)

National University Hospital (NUH)

Personal area network (PAN)

Bluetooth low energy (BLE)

Pulmonary artery (PA)

Esophagus (ES)

Rectum (RM)

Tympanic membrane (TM)

Middle ear (ME)

General anesthesia (GA)

National University of Singapore (NUS)

Institutional review board (IRB)

Finite element analysis (FEA)

National Instruments Data Acquisition (NI-DAQ)

Sum of Squared Error (SSE)

Mean Differences (MD)

Two-Node model (TNM)

Multiple Linear Regression (MLR)

Mean Squared Error (MSE)

Mean Absolute Error (MAE)

Error Standard Deviation (ESD)

Middle Ear Heat Balance (MEHB)

Critical Site Heat Balance (CSHB)

Personal Vital Status Monitor (P-VSM)

Group Coordinator (GC)

Backend Monitoring and Database System (BMDS)

Wireless Temperature Acquisition (WTA)

Personal Data Logger/Temperature Monitor (PDL/TM)

Tri-color LED indicator (TLight)

ZIGBEE (ZBEE)

Tri-axial digital accelerometer (ACC)

Device Coordinator (DC)

Inter-Integrated Circuit (I2C)

Area of interest (AOI)

Field of view (FOV)

Lithium-Ion (Li-Ion)

User Interface (UI)

Man-in-the-Middle (MITM)

Media Access Control (MAC)

User Data Packet (UDP)

Elderly Monitoring System (EMS)

Thermal-Motion (TMotion)

PIR Door (PIRD)

Wireless alert switch (AlertSW)

Wireless alert cancel switch (AlertCL)

Short Messaging Services (SMS)

Wake up time (WT)

Sleep time (ST)

Inactivity duration (IT)

Lying down duration (LT)

Maximum forehead temperature (TS)

Daily measured forehead skin surface temperature (MT)

Digital signal processor/processing (DSP)

Audio Analogue Front-end (AFE)

Dual Excitation (DE)

Active noise cancelation (ANC)

Filtered-X Least Mean Square (FXLMS)

Noise suppression (NS)

Finite impulse response (FIR)

Fast Fourier Transform (FFT)

Audio equalizer (AE)

Linear predictive coding (LPC)

Linear prediction (LP)

Line spectral frequencies (LSF)

Unilateral vocal cord paralysis (UVCP)

Thyroarytenoid muscle paralysis (TMP)

Chapter 1

Introduction

The healthcare industries are facing numerous difficult challenges due to aging populations and rising healthcare costs [1]. Innovative and proper use of technology can potentially address some of these difficult challenges and help to deliver quality healthcare to everyone while reducing cost and making optimal use of limited resources in terms of healthcare professionals and facilities. Technological advances in the domains of mobile and pervasive computing, wired and wireless communications, and sensor technologies are continuously contributing to new directions and opportunities in healthcare. New technological initiatives have the potentials to transform healthcare delivery by substantially improving healthcare processes while providing a unified communication framework for healthcare providers.

Population aging is an un-avoidable phenomenon becoming increasingly common in countries across the world. According to the United Nations World Population Aging Report 2013, older persons are projected to exceed the number of children for the first time in 2047. Currently around 65% of the world's older

persons live in developing countries and the number is expected to increase to 80% by 2050 [2]. Much of the world is facing a looming healthcare crisis with aging populations, shortages of family and professional care givers and rapidly increasing healthcare costs. The largest area of expenditure in many countries is health care, and such costs are likely to increase dramatically as the population ages. As people get older, the majority acquire multiple and chronic medical conditions. Such age-related chronic co-morbidities are often accompanied by physical and cognitive impairments that are liable to affect, with varying severity, basic and instrumental activities of daily living. Beyond a certain threshold of impairment, independent living becomes unsustainable without physical support and intervention. There is also an increased risk of mental illnesses, social isolation and loneliness that accompanies reduced mobility [3]. Asia and Europe are the two regions where a significant number of countries face population aging in the near future. In these regions within twenty years many countries will face a situation where the largest population cohort will be those over 65 and average age approach 50 years old. Of the roughly 150,000 people who die each day across the globe, about two thirds or 100,000 per day die of age-related causes [4].

1.1 Aging Population in Singapore

Between 1965 and 2015, Singapore's population grew from 1.9 million to 5.5 million. However, the number of citizens aged 65 and above is increasing rapidly, as population growth slows. The size of this group of citizens doubled from 220,000 in 2000 to 440,000, and is expected to increase to 900,000 by 2030 [5].

As a result, there are issues where two or fewer working adults are supporting both younger and elderly dependents. Figure 1.1 shows the age pyramid of resident population of 2005 and 2015 for male and female residents and one can easily imagine the chart's shape in next 10 years' time if the birth rate continues at the current pace. In addition, Singapore's life expectancy has increased by 10 years over the last three decades: from 72 years in 1980 to an average of 82 years in 2012. With the increasing life expectancy and low birth rates, the population face the prospect of a shrinking and aging citizen population and workforce [6].

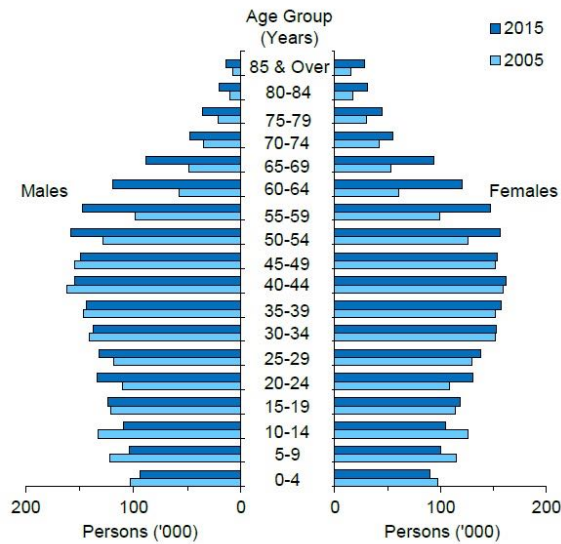


Figure 1.1: Age pyramid of resident population in Singapore

An alarming factor that always connects to the issue of low birth rate, is the ratio of working adults to senior citizen (above age 65) as depicted in Figure 1.2 [5]. Currently this ratio stands at around 5.7 and by 2030, it is expected that there would be only two working adults to support an elderly in Singapore. Moreover, senior citizens' makeup about a third of all one-person households [7], and according to this report [8], senior citizen population living alone may rise to 83,000 by 2030 from 42,100 in 2014. This means that ensuring these senior















Year	Elderly Citizen	Citizens in working-age band of 20-64 years of age	
1970			13.5
2000			8.4
2011			6.3
2015			4.8
2020			3.6
2025			2.6
2030			2.1

Figure 1.2: Singapore’s declining old-age support ratio

citizens have easy access to proper healthcare is going to be a challenge, and as such, it is vital to explore ways for the senior citizens to be more independent in taking care of themselves. It is best not only for the senior citizens, but the families and caregivers, to be aware of their health conditions all the time, preventing the onset of any sudden illnesses that may occur without their prior understanding of their own health.

1.2 Senior Citizen and Assistive Healthcare Technology

There are many electronics products and systems that use technology to promote health and well-being. Electronics sensors and video monitoring systems implementing remote health monitoring solutions such as vital signs monitors, fall detectors, door monitors, bed alerts, pressure mats and, smoke and heat detectors are examples of technologies that can improve senior citizens’ safety,

security and ability to cope at home [9]. For many senior citizens, assistive healthcare (AH) technology makes the difference between being able to live independently or having to get long-term nursing or home-healthcare. For others, it's critical to retain the ability to perform simple activities of daily living, like bathing and going to the bathroom. Many of those who use some form of assistive technology find they are able to reduce their dependencies on others and continue to live independently [10].

As senior citizens become increasingly tech-savvy, the role of technology will become bigger in making elder-care more operational and cost effective. Just as the aging population is embracing new technology, corporations and tech start-ups are recognizing that senior citizens make up a booming, and crucial, customer segment. The competitive marketplace is doing an incredible amount to improve the quality of life and increase life expectancy. As technological costs fall, and AH technology becomes more affordable and easier to use, an increased range of available products and services are within reach, and a larger number of senior citizens utilizing them. New generations of technologies promise radical advancements in AH. Utilizing AH technology to assist the senior citizen and disabled person to overcome disabilities and to improve quality of life represents the mainstream trend in many well-developed countries. Helping an aging parent remain independent and living by themselves becomes easier, thanks to the rapid technological advancements in AH products [11] [12].

AH technology is designed to fulfill or to assist in the specific functional needs of a person, allowing for an increased independence. AH technology can reduce long term healthcare costs by providing specialized equipments which allows

a senior citizen or a disabled person to independently perform basic physical activities, thus relieving caregivers from those duties. Some research has shown that AH technology adoption is most effective when the senior citizens or disables have a chance to physically experience the technology for a period of time prior to making decisions [13]. Therefore, a successful outcome is more likely, if the AH technology user has access to a trained AH technology specialist who can effectively assesses their needs, identify appropriate technology for them to try out and work closely with them so they can make an informed decision.

AH technology must be considered when a senior citizen or a disabled person is being transferred from a hospital care setting to a nursing home or to living independently. The transition between different care environments will determine the type of AH technology to adopt. It can mean the difference between completing tasks of daily living independently or needing some form of assistance from others. AH technology can allow a person to feel safe back at home and remains independent. In addition, with the appropriate technology, the need for costly home based healthcare services can be reduced. [11] [13]. With the application of appropriate technology, people with chronic medical conditions can remain independent and safe from accidents or deprivation, resulting in improved health. Augmentative and alternative communication devices are available to keep them connected to the world outside their homes [14]. Moreover, maintaining an independent high quality of life staves off depression [14] [15]. Clearly, the multiple benefits of keeping the aging population in their own homes are more than just an argument for cost savings. It is an issue of safety and improved quality of life.

1.3 Motivation

AH devices have been constantly evolving and with rapid advancement in technology, resulting in size reduction, incorporation of advanced monitoring and alerting features, and improved end-user experience. AH devices are not new and have been around, and have seen deployments in various segments of healthcare. Senior citizens and people with disabilities are the two major groups that can be shown to directly benefit from deployments of AH devices. The key AH technology features for senior citizens and disables are usually related to motion activity and behavioral monitoring, and assistive motion activity [16]. AH devices in the form of small wearable sensors can have diagnostic, as well as monitoring applications. Their current capabilities may include vital and physiological parameters monitoring and motion activity sensing. Vital and physiological parameters monitoring can assist in both diagnosis and ongoing treatment of a vast number of senior citizens and disables with cardiovascular, pulmonary and neurology related diseases such as hypertension, atrial fibrillation and seizures [17]. Home-based motion activity sensors may assist in fall detection and prevention and help maximize a senior citizen's independence and community participation. Remote monitoring systems have the useful potentials to mitigate problematic patients access issues. By comparing with patients in the urban areas, patients in rural areas travel further to see trained healthcare professionals and have worse outcomes for common medical conditions such as diabetes, hypertension and heart failure [17]. Wearable miniature sensors and reliable remote monitoring systems have the potential to extend the reach of healthcare professionals in urban areas to rural areas and decrease these dispar-

ities [18].

Vital and physiological parameters of interest in rehabilitation include heart pumping rate, respiratory rate, blood pressure, blood oxygen saturation, and muscle activity. The parameters can provide indicators of health status and have tremendous diagnostic value. Traditionally, continuous monitoring of vital and physiological parameters are possible only in the hospitals. But, with new AH developments in the field of sensors and wearable technology, the possibility of accurate, and real-time monitoring of vital and physiological parameters outside of a hospital is a reality. An area of growing interest in the field of wearable technology is the use of miniature wearable sensors to achieve early detection of changes in a patient's health or vital and physiological status that warrants high priority clinical intervention. Sensors to monitor vital signs (e.g., heart rate and respiratory rate) can be deployed, for instance, when monitoring patients with congestive heart failure or patients with chronic obstructive pulmonary disease undergoing clinical intervention [18] [19]. The major goal will be to achieve early detection of potential heart conditions by analyzing heartbeats and rhythms of the patients. Eliza *et al* [20] demonstrated a low-power wearable electro-cardiogram (ECG) monitoring system for multiple-patient remote monitoring. To detect ECG, systems and methods relying upon wearable sensors have been proposed and evaluated. Each patient was required to wear an electronic wearable device featuring a miniature ECG sensor with wireless communication interface. Patients' ECG signals were monitored within the comfort of their own homes and transmitted to a centralized remote monitoring server where the data were analyzed. Healthcare professionals and caregivers would

be notified in the event when abnormal heartbeats and rhythms were detected on any of the patients. This remote monitoring application will result in timely deployments of much needed medical interventions. Early detection and treatment are important goals to prevent worsening of clinical status and the need for emergency room care or hospital admission.

Integrating vital and physiological parameters monitoring in a wearable system often requires ingenious designs and novel sensor placements. Shaltis *et al* [21] developed a self-contained wearable cuff-less blood pressure monitor. The sensor integrated a novel height sensor based on two Microelectromechanical systems (MEMS) accelerometers for measuring the hydrostatic pressure offset of the sensor relative to the heart. The mean arterial blood pressure was derived from the sensor output amplitude by taking into account the height of the sensor relative to the heart. Asada *et al* [22] designed a ring sensor for measuring blood oxygen saturation and heart pumping rate. The ring sensor was completely self-contained and worn on the base of the finger like a ring. Potential applications of the ring sensor ranged from the diagnosis of hypertension to the management of congestive heart failure. Another example of ingenious design was a system developed by Corbishley *et al* [23] to measure respiratory rate using a miniaturized wearable acoustic sensor. The sensor was placed on the neck to record acoustic signals associated with breathing, which were filtered to obtain the signal modulation envelope. By developing techniques to filter out environmental noise and other artifacts, the authors managed to achieve accuracy greater than 90% in the measurement of breathing rate. Physiological monitoring has benefited significantly from developments in the field of flexible electronics circuits

and the integration of sensing technology into wearable devices [24]. Patterson *et al* [25] demonstrated a flexible, ear-worn low-power sensor for heart rate monitoring. The sensor was suitable for long-term monitoring due to its location and unobtrusive design. Although systems of this type have shown promising results, additional work appears to be necessary to achieve motion artifact reduction [26–28]. Proper attenuation of motion artifacts is essential to the deployment of wearable sensors. Nonetheless, further advances in signal processing techniques to mitigate motion artifacts are needed [18].

Remote monitoring systems using wearable sensors for applications in rehabilitations have largely relied upon inertial sensors for human motion activity detection and tracking [18]. Commonly used inertial sensors include accelerometers and gyroscopes. Often, magnetometer and to a certain extent global positioning system (GPS) receiver are used in conjunction with inertial sensor to improve motion tracking accuracy. Motion sensors are inexpensive, small, and require very little power, making them highly attractive to patients or senior citizens that require motion activity monitoring applications. Motion sensors would be deployed, for instance, in applications such as monitoring the effectiveness of home-based rehabilitation interventions in stroke survivors or the use of mobility assistive devices on senior citizens. Wireless communication is relied upon to transmit patient’s data to an access point and relay by using the Internet to a cloud based server or server located in a remote location. Emergency situations can be detected via data processing and alert messages are delivered to emergency healthcare personnel and care givers to provide immediate assistance to patients [18] [29].

Nakano *et al* [30] illustrated the use of non-intrusive infrared technologies to monitor two senior citizens with dementia. The purpose of the monitoring was to study the long-term rest-activity patterns of senior residents in care facilities. Using an infrared sensor system placed at 1.5m above the residents' beds, their activity along with their presence or absence from their bed was recorded over a defined period of time. Campo *et al* [31] designed an expert system for monitoring of senior citizen with dementia. The system was non-intrusive and did not require cameras and any form of wearable devices. The system tracked people and monitored their activities through the use of low cost positioning sensors. The system recorded and analyzed the person's movements and their whereabouts. The analysis results could provide healthcare personnel pre-warning information of an increased risk of fall or a decrease in mobility, and assist them in making decisions on prescribing medication or whether additional surveillance was needed. Makimoto *et al* [32] addressed wandering of senior citizens with dementia using tags in a long-term dementia care unit of a hospital in Seoul. Miura *et al* [33] discussed technology for tracking movements of senior citizens in residential care using tagged slippers and piezoelectric pressure mats. The authors indicated that for safety reason, pressure mats could only be placed below carpets. Hori *et al* [34] developed an ultrasonic sensor network system to remotely monitor the position of wheelchair bound senior citizen in a nursing home by tracking their movement. Schikhof *et al* [35] designed a bedroom monitoring system using a camera, a microphone and sensors to capture information pertaining to activities of daily living. The approach was viewed to be highly intrusive. Wood *et al* [36] proposed a wireless sensor network designed

for long-term remote health monitoring in the assisted living and residential environments. The goal was to adapt the operation of the system, including power management and privacy policy enforcement, to the individual life patterns of the senior citizen.

Health monitoring applications based on wearable devices often employ multiple sensors that are usually integrated into a sensor network either limited to body-worn sensors or integrating body-worn sensors and ambient sensors [18] [37]. Giansanti *et al* [38] developed an accelerometer-based device used for step counting for patients with Parkinson’s disease. Sazonov *et al* [39] developed an in-shoe pressure and acceleration sensor system that was used to classify activities including sitting, standing, and walking with the ability to detect whether subjects were simultaneously performing arm reaching movements. Aziz *et al* [40] used wearable sensors to monitor the recovery of patients after abdominal surgery. Several research projects have suggested that activity monitoring for well-ness applications have great potentials to increase exercise compliance in populations at risk. For example, wearable technology has been used to monitor physical activities in obese individuals [41–44].

An application of wearable devices that has received a great deal of attention among researchers and clinicians is the detection of epileptic seizures, first demonstrated by Dalton *et al* [45]. Primary and secondary compulsive epileptic crises (EC) cause a sudden loss of consciousness. These events are accompanied by stereotypical movements that one can observe in association with characteristic changes in the electroencephalogram (EEG). During the acute phase, the subject is completely unable to interact with the environment. To detect

EC, methods relying upon wearable sensors have been proposed and evaluated. Electroencephalographic sensors [38], tri-axial accelerometers on a wrist [46], combination of electromyography (EMG) and accelerometers [47], and electrodermal activity (EDA) [48] have been used to develop methods to distinguish EC from normal motor activities.

Most wearable devices and monitoring applications discussed, require data gathered be transmitted to a remote server such as a hospital server for analysis. For in-home monitoring, data can be aggregated using a personal computer and transmitted to the remote site over the Internet. Also, the availability of mobile telecommunication standards such as 4G means that pervasive continuous health monitoring is possible when the patient is outside the home environment.

1.4 Problems Formulation

In the prior art reviews conducted, a large majority of the researchers are focusing on developing AH technologies related to monitoring of vital and physiological parameters, and motion activities of the affected patients or senior citizens.

Well-known vital and physiological parameters include heart pumping rate, respiratory rate, blood pressure, blood oxygen saturation, and muscle activity are accurately measured by well-established sensors technologies. The parameters are important to determine a person's health condition, and many of these technologies have already been incorporated into wearable or portable AH devices that can be easily deployed outside of hospital environments into the comfort of homes of patients or senior citizens. An important vital parameter that is still

being measured within a clinical or hospital environment is the pertaining to the monitoring of human body Core Body Temperature (CBT). CBT is one of the important vital sign that must be monitored to ensure safe and effective care [49] for a critically ill patient. CBT is measured from the pulmonary artery (PA) by using a PA catheter inserted into the PA of a sedated patient. This risky procedure is currently the only known method to obtain an accurate CBT measurement that can be considered as a gold standard for CBT, and this method has not been attempted outside the hospital environment. In sports medicine, CBT is also used as an important indicator to prevent heat related injuries in sports personnel performing strenuous physical activities [50] [51], and it is neither safe nor practical to measure CBT of sports personnel via PA catheters. In attempts to replace this risky procedure, many researchers have searched for alternative CBT sites on a human body, and to date, the tympanic membrane (TM), esophagus (ES) and rectum (RM) are the identified alternative CBT sites. Many researchers actually focus on correlating temperature measurements from alternative sites with the actual CBT (from PA) [52–55], and not so much in developing new technologies, new methods or new CBT sites that deliver accurate results that one day may potentially replace the PA.

Human motion activities monitoring of senior citizens living by themselves are important to ensure their safety and physical wellbeing. Over the years, various methods and algorithms, range from simple to extremely complex were developed to interpret human motion activity patterns so as to inform caregivers on the senior citizens current physical health conditions and to predict any potential health related problems that may come along. In most cases, due to privacy

concerns, motion activity monitoring has to be non-intrusive and according to Peetoom *et al* [56], passive infrared (PIR) based motion activity sensor is one of the most adopted sensor by majority of the researchers, with the first evidence of deployment in 1995 [57]. Increasingly complex algorithms have been developed in-order to improve on the sensor detection accuracy, and may reached a level where further improvements are no longer possible due to costs or technological constrains.

Another form of AH technology that is not mentioned until now and receives the least attention is related to human voice communication. Audible voice communication is often taken for granted by many. Patients and senior citizens who lose their ability to communicate properly due to disease or advance aging suffer in silence. Their health may deteriorate rapidly due to other factor such as depression, and not from the disease. AH devices in the form of communication assistive devices are available to assist these cluster of patients, but they are not popular due to size, performance and cost. Patient or senior citizen with weak vocal cord is usually are treated with surgical procedure or physiotherapy [58], and only the most severe total laryngectomy patient is provided with an assistive device in the form of an artificial voicebox (electrolarynx) [59].

This thesis identifies the three main problems of the current AH technologies and devices pertaining to improving patient's or senior citizen's quality of life. The first problem is pertaining to the methods used in monitoring of human CBT for vital and physiological parameter, the second problem is related to non-intrusive monitoring of human motion activities, and the third problem is about assistive human voice communication.

The main objective of this thesis is to solve the well-defined problems that results in the design and development of novel AH devices that are to be used on patients or senior citizens in the area of (a) human body vital sign and physiological parameters monitoring, (b) motion activity monitoring, and (c) assistive communication, for the primary purpose of improving their quality of life.

1.5 Thesis Contributions and Organization

This thesis contains the results of an industrial-track PhD research which are focused on the development of technologies for assistive healthcare and monitoring, all pulled by real and significant clinical needs, and is structured in seven chapters with five main chapters (Chapter 2 - 6). Chapter 2 involves the formulation of a common hardware and software system framework for sustainable and mobility technologies for assistive healthcare and monitoring. It spans across all the prototypes developments for three types of AH devices featured in this thesis. They all share similar requirements in scalability, mobility, form factor, power consumption and cost as they are all designed with uptake efficacy as an end objective. They all leverage on an appropriate synergy of constituent technologies in low power embedded systems, wireless communications networks in ZIGBEE, Bluetooth and GSM (Global System for Mobile Communications), and sensing and instrumentation, and share a unified design architecture which allows these technologies to be integrated where appropriate. The thesis may thus be regarded as a collation of results enabling an advance in technology frontiers to allow novel healthcare applications, building on high power and cost

efficiency, embedded and wireless sensing platforms.

Chapter 3 and 4 focus on the research related to human CBT measurement, the discovery of potentially new CBT site and its corresponding temperature model, and finally a microcontroller unit (MCU) based hardware and software development of a portable CBT measurement device. These chapters are the outcome of a collaboration with Defense Science Organization (DSO) to deal with the many cases of heat related injuries during physical exercises due to inadequate CBT monitoring. Precise knowledge of CBT during these exercises is critical to optimize performance and to prevent common heat related injuries. Chapter 3 covers the re-visiting of the TM vicinity as CBT measurement site, where various known alternative CBT sites are reviewed, and introducing the middle ear (ME) cavity as a new potential CBT site. Experiments involving a live primate were conducted in-order to collect data off line and analyze to establish the various temperature relationships between the ME cavity with the known CBT sites. Chapter 3 also covers the analysis of temperature data and development of an accurate temperature inference model to represent the temperature behavior of the ME cavity, and further extends the model to represent behavior of other CBT sites. Gain-Scheduled lookup table is also introduced to improve on the model output accuracy, and finally Chapter 4 depicts the detailed hardware and software development of VitalMON - a wearable CBT measurement device that is minimally invasive, suitable for field use and accurate for clinical adoption. VitalMON provides a complete CBT measurement solution to replace the current slow rectal thermometry and costly ingestible wireless pill thermometers in continuous CBT monitoring. The infrared Thermopile Sensors Array (TSA)

is used in the VitalMON to optically acquire the thermal infrared emissions from the human TM surface without any physical contact. This is the first such application of the TSA to the best of the knowledge of the candidate. The on-board MCU determines the CBT by processing the captured infrared data, and sends via Bluetooth the CBT value to a small data processing module. VitalMON transmits local and remote alerts to the local and remote medical personnel via ZIGBEE and GSM wireless networks if an impending heat related injury is predicted or detected. VitalMON also incorporates an accelerometer based motion detector that monitors user for potentially damaging fall (or impact) and an alert switch that can be used to request for assistance. The architecture adopted is scalable and can be expanded from a single user scenario to a full battalion one. Apart from contributions in the hardware design and optimization to meet the requirements of the application, there are novel results pertaining to the analysis and re-look at the TM temperature as a better CBT reference than current gold standards for continuous CBT monitoring. Dynamic modeling techniques are derived to yield highly accurate indications of the CBT able to meet the highly stringent requirement of DSO. In order to determine its performance accuracy and reliability, VitalMON has been tested on five volunteers with favorable CBT readouts, and currently undergoing a full trial by DSO.

Chapter 5 highlights on the need to develop e-Care - a new motion activity monitoring system for monitoring lone senior citizens staying by themselves. This chapter is pulled by an aging demography in Singapore and consequent of collaboration/discussions with Southwest CDC (Community Development Council), Ministry of Health and Family Welfare, Housing Development Board (HDB)

and LionsBefrienders and other welfare communities. e-Care is specifically designed for use by senior citizens to allow them to age in grace in their own homes as there is an increasing trend in the number of senior citizens staying by themselves in small apartments. In an increasing number of unfortunate situations, senior citizens lost their lives in their own apartments without anyone knowing or due to help arrived too late. e-Care is a thermal-motion detection system that continuously tracks movements behaviors of lone senior citizens staying in their own homes. e-Care uses the TSA as a very low resolution, non-intrusive and privacy protected thermal imager for the purpose of thermal motion detection and analysis of live human subjects. An on-board MCU processes the captured thermal images to determine motion information, and if required, remote alerts are sent via the GSM wireless networks to the designated caregivers. Having establish the fact that using only PIR motion sensor for the intended purpose may not be able to progress further in achieving higher detection accuracy due the sensor's limitations, the TSA is introduce not as a replacement, but to complement it. TSA is able to accurately detect thermal signature of a human within its defined field of view. By using the PIR sensor and TSA data fusion, a highly reliable form of motion activity monitoring can be achieved. By installing e-Care in apartments for senior citizens, occupants' movements behaviors are continuously tracked, and any abnormal lack of thermal motions activities will be reported. The thermal sensors can also allow the temperature of the users to be monitored in a controlled setting, thus enabling a first line of defense in temperature monitoring during the outbreak of diseases such as severe acute respiratory syndrome (SARS). Thus, timely and potential live saving assistance can be rendered. The

prototypes of e-Care have been trialed in homes of several senior citizens and functionality tests were successfully concluded.

Chapter 6 illustrates pVoice, a portable voice AH device for enhancing vocal communication of senior citizen or individual who suffers from mild to moderate speech dysfunction arising from vocal cord paralysis due to disease or advance aging. This chapter is the result of a collaboration with the Ear Nose and Throat (ENT) Department of the National University Hospital (NUH). pVoice is intended to offer both augmentative and corrective speech functions to users with vocal cord paralysis who can still speak albeit poorly and who are difficult to be understood. Having identified that patients with mild to moderate form of vocal cord paralysis has only physiotherapy or surgical option to address the problem, this chapter present a detail construction of a portable and wearable voice assistive device that can be offered as an alternative to conventional treatments. pVoice serves to improve vocal communication in the form of enhancing the clarity and loudness by processing throat vibrations signals sampled from a throat vibration sensor physically attached to the throat surface of the user. The processed voice is regenerated to drive a miniature magnetic speaker that serves as an artificial voice box for the user, thus augmenting the user's weak voice with a processed and sufficiently strong voice. Signal processing algorithm in pVoice is capable of real-time human voice processing, not only in terms of amplification but also selective and customized speech enhancement such as speech envelope detection, noise suppression, frequency bands equalization and formants enhancement, thus assisting users who have problems communicating in the usual manner and existing assistive devices often result in a monotonous

”robotic” tone. Apart from enhancing voice communication, pVoice is also a wearable device for e-Care, for monitoring motion activity and provides manual alert request for use by senior citizen. pVoice has been successfully tested at NUH on groups of patients with mild to moderate vocal cord paralysis.

The thesis concludes in Chapter 7 with the summary of the main contributions of the work presented and possible future work.

Chapter 2

Common Framework for Assistive Healthcare and Monitoring

2.1 Introduction

While technology has contributed positively towards humanity in many aspects, huge potential remains to be tapped in the area of assistive healthcare (AH). Eighty seven percent of the 195 countries in the world are developing ones, and together, they represent a huge 84% of the total global population [60]. Conversely, the healthcare spending of these countries only constitutes 11% of the total healthcare spending of the world, primarily due to the lagging economies, poverty and the very low doctor-to-patient ratios. Despite lagging in general healthcare, many of these developing countries are well equipped with basic mobile phone based communication and Internet access largely due to the successful

penetration of telecommunication technologies. In 2015, statistics show that 68% of the world's total number of Internet users resides in developing countries [61]. With the availability of the basic infrastructures, it is structurally viable to deploy AH technology in developing countries to help bridge the gaps of quality healthcare to the population at large and bring forth the following benefits:

- **Cost savings:** AH devices can be deployed to homes of patients or senior citizens, and they are remote monitored from a central location. Healthcare professional only visits when needs arise. The optimization of manpower resources results in better cost control.
- **Easy accessibility:** patients and senior citizens can have AH deliver to the doorsteps of their own homes, and do not require the need to travel often in order to seek medical advices as their health related parameters can be remotely monitored.
- **Quality of service:** optimize the distribution of limited healthcare resources to the mass population at large.

This chapter details the creation of a common hardware framework of a proposed AH system. Three AH devices are developed to demonstrate the viability of the proposed framework. The three AH devices are developed to cover the healthcare area pertaining to monitoring of vital core body temperature (health vital sign), motion activity/inactivity monitoring and alert management for senior citizens, and improvement of vocal communication of patient and senior citizens suffering from vocal cord paralysis due to disease or advanced aging. The devices handle and solve unique non-overlapped issues related to healthcare with different types of sensing technologies, and are technically challenging to

have a common framework representing all three. However, a common framework is still possible as the core technologies that form the basic (core) building blocks remain largely the same.

This chapter focuses directly on the various building blocks that form the common hardware framework through appropriate selection of existing technologies. The framework presented in this chapter will be the base upon which subsequent works, as explained in the next few chapters, are developed to build the three types of AH devices.

2.2 Proposed Framework

The main requirements to be met by the proposed framework forming the core building blocks are listed as follows:

1. Low power microcontroller unit (MCU) with signal processing capability:
16/32-bit MCU with internal hardware capable of performing basic digital signal processing algorithms. The MCU is tasked to implement custom firmware and algorithms for all the three assistive health devices, and is capable of performing in various power saving mode by ways of controlling its operating frequency and on-chip peripherals.
2. Wireless personal area network (PAN): ZIGBEE based wireless personal area network with mesh topology for reliable and moderate bandwidth wireless data communication among various sensing devices. The network must have the ability to perform self-discovery, self-healing and self-routing when new devices are added and faulty devices are removed, and sustain a reliable end to end communication channel with a reasonable data rate

of at least 38,400 bps.

3. Wireless point-to-point simple network: Bluetooth low energy (BLE) based simple network connectivity for reliable and low bandwidth communication between two short range devices at a maximum distance of 2m. The network must ensure reliable end-to-end virtual connectivity with low data rate of at least 9,600 bps. Typical usage example of the simple network is for replacing physical wires of small sensors connecting to a primary data acquisition unit where data processing is usually done. It can also be used by a low power wearable device to connect to a handheld communication device (e.g., smartphone), and utilize the facility in the handheld communication device for the purpose of transmitting information (sensor data, alerts, etc.) over to a remote server for follow-up actions.

4. Sensors

- (a) Thermal based non-contact ambient sensor: With concerns regarding to issue of unintended privacy invasion, sensors deployed must not have the capability of capturing live video images. Sensors operating in the thermal infrared spectrum are chosen for this very purpose of protecting the privacy of the users. Two types of sensors selected are:
 - (a) passive infrared (PIR) motion sensor for motion detection, and (b) low resolution infrared thermopile sensors array (TSA) for temperature measurement and low resolution thermal image analysis. Thermal image is used due to its inherently low resolution characteristic where issue regarding invasion of privacy is not a concern.
- (b) Inertial sensor: digital tri-axial accelerometer (ACC) is used in wear-

able devices for the purpose of motion activity and fall/impact detections.

(c) Contact vibration sensor with analogue front-end: Contact vibration sensor (CVS) is used for detection and analysis of voice induced vibration signal. The sensor is used primarily for detecting of vibration signal induced from weak voice in a patient or an elderly person with weak vocal cord. The analogue front-end is used for the purpose of signal pre-conditioning before being processed by the MCU.

5. Broadband communication endpoint: Broadband communication is identified as one of the core building block. There is a requirement where captured data is transmitted to a remote server for processing by using the existing broadband communication infrastructure. The GSM (Global System for Mobile Communications) mobile network and the Internet are the two types of broadband communications infrastructure that are the most commonly used. The two endpoints selected for broadband communication are: (a) GSM modem for sending data via the GSM network, and (b) Internet Access Point for sending data via the Internet.

6. Location based service: Global positioning system (GPS) receiver is used to determine current geographical location.

Not all of these core building blocks are to be used concurrently. Each of the system designed contains some but not all of the building blocks.

2.3 System Architecture Overview

2.3.1 System Architecture

A conceptual representation of an AH hardware framework for remote monitoring is depicted in Figure 2.1. The figure represents an integrated AH system that integrates and manages healthcare resources with the help of sensing technology and established communication networks. The components within the framework is built from all the core building blocks defined earlier. Wearable sensors are used to gather physiological and motion data thus enabling patient's or senior citizen's status monitoring. Sensors are deployed according to the health application of interest. Sensors to monitor vital signs (e.g. heart rate, respiratory rate, and core body temperature) are deployed, for instance, when monitoring patients with congestive heart disease or senior citizens with pulmonary disease that require or undergoing long term treatments. Sportsmen or military personnel undergoing strenuous physical activities will also benefit where heart rate, respiratory rate and core body temperature (CBT) can be simultaneously monitored for early signs of heat exhaustion that warrant immediate medical attentions.

Wireless communication is relied upon to transmit patient's data to a remote server via the Internet or GSM communication networks. Emergency request for assistance can be manually activated by the patient, and alert is sent to family members or caregivers or emergency service center to provide immediate assistance to patient. Healthcare professionals can remote monitor patient's health status and be notified in case a medical intervention has to be made.

Despite the potential advantages of a remote monitoring system relying on

wearable sensors like the one described previously, there are significant challenges ahead before such a system can be deployed on a large scale basis. These challenges include barriers such as initial investment costs required to set up the required support infrastructure, technological limitations on power consumption that lead to short battery usage time, and outdated communication infrastructure that render electronics communication unreliable.

2.3.2 Hardware Setup

The AH system employs a series of autonomous embedded devices that are connected together via a secured wireless PAN. Each individual component is a smart device incorporating its own MCU. The hardware requirements for setting up an AH system depends on the targeted user and type of monitoring (sensors) required. This thesis focuses on three type of AH hardware implementations: (a) VitalMON - wearable device for real-time monitoring of CBT, (b) e-Care - motion activity monitoring and alert system, and (c) pVoice - portable (wearable) voice assistive device. Table 2.1 depicts a summary core building blocks used by each the three developed AH hardware in accordance to the proposed framework. The hardware setups will be discussed in great detail in Chapter 4, 5 and 6 respectively.

Table 2.1: Summary of core building blocks used by VitalMON, e-Care and pVoice in accordance to the proposed AH framework.

AH Device	MCU	PAN	BLE	Sensors				Broadband		GPS
				PIR	TSA	ACC	CVS	GSM	Internet	
VitalMON	✓	✓	✓	✗	✓	✓	X	✓	✓	✓
e-Care	✓	✓	✗	✓	✓	✗	✗	✓	✓	✗
pVoice	✓	✓	✓	✗	✗	✓	✓	✗	✗	✓

2.4 Low Power 16/32-Bit Microcontroller Unit

The MCU is the most important computational element within the proposed framework. A MCU implements custom algorithms for each peripheral devices found within the framework. Each sensor node has a MCU loaded with custom firmware that controls the behavior of the node and also handles communication with others. The chosen MCU must: (a) contains a rich set of internal peripherals so as to minimize chip counts and to reduce physical hardware size and to provide native interface support (e.g., serial, SPI, I2C, etc.) for various sensors, (b) must have performance optimization that allows different voltage and frequency settings for a wide range of power constraint (power saving) based performance with low current (μA) sleep or suspend modes, (c) must contains hardware support for basic digital signal processing functions such as hardware multiplier and barrel shifter in order efficiently execute basic signal processing algorithms without performance penalty, and (d) sufficient non-volatile and volatile memories for implementation of firmware and algorithm.

For the proposed framework, Renesas RL78 based [62] 16-bit MCU and Microchip dsPIC [63] digital signal controller based MCU are used. Renesas MCU is used extensively in VitalMON and e-Care due to its small footprint and optimized for battery powered applications. Microchip based MCU is chosen for pVoice for its built-in signal processing hardware support. Both MCU contain rich sets of internal peripherals and require minimal external support IC chips, thus suitable for wearable devices.

2.5 Wireless Personal Area Network

Wireless PAN is a form of localized wireless network for use in wireless sensors communication. The most common PAN infrastructure is the ZIGBEE and is one of the most established in terms of link reliability and cost, and is the most popular industry wireless mesh networking standard for connecting sensors, instrumentation and control systems. ZIGBEE's low power consumption, built-in security method and ratified specifications make it very suitable to be used with healthcare based sensor devices [64]. ZIGBEE follows IEEE 802.15.4 specification, and is very robust and reliable even in a noisy RF environment with no data packet lost or dropped [65].

ZIGBEE PANs are implemented in VitalMON, e-Care and pVoice where reliable wireless sensors communication are required. Telegesis ZIGBEE ETRX357 [66] based controller is used for the purpose. In VitalMON, ZIGBEE PAN is used to form a mesh type of inter-connecting wearable sensors topology for sports and military personnel performing strenuous activities. Each user is a moving sensor node, and ZIGBEE is used to form and maintain a PAN that changes dynamically as users join and leave the PAN.

In e-Care and pVoice, the wireless peripherals such as the wireless sensor modules and wireless emergency switch modules communicate wirelessly to a local Base Station in an apartment of an elderly that detects motion inactivity and manages alert. The peripheral nodes are in fixed location on the apartment's walls and each node position may not be ideal as it may be affected by concrete walls that may attenuate or corrupt RF signals reaching the Base Station. A reliable form of communication method is required where each node is also a

message router for relaying messages to the Base Station when direct communication is not possible. ZIGBEE PAN is used to form a secured mesh type of inter-connecting peripheral nodes topology where message relaying is possible.

2.6 Wireless Point-to-Point Simple Network

Wireless point-to-point simple network is used to replace the traditional wired connections of sensors attached to a primary data acquisition device. With the advancement of low power wireless technologies, increasing types of modern sensors have the options to have wireless connectivity so as to ease wiring burdens.

In VitalMON, the wireless point-to-point simple network using BLE is used for the purpose of connecting a small wearable device performing core body temperature measurement (at the user's ear) to a more powerful data processing and communication device located at a very short distance away (attached to a belt on the user's waist). The adoption of BLE removes the physical wiring which is an inconvenience to the user. BLE is used by pVoice to securely connect to an elderly user's smartphone for the purpose of using the smartphone's GSM network for sending SMS alert messages to inform assigned caregivers during an emergency situation.

2.7 Thermal Infrared and Inertial Sensors

Thermal infrared and inertial sensors are the sensing methodologies that are also the important elements of the proposed AH framework. Thermal infrared sensors are used due to its unobtrusive sensing method. Inertial sensor such as a digital tri-axial accelerometer is commonly associated with accurate motion

activity detection. Inertial sensor is usually incorporated into a wearable device for motion and behavioral monitoring.

2.7.1 Infrared Thermopile Sensors Array

Melexis MLX90620 [67] TSA measures target temperature within its field of view of a target. A 16×4 rectangle array of thermopile sensors [68] measure the thermal infrared radiation generated at target and convert each of the measured value to equivalent in temperature, thus resulting in an array of temperature values that represents a crude and very low resolution thermal image [69–71]. The thermal image of a human subject captured by the TSA does not in any way resembles the original shape and contour of the subject, and it will not cause issues pertaining to invasion of privacy.

TSA is used in VitalMON (Chapter 4) as a temperature sensor in a wearable CBT monitoring device for measuring surface temperature of a human tympanic membrane. It is positioned at a direct line of sight with the tympanic membrane and measures the highest temperature spot. TSA is used in e-Care (Chapter 5) for detecting human body temperature, and human sleep and standing/sitting postures. In both applications, the TSA must be interfaced to a MCU for proper operation in control and in thermal image acquisition.

2.7.2 Passive Infrared Motion Sensor

PIR motion sensor is used as the basic sensing element for human motion activity detection. Objects that give off heat reflect electromagnetic radiation in the infrared spectrum between $0.7\mu\text{m}$ and $300\mu\text{m}$ [72]. The infrared radiation that is reflected from the human body has a wavelength of about $10\mu\text{m}$. The

infrared filter on the sensor only allows infrared wavelength of $10\mu\text{m}$ to penetrate through. This helps to reduce the effect that non-targeted sources of infrared radiation (other than humans) have on the sensor thereby reducing false motion activity detection.

Parallax PIR motion sensor (555-28027) [73] is used as an important motion activity sensing element in the e-Care system (Chapter 5) for motion activity/inactivity detection of lone senior citizens staying by themselves. Multiple sensors with its supporting electronics hardware are installed to provide full sensing coverage in studio apartments of the lone elderly. PIR sensors have been commonly used for the estimation of amount and type [74] [75] of daily activity. It is a sensor of choice as it provides continuous and unobtrusive behavioral monitoring, and is usually installed as part of wireless sensor networks for supporting healthcare for aging in place and promoting independence in assisted living [76] [77].

2.7.3 Tri-axial Accelerometer based Motion Sensor

Inertial sensor such as the low-cost and low-power Microelectromechanical systems (MEMS) accelerometer is used to detect motion activity. A tri-axial accelerometer is effective in detecting human motion activity in 3-axes degree of freedoms [78]. It is included in a wearable device for the purpose of human motion activity monitoring and fall detection [78] [79]. Analog Devices ADXL345 [80] digital tri-axial accelerometer is used to detect human motion activity in VitalMON (Chapter 4) and in pVoice (Chapter 6).

2.8 Contact Vibration Sensor with Analogue Front-end

In healthcare, vibration sensing can be used for impact-based fall detection [81]. This sensing method works on the presumption that the vibration pattern generated by human fall is different than that produced by other daily living activities and normal non-human object falling. Other type of application includes measuring shivering level in a critically ill patient undergoing therapeutic temperature modulation [82].

pVoice uses an external throat microphone (laryngophone) as a contact vibration sensor for detecting the speech-induced weak vibration signals from the throat surface of a patient or an elderly user with weak vocal cord. An analogue front-end circuit conditions the vibration signal with an appropriate pre-amplification gain which is adjusted automatically to prevent signal clipping. The conditioned signal is processed by pVoice signal processing algorithm to regenerate an improved and audible speech signal.

2.9 Broadband Communication and Location based Service

Broadband communication is an important feature for all the three developed AH devices. Broadband communication allows alert messages to reach the designated caregivers or healthcare providers. In VitalMON and e-Care, broadband communications are provided by the built-in GSM mobile communication hardware. pVoice accesses the broadband communication function by using BLE

to connect to a user's smartphone.

Both VitalMON and pVoice use the location based service provides geographical location information from the built-in GPS hardware. The information allows caregivers or healthcare providers to know the exact locations of alerts.

2.10 Summary

In this chapter, a common framework for implementing AH devices and system is proposed. The important core components that form the common building blocks have been properly identified and discussed on its intended use in building practical AH devices. This framework presented here will be used in this thesis to implement further works and develop solutions toward practical AH devices.

Chapter 3

Core Body Temperature

Sensing: Re-visiting the

Tympanic Membrane Vicinity

and Temperature Modeling

3.1 Introduction

Core body temperature (CBT) is an important indicator of the human health and endurance performance. The characteristics of CBT and the ideal measurement site have attracted extensive research in both clinical and the physiological domains. CBT is generated from the well-perfused tissues of the vital organs [83] [84] and thus, it remains relatively stable since heat distribution within these tissues is attained at a fast rate. As a result, the CBT of a healthy human body rarely differs and it is very close to the temperature of blood flowing in

the pulmonary artery (PA) [85] [86]. The blood temperature of the PA (T_{pa}) is often taken as the gold standard in CBT measurement [52] [85–87]. However, the measurement of T_{pa} is an invasive and high risk procedure, requiring the insertion of a PA catheter. Thus, T_{pa} measurement is mainly restricted to critical care monitoring within a hospital environment [52], wherein cardiac or critically ill patients are being monitored round the clock.

Apart from the PA, the esophagus (ES) and rectum (RM) are other sites to measure CBT [52–55]. The ES site requires rather invasive process to access, while the RM site is rather inconvenient in term of its accessibility. These sites are inherently less risky compared to the PA and certain considerations have to be observed in order to obtain accurate and consistent temperature measurements. ES temperature (T_{es}) is accurate when the probe is positioned at the lower fourth of the ES which is closer to the heart and aorta. If the probe is located too high up in the ES, the reading will be affected by tracheal air due to the breathing process [88] [89]. T_{es} can be a good candidate for the CBT due to its responsiveness which is on-par with T_{pa} [90], but due to the sensitivity to proper probe placement, the distress caused to patient during measurement and the associated cost and time, the ES is also not a common site for CBT.

RM Temperature (T_{rm}) is considered as an indicator of deep tissue and critical tissue temperatures [88]. The large tissue mass surrounding the rectum provides for a stable temperature reading that is shielded from the surrounding environmental temperature [88] [91]. However, T_{rm} is not suitable as an indicator of CBT when there is a need to pick up rapid changes in the CBT [91] [92]. When the human body is at thermal equilibrium, T_{rm} is a reliable substitute of

the CBT. But when the CBT is undergoing a transient period, T_{rm} is sluggish to pick it up as it exhibits slow response to changes in heat input and losses, and follows rather than leads the body's thermoregulatory reactions [91] [92]. Hence, T_{rm} is limited in the ability to respond to thermal transients involving sudden or abrupt changes to CBT. For a critically ill patient, changes in CBT is crucial to determine the next treatment protocol [83] [85]. Such limitations have led to the suitability of T_{rm} to determine CBT being repeatedly questioned, though till now, the rectum is still a widely used CBT site due to the relatively efficient and stable measurements.

There is general acceptance in the literature that T_{rm} is a reliable approximation of CBT [88] [93]. Despite its widespread use, the relative invasiveness and social stigma attached to T_{rm} measurement coupled with necessary dangling wire connections between the temperature sensor and the measuring device make T_{rm} monitoring of subjects while exercising in the field problematic. Thus, one of the most reliable and comfortable solution would be to use an ingestible thermometer pill [94–96]. The pill is ingested and transmits a temperature signal, relative to the surrounding gastrointestinal temperature, by radio wave to an external wearable receiver for data logging or instant temperature display. The pill is well-known to detect elevated CBT during sport activities [94–97]. OBrien *et al* [98] used the temperature pill to show that it provides valid measurements of CBT compared to both T_{rm} and T_{es} during rest and prolonged cycling exercise.

The aforementioned sites are not amenable towards general use or temperature monitoring in active personnel. Generally, all of them pose a certain amount of risk and discomfort (as well as embarrassment (e.g., T_{rm} measurement)) from

the user perspectives and they can incur rather high costs. The ideal CBT site has, by far, remained elusive to-date. Thus, research continues to be undertaken to explore alternative temperature measurement sites which are conducive for general and continuous monitoring purposes, and are reliable sufficiently as an indicator of the CBT. One such site is the tympanic membrane (TM). TM temperature (T_{tm}) measurement via infrared thermometry has been touted as a potential replacement for the invasive temperature measurement procedures discussed. The safe, least invasive and arguably most comfortable way of measuring T_{tm} , however, is not yet a de-facto standard to-date; not when there are still unresolved issues pertaining to its accuracy and stability relative to measurements from other sites [84] [87] [89] [93].

Benzinger [99–101] first demonstrated the feasibility of T_{tm} measurement as an indicator of CBT using a thermocouple temperature probe engaging the surface of a TM with the ear canal sealed off from the environment. The pioneered method of TM temperature measurement requiring the temperature probe to engage the TM is depicted in Figure 3.1. Benzinger hypothesized that the TM, being in close proximity to the hypothalamus and to the internal carotid artery (and since the internal carotid arterial blood flow perfuses the TM), is most suitable for accurate indication of CBT. To support his hypothesis, Benzinger produced measurements of T_{tm} obtained from his probe and measurement approach, showed them to be stable, reproducible and responsive to thermal stresses of various kinds, and also demonstrated T_{tm} to be more responsive than T_{rm} in indicating CBT. The method however carries a risk of TM perforation.

On the other hand, subsequent studies by McCaffrey *et al* [102] and Nielsen

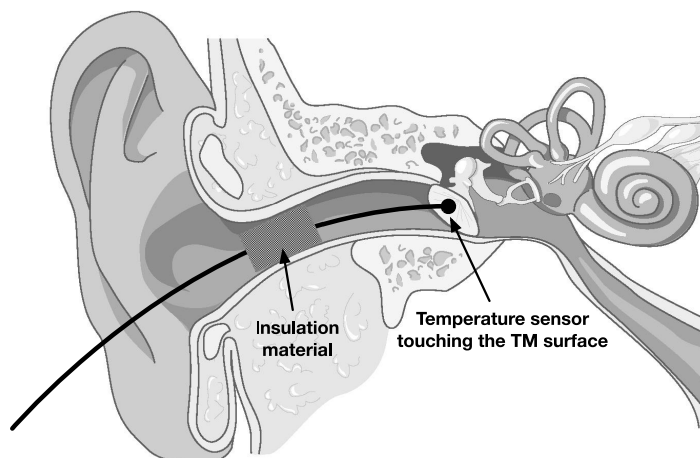


Figure 3.1: TM temperature measurement pioneered by Benzinger.

[103] indicated that head cooling, particularly when the cooling is directed at the facial area, decreases T_{tm} . McCaffrey *et al* showed that by heating and cooling localized regions of the head, T_{tm} of human subjects were non-proportionally affected by changes in the skin temperature of the head. These results meant T_{tm} , by itself, is not a good indication of CBT since it is affected by other variables.

However, Brinnel and Cabanac [104], and Sato *et al* [105] furnished data to show that T_{tm} is still reliable for this purpose if the measurement spot on the TM is chosen with care and an adequately directed probe is used to acquire the measurements. Brinnel and Cabanac suggested that the lower anterior quarter of the TM (Figure 3.2) has a higher temperature on the surface of the TM and a temperature measurement from a point in this region is least sensitive to head cooling. Sato *et al* performed similar experiments as Brinnel and Cabanac, and they determined the highest measured temperature spot on the TM with a trial and error approach of probe positioning until the hotspot is found. They produced results, with the probe engaging this spot on the TM, showing

the measurements obtained were least sensitive to the effects of head cooling. However, they did not define the point of measurement.



Figure 3.2: TM of the right ear showing a temperature measurement spot at the lower anterior quarter (pointed by the arrow).

These works were done with the probe engaging the surface of the TM which is neither practical nor safe from perforation of the TM when taking measurements from awake patients, especially when measurements are required continually. However, the need to engage the TM can be understood since the surface of the TM is not flat but conically shaped and a physical contact is essential to ensure that the measurements from all sites on the surface can be compared in a fair manner. The ideal spot which can be easily located for measurement has also not been clearly specified and substantiated by previous studies.

This chapter is motivated by the above-mentioned issues and gaps in allowing T_{tm} to be used as an inference to CBT. In addition, this chapter sought to explore, to the best of knowledge for the first time, an alternate CBT measurement site in the middle ear (ME) cavity. Being located at the inner side of the TM, this chapter aimed to shed light on the existing gaps in the use of the ear as a CBT site. The ME cavity resembles a rectangular chamber with four walls,

a ceiling and a floor. The lateral wall being the TM, the ceiling (or superior wall) is a thin plate of bony structure that separates the chamber from the cranial cavity and the brain, and the floor (or inferior wall) is another thin bony plate that separates the chamber from the jugular vein and the carotid artery. The posterior wall partly separates the chamber from the mastoid antrum. The anterior wall is the opening of the eustachian tube, which connects the chamber with the nasopharynx. The medial wall separates the chamber from the inner ear [106]. This site selection is appropriate since the ME cavity is very near to the brain (ceiling), jugular vein and carotid artery (floor), and it is surrounded by highly perfused tissues. The temperature at this cavity (T_{me}) can potentially reflect a stable temperature to infer CBT. The reason for the lack of effort in the exploration of this site may be attributed to the difficulty in the access to the ME. However, in recent years, advances in medical surgery have led to the simplification of the procedure to carry out a ventilation tube insertion on the TM to an office-based procedure [107] [108] without any need for general anesthesia (GA). A channel can thus be readily created to access the ME via the tube for temperature measurements. An alternate access path is also possible through the Eustachian tube [109].

This chapter aims to:

1. Examine the surface temperature distribution at a small but within constant proximity from the TM, and the identification of a clear landmark for the measurement of T_{tm} . The results can be potentially useful in the design of TM thermometers to infer close readings to CBT in the face of environmental cooling.

2. Benchmark the ME temperature against current CBT sites (including the TM), with a side objective to observe if T_{me} shows characteristics which can be observed from T_{tm} . The results can potentially be useful towards further exploration of the ME as a CBT site. The cooling effects on the measurements of T_{tm} , the relative responsiveness and repeatability of measurements in T_{es} and T_{rm} , and the correlation among temperatures from the various sites fully verified.
3. Derive dynamic heat balance models describing heat flows in the ME cavity vicinity and other CBT sites.

3.2 Exploration Focal Points

It should be acknowledged at the outset that the study of CBT is an extensive and challenging one. It is not realistic to expect an exhaustive and comprehensive set of results from any single and specific work due to the complexity and the nature of the human body and the constituent organs, as well as the dynamic interactions with endogenous and exogenous influence. This section seeks to focus on two specific issues (1. Temperature Uniformity in the TM Vicinity, and 2. ME Cavity as CBT Site) to revisit the TM vicinity as a potential CBT site. These two issues will be clearly formulated with respect to the background work and gaps, and the exploration approaches projected to align with the experiments and results which will be presented in the ensuing subsections.

Necessary approval from the SingHealth Institutional Animal Care and Use Committee (IACUC) has been sought prior to the commencement of the experiments involving a live animal subject. The IACUC reviewed the experiments

procedures and concluded that the experiments were proper, ethical and humane, hence approval was given to proceed with the experiments as planned.

3.2.1 Ethical Issue in Animal Testing

A live adult primate was engaged for two rounds of experiments involving: (a) elevation of primate body temperature up to 42 °C, (b) measurement of temperatures from the rectum and esophagus, (c) measurement of temperature from the surface of the TM, and (d) measurement of temperature from ME cavity. Prior to the experiments, approval from the Institutional Animal Care and Use Committee (IACUC) has been sought and approved. The experiments were designed and carried out at SingHealth Experimental Medicine Center that conformed to the National Advisory Committee for Laboratory Animal Research (NACLAR) guidelines. Throughout the entire experiment runtime, the primate was sedated with general anaesthesia (GA) and its vital signs were closely monitored by a veterinarian. Appropriate medical treatments and sufficiently long rest duration was enforced on the primate in-order to allow it to fully recover before being subjected to another round of experiment of the same nature.

The primate was euthanized after two rounds of experiments.

3.2.2 Temperature Uniformity in the TM Vicinity and Measurement Point Selection

While the outer ear is an excellent site for temperature measurements, it is well-known that the readings from commercial ear thermometers are lacking in repeatability and accuracy [84] [87] [89] [93]. One main reason for this phenomenon is the different ear anatomy from one person to the next, and thus the

difficulty in the design of a general-purpose probe which can be inserted into the outer ear with good sealing from the environment and with the probe distal end well directed at a desirable measurement point. This issue warrants an initial investigation on the ideal measurement point or region within the ear. The finding indicates the importance to orientate the probe to a specific ear anatomy. Previous studies [102] [103] have shown that arbitrary measurement points on the TM can lead to measurements that are very sensitive to external effects such as face cooling.

Brinnel and Cabanac [104], and Sato *et al* [105] proposed probes engaging the TM surface at restricted points on the TM, but the exact location of these points were not clear nor in concurrence. Brinnel and Cabanac suggested a measurement spot at the lower anterior quarter of the TM would have the highest temperature and is least sensitive to head or face cooling. Sato *et al* also sought to find the hottest spot on the TM with trial and error by positioning the probe until the hotspot was found. The probe was engaged to the TM at all the measurement points so that the results can be interpreted on a level field with respect to the convective heat losses which will be minimized with contact. This common requirement to physically engage the TM is reasonable and sound since the TM is not flat but conically shaped. Engaging the TM is a way to ensure all temperatures are taken at the same proximity to the TM in order to fairly select the hottest spot. However, in practice, it is unrealistic and unsafe to take T_{tm} measurement this way, with the probe engaging the TM in a conscious individual.

The selection of the hottest spot is a common recommendation from the above

mentioned studies [104] [105], though Sato *et al* did not put a boundary to the spot while Brinnel and Cabanac suggested the lower anterior quarter shown in Figure 3.2. Choosing the spot with the highest temperature is reasonable too since this is likely to be the point where it is most stable against environmental influence. However, it is noteworthy that these experiments were conducted in settings wherein the environment temperature was lower than the CBT. Should the opposite happen, heat flow would change direction and the coolest point could be sought instead when the body seeks to thermoregulate and maintain CBT against external heat stress.

Preliminary tests and simulation were done to explore the uniformity of temperature distribution on the TM. A non-contact thermopile sensors array (TSA) was used to measure the surface temperature of the TM of a healthy volunteer. A clinical speculum of an appropriate size was first inserted into the ear canal to straighten it. The TSA was positioned within the speculum to measure the temperature of the exposed TM. The Melexis MLX90620 TSA [67] was used which contains 64 infrared pixels arranged in a 16×4 rectangle area with an optical field of view of 60° to detect infrared induced thermal radiation. It can measure temperatures without making direct contact with the TM. Each pixel has a 16-bit temperature measurement resolution, and all pixels have been factory calibrated with an accuracy of $\pm 1.5^\circ C$ for temperature measurements within the range of 0 to $50^\circ C$. Figure 3.3 depicts the measurement results showing the flattened temperature uniformity map of the ear canal space wherein the dotted line rectangle contains the temperature measurements of the TM. Here, the interest is to show up the temperature deviation across the TM and the canal area. Thus,

different shades of color were used represent the relative temperatures. Shades of blue represents the lowest temperature, followed by green, yellow and red (highest temperature). In this measurement, due to the anatomical constraint, only half of the TM was exposed to the direct line of sight of the TSA. The measured temperatures are non-uniform across the view window including the TM. The measurement results in Figure 3.4 show the effects of face cooling. In general, with the cooling, it can be observed that the TM temperatures as well as those at the surrounding ear canal walls lowered in response to the cooling, though not at the same proportion. The region with the highest temperature is observed (and marked as "TMA") within the demarcated TM area. The "TMA" area in Figure 3.4 is observed to be less sensitive to the effects of face cooling.

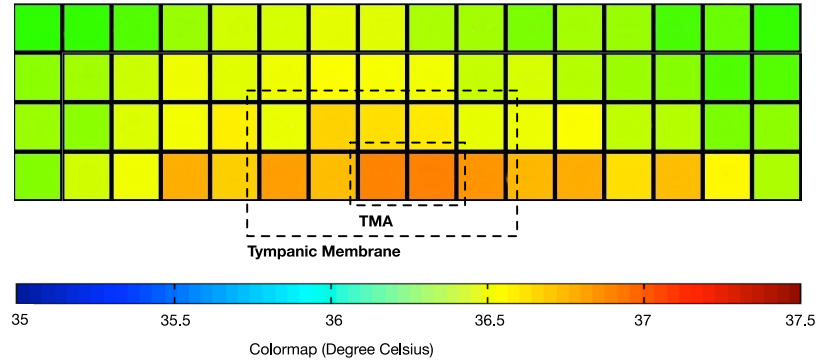


Figure 3.3: Temperature uniformity map of the left ear.

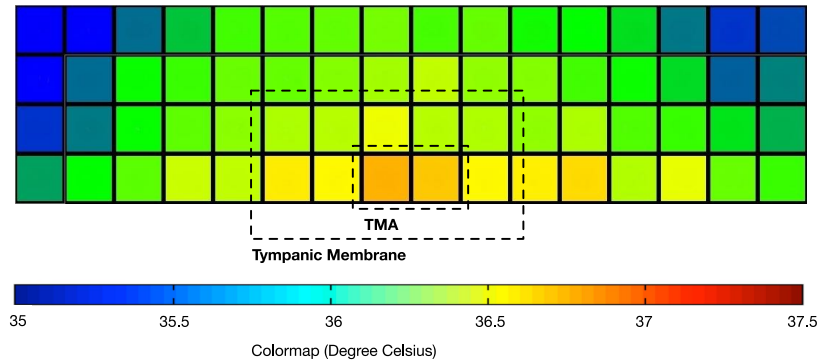


Figure 3.4: Temperature uniformity map of the left ear under face cooling.

Finite Element Analysis (FEA) simulation was performed on a model of a human ear canal (EC) and ME compartment (Figure 3.5). The tissues and bones parameters were selected to closely match those of reported human tissues and bones at these two sites. The purpose of the FEA is to verify the temperature non-uniformity on the TM surface and at 1mm above the surface. The TM was modeled as a circular disc of 9mm in diameter and 0.1mm thick with malleus, incus and stapes bones attached from behind, and the front attached to the EC. The EC was modeled as an air filled hollow cylinder of 9mm in diameter and 25mm in length. The ME was modeled as a rectangular compartment with six walls, and the TM was attached to the lateral wall. It is assumed that the superior wall is near to the brain, the inferior wall near to the carotid artery supplies the main heat source to the ME compartment and the perfused tissues surrounding the ME and the EC serve as heat sources. In the FEA simulation, the initial steady state temperatures of the malleus, incus and stapes bones location within the enclosed ME were correlated to the heat emitted from the brain, the carotid artery and the perfused tissues.

The TM temperature uniformity map of the TM surface is shown in Figure 3.6(a). From this simulation, the area near to the malleus bone is observed to register the highest temperature. This may indicate that the point of maximum temperature may not necessarily always be sited in the lower anterior quadrant [104] and depending on individual ear anatomy may lie elsewhere. The temperature uniformity map at 1mm above the TM surface is depicted in Figure 3.6(b). Here, while the temperatures may be lower generally due to convective losses, the uniformity has remained rather consistent with the that at the TM

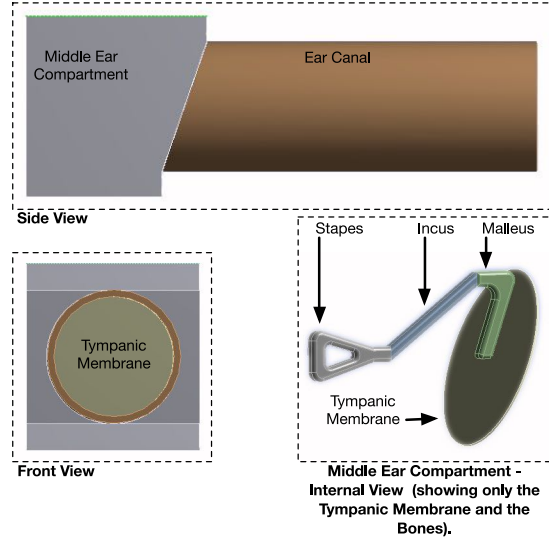


Figure 3.5: Human Ear Model used in Finite Element Analysis.

surface (Figure 3.6(a)). It may not be necessary to physically engage the TM for the purpose of locating the highest temperature point.

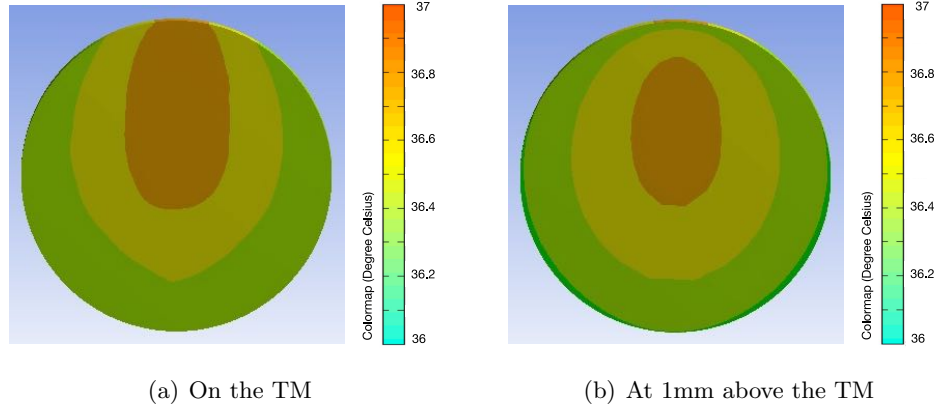


Figure 3.6: FEA showing temperature uniformity

With these observations, the next aim is to experimentally obtain temperatures at accessible and potential points on the TM without a physical engagement of the TM, but maintaining the same small but uniform proximity from probe to TM, using a modified probe capable of proximity sensing. Temperature uniformity of these points on the TM would be recorded and verified, and from the

results, select the most appropriate point for measurement. As potential candidates, the selected points are: (a) a point in front of the malleus bone (Point A1), (b) a point in the lower anterior quarter (Point B1), and (c) a point at the distal end of the ear canal nearest to the TM (Point C1) (Figure 3.7). Point A1 was chosen because the tissue near to the malleus is thicker and accordingly a likelihood of a higher concentration of blood vessels [110]. Our conjecture, following the FEA analysis, is that this point has a larger thermal mass than those further away from the malleus bone. Point B1 is at the lower anterior quarter of the TM. It was selected as suggested by Brinnel and Cabanac [104]. Point C1 lies on the canal just adjoining to the TM. It was selected to serve as a comparison to A and B measurements, and it would represent the point at which temperature is typically taken with a wrongly directed ear thermometer.

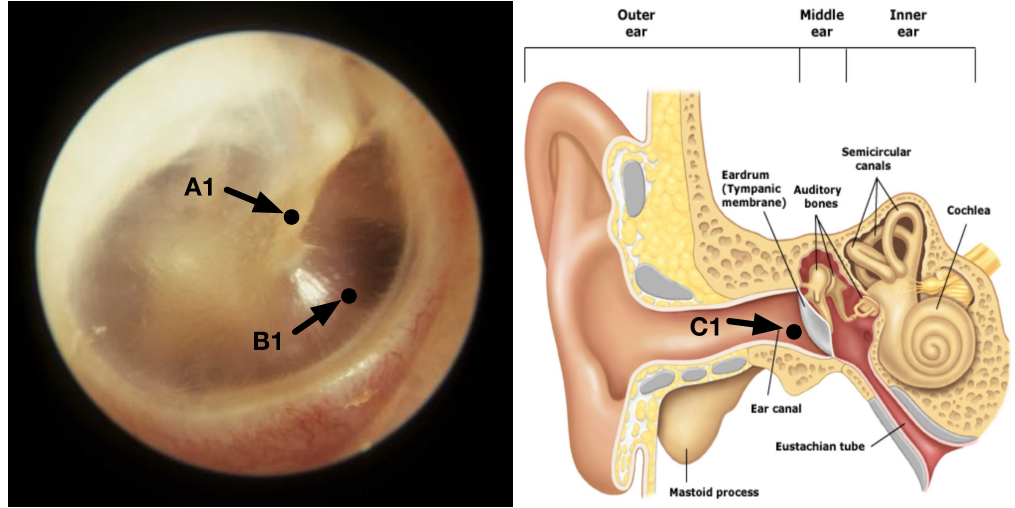


Figure 3.7: TM of the right ear with temperature measuring points labeled as A1, B1 and C1.

Experiment 1 was conducted to enable this investigation. In Experiment 2 on a sedated primate, the effects of facial cooling on T_{tm} were verified by measuring T_{tm} in both ears but fanning only one side of the face. The effects on other CBT

sites, including the ES and RM, would also be studied.

The outcomes from this investigation will be beneficial in the design of ear thermometers to infer a temperature that is most representative of CBT.

3.2.3 ME Cavity as CBT Site

As explained in Section 3.1, the ME cavity is closest to the brain than the other CBT sites. It holds unexplored potential to be an usable CBT measurement site. Till recently, accessing the ME space is challenging and it is not a natural approach for the purpose of taking a temperature reading. However, with the advent in technology, it is now a simple office-based procedure [107] [108] to incise a small opening in the TM and to maintain a small opening with a ventilation tube. An alternate access to the ME space is via the Eustachian tube which can be facilitated too in an office setting.

An experiment (Experiment 3) on a sedated primate was completed to log temperatures from the middle ear and other CBT sites (ES, RM) under passive hyperthermia. A Cynomolgus monkey age 6 years old weighting 5 Kg was used for the experiment. In addition, it is known that the administration of GA will lower CBT [83] [55]. An interesting time window, when the GA is removed during the experiment, is available for scrutiny into the relative responsiveness of the CBT candidates following a change in CBT due to the influence of GA.

From the results of these tests in Experiment 3, the temperature measured at two different points on the TM are compared against the temperature measured from the ME (presumed as the CBT benchmark) to show the sensitivity of the T_{tm} measurements with respect to locations.

3.3 Re-visiting the TM Vicinity: Design of Experiments and Equipments

The setup of the experiments and the procedures prescribed are highlighted to provide the background in the interpretation of the experiments and results subsequently. The key equipment used in these experiments include the temperature probes and the custom heating chamber. The details of these equipment are given in the ensuing subsections.

3.3.1 Temperature Probes

Clinical temperature probes supplied by Exacon Scientific A/S were used in the experiments (Figure 3.8). The thermistor-based probes for measuring T_{tm} , T_{me} , T_{es} and T_{rm} have a consistent measurement accuracy of ± 0.1 °C for a temperature range between 25 and 50 °C. The National Instruments Data Acquisition (NI-DAQ) system was used with a custom-built temperature recording software for automated temperature data acquisition from the attached temperature probes. The sampling interval was set to 0.1 second. The probes were first calibrated by immersing them in a glass container with 500ml of distill water at an initial temperature of 30 °C. The glass container was placed in a heating chamber with the interior air temperature set to 65 °C. The water was slowly heated within the chamber until it reached the target temperature of 50 °C. The variations in temperature were logged for each of the probes. Using the temperature profile of the T_{rm} probe as a reference, the calibration curves were derived for each of the temperature probes to ensure they were equalized to give homogeneous response in the experiments.

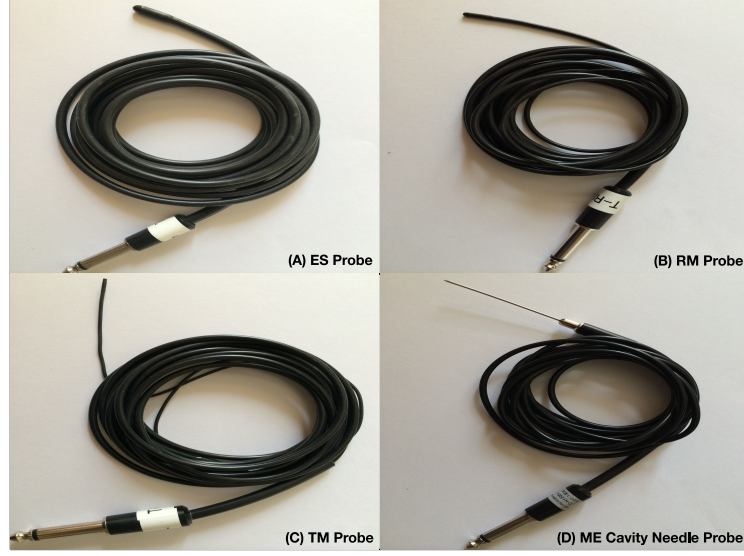


Figure 3.8: Clinical Temperature Probes supplied by Exacon Scientific A/S for use in Experiments 1 - 3.

In Experiment 1, it was a deliberate intent that, unlike previous work, the probe would not physically engage the TM at these points, but at a very small but consistent proximity to them to observe the temperature difference between them in a way more typical of how a TM temperature is taken. Modification to the T_{tm} probe was done to achieve this. It was retrofitted with a Keyence Reflective Fibre Unit (Model: FU-46 attached to a matching Fibre Amplifier Model: FS-N11N) at 1mm behind the sensing tip (Figure 3.9). This allowed the handler of the probe to be prompted when the probe was brought to a distance of $<1\text{mm}$ from the defined measurement point for temperature measurement.

3.3.2 Heat Chamber and Probes Setup

A custom-built heat chamber similar to a small size incubator was designed and fabricated for the purpose of elevating the primate's body temperature (full body passive hyperthermia) under controlled environment (Figure 3.10) in Experiments 2 and 3. The primate was sedated with GA in the chamber with

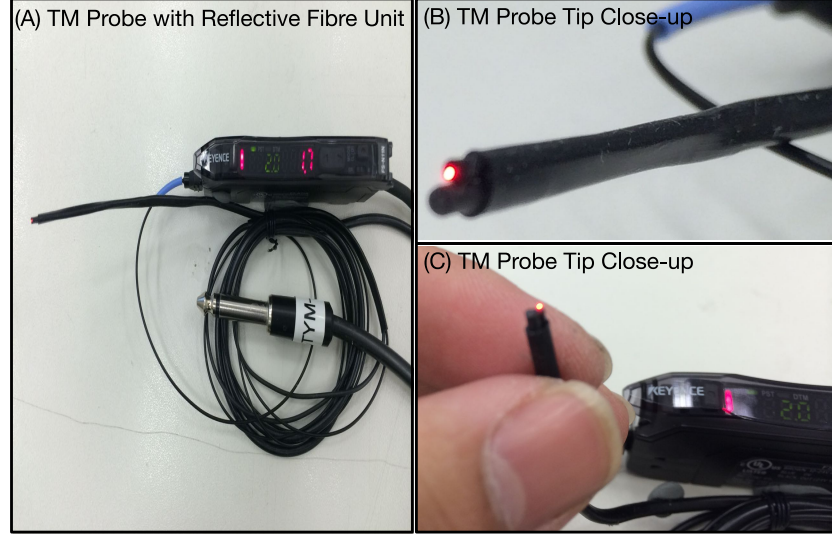


Figure 3.9: Clinical TM Probe supplied by Exacon Scientific A/S retrofitted with a Keyence Reflective Fibre Unit for use in Experiment 1.

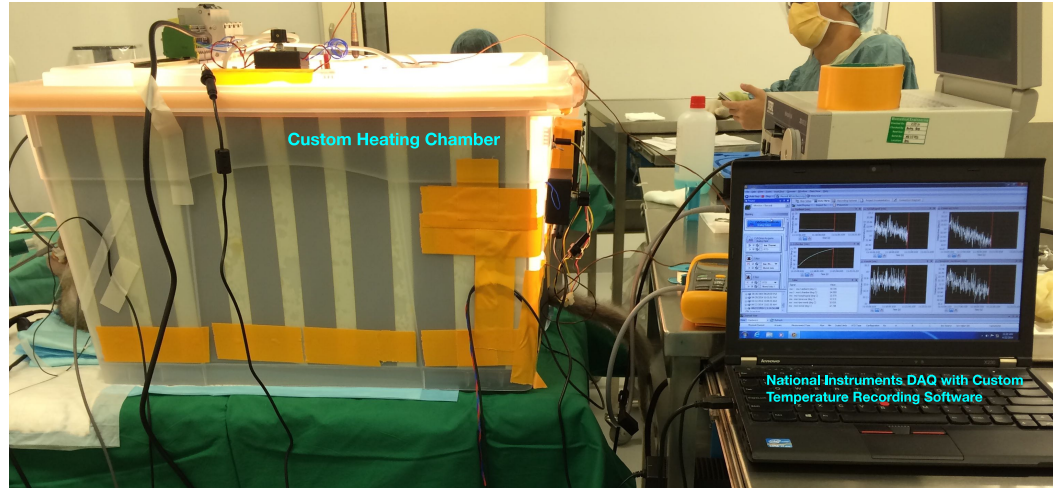


Figure 3.10: Custom heating chamber constructed for use in Experiments 2 - 3.

the body from the neck downwards fully enclosed within the chamber. Only the head was exposed to external ambient temperature of the clinic (T_{am}). The trapped air in the interior of the chamber was heated with a 300W electric filament heater to reach a chamber temperature ($T_{ch} = 65\text{ }^{\circ}\text{C}$). Fans, controlled by an electronic thermostat, were used to circulate the heated air in-order to ensure temperature was distributed evenly $T_{ch} \pm 2\text{ }^{\circ}\text{C}$ within the chamber. T_{ch} was

maintained until the primate's esophageal temperature reached 42 °C (the limit approved by IACUC), after which the heater was turned off before the chamber was opened to begin the cool-down process. Temperature probes were inserted into the primate's body at defined measurement locations to measure the temperatures at these sites. Additional probes were used to measure T_{ch} and T_{am} . Measurements were sampled every 0.1 second interval at each of the temperature probes. The raw temperature data sampled from the temperature probes were processed to remove noises and calibrated to ensure uniform responses. The procedures behind the three controlled experiments are elaborated in the ensuing subsections.

3.3.3 Scientific Validity of the Primate Experiments

Several independent studies have examined the thermoregulatory responses of primates to heat exposures. Resting and exercise studies have primarily concentrated on mechanisms of thermal balance [111–114], metabolic rate [113], and manipulation of central mechanisms responsible for thermoregulation activities [115–117]. Gisolfi *et al* [111] and Johnson *et al* [112] independently demonstrated in experiments that the active eccrine sweat glands in the hairy skin of a primate is similar to those of a human, and the physiological control of evaporative heat loss due to eccrine sweating in the primate is also very similar to that found on human. The findings suggested that the primate can serve as an excellent thermoregulatory model to study physiology of sweating.

Johnson *et al* [113] performed a thermal balance study on four male unanesthetized, non heat-acclimated primates and observed that the physiological control of eccrine sweating and metabolic heat production, and the physiological

control of evaporative heat loss due to eccrine sweating in the primates are similar to that found in human. Oddershede *et al* [114] performed an experiment that observed the primate's body fluid and hematologic adjustments during heat acclimation. The experiment has provided a complete body fluid compartment analysis during heat acclimation in the primate, and suggested that the primate may serve as a primate model for further studies of body fluid shifts during long-term resting controlled heat acclimation that cannot be safely performed on a human.

Barney *et al* [115], Gisolfi *et al* [116] and Myers *et al* [117] manipulated the primate's central mechanisms responsible for thermoregulation activities with physiologically active lipid compounds [118] and Calcium compounds in experiments that cannot be safely and ethically performed on a human. The experiments documented the primate's body thermoregulatory responses to the various chemical compounds used that may be useful in studies related to hyperthermia and temperature acclimation.

Heaps *et al* [119] demonstrated that primate can be used as a research model for the associated fatigue factors during exercise and heat stress by integrating the exercise into a multidimensional primate model originally proposed by Constable *et al* [120]. The study was designed to establish baseline data on the physiological and metabolic responses of the primate to exercise at three environmental temperatures (15, 25 and 35 °C). These measures allow some comparison of the responses of the primate to that of humans to determine the potential validity of the use of the primate as a model for metabolic and environmental stress research. The study characterized the metabolic and thermoregulatory

responses of primates base on two common occupational stress mechanisms: (a) work, and (b) varied environmental heat load, and compared the responses of the primates to that of humans.

Overall, the studies have consistently demonstrated many similarities between the thermoregulatory systems of primates and human subjects, demonstrated that the primate exhibits a physiological response to exercise stress similar to that seen on human, and validated the use of primate as a model for metabolic and environment stress research. Thus, a primate is considered as an appropriate model for conducting selected thermoregulatory experiments due to the reason that research in the area of physiological stress cannot always be performed with human subjects for various safety and ethical reasons.

3.3.4 Experiment 1

In Experiment 1, temperature measurements using the probe (retrofitted with proximity sensing) were taken at the defined points (A1, B1 and C1) on the TM surface of a healthy human adult volunteer.

The ear canal has a diameter of about 5-8mm in adults. Even though the modified probe has an outer diameter of 2.3mm, there is limited manoeuvring space to accurately access more points and not cause distress to the volunteer. The three points (A1, B1 and C1) defined earlier in Section 3.2.2 were located for measurements; Point A1 in the vicinity of the malleus bone, Point B1 in the lower anterior quarter, and Point C1 at the distal end of the ear canal closest to the TM as shown in Figure 3.7.

Under the view of a surgical microscope in a clinical setting with an ambient temperature of 22.5 °C, an otolaryngologist guided the modified probe to the

three points. The proximity sensor provided an alert when the probe reached a preset value of 1mm from the TM. The same proximity was observed for measurements at all the three points. Steady state temperatures were logged after the measurements have stabilized.

3.3.5 Experiment 2

Experiment 2 was conducted to observe the effects of facial cooling on T_{tm} , T_{es} and T_{rm} measurements. Probes were inserted by a veterinarian into a sedated primate to acquire real-time temperatures at these sites when it is placed within the heat chamber set to a temperature of $T_{ch} = 65\text{ }^{\circ}\text{C}$. At the mid-point during the passive hyperthermia process, convection skin cooling was initiated at the head area near to the left ear (left face fanning) by blowing cold air at $T_{am} = 20\text{ }^{\circ}\text{C}$ with a small electric fan. The head area near to the right ear was shielded from the cooling process. Four temperature probes were used throughout the experiment: (a) Left TM probe touching the left TM's surface for measuring $T_{tm,L}$, (b) Right TM probe touching the right TM's surface for measuring $T_{tm,R}$, (c) RM probe was inserted via the anal sphincter for measuring T_{rm} , and (d) Esophageal probe was inserted into the esophagus for measuring T_{es} .

3.3.6 Experiment 3

In Experiment 3, the temperature of ME cavity was measured, for the first time, on its suitability as an inference to CBT. There were two parts to this experiment: Experiment 3A and Experiment 3B. In Experiment 3A, T_{me} was benchmarked against T_{tm} and T_{rm} with the sedated primate undergoing full body hyperthermia within the chamber set to $T_{ch} = 65\text{ }^{\circ}\text{C}$. Note that Experiment

2 and Experiment 3 were carried out on the same primate but the trials were separated by two months. Three temperature probes were used: (a) A needle probe to perforate the left TM to reach the ME ear cavity just in front of the malleus bone for measuring T_{me} , (b) TM probe engaging the right TM's surface to measure T_{tm} , and (c) RM probe inserted via the anal sphincter to measure T_{rm} .

Experiment 3B presented an ideal opportunity in the experiment setting to trigger a change in the CBT and to observe the relative measurements at various sites including the ME. The CBT trigger (approved by IACUC) was achieved by halting the administration of GA for 15 minutes, 2 hours and 51 minutes into the experiment. An additional probe was inserted into the primate's esophagus to measure T_{es} . Thus, a total of four temperature probes were used to each measure T_{me} , T_{tm} , T_{es} and T_{rm} throughout this experiment.

Two different spots were selected on the TM for the measurements of T_{tm} in Experiments 3A and 3B. By comparing with T_{me} , the sensitivity of the measurement points on T_{tm} could also be observed.

3.4 Re-visiting the TM Vicinity: Results and Discussions

The results from the experiments are interpreted and analyzed according to the two focal points of the paper.

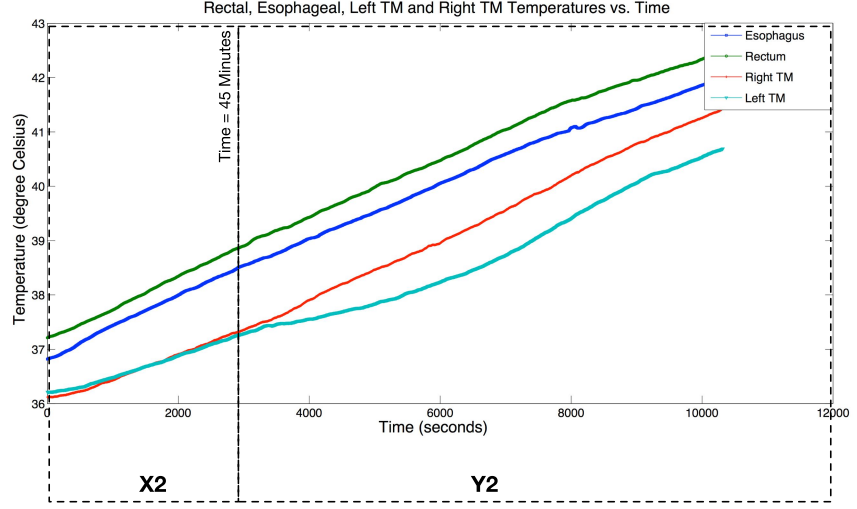


Figure 3.11: ES, RM and TM (left and right) temperature plots for primate body temperature measurement. Experiment results are split into two test scenarios for Experiment 2: (1) X2 - Full Body Hyperthermia, and (2) Y2 - Full Body Hyperthermia with Left Face Fanning.

3.4.1 Temperature Uniformity in the TM Vicinity and Measurement Point Selection

The ambient temperature T_{am} , $T_{tm,A}$ at point A1 and $T_{tm,B}$ at point B1 of the TM, as well as the ear canal temperature T_{cn} at Point C1 were measured as 22.5, 37.0, 36.4 and 36.1 °C respectively at steady state. As suggested by Sato *et al* [105], the spot with the higher temperature is the preferred spot since this point is likely to be the least sensitive to ambient disturbances. An interesting observation from the results is that Point B1 registered a lower temperature than Point A1, and Point B1 is within the lower anterior quadrant of the TM suggested by Brinnel and Cabanac [104] to capture a temperature measurement. These results show that arbitrary point selected in this region may not necessarily return a highest temperature compared to other points on the TM surface. If such a point does exist in this quadrant, it may require a search over the zone to pick up the highest temperature point. On the other hand, Point A1 which is at

the malleus bone can be more easily located to focus the probe at. This is also intuitive since Point A1 is at the part of the TM which is thicker compared to the lower anterior quadrant and that may translate into a higher thermal resistance against ambient disturbances, as the FEA also showed.

The stability of $T_{tm,A}$ was additionally studied for resilience against temperature rise at the skin from peripheral vasodilation. The subject did a very short exercise of push-ups and sit-ups lasting at a leisurely pace over not more than 5 minutes, to induce metabolism to increase at the legs, hands and stomach muscles. Over this short duration, the body's thermoregulatory system is expected to seek a balance between the maintenance of the body's core temperature and the release of perspiration to cool the body. Thus, vasodilation will occur to cause an increase in blood flow to transport excess heat generated from affected muscle tissues to the skin. Measurement taken at the canal (Point C1) registered a rise to $36.7\text{ }^{\circ}\text{C}$ while $T_{tm,A}$ remained resilient at the same $37.0\text{ }^{\circ}\text{C}$.

The sensitivity and effects of facial cooling on the temperatures from the various measurement sites can be observed from the results of Experiment 2. The initial temperature readouts from the temperature probes attached to the primate's body were: (1) Rectum, $T_{rm} = 37.2\text{ }^{\circ}\text{C}$, (2) Esophagus, $T_{es} = 36.8\text{ }^{\circ}\text{C}$, (3) Left-TM surface, $T_{tm,L} = 36.2\text{ }^{\circ}\text{C}$, and (4) Right-TM surface $T_{tm,R} = 36.1\text{ }^{\circ}\text{C}$. 45 minutes into the experiment, convection skin cooling was introduced at the head area near to the left ear (left face fanning). Figure 3.11 shows the collected temperature readings at the four measurements points on the primate's body. For clarity of view and interpretation, the plot is split into the two different test scenarios: (1) X2 - Full Body Passive Hyperthermia only, and (2) Y2 - Full

Body Passive Hyperthermia with Left Face Fanning. T_{es} served as the reference temperature to compare against the $T_{tm,L}$ and $T_{tm,R}$.

Figures 3.12(A) and 3.13(A) respectively show the relationships, between $T_{tm,L}$ and T_{es} , and between $T_{tm,R}$ and T_{es} over the full time period of Experiment 2 ($X2 + Y2$ test scenario). The corresponding Bland-Altman plots are shown in Figures 3.12(B) and 3.13(B). Correlation analyses show strong correlations between T_{es} and both $T_{tm,L}$ (Pearson correlation coefficient (r) = 0.982, Sum of Squared Error (SSE) = 0.25, Probability in support of a null hypothesis (p) < 0.001) and $T_{tm,R}$ (r = 0.996, SSE = 0.15, p < 0.001). r indicates that the closer the coefficients are to +1.0 or -1.0, the greater the strength of the linear relationship. p indicates the likelihood the observed results are due to chance. Bland-Altman analyses show the mean differences (MD) between these temperatures ($T_{tm,L}, T_{es}$) and ($T_{tm,R}, T_{es}$) are $-1.408^{\circ}C$ and $-0.963^{\circ}C$, and the $1.96SD$ are $-0.768^{\circ}C$ and $-0.606^{\circ}C$, respectively. No proportional errors are observed since there is no correlation between the x and y variables in the Bland-Altman plots. The dynamic response of T_{es} , $T_{tm,L}$ and $T_{tm,R}$ are stable and steadily increasing with chamber heating. Both $T_{tm,L}$ and $T_{tm,R}$ indicate very strong correlations with T_{es} with $r \rightarrow 1$ even with left face fanning throughout the experiment ($X2 + Y2$ test scenario) though the correlation is higher on the right side. However, the respective SSE and $|MD|$ vary clearly with $SSE = 0.25$ and $|MD| = 1.408^{\circ}C$ for $T_{tm,L}$, and $SSE = 0.15$ and $|MD| = 0.963^{\circ}C$ for $T_{tm,R}$. Notably, there is a 40% in reduction of SSE , and 31.6% in reduction of $|MD|$ for $T_{tm,R}$, compared to $T_{tm,L}$. Thus, the effects of face fanning on T_{tm} can be observed from this analysis.

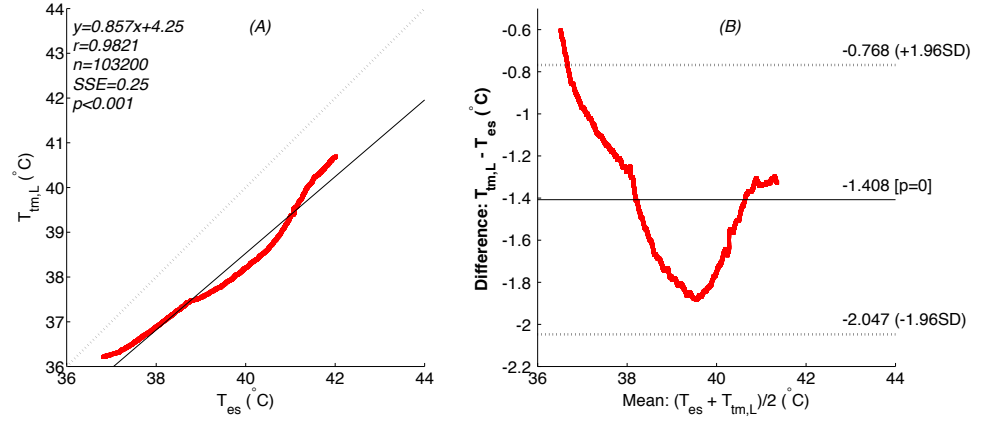


Figure 3.12: Analytical results for Experiment 2 that illustrate the effects of full body hyperthermia + full body hyperthermia with left face fanning ($X2 + Y2$ test scenarios) on the left TM temperature. (A) Relationship between left TM temperature ($T_{tm,L}$) and ES temperature (T_{es}), and (B) the respective Bland-Altman plot.

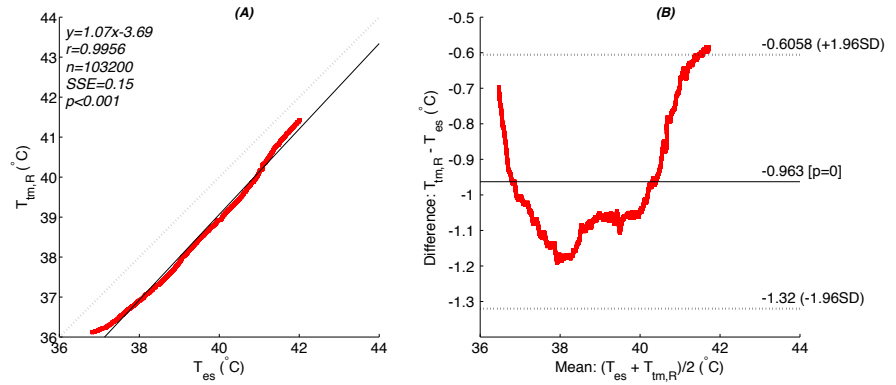


Figure 3.13: Analytical results for Experiment 2 that illustrate the effects of full body hyperthermia + full body hyperthermia with left face fanning ($X2 + Y2$ test scenarios) on the right TM temperature. (A) Relationship between right TM temperature ($T_{tm,R}$) and ES temperature (T_{es}), and (B) the respective Bland-Altman plot.

The earlier analysis was done to compare T_{tm} in both ears with one side of the face undergoing fanning. It will be interesting too to examine the correlation on the side with fanning, before and after the onset of fanning. This analysis will show too if it is feasible to adopt a single CBT inference model

for T_{tm} in the presence of such ambient interactions. To this end, the experimental data in Figure 3.11 is partitioned into two sets corresponding to the $X2$ and $Y2$ tests scenarios (i.e., at $t = 45$ minutes) and performed similar analyses as in Figure 3.12. Figure 3.14 and 3.15 show the correlation and Bland-Altman plots for the $X2$ test scenario for both ears, and Figure 3.16 and 3.17 show the same for the $Y2$ test scenario. Correlation analyses demonstrate strong correlation between the T_{es} and both $T_{tm,L}$ ($r = 0.994, SSE = 0.033, p < 0.001$) and $T_{tm,R}$ ($r = 0.995, SSE = 0.036, p < 0.001$) for $X2$, and $T_{tm,L}$ ($r = 0.98, SSE = 0.21, p < 0.001$) and $T_{tm,R}$ ($r = 0.998, SSE = 0.078, p < 0.001$) for $Y2$. Bland-Altman analyses indicate values of MD and $1.96SD$ between the T_{es} and both $T_{tm,L}$ ($MD = -0.978^\circ C, 1.96SD = -0.647^\circ C$), and $T_{tm,R}$ ($MD = -0.999^\circ C, 1.96SD = -0.763^\circ C$) for $X2$, and $T_{tm,L}$ ($MD = -1.56^\circ C, 1.96SD = -1.141^\circ C$), and $T_{tm,R}$ ($MD = -0.95^\circ C, 1.96SD = -0.562^\circ C$) for $Y2$. The values of SSE and $|MD|$ prior to the introduction of left face fanning ($X2$ test scenario) are relatively small at 0.033 and $0.978^\circ C$ respectively for left ear, and at 0.036 and $0.999^\circ C$ respectively for right ear, and both left and right ear have very similar values. With the introduction of fanning ($Y2$ test scenario), SSE and $|MD|$ are 0.21 and $1.56^\circ C$ respectively for left ear, and at 0.078 and $0.95^\circ C$ respectively for right ear. Data for both ears are being compared during fanning and observe that SSE and $|MD|$ are relative higher for the left ear than the right ear. This issue highlights the difficulty of using a soft approach to infer the CBT solely from T_{tm} when it is affected by other factors such as environmental disturbances in this case. Measurements of these disturbances are necessary to serve as additional inputs to the model. To minimize these effects, a spot on

the TM which is resilient to these effects would be necessary.

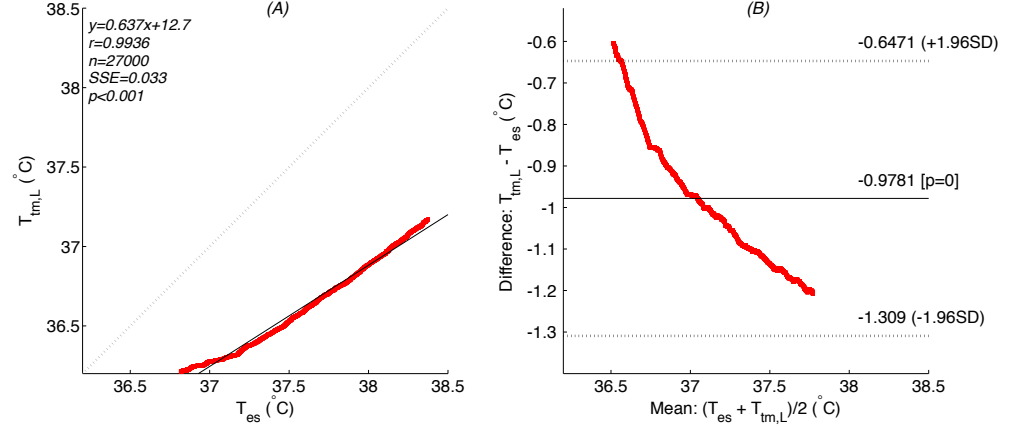


Figure 3.14: Analytical results for Experiment 2 that illustrate the effects of full body hyperthermia ($X2$ test scenario) on the left TM temperature. (A) Relationship between left TM temperature ($T_{tm,L}$) and ES temperature (T_{es}), and (B) the respective Bland-Altman plot.

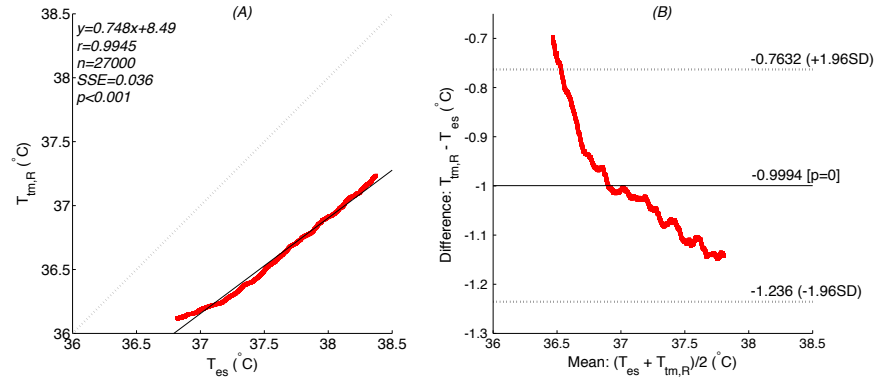


Figure 3.15: Analytical results for Experiment 2 that illustrate the effects of full body hyperthermia ($X2$ test scenario) on the right TM temperature. (A) Relationship between right TM temperature ($T_{tm,R}$) and ES temperature (T_{es}), and (B) the respective Bland-Altman plot.

Figure 3.18(A) depicts the relationships, between T_{rm} and T_{es} measured during the experiment for the full time period of Experiment 2 ($X2 + Y2$ test scenario). The corresponding Bland-Altman plot is shown in Figures 3.18(B). Correlation analysis indicate close to perfect correlation ($r \rightarrow 1$) between the

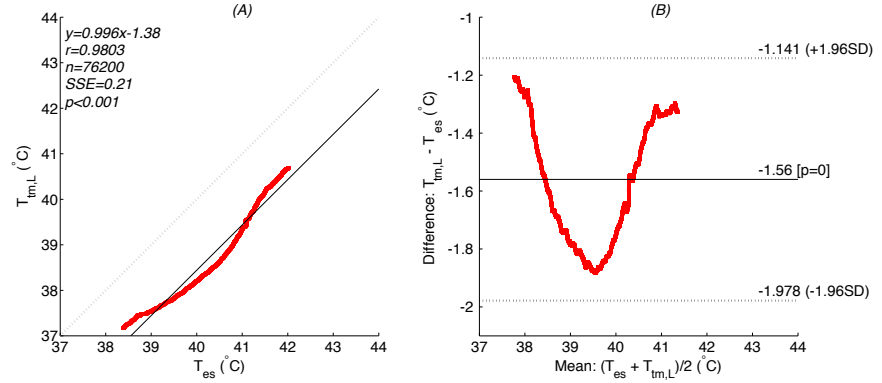


Figure 3.16: Analytical results for Experiment 2 that illustrate the effects of full body hyperthermia with left face fanning (Y2 test scenario) on the left TM temperature. (A) Relationship between left TM temperature ($T_{tm,L}$) and ES temperature (T_{es}), and (B) the respective Bland-Altman plot.

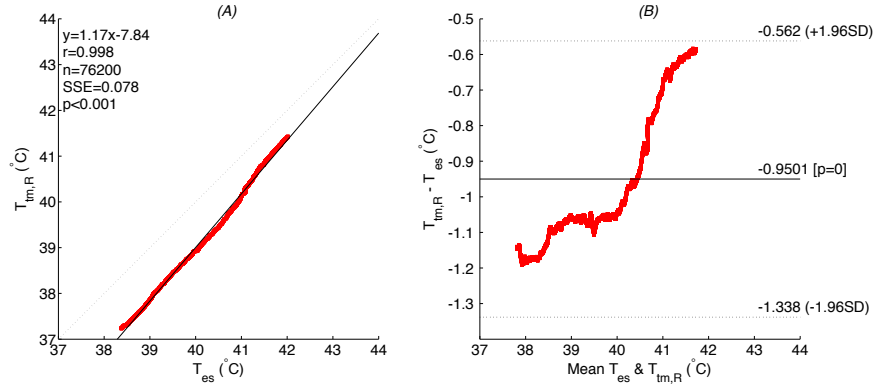


Figure 3.17: Analytical results for Experiment 2 that illustrate the effects of full body hyperthermia with left face fanning (Y2 test scenario) on the right TM temperature. (A) Relationship between right TM temperature ($T_{tm,R}$) and ES temperature (T_{es}), and (B) the respective Bland-Altman plot.

T_{es} and T_{rm} ($r = 0.9998$, $SSE = 0.029$, $p < 0.001$). Bland-Altman analysis shows the mean difference between temperatures T_{rm} and T_{es} is $+0.428$ °C, and the 1.96SD is $+0.561$ °C. The data analyses clearly indicate that T_{rm} is not affected by left face fanning, hence incurring a comparatively small SSE and MD .

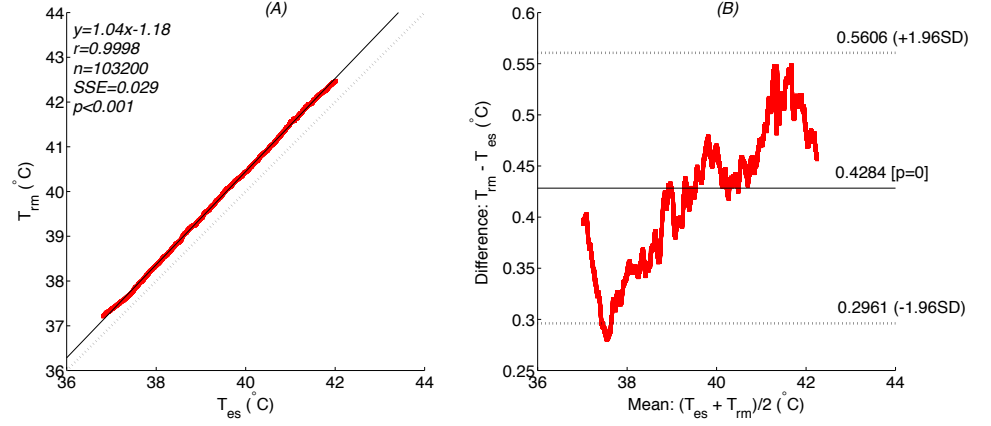


Figure 3.18: Analytical results for Experiment 2 that illustrate the effects of full body hyperthermia + full body hyperthermia with left face fanning ($X2 + Y2$ test scenarios) on RM and ES temperatures. (A) Relationship between RM temperature (T_{rm}) and ES temperature (T_{es}), and (B) the respective Bland-Altman plot.

3.4.2 ME Cavity as CBT Site

Figure 3.19 reflects temperature measurements from Experiment 3A at the various sites: (1) Rectum, measuring T_{rm} (reference point), (2) Left middle ear cavity, measuring T_{me} , and (3) Right TM, measuring $T_{tm,R}$.

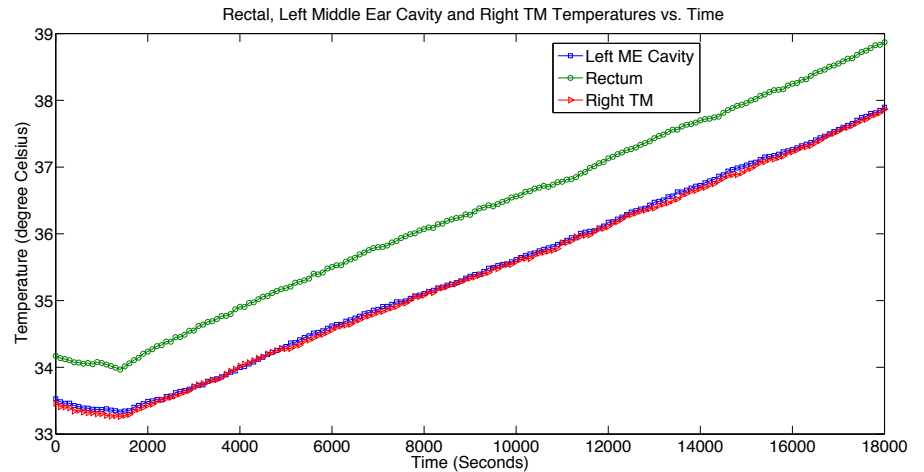


Figure 3.19: T_{rm} , T_{me} and $T_{tm,R}$ vs. Time plots that depict behavior of each measurement site in Experiment 3A (No GA Disruption).

Figures 3.20(A) and 3.21(A) show the relationships, respectively between

$T_{tm,R}$ and T_{rm} , and between T_{me} and T_{rm} over the full time period of Experiment 3A. The corresponding Bland-Altman plots are shown in Figures 3.20(B) and 3.21(B). Correlation analyses demonstrate very strong correlations ($r \rightarrow 1$) between the T_{rm} and both the $T_{tm,R}$ ($r = 0.9997, SSE = 0.03, p < 0.001$) and the T_{me} ($r = 0.9997, SSE = 0.029, p < 0.001$). Bland-Altman analyses show the MD between these temperatures ($T_{tm,R} - T_{rm}$ and $T_{me} - T_{rm}$) are $-0.968^\circ C$ and $-0.931^\circ C$, and the $1.96SD$ are $-0.855^\circ C$ and $-0.835^\circ C$, respectively, and no proportional errors are observed. The dynamic response of T_{rm} , T_{me} and $T_{tm,R}$ are stable and steadily increasing with the chamber heating. From the data analysis, all the temperature pairs are observed, their correlation coefficient $r \rightarrow 1$, which suggest strong correlation for each temperature pair, indicating T_{me} and $T_{tm,R}$ correlate very well with T_{rm} .

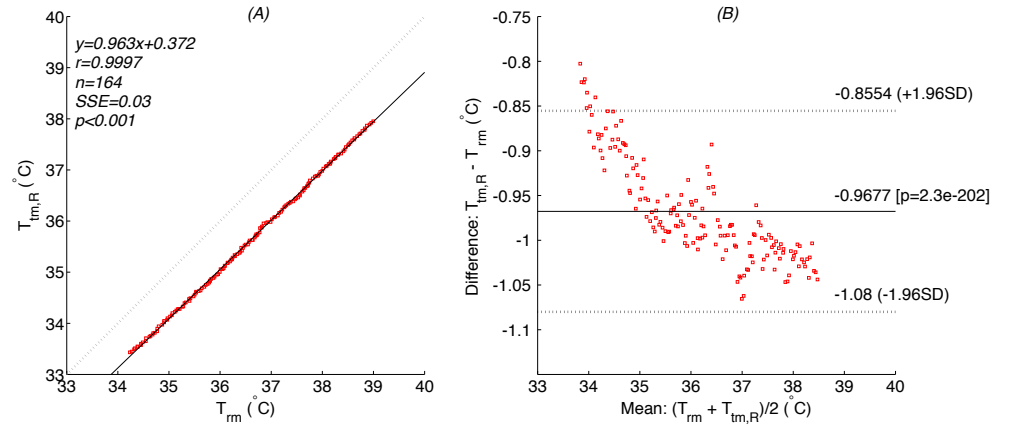


Figure 3.20: Analytical results for Experiment 3A that illustrate the effects of full body hyperthermia on the right TM temperature. (A) Relationship between right TM temperature ($T_{tm,R}$) and RM temperature (T_{rm}), and (B) the respective Bland-Altman plot.

In Experiment 3B, the effects of a GA disruption and the corresponding change in CBT were observed from temperature measurements at various sites. The procedures of Experiment 3A were again carried out and in addition, a probe

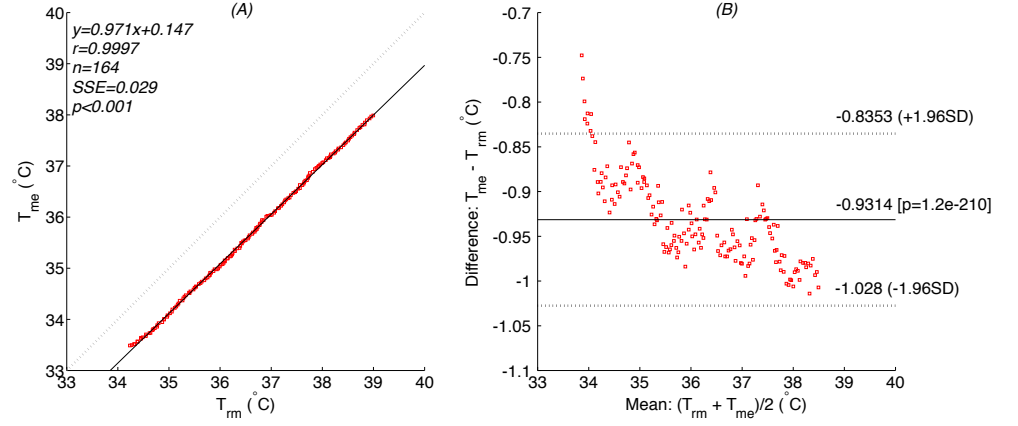


Figure 3.21: Analytical results for Experiment 3A that illustrate the effects of full body hyperthermia on the left middle ear cavity temperature. (A) Relationship between left middle ear cavity temperature (T_{me}) and RM temperature (T_{rm}), and (B) the respective Bland-Altman plot.

was inserted into the esophagus to measure T_{es} . At 2 hours and 51 minutes into the experiment, the administration of GA was stopped for 15 minutes. Figure 3.22 shows the measurements at all the selected sites during the time window when GA was disrupted.

It is well-known that the administration of GA will lower CBT [83] [55]. This was observed at the start of all experiments when GA was administered. Temperature measurements at all sites in steady state were well below the healthy temperature range. After GA was halted in Experiment 3B, Based on observation of Figure 3.22, a clear and steeper change in the gradient of T_{me} (marked with a circle in the figure) showing an increase in the rate of change of T_{me} . This observation is consistent with the presumption that the primate's body thermoregulation function was gradually being restored with the removal of GA. This phenomenon is only observed in the T_{me} measurements and not evident from a visual inspection of other measurements over the same duration.

Correlation analysis was carried out on the data tabulated in Figure 3.22.

The data was segmented into two measurement groups separated at $t = 2.85$ hours (2 hours and 51 minutes) boundary: (1) G_1 - Primate was administered with GA in a continuous and controlled manner, and (2) G_2 - GA administration to the primate was halted for 15 minutes.

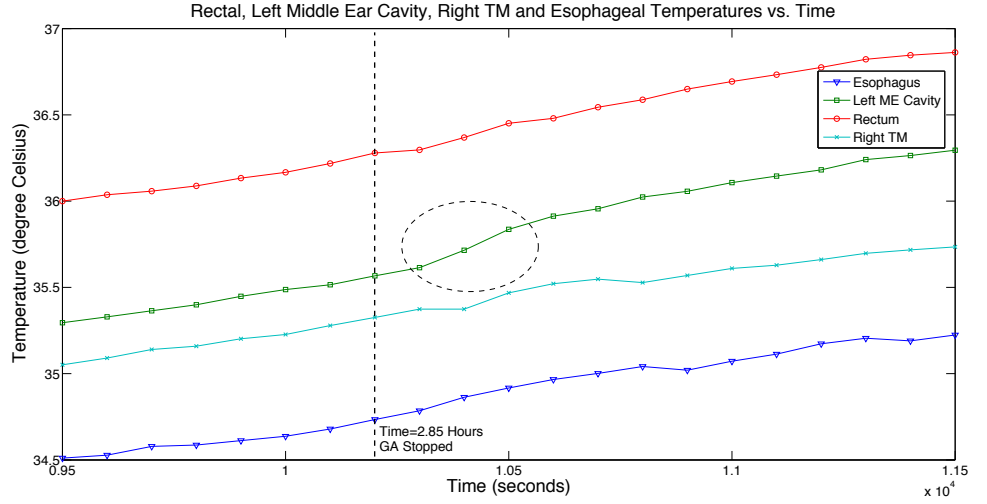


Figure 3.22: T_{rm} , T_{me} and $T_{tm,R}$ vs. Time plots that depict behavior of each measurement site with GA being disrupted in Experiment 3B.

The data in G_1 group was first analyzed. Figure 3.23 depicts (A) the correlations between T_{es} and T_{me} and (B) its corresponding Bland-Altman plot. Correlation analysis demonstrate strong correlation between T_{es} and T_{me} ($r = 0.995$, $SSE = 0.009$, $p < 0.001$). Bland-Altman analysis shows the mean difference between temperatures T_{es} and T_{me} is $+0.812^\circ\text{C}$, and the 1.96SD is $+0.851^\circ\text{C}$. The data in G_2 group was next analyzed and Figure 3.24(A) depicts the correlation between T_{es} and T_{me} , and Figure 3.24(B) its corresponding Bland-Altman plot. Correlation analysis still demonstrates a strong correlation between T_{es} and T_{me} ($r = 0.971$, $SSE = 0.02$, $p < 0.001$). Bland-Altman analysis shows the mean difference between temperatures T_{es} and T_{me} is $+0.852^\circ\text{C}$, and the 1.96SD is $+0.915^\circ\text{C}$.

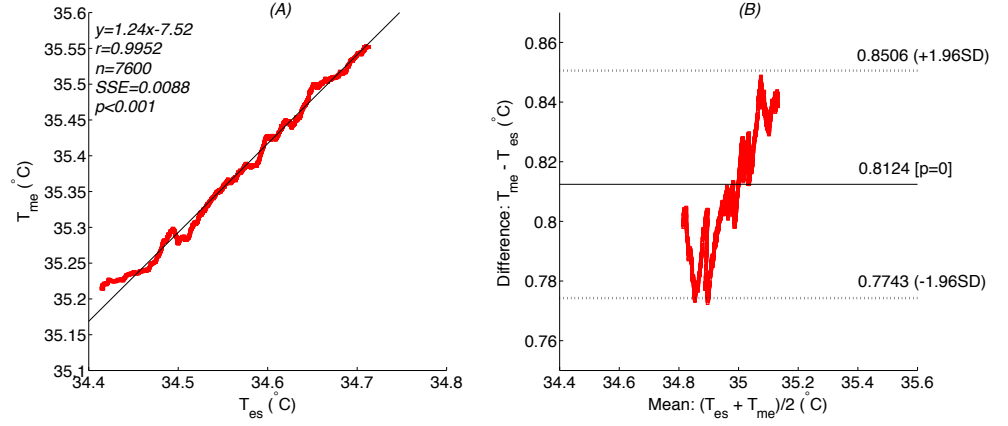


Figure 3.23: Analytical results for Experiment 3B that illustrate the effects of full body hyperthermia with GA on the left middle ear cavity temperature. (A) Relationship between left middle ear cavity temperature (T_{me}) and esophageal temperature (T_{es}), and (B) the respective Bland-Altman plot.

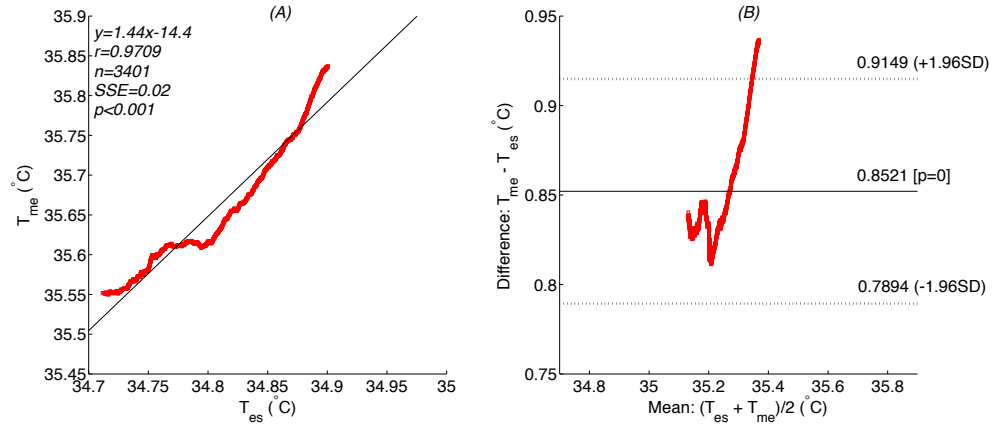


Figure 3.24: Analytical results for Experiment 3B that illustrate the effects of full body hyperthermia with GA halted (for 15 minutes) on the left middle ear cavity temperature. (A) Relationship between left middle ear cavity temperature (T_{me}) and esophageal temperature (T_{es}), and (B) the respective Bland-Altman plot.

For comparison purpose, similar analyzes were conducted for (T_{es} , $T_{tm,R}$) and (T_{es} , T_{rm}) for both G_1 and G_2 data groups. Figure 3.25 to 3.28 depict the correlation plots together with their respective Bland-Altman plots. A summary of results are shown in Table 3.1 with consistent $p < 0.001$ for all. From the table,

it can be observed that, $r \geq 0.99$, and $SSE \approx 0.01$ for all the temperature pairs in the G_1 group, showing they are very highly correlated for temperature data in the G_1 group.

A small drop in r is observed, and increase in SSE values when the data from G_2 group for the correlation pairs of (T_{es}, T_{me}) . Other correlation pairs consistently maintain $r \geq 0.99$ and $SSE \approx 0.01$ in both G_1 and G_2 groups. Thus, there is a deviation in T_{me} measurements following the GA change which is not seen in the other temperature measurements.

In addition, from the results of Experiments 3A and 3B, The differences between $T_{tm,R}$ and T_{me} are compared over two separate tests. Measurements of $T_{tm,R}$ were taken at two different points. An observation was made from from Experiment 3A, that T_{me} and $T_{tm,R}$ measurements were closely identical (Figure 3.19) and the measurements from Experiment 3B showed a notably greater difference between them with T_{me} being the higher measurement in both cases (Figure 3.22). In Experiments 3A and 3B, the temperature measurement points at the right TM were selected differently. The primate's ear canal is very restrictive (much more so than the human) to the insertion of the probe. There is no luxury of space to visually position the probe. In Experiment 3A, the vet could feel the presence of the bone when he engaged the TM with the probe, but in Experiment 3B, there was no 'hard' contact feel. Thus, two distinctly different points could be invariably used in the experiments. Hence, the same observation as in Experiment 1 can be made that the T_{tm} measurement is sensitive to the measurement point.

It was also also observed from Experiment 3B, $T_{tm,R}$ measurement was higher

that T_{es} , but in Experiment 2, $T_{tm,R}$ was consistently lower than T_{es} . It has been reported that the T_{tm} is higher than T_{es} [89] [90] [104]. The differentials between $T_{tm,R}$ and T_{rm} are rather similar in both experiments, but the differentials between T_{es} and T_{rm} are different. It has been noted in previous studies that T_{es} measurement is sensitive to the placement of the probe and that a lower temperature can be obtained if it is too high up in the esophagus [88] [89].

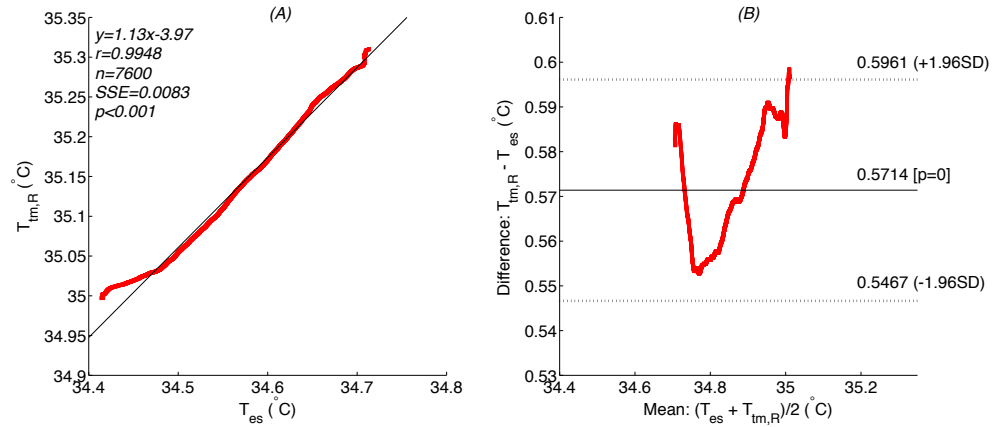


Figure 3.25: Analytical results for Experiment 3B that illustrate the effects of full body hyperthermia with GA on the right TM temperature. (A) Relationship between right TM temperature ($T_{tm,R}$) and esophageal temperature (T_{es}), and (B) the respective Bland-Altman plot.

Table 3.1: Correlations and Bland-Altman Analyzes results for Experiment 3B.

Temperature-Pair	Analyzes Results			
	r	SSE	MD	$1.96SD$
G_1				
T_{es}, T_{me}	0.995	0.009	+0.812	+0.851
$T_{es}, T_{tm,R}$	0.995	0.008	+0.571	+0.596
T_{es}, T_{rm}	0.993	0.01	+1.514	+1.544
G_2				
T_{es}, T_{me}	0.971	0.02	+0.852	+0.915
$T_{es}, T_{tm,R}$	0.994	0.005	+0.569	+0.599
T_{es}, T_{rm}	0.993	0.006	+1.526	+1.543

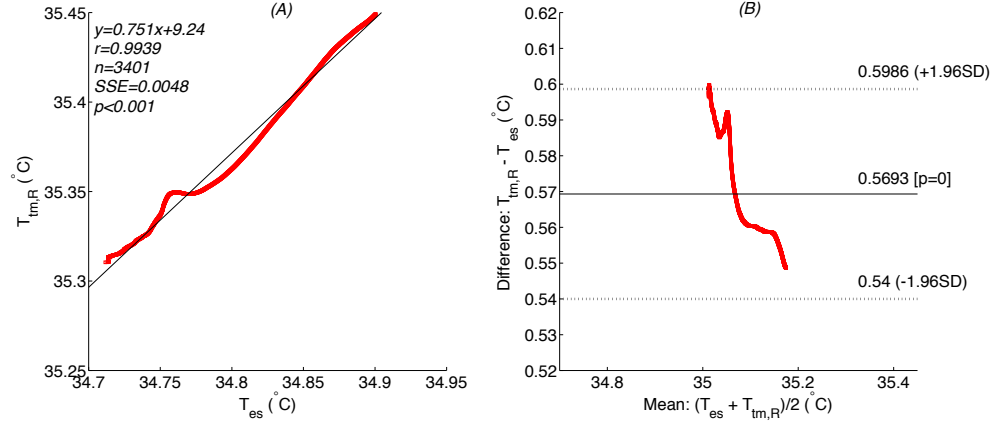


Figure 3.26: Analytical results for Experiment 3B that illustrate the effects of full body hyperthermia with GA halted (for 15 minutes) on the right TM temperature. (A) Relationship between right TM temperature ($T_{tm,R}$) and esophageal temperature (T_{es}), and (B) the respective Bland-Altman plot.

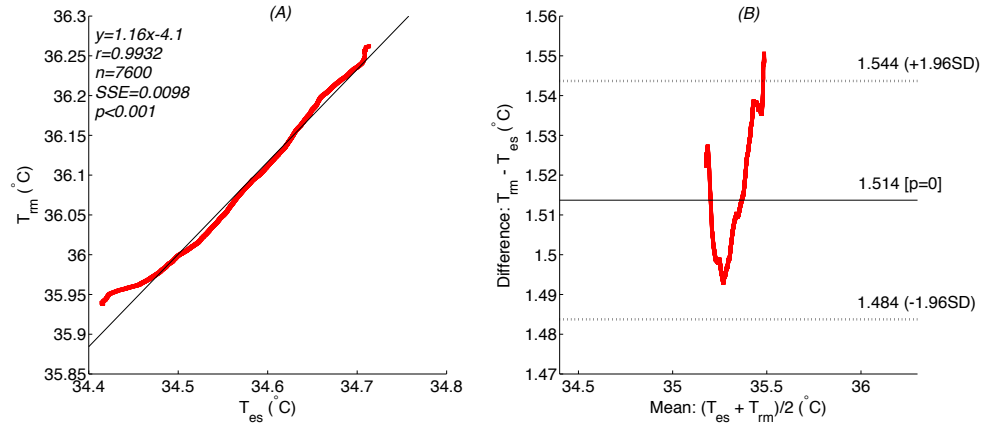


Figure 3.27: Analytical results for Experiment 3B that illustrate the effects of full body hyperthermia with GA on the RM temperature. (A) Relationship between RM temperature (T_{rm}) and esophageal temperature (T_{es}), and (B) the respective Bland-Altman plot.

3.4.3 Other Observations

The results from Experiment 1, 2 and 3 suggested that T_{tm} can be used to infer CBT if the probe is directed at a point on the TM where stable measurements can be obtained. Otherwise, the effects on the measurements (such as head cooling) should be considered and used to compensate the actual measurements.

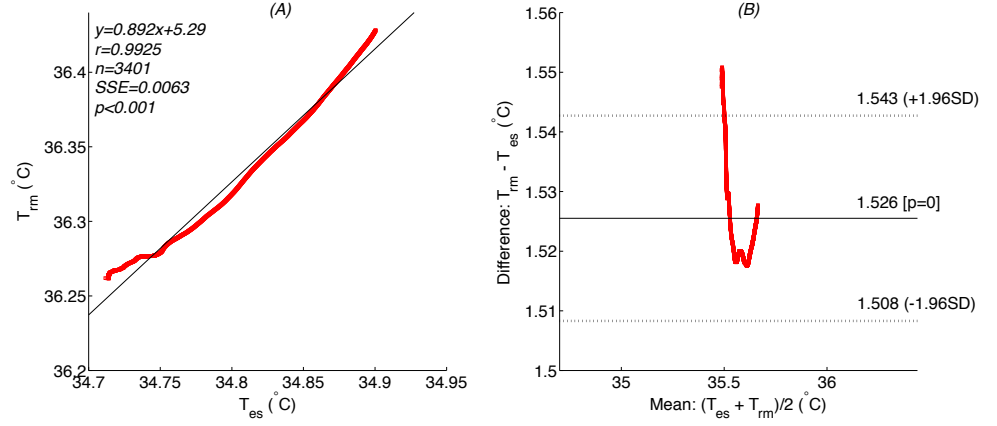


Figure 3.28: Analytical results for Experiment 3B that illustrate the effects of full body hyperthermia with GA halted (for 15 minutes) on the RM temperature. (A) Relationship between RM temperature (T_{rm}) and esophageal temperature (T_{es}), and (B) the respective Bland-Altman plot.

The latter may not be efficiently viable from a practical perspective.

The measurements from the ME cavity were more responsiveness to changes in CBT. Inferencing a faster dynamical variable T_{me} from a slower one T_{tm} is not easily achieved as it may require the computation of higher derivatives of the slower measurements and this is not practically viable if there exists significant measurement noise. A calibrated relationship between the two variables in the steady state may be more realistic in a soft model. However, this would require a situation wherein temperatures can be allowed to settle down with no additional heat stress or sink occurring in the process, which may or may not be detectable. Dynamically inferencing the CBT from a more sluggish measurement is thus a challenge which has not been truly resolved. Direct measurements of temperature from the ME cavity may represent one approach when real-time and dynamic indications of the CBT is needed.

3.5 Modeling of Dynamics Between ME Cavity and TM Temperatures

This section discuss in great detail the modeling of dynamics between ME cavity and TM temperatures. The various steps taken with regards to the derivation of the temperature model are explained, and assumptions made are properly justified.

3.5.1 ME Heat Balance Model

T_{me} is demonstrated in Section 3.4.2 to be very responsive to changes in CBT. It is able to pick up small changes which are not evident in the temperatures at the rectum and esophagus, and it is more robust to changes in ambient conditions relative to T_{tm} . This approach is especially useful for the monitoring CBT of sports or military personnel performing strenuous physical activities for early signs of heat related injuries [121] which has to be continuously done in an efficient and non-invasive manner, with high accuracy. Driven by these motivations, the aim is to derive a dynamic ME Heat Balance (MEHB) model describing heat flows in the ME cavity vicinity.

The Two-Node model (TNM) by Gagge *et al* [122] [123] is used to provide the baseline relationship to represent heat transfers localized to the vicinity of the ME. The generic equation is given in Eqn. (3.1), where Q_b is the rate of change of the heat content of that point in terms of heat flow rate per unit area (heat flux); M_b is the rate of metabolic energy expenditure per unit area; W_b is the rate of external work per unit area (+ for work against external forces, - for eccentric or negative work); R_b is the rate of radiant heat exchange per

unit area; C_b is the rate of convective heat exchange per unit area; D_b is rate of conductive heat exchange per unit area; and E_b is the rate of evaporative heat exchange per unit area.

$$Q_b = M_b - (\pm W_b) \pm (R_b + C_b + D_b) - E_b \quad (3.1)$$

The areas of interest of the dynamical model here is the TM, interacting essentially with the environment within the ear canal on one side and the ME cavity on the other. The TM is thin and concave in nature [109], and it is located at the distal end of the external auditory canal, forming a thin barrier separating the auditory canal from the ME cavity. The TM outer surface facing the canal is exposed to the ambient air while the inner surface facing the ME cavity is part of the cavity wall. Since the TM is extremely thin, heat from the surface is mostly lost to the ambient environment via convection and radiation due to the relatively larger interacting contact area compared to the edge of the TM that is attached to canal wall. Thus, the conduction heat loss to the canal wall is negligible.

The TM is shielded from the ambient air turbulence as it is sited at the distal end of the canal, if temperature measurements are indeed taken at the TM (Chapter 3). The TNM can be reduced with the specific situations at the TM. First, $M_b \approx 0$ since there is negligible heat generation by the thin TM tissue; $W_b = 0$ at this passive point; $E_b = 0$ with no sweat glands in this area; $D_b \approx 0$ with negligible conductive heat exchange.

Thus, at the interface with the ambient environment, Eqn. (3.1) can be reduced to Eqn. (3.2) with only the dominant convection and radiant heat

terms. In Eqn. (3.2), q_{am} refers to the heat flow rate from the TM to the ambient environment; T_{tm} and T_{am} are the TM and ambient temperatures in Kelvin. The convection heat transfer term can be represented as $h_{ca}A_{tm}(T_{tm}-T_{am})$ [124] [125] [126] [127] where h_{ca} is the heat transfer coefficient and A_{tm} is the effective area of the TM. The radiant term is represented by $\Delta_{am} = \sigma\epsilon_{ra}A_{tm}(T_{tm}^4 - T_{am}^4)$ [126] [127] in Eqn. (3.3) to account for the heat transfer through thermal radiation from the surface of the TM, where $\sigma\epsilon_{ra}$ is the TM surface radiant heat transfer coefficient; $\sigma = 5.6704 \times 10^{-8} J/(s \cdot m^2 \cdot K^4)$ is the Stefan-Boltzmann constant and ϵ_{ra} is the surface emissivity constant of the TM. Δ_{am} can be re-written as $h_{ra}A_{tm}(T_{tm} - T_{am})$ with h_{ra} defined in Eqn. (3.4) as a temperatures (T_{tm} and T_{am}) dependent coefficient. The relative strength of the radiant term is expected to be small due to the absence of a physical receiving surface perpendicular to the TM to facilitate the radiant heat exchange [126], resulting in a small and uneven radiant heat transferred to the surface of the ear canal in the vicinity of the TM [126] [128]. In the analysis of the results subsequently in Section 3.6, this component will be calibrated from the data collected to verify the significance of its contribution.

$$q_{am} = h_{ca}A_{tm}(T_{tm} - T_{am}) + \Delta_{am} \quad (3.2)$$

$$\Delta_{am} = \sigma\epsilon_{ra}A_{tm}(T_{tm}^4 - T_{am}^4) \Rightarrow \Delta_{am} = h_{ra}A_{tm}(T_{tm} - T_{am}) \quad (3.3)$$

$$h_{ra} = \sigma\epsilon_{ra}(T_{tm} + T_{am})(T_{tm}^2 + T_{am}^2) \quad (3.4)$$

Next, the other side of the interface with the ME cavity, serving as the primary heat source to the TM, will be similarly examined. The inner surface

of the TM constitutes a wall of the ME cavity. The ME cavity is an enclosed area with an air pocket, and the heat circulation from this area to the TM is dominated primarily by convection and radiation processes. However, within the cavity, heat transfer through conduction is more significant than at the other side due to the two conductive channels: (a) via the edge of the TM where it joins the side walls of the ME [109], (b) via the malleus bone which engages the inner surface of the TM [109]. Heat transfer via radiation may also be present since the walls of the cavity are potential radiation sources, and the TM is the potential receiving surface [109] [126]. Thus, effective heat flows q_{tm} from within the ME cavity to the TM is given in Eqn. (3.5). T_{me} is the temperature of the ME cavity (in Kelvin). h_{ct} represents the lumped convective and conductive heat transfer coefficient for the heat transfer from an effective area A_{me} of the ME cavity to the TM. ϵ_{rt} is the surface emissivity constant of the ME cavity.

The ME cavity is able to store heat energy and it can be thought of as a thermal capacitor denoted by C_{me} (heat storage element). There is thus another flow from the heat stored in this energy bank which is represented by $C_{me} \cdot \frac{d}{dt}(T_{me} - T_{tm})$. Finally and similar to Eqn (3.2), the radiant term $\Delta_{tm} = \sigma\epsilon_{rt}A_{me}(T_{me}^4 - T_{tm}^4)$ captures the heat transfer through thermal radiation from the wall of the ME cavity. Δ_{tm} can be similarly re-written as $h_{rt}A_{me}(T_{me} - T_{tm})$ with h_{rt} defined in Eqn. (3.7). The relative strength of the radiant term will similarly be calibrated from the results subsequently in Section 3.6.

$$q_{tm} = h_{ct}A_{me}(T_{me} - T_{tm}) + C_{me} \cdot \frac{d}{dt}(T_{me} - T_{tm}) + \Delta_{tm}, \quad (3.5)$$

$$\Delta_{tm} = \sigma\epsilon_{rt}A_{me}(T_{me}^4 - T_{tm}^4) \Rightarrow \Delta_{tm} = h_{rt}A_{me}(T_{me} - T_{tm}), \quad (3.6)$$

$$h_{rt} = \sigma\epsilon_{rt}(T_{me} + T_{tm})(T_{me}^2 + T_{tm}^2). \quad (3.7)$$

Finally, to get the dynamic equation relating T_{me} to T_{tm} and T_{am} , the principle of energy conservation is used as in Eqn (3.8).

$$q_{tm} - q_{am} = C_{tm} \cdot \frac{d}{dt}T_{tm}. \quad (3.8)$$

Thus,

$$T_{me} = (1 + \frac{h_{ca}A_{tm}}{h_{ct}A_{me}})T_{tm} - (\frac{h_{ca}A_{tm}}{h_{ct}A_{me}})T_{am} + (\frac{C_{tm} + C_{me}}{h_{ct}A_{me}})(\frac{d}{dt}T_{tm}) - C_{me}(\frac{d}{dt}T_{me}) + \Delta, \quad (3.9)$$

$$\Delta = \frac{1}{h_{ct}A_{me}}(\Delta_{am} - \Delta_{tm}) = -(\frac{\sigma\epsilon_{rt}}{h_{ct}})T_{me}^4 + (\frac{\sigma\epsilon_{rt}A_{me} + \sigma\epsilon_{ra}A_{tm}}{h_{ct}A_{me}})T_{tm}^4 - (\frac{\sigma\epsilon_{ra}A_{tm}}{h_{ct}A_{me}})T_{am}^4. \quad (3.10)$$

3.5.2 Graphical Representation of MEHB Model

The MEHB model represented by Eqn. (3.9), can be represented graphically by using an equivalent electric circuit by drawing on the analogy between a thermal and an electrical system [129] [130] summarized in Table 3.2. Figure 3.29 shows the the MEHB model constructed in a graphical form. Figure 3.30 shows the MEHB model (in graphical form) superimposed on the anatomy of a human ear to illustrate the matched locations of the model components.

Table 3.2: Electrical-Thermal Analogy

Electrical	Thermal Equivalence	
	<i>Element</i>	<i>S.I. Unit</i>
Voltage	Temperature	K
Current Density	Heat Flux	$W \cdot m^{-2}$
Resistor	Thermal Resistance	$K \cdot W^{-1}$
Capacitor	Heat Storage Element (Thermal Capacitance)	$J \cdot K^{-1}$

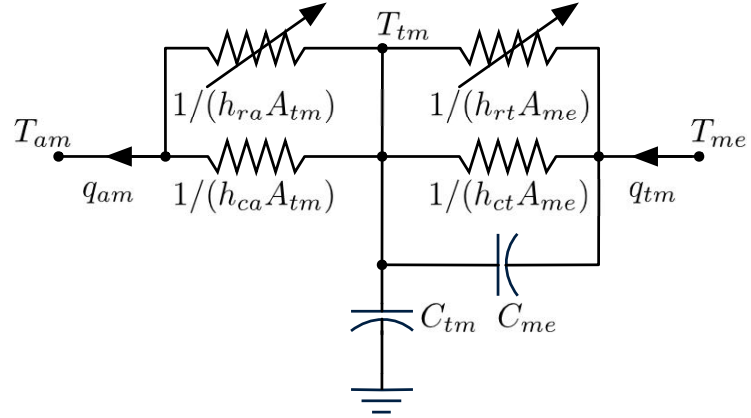


Figure 3.29: Graphical representation of the MEHB model.

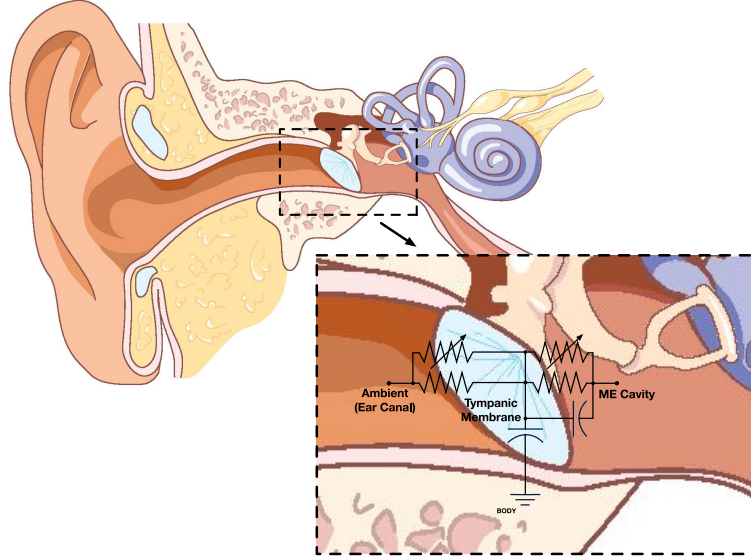


Figure 3.30: Anatomy of a human ear with superimposed MEHB model in graphical form.

3.5.3 Inference Procedures

Eqn. (3.9) and (3.10) constitute the MEHB model to infer the ME temperature from the TM temperature. To apply the model for this purpose will entail first estimating the model parameters from data which will be elaborated in the next subsection. Thereafter, only TM temperature measurements along with this model will serve to infer the ME temperatures which are unavailable

beyond the construction phase of the model. Eqn. (3.9) is a quartic polynomial in T_{me} . Thus, this inference requires the solution of this high order polynomial which is tedious computationally and yet may yield multiple solutions which require further elimination from physical principles.

In this section, an efficient method for this inference procedure is proposed. The method leverages on the basis that the Δ term though small is behind the complications, without which essentially, the relationship between T_{me} and T_{tm} is linear. As illustrated in the next subsection, this term creates a similar difficulty in the parameter estimation phase as it pushes the model out of a linear regression form and thus requiring a numerical search method for parameter estimation in the raw form. It is noted that the linear dynamical relationship is the dominant relationship [127] [128]. The relative size of Δ is expected to be small and its significance will be calibrated with the data and results in Section 3.6. The inference procedure highlighted in Step 1.1 to Step 1.3 is thus proposed.

- *Step 1.1:* By setting $\Delta = 0$ in Eqn. (3.9), \tilde{T}_{me} is obtained directly from T_{tm} and Eqn. (3.11).

$$\tilde{T}_{me} = a_1 T_{tm} + a_2 T_{am} + a_3 \left(\frac{d}{dt} T_{tm} \right) + a_4 \left(\frac{d}{dt} T_{me} \right), \quad (3.11)$$

where

$$a_1 = \left(1 + \frac{h_{ca} A_{tm}}{h_{ct} A_{me}} \right), \quad a_2 = - \left(\frac{h_{ca} A_{tm}}{h_{ct} A_{me}} \right), \quad a_3 = \left(\frac{C_{tm} + C_{me}}{h_{ct} A_{me}} \right), \quad \text{and} \quad a_4 = -C_{me}.$$

Note that Eqn. (3.11) incorporates a transfer function between frequency transforms of T_{me} and T_{tm} with a zero and a pole representing the dynamics

present.

- *Step 1.2:* Using \tilde{T}_{me} in lieu of T_{me} , $\tilde{\Delta}$ is evaluated with Eqn. (3.10), resulting in Eqn. (3.12).

$$\tilde{\Delta} = b_1 \tilde{T}_{me}^4 + b_2 T_{tm}^4 + b_3 T_{am}^4, \quad (3.12)$$

where

$$b_1 = -\frac{\sigma \epsilon_{rt}}{h_{ct}}, \quad b_2 = \left(\frac{\sigma \epsilon_{rt} A_{me} + \sigma \epsilon_{ra} A_{tm}}{h_{ct} A_{me}} \right), \quad \text{and} \quad b_3 = -\frac{\sigma \epsilon_{ra} A_{tm}}{h_{ct} A_{me}}.$$

- *Step 1.3:* The final estimate of T_{me} (\bar{T}_{me}) is determined from \tilde{T}_{me} and $\tilde{\Delta}$ with Eqn. (3.13).

$$\bar{T}_{me} = \tilde{T}_{me} + \tilde{\Delta}. \quad (3.13)$$

3.5.4 Model Parameter Estimation

In general, a numerical search is needed to obtain the coefficients of Eqn. (3.9) since the model is not in the linear regression form. The presence of Δ pushes the model out of a linear regression form which otherwise the dominant linear dynamical relationship is representative. An approach towards parameter estimation, analogous to the inference procedure, is adopted here. When executed collectively, both the parameter estimation and subsequent T_{me} inference are thus synchronized effectively to yield a final estimation. By virtue of the order of execution, the parameter estimation procedure treats Eqn. (3.12) as the dominant model with Eqn. (3.13) as the residual part of the dominant model. When the model is used for inference of T_{me} , the same order is used.

The Multiple Linear Regression (MLR) based parameter estimation algorithm will be first reviewed briefly in the next subsection, and the proposed steps for parameter estimation of the model represented in Eqn. (3.9) will be presented thereafter.

3.5.4.1 Multiple Linear Regression Algorithm

A linear regression model, with four input variables and one dependent output, is given in Eqn. (3.14). Y is a response (output) vector of size ψ , X is the input matrix of dimension $(\psi \times 4)$, ϕ is a parameter vector of size 4 with ϕ_1 , ϕ_2 , ϕ_3 and ϕ_4 as the parameters, and ϵ_g is a random error vector of size ψ with zero mean and follows a Gaussian distribution. Eqn. (3.15) shows the composition of Y , X , ϕ and ϵ_g . The i^{th} element of Y is given in Eqn. (3.16). The MLR based algorithm yield the optimal parameters by minimizing an objective function S such that S is minimum for all parameters defined in ϕ . S can be formulated in Eqn. (3.17) as the sum of square error (SSE) between measured output Y and the fitted output \hat{Y} with parameter vector $\hat{\phi} = [\hat{\phi}_1, \hat{\phi}_2, \hat{\phi}_3, \hat{\phi}_4]^T$. $\hat{\phi}$ is then the least squares estimator with a direct solution defined in Eqn. (3.18) of ϕ for known values of Y and X . By solving for Eqn. (3.18) based on an ordinary least square estimator, the coefficients in $\hat{\phi}$ can be effectively determined. The fitted \hat{Y} can then be determined from X and $\hat{\phi}$ with Eqn. (3.19).

$$Y = X\phi + \epsilon_g, \quad (3.14)$$

$$Y = \begin{pmatrix} Y_1 \\ Y_2 \\ \dots \\ Y_\psi \end{pmatrix}, X = \begin{pmatrix} X_{11} & X_{12} & X_{13} & X_{14} \\ X_{21} & X_{22} & X_{23} & X_{24} \\ \dots & \dots & \dots & \dots \\ \dots & \dots & \dots & \dots \\ X_{\psi 1} & X_{\psi 2} & X_{\psi 3} & X_{\psi 4} \end{pmatrix}, \phi = \begin{pmatrix} \phi_1 \\ \phi_2 \\ \phi_3 \\ \phi_4 \end{pmatrix}, \epsilon_g = \begin{pmatrix} \epsilon_{g1} \\ \epsilon_{g2} \\ \dots \\ \epsilon_{g\psi} \end{pmatrix}. \quad (3.15)$$

$$Y_i = \phi_1 X_{i,1} + \phi_2 X_{i,2} + \phi_3 X_{i,3} + \phi_4 X_{i,4} + \epsilon_{gi}. \quad (3.16)$$

$$S(\hat{\phi}) = \sum_{i=1}^{\psi} (Y_i - \hat{\phi}_1 X_{i,1} - \hat{\phi}_2 X_{i,2} - \hat{\phi}_3 X_{i,3} - \hat{\phi}_4 X_{i,4})^2. \quad (3.17)$$

$$\hat{\phi} = (X^T X)^{-1} X^T Y. \quad (3.18)$$

$$\hat{Y} = X \hat{\phi}. \quad (3.19)$$

3.5.4.2 Proposed MLR-based Model Parameters Estimation Procedure

To alleviate the need for a tedious numerical search procedure with potential convergence issues, a three-steps approach, synchronizing with the inference procedure, is proposed to leverage on the efficient solutions associated with a MLR model.

- *Step 2.1:* Eqn. (3.11) contains a_1 , a_2 , a_3 and a_4 parameters and it represents the dominant linear dynamical relationship which is in a MLR form. These parameters are first estimated with Eqn. (3.18) by using T_{tm} , $(\frac{d}{dt}T_{tm})$, $(\frac{d}{dt}T_{me})$ and T_{am} datasets. a_1 , a_2 , a_3 and a_4 are thus determined for Eqn. (3.11).
- *Step 2.2:* Eqn. (3.11), with the parameters computed in Step 2.1, is used

to generate \tilde{T}_{me} dataset from the same inputs T_{tm} , $(\frac{d}{dt}T_{me})$ and T_{am} . The residual $\tilde{\Delta}$ can be generated from Eqn. (3.20).

$$\tilde{\Delta} = T_{me} - \tilde{T}_{me} \quad (3.20)$$

- *Step 2.3:* Running the MLR parameter estimation algorithm again for the quartic term in Eqn. (3.12) with $\tilde{\Delta}$, \tilde{T}_{me}^4 , T_{tm}^4 and T_{am}^4 , the remaining parameters b_1 , b_2 and b_3 can be estimated.

3.6 Model Verification: Experiment and Results

An experiment (similar to an experiment conducted in Section 3.3) was performed on a sedated primate to log temperatures at several temperature measurement sites, including T_{me} and T_{tm} at the head region and T_{es} and T_{rm} at the lower body region. The experiment setup and the procedures prescribed will be next highlighted to provide the background for the interpretation of the experiment results which will be furnished subsequently.

3.6.1 Setup and Procedures

Temperature probes and heating chamber from experiments in Section 3.3 (Figure 3.8 and 3.10) were used in this experiment. Four temperature probes were used to acquire the temperatures from the primate: (a) A needle probe perforating the left TM to reach the left ME cavity near to the malleus bone for measuring T_{me} , (b) TM probe engaging a high temperature spot on the surface at lower anterior quarter of the right TM (vicinity of the cone of light) as recommended by Brinnel and Cabanac [104] for measuring T_{tm} that provides

stable temperature readings, (c) esophageal probe inserted into the lower forth of the ES, and (d) RM probe inserted into the anal sphincter for measuring T_{rm} . Additional probes were used to measure the chamber (T_{ch}) and ambient (T_{am}) temperatures. A heating chamber was used to elevate the primate's body temperature in controlled environment.

3.6.2 Results and Discussions

Figure 3.31 shows the temperature measurements obtained from the experiment. To facilitate the modeling process, the measurements were recorded in Kelvin. The total experiment runtime (t) was 7.13 hours (25674s). At the start of the heating chamber operation (at $t > 0$), following the initial response to GA, slow and steadily increase in temperatures were observed at all the four measurement sites. The heating ceased when T_{rm} reached 313.15K (40°C) and the heating chamber was then opened to expose to the cold ambient air at T_{am} which began the cooling down process.

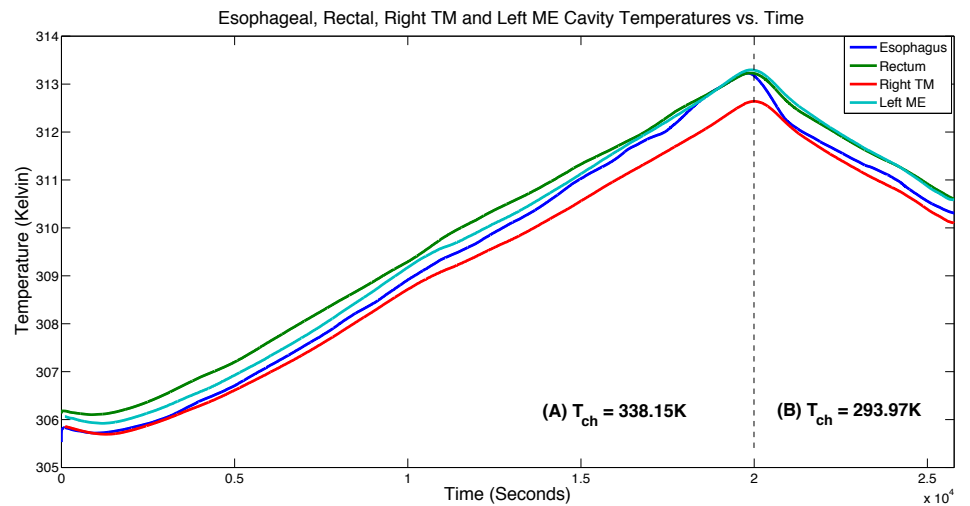


Figure 3.31: T_{es} , T_{rm} , T_{tm} and T_{me} vs. Time plots from the Experiment.

A slower response in T_{rm} during the initial rise in temperature was observed

relative to T_{me} . The T_{es} has higher fluctuations when compared to the rest of the temperatures data acquired from the other measurements sites. Like the rest of the temperature probes used in the experiment, the T_{es} temperature probe is a contact probe. Thus, any un-intended movements resulted in inaccurate temperature measurements. It is also a well-known fact that improperly positioned T_{es} probe can easily be affected by the aspiration of air from the lungs [88] [89]. During the experiment, the T_{es} probe was positioned and securely fastened in-order to minimize any unwanted movement of the probe within the primate's body. However, there were occurrences of involuntary chest muscles movements due to unwarranted heavy breathings that significantly contributed to the small probe movements. Thus, the unwarranted probe movements coupled with the non-optimized positioning of the probe within the primate resulted in significantly high fluctuations in the temperature measurement data, hence significantly affected the measurement accuracy.

Measurements were performed at every one second interval throughout the experiment runtime. A total of 25674 temperature data points were collected. The data was split into *CONFIG* dataset wherein data was sampled at every 50 seconds interval to get a total data size of 513 and *VERIFY* dataset wherein data was sampled every 3 seconds interval for a total data size of 8558. The *CONFIG* dataset was used to determine the parameters of the MEHB model, and the *VERIFY* dataset was subsequently used for calibrating the model performance.

Following the prescribed procedures for parameter estimation in Section 3.5.4, the models were obtained as Eqn. (3.21) and (3.22).

$$\tilde{T}_{me} = 1.062T_{tm} - 0.064T_{am} + (86.365)\left(\frac{d}{dt}T_{tm}\right) + (0.194)\left(\frac{d}{dt}T_{me}\right), \quad (3.21)$$

$$\tilde{\Delta} = -(2.698 \times 10^{-11})\tilde{T}_{me}^4 + (2.862 \times 10^{-11})T_{tm}^4 - (1.82 \times 10^{-12})T_{am}^4. \quad (3.22)$$

Model cross validation was done by comparing the model's prediction \bar{T}_{me} generated from the data in the *VERIFY* dataset with the actual T_{me} temperature in the same dataset. Benchmarks are useful to serve as the basis to assess the accuracy. The following benchmarks were computed:

- T_{tm} serving directly as estimate to T_{me} . Such a direct inference is inevitably done if there is no ME data for modeling.
- A static relationship of T_{tm} and T_{me} ($\hat{T}_{me} = 1.058T_{tm} - 17.59$), obtained from least squares fitting, was used to provide an estimate to T_{me} . Such relationships are commonly adopted in thermal instruments to match temperatures at different sites.
- \tilde{T}_{me} and \bar{T}_{me} were both used as the estimate to T_{me} . This will allow us to observe the significance of the radiant term Δ .

In all the comparisons, statistical indicators including the Mean Squared Error (*MSE*), Mean Absolute Error (*MAE*) and the Error Standard Deviation (*ESD*) were generated. These error statistics were computed with respect to deviation from the raw T_{me} data captured. The percentages in the square brackets show the relative improvements in these indicators for the different model inferences compared to using T_{tm} as a direct inference. The results can be seen in Table 3.3. The bold fonts pick out the *MAEs* meeting the 0.01K target. Figure 3.32 shows the profile of the T_{me} inference errors over time for each inference approach using T_{tm} . The significant improvements from the use of the dynamical models are very evident in this figure over the entire duration of the experiment.

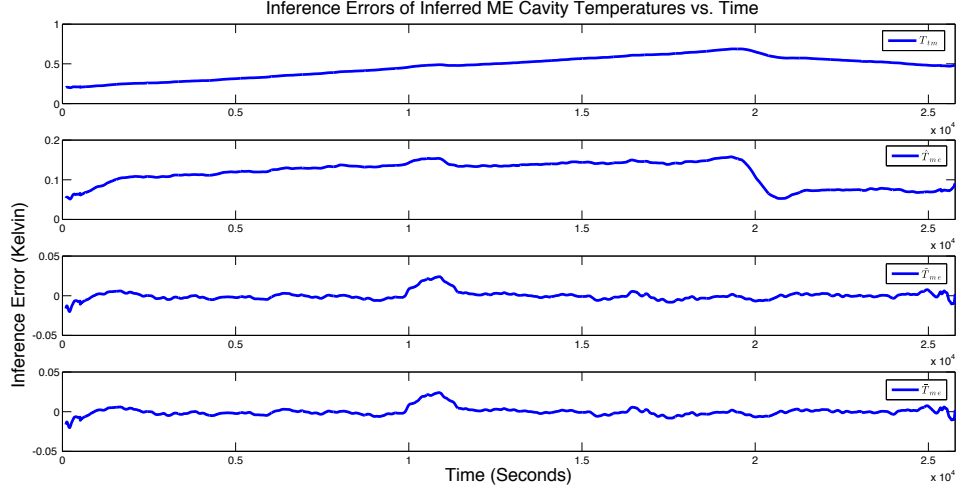


Figure 3.32: Inference Errors associated with the inferred ME temperatures (T_{tm} , \hat{T}_{me} , \tilde{T}_{me} and \bar{T}_{me}) vs. Time plots using the *VERIFY* dataset.

Table 3.3: MEHB Model Benchmarks for T_{me}

Benchmark	Inference Errors (K)			
	T_{tm}	\hat{T}_{me}	\tilde{T}_{me}	\bar{T}_{me}
<i>dataset = CONFIG</i>	$(\times 10^{-1})$	$(\times 10^{-1})$	$(\times 10^{-5})$	$(\times 10^{-5})$
<i>MSE</i>	2.35	0.144 [93.87%]	2.85 [99.99%]	2.85 [99.99%]
<i>MAE</i>	4.67	1.160 [75.16%]	344 [99.26%]	342 [99.27%]
<i>ESD</i>	1.33	0.301 [77.37%]	409 [96.92%]	411 [96.91%]
<i>dataset = VERIFY</i>				
<i>MSE</i>	2.35	0.144 [93.87%]	2.82 [99.99%]	2.83 [99.99%]
<i>MAE</i>	4.67	1.160 [75.16%]	342 [99.27%]	340 [99.27%]
<i>ESD</i>	1.33	0.300 [77.33%]	407 [96.94%]	409 [96.92%]

From these results, it is observed that the inference error using T_{tm} as the direct inference to T_{me} is the highest with both *CONFIG* and *VERIFY* datasets. The inference error of T_{tm} , depicted in Figure 3.32, illustrates a time dependent profile where a relatively large error magnitude is observed over the entire duration of the experiment. The error appears to be accumulating with the rising and falling trend of T_{tm} (in Figure 3.31). This shows that if a high accuracy of estimation of T_{me} is needed such as for the monitoring of sportsmen or military personnel down to 0.01K, a direct measurement is not sufficient even if

the TM probe is well directed. The relatively large ESD value also indicates the two sites are distinct though close. Improvements were readily observed when a static inference model \hat{T}_{me} was applied, where the inference error was observed to be less time dependent due to the nominally flat error magnitude plotted with respect to the experiment time duration, though the accuracy still fell short of the $0.01K$ target due to the comparatively large offsets. When the MEHB model was used to infer both \tilde{T}_{me} and \bar{T}_{me} , significant improvements were observed. The inference errors were small and exhibited time independence, and in most cases were close to 0. The errors were almost equivalent in magnitude for both \tilde{T}_{me} and \bar{T}_{me} . Very marginal improvement and reduction in *MAE* and *ESD* can be observed in \bar{T}_{me} . This shows that the radiant elements were rather insignificant from this part of the human body during the experiment, or that the thermistor probes used were not picking up the radiant component sufficiently due to the small surface diameters of the probes.

Figure 3.33 shows the plots of inferred \tilde{T}_{me} and \bar{T}_{me} , and measured T_{me} for the *VERIFY* dataset showing the measured temperatures during the heating and cooling phases. The inferred temperature plots follow the measured (reference) temperature plot closely.

From the benchmarking results tabulated in Table 3.3, the MEHB model exhibits a very high level of accuracy with both *CONFIG* and *VERIFY* datasets which achieve $\leq 0.01K$ accuracy in the *MAE*. *CONFIG* temperature dataset of only 513 in size was effectively used to determine the coefficients of the MEHB model that has remained valid for the *VERIFY* dataset which is 8558 in size; indicating these coefficients are able to model a wide range of temperature change

in the primate.

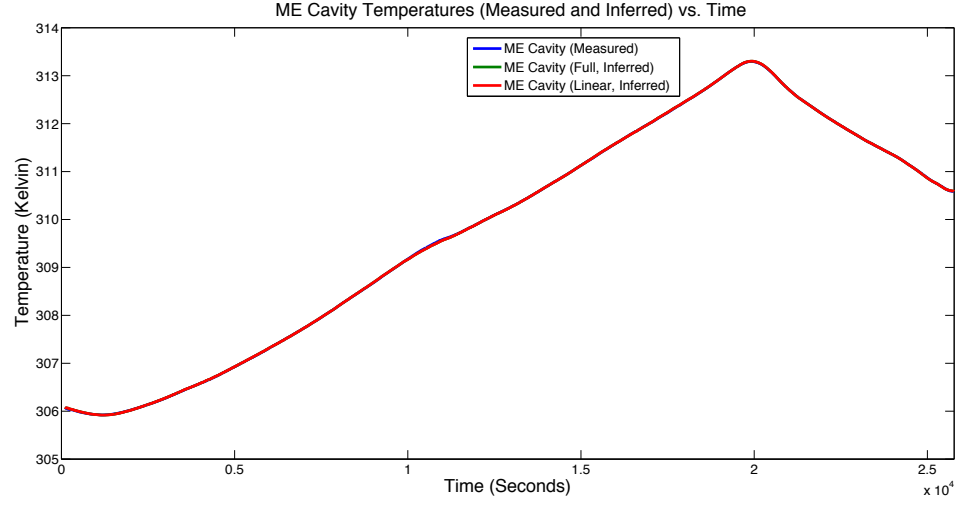


Figure 3.33: Inferred \tilde{T}_{me} and \bar{T}_{me} , and measured T_{me} vs. Time plots using the *VERIFY* dataset.

3.7 Model Extensions to ES and RM CBT Sites

3.7.1 Critical Site Heat Balance (CSHB) Model

The MEHB model has been demonstrated to perform satisfactorily in the inference of T_{me} from T_{tm} . It is interesting to explore its extension to other CBT sites further from the TM such as the ES and the RM since the temperatures at these sites were also acquired in the same experiments.

To this end, the graphical representation of MEHB model in Figure 3.29 is still adopted but with the temperature of T_{me} substituted with the temperatures at the ES (T_{es}) and the RM (T_{rm}) respectively. Since the radiant terms do not have significant contributions to the model accuracy, they are ignored. Figure 3.34 shows the modified models (from MEHB) capturing the TM-ES and TM-RM relationships. In addition, since these sites are further apart from the TM,

the accuracy of the model may be enhanced by modeling the extended heat transfer pathways from these CBT sites as shown in the dotted part of Figure 3.34. These extensions contribute second derivatives to the dynamic equation Eqn. (3.9).

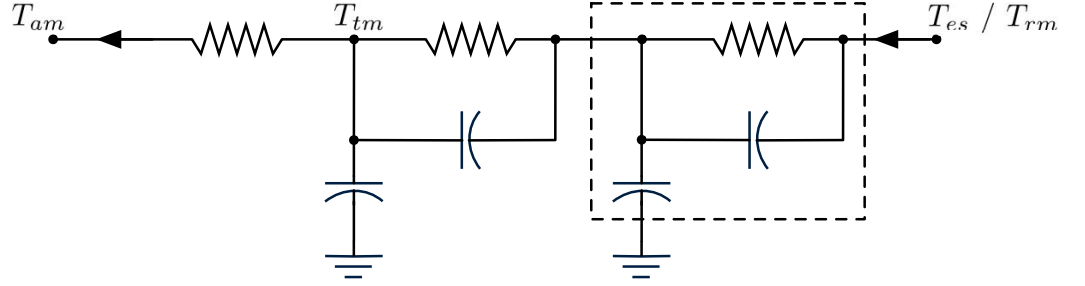


Figure 3.34: Modified model (from MEHB) representing the TM-ES and TM-RM relationships.

A new model equation is derived from the MEHB model to infer T_{es} . Eqn 3.23 depicts the new Critical Site Heat Balance (CSHB) model with an extended heat transfer pathway that incorporates a transfer function between frequency transforms of \check{T}_{es} and T_{tm} with *two* zeros and *two* poles representing the dynamics present. γ represents a new sets of coefficients that has to be determine by using the method prescribed in Section 3.5.4 and ignoring the radiant term. The derivatives present in the new model may contribute to the instability of the output as any noise or spikes present in the respective temperature data will be amplified by the derivatives. In order to prevent this issue from occurring, moving average filters are used to individually filter each temperature input to the model prior to the computation of the derivatives. A moving average filter with a sliding window size 80 discrete samples is implemented for each input. By using the filter, past 79 temperature data are used to calculate the average value of the present temperature input. The moving average filter is optimal

for a common task of reducing random noise while retaining a sharp step response [131] [132] [133]. Thus, any unwanted noise or spike presents at each input will be removed by the averaging effect. Eqn. (3.23) can be easily modified for inferring RM temperature (T_{rm}) by substituting the terms containing T_{es} with T_{rm} .

$$\check{T}_{es} = K\gamma \quad (3.23)$$

where,

$$K = \begin{bmatrix} T_{tm} & T_{am} & \frac{d}{dt}T_{tm} & \frac{d}{dt}\check{T}_{es} & \frac{d^2}{dt^2}T_{tm} & \frac{d^2}{dt^2}\check{T}_{es} \end{bmatrix} \quad (3.24)$$

$$\gamma = [\gamma_1 \ \gamma_2 \ \gamma_3 \ \gamma_4 \ \gamma_5 \ \gamma_6]^T \quad (3.25)$$

3.7.2 CSHB Model Verification and Discussion

Table 3.4 and 3.5 contain the results showing the models inferring T_{es} and T_{rm} respectively, from T_{tm} and T_{am} measurements. Benchmarks similar to those used in Section 3.6.2 are adopted with some variations:

- T_{tm} directly inferring T_{es} and T_{rm} ,
- Static relationships of T_{tm} and T_{es} ($\hat{T}_{es} = 1.059T_{tm} - 17.94$) and, T_{tm} and T_{rm} ($\hat{T}_{rm} = 1.015T_{tm} - 4.175$),
- \tilde{T}_{es} and \tilde{T}_{rm} (original model without extended heat transfer pathway),
- \check{T}_{es} and \check{T}_{rm} .

The results, tabulated in Table 3.4 and 3.5, show the same trend of reduction of modeling errors with the structure of the dynamic model used for the inference of T_{me} . Figure 3.35 and Figure 3.36 show the inferred versus actual T_{es} and T_{rm}

respectively. The inference errors are shown over the duration of the experiment in Figures 3.37 and 3.38. The significant improvements from the use of the dynamic models over static models are similarly evident. The extended pathway to capture the longer heat transfers from these more remote sites resulted in only marginal improvements to the accuracy. The $MAEs$ achieved in inferring T_{es} and T_{rm} are respectively about $0.05K$.

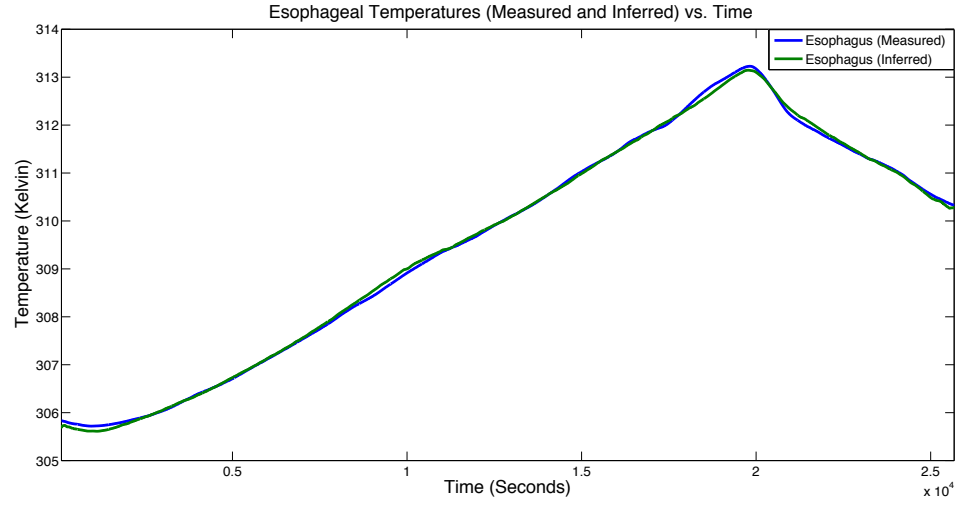


Figure 3.35: Inferred \check{T}_{es} and Actual T_{es} vs. Time

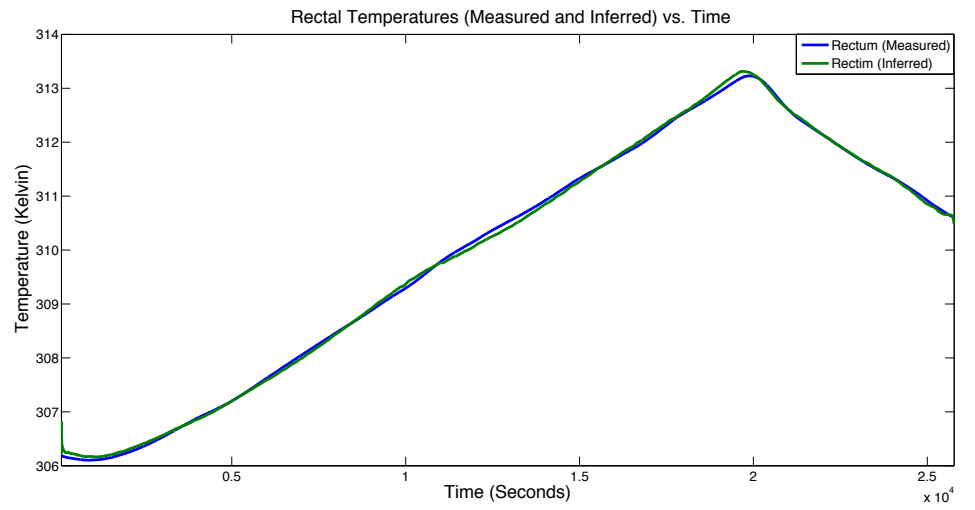


Figure 3.36: Inferred \check{T}_{rm} and Actual T_{rm} vs. Time

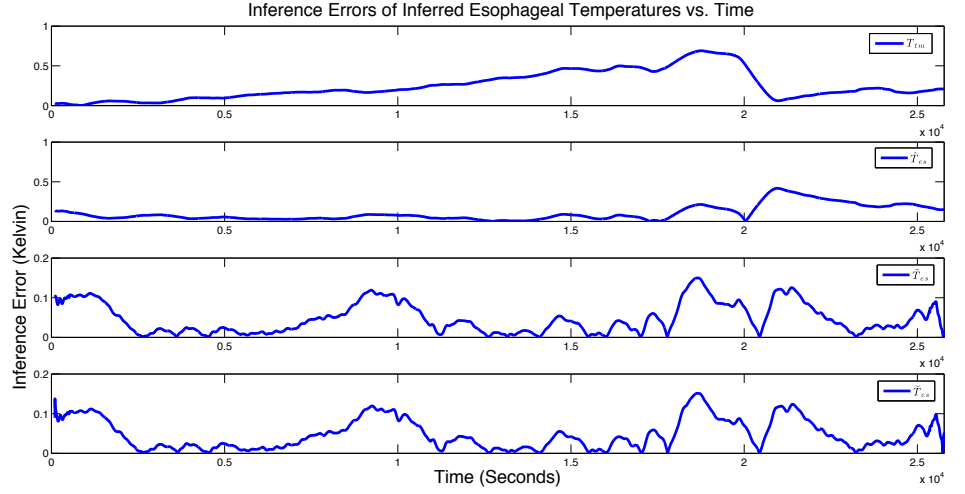


Figure 3.37: Inference Errors showing the various Inferred Esophageal Temperatures vs. Time plots using the *VERIFY* dataset.

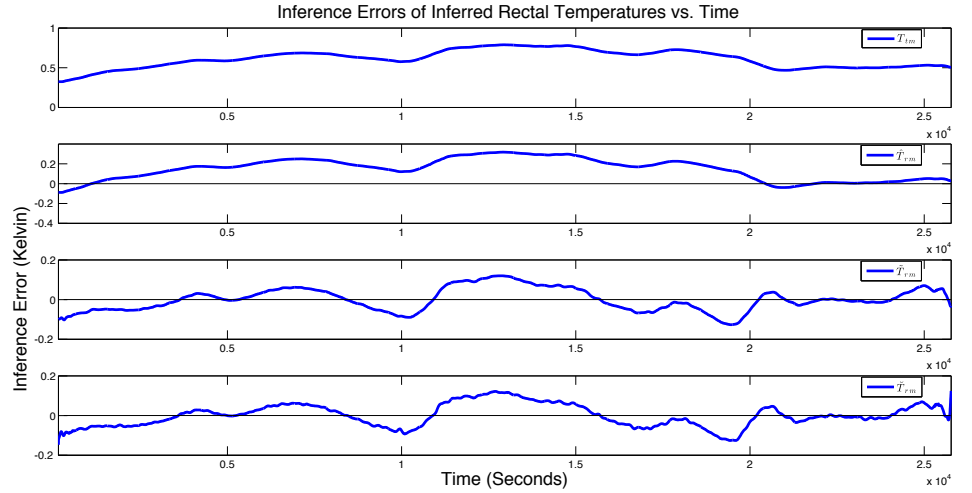


Figure 3.38: Inference Errors showing the various Inferred RM Temperatures vs. Time plots using the *VERIFY* dataset.

Figure 3.39 compares the inference errors across the three sites of ME, ES and RM using T_{tm} . The sites which are best inferred from T_{tm} are the ME, RM and ES in a decreasing order of accuracy, with close *MAEs* observed at the RM and ES. It may be noted that the logged records of T_{es} show rather large changes at certain times possibly due to the sensitivity of the temperature measurements with respect to the actual location of the probe inserted into the esophagus

Table 3.4: CSHB Model Benchmarks for T_{es}

Benchmark	Inference Errors(K)			
	T_{tm}	\hat{T}_{es}	\tilde{T}_{es}	\check{T}_{es}
<i>dataset = CONFIG</i>	($\times 10^{-1}$)	($\times 10^{-1}$)	($\times 10^{-3}$)	($\times 10^{-3}$)
<i>MSE</i>	0.93	0.199 [78.61%]	3.66 [96.06%]	3.66 [96.06%]
<i>MAE</i>	2.48	1.036 [58.20%]	47.43 [80.86%]	47.42 [80.86%]
<i>ESD</i>	1.78	0.957 [46.12%]	37.64 [78.82%]	37.54 [78.87%]
<i>dataset = VERIFY</i>				
<i>MSE</i>	0.93	0.199 [78.62%]	3.66 [96.06%]	3.66 [96.06%]
<i>MAE</i>	2.48	1.036 [58.20%]	47.43 [80.86%]	47.40 [80.89%]
<i>ESD</i>	1.75	0.957 [46.12%]	37.64 [78.82%]	37.56 [78.84%]

Table 3.5: CSHB Model Benchmarks for T_{rm}

Benchmark	Inference Errors (K)			
	T_{tm}	\hat{T}_{rm}	\tilde{T}_{rm}	\check{T}_{rm}
<i>dataset = CONFIG</i>	($\times 10^{-1}$)	($\times 10^{-1}$)	($\times 10^{-3}$)	($\times 10^{-3}$)
<i>MSE</i>	3.84	0.327 [91.48%]	3.25 [99.15%]	3.19 [99.17%]
<i>MAE</i>	6.10	1.522 [75.04%]	46.75 [92.33%]	46.43 [92.39%]
<i>ESD</i>	1.12	0.978 [12.52%]	32.18 [71.23%]	32.18 [71.23%]
<i>dataset = VERIFY</i>				
<i>MSE</i>	3.85	0.327 [91.48%]	3.24 [99.16%]	3.30 [99.14%]
<i>MAE</i>	6.10	1.523 [75.04%]	46.69 [92.35%]	46.71 [92.34%]
<i>ESD</i>	1.11	0.978 [12.52%]	33.39 [70.04%]	33.39 [70.04%]

which is difficult to maintain in the experiment when the breathing of the primate changed rapidly following real-time changes to the administration of anesthesia in the experiment. These outliers are non-systematic and such transitional changes are beyond what the model, without consideration of additional inputs, is able to account for. The inference errors at the middle ear are smaller in magnitude, though they also exhibit peaks observed at the key transitional moments.

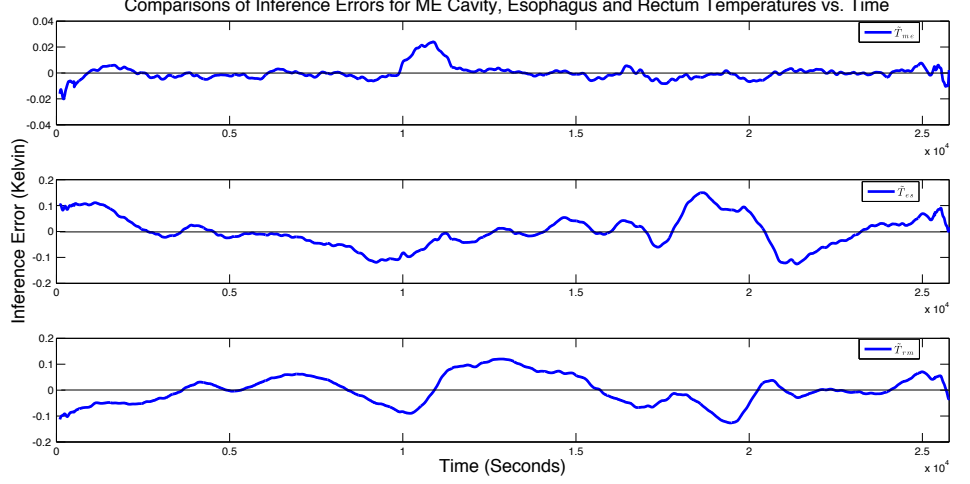


Figure 3.39: Comparison of Inference Errors for ME Cavity, Esophagus and Rectum Temperatures vs. Time plots using the *VERIFY* dataset.

3.8 Model Improvement with Gain-Scheduled Lookup

Table

The CSHB model derived in Section 3.7 to infer T_{es} has a single set of model coefficients γ obtained from the experiment datasets (in Section 3.6.2). Due to additional dynamics associated with the extended pathway, this single model cannot adequately capture the intricate heat exchanges which may depend both on the temperature level and its trend (rising or falling), hence the $MAE \leq 0.01K$ accuracy cannot be similarly achieved. By partitioning T_{tm} into various smaller temperature sub-ranges, a number of independent CSHB model characterized by a different set of refined coefficients can be used for each of this sub-range. The rationale of utilizing multiple CSHB models is to independently fit smaller T_{tm} temperature ranges of the experiment datasets with more accurate model parameters relating to the specific type of dynamics over that range. Thus, the collation of the sub-ranges is equivalent to a full T_{tm} tempera-

ture range with highly accurate models for temperature inference, which is not achievable with only a single CSHB model.

The proposed GS-CSHB model implements multiple independent CSHB models by leveraging on the well-known method of Gain-Scheduled (GS) lookup table [134–138]. Figure 3.40 depicts a high-level conceptual functional block diagram of the proposed GS-CSHB model. The figure depicts an original CSHB model C being augmented by a GS lookup table with table search function D and gradient detector M . Adding a GS lookup table to a CSHB model improves the functionality of the original model with configurable CSHB coefficients vector γ that can be loaded on-demand to cater for different T_{tm} temperature range and improves on the overall temperature inference accuracy.

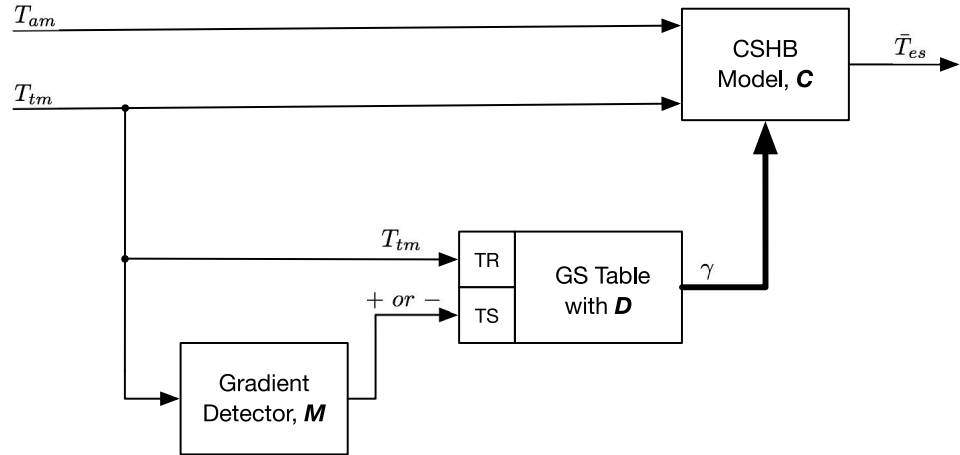


Figure 3.40: Proposed GS-CSHB Functional Block Diagram

3.8.1 Gradient Detector

Gradient Detector M is included to address the asymmetrical T_{tm} rise and fall characteristics within the same temperature range. The asymmetrical temperature characteristic is mainly due to metabolism and thermoregulatory re-

sponses [139] [140], and some environmental factors such as ambient temperature and humidity. M detects positive (+) and negative (−) gradient signs of T_{tm} by continuously calculating its first derivative (gradient) based on past and present values of T_{tm} with respect to sample time $t = 1, 2, 3, \dots$. The gradient m of T_{tm} is determined with Eqn. (3.26). To alleviate the effects of noise, m is subject to a moving average filter to yield \bar{m} . A positive \bar{m} indicates rising T_{tm} while a negative \bar{m} indicates otherwise. M outputs ”+” and ”−” gradient signs and is connected to the TS input of D . Eqn. (3.27) depicts the model M as a discrete T_{tm} gradient detector that outputs a ”+” gradient sign indicating rising temperature, and ”−” indicating falling temperature.

$$m[t] = T_{tm}[t] - T_{tm}[t - 1] \quad (3.26)$$

$$M(T_{tm}) = \begin{cases} + & \bar{m}[t] \geq 0 \\ - & \bar{m}[t] < 0 \end{cases} \quad (3.27)$$

3.8.2 GS Lookup Table

Table 3.6 depicts a generic layout of the GS lookup table. Internally, the lookup table consists of: (a) Table index (IDX) column with rows of ascending integers 1, 2, 3, ..., I , (b) Defined T_{tm} temperature range (TR) column with sorted rows of temperature values indicating T_{tm} temperature range $R_1, R_2, R_3, \dots, R_{k+1}$ where $k + 1$ corresponds to the number of partitions applied to the temperature dataset, (c) Temperature gradient sign column (TS) with rows of gradient signs ideally for each temperature range in associated with ”+” and ”−” but this depends on the data collected from the experiment, and (d) CSHB

coefficients column (γ) with rows of calibrated CSHB coefficients. TR column records the sorted (in ascending order) temperature range information, and it is populated by using the boundary information of the partitioned subsets of T_{tm} experiment dataset where the lowest and highest temperature values of each subset constitute the required temperature range. TS column records the temperature gradient sign (rising and falling temperature characteristic) for each T_{tm} subset. "+" is entered into the corresponding TS row if the corresponding T_{tm} subset shows positive gradient (rising temperature), and a "-" for negative gradient (falling temperature). When a defined T_{tm} subset contains both positive and negative gradients for its temperature data, "+" or "-" temperature gradient determines the correct γ . The γ column houses the optimal CSHB coefficients for each T_{tm} subset. $\gamma_1, \gamma_2, \dots, \gamma_6$ elements in γ columns are calculated by using Multiple Linear Regression (MLR) based parameter estimation algorithm reviewed in Section 3.5.4.

Table 3.6: Layout of GS Lookup Table

IDX	TR	TS	CSHB Coefficients (γ)					
			γ_1	γ_2	γ_3	γ_4	γ_5	γ_6
1	R_1^+	+	γ_{11}	γ_{21}	γ_{31}	γ_{41}	γ_{51}	γ_{61}
2	R_1^-	-	γ_{12}	γ_{22}	γ_{32}	γ_{42}	γ_{52}	γ_{62}
3	R_2^+	+	γ_{13}	γ_{23}	γ_{33}	γ_{43}	γ_{53}	γ_{63}
4	R_2^-	-	γ_{14}	γ_{24}	γ_{34}	γ_{44}	γ_{54}	γ_{64}
...
...
I	R_{k+1}^-	-	γ_{1I}	γ_{2I}	γ_{3I}	γ_{4I}	γ_{5I}	γ_{6I}

Eqn. (3.28) models the lookup table search function of D . D interfaces externally by having TR and TS inputs ports and a γ output port. The respective inputs are logically linked to the TR and TS data columns. D searches based on the inputs conditions, and when a match is found, it determines the table index from the corresponding IDX column, and extracts the respective CSHB

coefficients from the γ column based on the table index. TR input connects to the real-time T_{tm} data that indicates the T_{tm} temperature range. TS input reads temperature "+" and "-" gradient signs information indicating positive (temperature rising) or negative (temperature falling) gradients of T_{tm} .

$$\gamma = D(T_{tm}, M(T_{tm})) \quad (3.28)$$

D is a search operator that linearly searches through every available row of the lookup table in-order to check for a match, and correctly extracts γ . A brief summary of the lookup table D search procedure:

- Step 3.1: Initialize $Index = 1$.
- Step 3.2: Read real-time TR and TS inputs ports.
- Step 3.3: If $T_{tm} \in TR(Index)$ and $M(T_{tm}) = TS(Index)$ than goto Step 3.6, else continue to Step 3.4.
- Step 3.4: Increment $Index$ by 1.
- Step 3.5: Goto to Step 3.3
- Step 3.6: $\gamma = D(T_{tm}, M(T_{tm}))$ and goto Step 3.1

3.8.3 Partitioning Procedure for Experiment Dataset

A pre-processing procedure is used to systematically partition the temperature experiment datasets and to properly define the T_{tm} temperature range associated with each partition.

Assuming T_L and T_H are the respective minimum and maximum values for T_{tm} in the dataset and that $k + 1$ partitions are specified. The $k + 1$ sub-ranges of temperatures can thus be defined as: $(T_L < R_1 < \beta_1)$, $(\beta_1 < R_2 < \beta_2)$,

$(\beta_2 < R_3 < \beta_3), \dots (\beta_k < R_{k+1} < T_H)$. $\beta_1, \beta_2, \beta_3, \dots, \beta_k$ are the boundary information of the partitioned subsets of T_{tm} experiment dataset defined by $\beta_j = T_L + j \left(\frac{T_H - T_L}{k+1} \right)$, and $j = 1, 2, 3, \dots, k$.

For each identified T_{tm} temperature sub-range, there exists a CSHB model with a set of coefficients. Thus, $k+1$ independent models and sets of coefficients exist. k controls the number of sub-ranges, and by increasing k , minimizing the MAE of the models is attempted by having a collation of models, each applicable to a specific sub-range. Thus, a guideline to change k is to increase it to a level where the overall MAE is minimized to the acceptable level, and the specification in the application dictates $MAE \leq 0.01K$. The dataset partitioning procedure is intuitive and requires several iterations to achieve the final desired outcome, and can be easily implemented as an automated process by using the commonly available MATLAB software. A brief summary of the dataset partitioning procedure:

- Step 4.1: Set $k = 1$.
- Step 4.2: Determine $\beta_1, \beta_2, \beta_3, \dots, \beta_k$ from k . Create new $k+1$ sub-ranges of temperature.
- Step 4.3: Determine CSHB model for each subset.
- Step 4.4: Determine overall MAE from all the subsets.
- Step 4.5: If $MAE \leq 0.01K$ then stop; else continue to Step 4.6
- Step 4.6: Increment k by 1; If $k < \text{SIZE}(T_{tm})$ then go to Step 4.2; else clear $k = 0$ and stop.

$k \geq 1$ indicates a successful partitioning of the T_{tm} range which achieves $MAE \leq 0.01K$.

3.8.4 GS-CSHB Model Verification and Discussion

3.8.4.1 Construction of GS Lookup Table

The data partitioning procedure discussed in Section 3.8.3 is used to partition T_{es} and T_{tm} experiment datasets in the *CONFIG* group. Table 3.7 depicts a summary of the dataset partitioning procedures starting from $k = 1$ and ends at $k = 7$. The *MAE* is observed to decrease as k increases. $k = 7$ creates 8 subsets (various T_{tm} temperature range) from the experiment datasets and overall $MAE \leq 0.01K$ meets the required specification. The sorted temperature regions boundaries of $\beta_1, \beta_2, \beta_3, \dots, \beta_7$ define the various T_{tm} temperature range. Thus, there are 8 independent sets of (T_{tm}, T_{es}) datasets pairs, and each datasets pair are uncorrelated. Each dataset pairs inherits a calibrated CSHB model with a set of CSHB coefficients, resulted fine-grain inference improvement in each T_{tm} temperature range.

Table 3.7: Number of subsets in T_{es} Experiment dataset and its corresponding *MAE*

k	Subsets	<i>MAE</i>	Meet Specification
1	2	0.047	No
2	3	0.029	No
3	4	0.020	No
4	5	0.017	No
5	6	0.015	No
6	7	0.015	No
7	8	0.010	Yes

With the successful partitioning of (T_{tm}, T_{es}) experiment datasets, one of the most important step towards realizing GS-CSHB model for inferring T_{es} is to construct the GS lookup table specifically used for T_{es} inference. There is a total of 8 known subsets (or partitions) in T_{tm} dataset being identified and paired

with corresponding 8 subsets in T_{es} dataset. Thus, various T_{tm} temperature range are automatically defined from all the (T_{tm}, T_{es}) subsets, and the optimal CSHB coefficients for each temperature subsets pairs are also known from the partitioning procedure. With all the available information, the creation of GS lookup table is straightforward. If the entire T_{tm} dataset collected from the experiment is examined, there are instances showing T_{tm} rise and fall over the whole experiment duration. Thus, within the newly constructed GS lookup table, certain subsets have both positive and negative temperature gradients (contains both "+" and "-" gradient signs).

3.8.4.2 Inference Results and Discussion

Eqn. (3.23), (3.24) and (3.25) constitute only the CSHB model to infer T_{es} from the measured T_{tm} and T_{am} based on CSHB model coefficients vector γ . To apply the CSHB model for this purpose will entail first estimating the model parameters from experiment datasets. Thereafter, only T_{tm} measurements along with this model will serve to infer the T_{es} which is unavailable beyond the construction phase of the model. The improved GS-CSHB model requires different γ for different T_{tm} temperature range. Thus, an accurate temperature inference with $MAE \leq 0.01K$ is possible. The configured GS-CSHB is to be benchmarked against the original inferred results tabulated in Table 3.4 in order to gauge on its improvement over the CSHB model.

Benchmarks similar to those used in Section 3.6.2 are adopted with some variations:

- T_{tm} serving directly as estimate to T_{es} .

- \check{T}_{es} obtained from CSHB model.
- \bar{T}_{es} obtained from GS-CSHB model.

The results can be seen in Table 3.8. The bold fonts pick out the MAEs meeting the $0.01K$ target. Figure 3.41 shows the profile of \bar{T}_{es} inference error over time with GS-CSHB inference approach using T_{tm} . The significant improvements from the use of the GS-CSHB model is very evident over the entire duration of the experiment. Figure 3.42 shows the inferred versus actual (measured) T_{es} of the GS-CSHB model. Substantial improvements (compared to Figure 3.35) can be readily observed in Figure 3.42 where GS-CSHB is deployed, where the inferred and actual (measured) T_{es} are very closely matched, and significant improvements in the MSE, MAE and ESD are evident. The MAE achieved in inferring \bar{T}_{es} is $\leq 0.01K$. It is interesting to note that by analyzing error plots of Figure 3.41, the inference error for \bar{T}_{es} tends to be close to zero with small fluctuations. This characteristic is likely due to the effects of temperature path modeling of the CSHB model.

Table 3.8: GS-CSHB Model Benchmarks for T_{es}

Benchmark	Inference Errors(K)		
	T_{tm}	\check{T}_{es}	\bar{T}_{es}
<i>dataset = CONFIG</i>	($\times 10^{-1}$)	($\times 10^{-3}$)	($\times 10^{-3}$)
<i>MSE</i>	<i>0.93</i>	3.66 [96.06%]	0.25 [99.89%]
<i>MAE</i>	<i>2.48</i>	47.42 [80.86%]	10.58 [97.73%]
<i>ESD</i>	<i>1.78</i>	37.54 [78.87%]	11.91 [91.06%]
<i>dataset = VERIFY</i>			
<i>MSE</i>	<i>0.93</i>	3.66 [96.06%]	0.19 [99.92%]
<i>MAE</i>	<i>2.48</i>	47.40 [80.89%]	9.24 [98.02%]
<i>ESD</i>	<i>1.75</i>	37.56 [78.84%]	10.63 [92.00%]

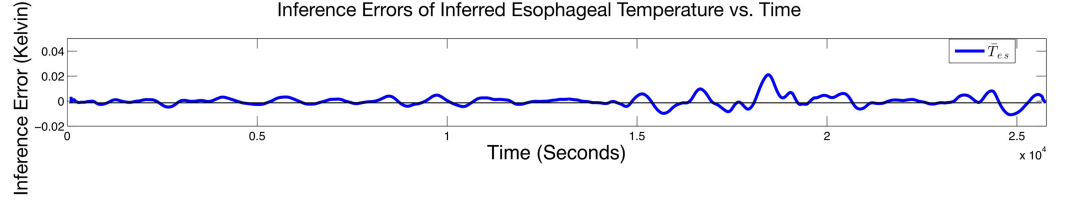


Figure 3.41: Inference Errors showing the various Inferred Esophageal Temperatures vs. Time plots using the *VERIFY* dataset.

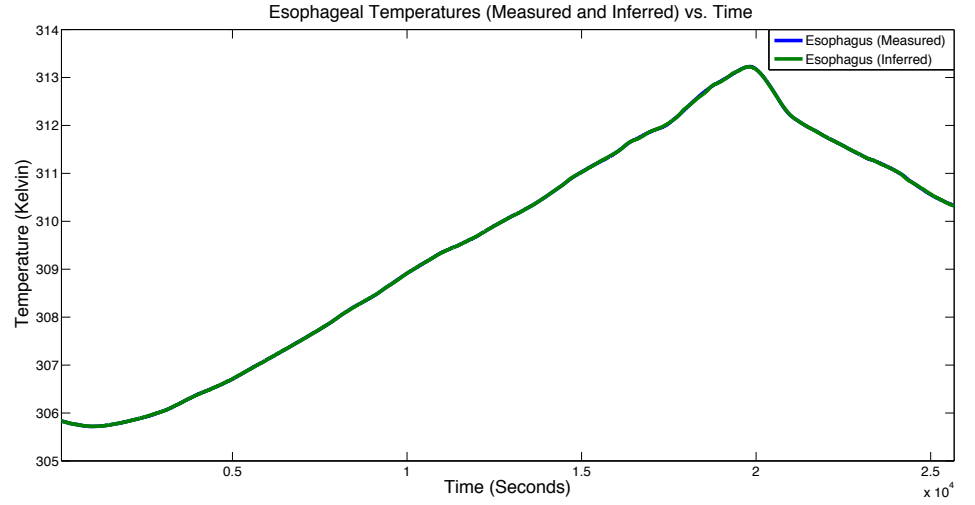


Figure 3.42: Inferred \bar{T}_{es} and Actual T_{es} vs. Time (using GS-CSHB Model)

From the benchmarking results tabulated in Table 3.8, the proposed GS-CSHB model exhibits a very high level of accuracy with both *CONFIG* and *VERIFY* datasets which achieve $\leq 0.01K$ accuracy in the MAE. The introduction of GS enhancement to the original CSHB model greatly improves the model output accuracy. *CONFIG* temperature dataset of only 513 in size was effectively used to determine the model coefficients at various T_{tm} temperature range that has remained valid for the *VERIFY* dataset which is 8558 in size; indicating GS with the multiple calibrated sets of model coefficients are able to model a much wider range of temperature change in the primate, and also effectively enhances the extended pathway of heat transfer function featured in the original CSHB model, for modeling of heat transfers to the TM from sites other than the ME.

3.8.5 GS-CSHB Model Extensions to ME and RM CBT Sites

The proposed GS-CSHB model has been demonstrated to perform satisfactorily in the inference of T_{es} from T_{tm} and T_{am} . It is interesting to explore its extension to CBT sites such as the ME and RM sites since the temperatures at these sites were also acquired in the same experiment. Table 3.9 and 3.10 contain the results showing the models inferring T_{me} and T_{rm} respectively, from T_{tm} and T_{am} measurements. Benchmarks similar to those used in Section 3.6.2 are adopted (with minor modifications):

- T_{tm} directly inferring T_{me} and T_{rm} .
- \tilde{T}_{me} and \tilde{T}_{rm} obtained from MEHB and CSHB models respectively.
- \check{T}_{me} and \check{T}_{rm} obtained from GS-CSHB model.

Figure 3.43 depicts the inferred versus actual (measured) T_{me} for the GS-CSHB models, and Figure 3.44 respectively for T_{rm} . The respective inference errors are depicted over the duration of the experiment in Figures 3.45 and 3.46. The inferred T_{me} from both the original MEHB (Figure 3.33) and the GS-CSHB models are demonstrated with only marginal improvements as both models produce outputs that are well within the $MAE \leq 0.01K$ limit. Figure 3.43 depicts T_{me} inference utilizing GS-CSHB model and shows highly accurate result (similar to Figure 3.33) as compared to the actual (measured) T_{me} plots. By analyzing the error plot of Figure 3.45, the inference error for T_{me} using GS-CSHB model (\check{T}_{me}) shows some marginal improvements over the MEHB model (\tilde{T}_{me}). It is interesting to note that the MEHB model for accurate inference of T_{me} included the non-linear radiant component that is purposely omitted in the GS-CSHB

model. The GS-CSHB model (without the non-linear radiant component) has been demonstrated to be capable of inferring T_{me} for the required accuracy by having a number of linear models to capture varying dynamics over the temperature range. On the surface, the proposed GS-CSHB model yield little benefit over the CSHB model in inferring accurate T_{me} . However, by using the GS-CSHB, the non-linear component can be omitted without sacrificing the overall output accuracy.

The CSHB model failed to achieve $MAE \leq 0.01K$ for inferring T_{rm} , with the best performance capped at $MAE \approx 0.05K$. This is mainly due to the longer heat transfer distance from the RM site to the TM site. The extended pathway to capture the longer heat transfers from the more remote site even though resulted in improvement to the overall inference accuracy but is still insufficient to meet the $MAE \leq 0.01K$ requirement. Un-modeled metabolism activities along this extended pathway may also affects the final inference result. These outliers are non-systematic and such transitional changes are beyond what the model, without consideration of additional inputs or coefficients changes, is able to account for. By using the proposed GS-CSHB model, accurate inference of T_{rm} is easily achievable for $MAE \leq 0.01K$ for both *CONFIG* and *VERIFY* datasets as depicted in Table 3.10. The area of improvements introduced by the GS-CSHB model are evident in all the *MSE*, *MAE* and *ESD* benchmark parameters. Figure 3.44 depict T_{rm} inference plots using GS-CSHB model, and shows highly accurate inference result as compared to the actual (measured) T_{rm} plot. By analyzing error plot of Figure 3.46, the T_{rm} inference error using GS-CSHB model (\bar{T}_{rm}) also depicts significant improvement over the CSHB model (\check{T}_{rm}). The

GS algorithm introduced to the GS-CSHB model, resulted in timely coefficients change across different T_{tm} temperature range. Each identified temperature region has its own calibrated model coefficients, hence effectively caters to the non-systematic problems encountered earlier from a single model coefficients. The proposed GS-CSHB model has demonstrated significant benefit over the MEHB and CSHB models in inferring accurate T_{rm} by the overall improvements of the MAE .

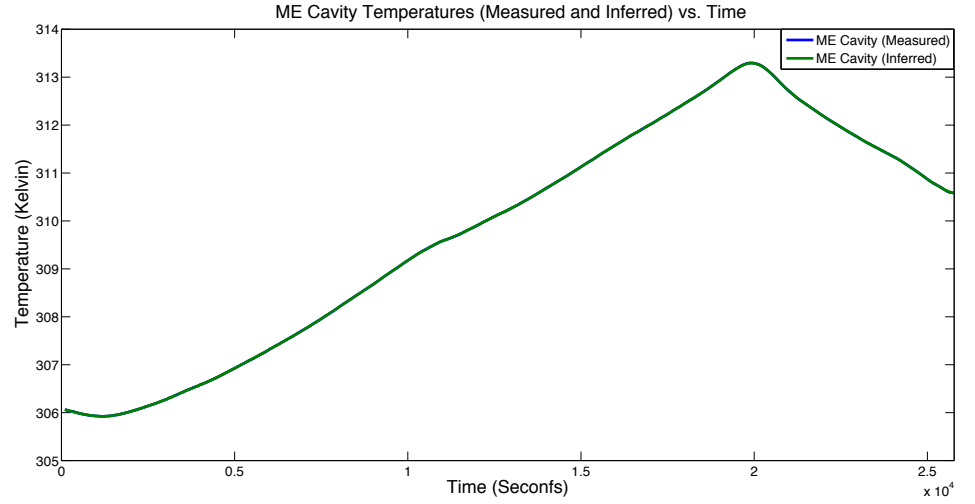


Figure 3.43: Inferred \check{T}_{me} and Actual T_{me} vs. Time (using GS-CSHB Model)

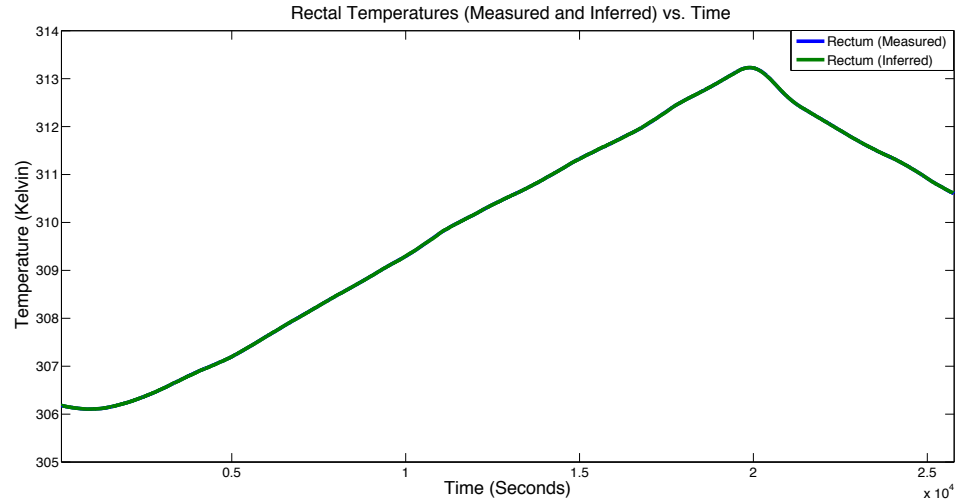


Figure 3.44: Inferred \bar{T}_{rm} and Actual T_{rm} vs. Time (using GS-CSHB Model)

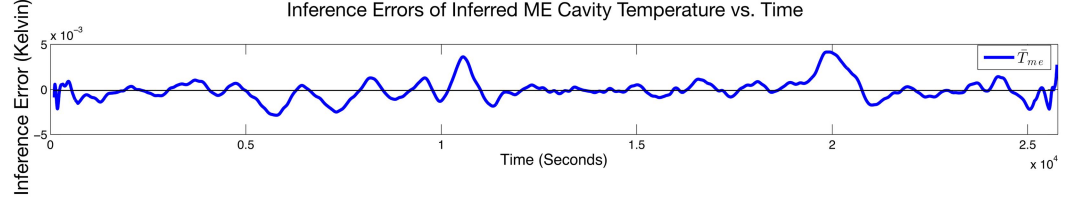


Figure 3.45: Inference Errors showing the GS-CSHB Inferred ME Temperature vs. Time plots using the *VERIFY* dataset.

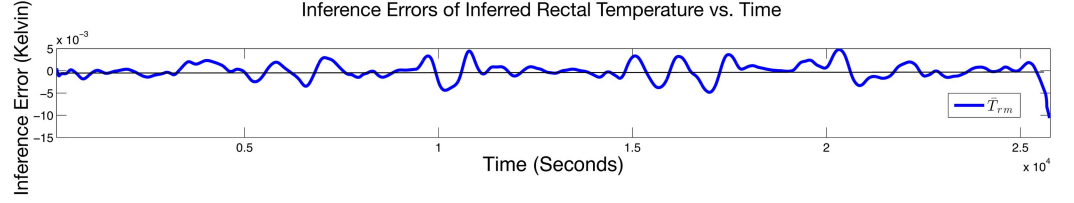


Figure 3.46: Inference Errors showing the GS-CSHB Inferred RM Temperatures vs. Time plots using the *VERIFY* dataset.

Table 3.9: GS-CSHB Model Benchmarks for T_{me}

Benchmark	Inference Errors (K)		
	T_{tm}	\tilde{T}_{me}	\check{T}_{me}
<i>dataset = CONFIG</i>	$(\times 10^{-1})$	$(\times 10^{-3})$	$(\times 10^{-3})$
<i>MSE</i>	2.35	0.029 [99.99%]	0.14 [99.94%]
<i>MAE</i>	4.67	3.42 [99.27%]	9.54 [97.95%]
<i>ESD</i>	1.33	4.11 [96.91%]	6.93 [94.80%]
<i>dataset = VERIFY</i>			
<i>MSE</i>	2.35	0.028 [99.99%]	0.003 [99.99%]
<i>MAE</i>	4.67	3.40 [99.27%]	1.12 [99.76%]
<i>ESD</i>	1.33	4.09 [96.92%]	1.25 [99.06%]

Table 3.10: GS-CSHB Model Benchmarks for T_{rm}

Benchmark	Inference Errors (K)		
	T_{tm}	\tilde{T}_{rm}	\bar{T}_{rm}
<i>dataset = CONFIG</i>	$(\times 10^{-1})$	$(\times 10^{-3})$	$(\times 10^{-3})$
<i>MSE</i>	3.84	3.19 [99.17%]	0.13 [99.95%]
<i>MAE</i>	6.10	46.43 [92.39%]	9.12 [98.04%]
<i>ESD</i>	1.12	32.18 [71.23%]	6.61 [95.04%]
<i>dataset = VERIFY</i>			
<i>MSE</i>	3.85	3.30 [99.14%]	0.008 [99.99%]
<i>MAE</i>	6.10	46.71 [92.34%]	1.71 [99.63%]
<i>ESD</i>	1.11	33.39 [70.04%]	2.21 [98.34%]

3.9 Summary

In this chapter, the TM vicinity as a potential measurement site for CBT was revisited. Two issues were explicitly targeted and experiments were carried out to verify the hypotheses and previous observations. First, the non-uniformity of temperature on the TM surface was shown using a probe positioned at a pre-defined proximity to the TM at predefined points. A point in front of the malleus bone (A1), a point in the lower anterior quadrant (B1) and a point at the distal end of the ear canal (C1) were selected for evaluation. Point A1 registered the highest steady state temperature and showed stability in indicating the CBT. Facial cooling has been verified to affect TM temperatures, but this sensitivity can be reduced by directing the measurement probe at the desired point. Secondly, the ME cavity was explored for the first time as a CBT site. The rapid responsiveness of the ME temperature towards a change in the CBT was observed relative to other sites. From the measurements, it is generally difficult to infer this change in ME temperature from the temperatures measured at the other sites. The ME cavity appears to be a potential CBT site to explore when real-time continuous measurements of CBT are necessary.

A MEHB mathematical dynamical model based on first principles which relates the relationship between the temperatures at the ME, TM and the ambient temperature has been successfully derived. Efficient procedures for the parameter estimation of the model, as well as the inference of the ME temperature from TM temperature are proposed and adopted. A model based on these algorithms were then built using real-time data from a live primate and the model was subsequently validated using extended measurements from the same primate to show

the high accuracy in the inference of the ME temperature from measurements of TM and ambient temperature only, benchmarked against other models.

The MEHB model is extended to CSHB model to infer temperatures at CBT sites further away from the ME cavity, and CBT sites at the esophagus and the rectum were discussed. Figure 3.39 provides a comparison of the inference errors for temperatures at the ME cavity, ES and the RM. The most accurate temperature inference with minimal inference error is observed to be from the ME cavity due to its close proximity to the TM. The ES and the RM being located further away exhibit higher inference errors even though higher order derivatives are included into the model.

The CSHB model is further improved into GS-CSHB model. The enhanced GS-CSHB model is realized from the augmentation of the CSHB model with a gradient detector and a GS lookup table. The combinations resulted in a customized, on-demand model coefficients configuration attachment that is shown to be effective in integrating into the CSHB model. The model was subsequently validated using measurements from the same primate to show the high accuracy in the inference of the ME, ES and RM temperatures from measurements of TM and ambient temperature only, and benchmarked against the CSHB model. The inference accuracy of $MAE \leq 0.01K$ is achievable for all the three sites, thus demonstrating the GS-CSHB model to be highly robust, and can be applied in a future work for continuous monitoring of active sportsmen/military personnel undergoing training to an accuracy of $0.01K$.

Chapter 4

Core Body Temperature

Sensing: VitalMON, a

Minimally Invasive System for

Mobile Monitoring

4.1 Introduction

Heat exhaustion is an acute and life-threatening condition [121] caused by excessive exposure to heat and dehydration. It occurs when the human body can no longer dissipates heat adequately because of extreme environmental conditions or increased metabolic heat production from within. Heat exhaustion may progress to heatstroke when the body's thermoregulatory mechanisms become overwhelmed and fail, ultimately causing heat related injuries leading to brain and organ damage or even death. In military exercise and sports activities, heat

exhaustion is a dangerous reality. In order to detect signs of heat exhaustion, the core body temperature (CBT) has to be continuously monitored. The temperature pill method of temperature measurement reviewed in Chapter 3 is expensive relative to other methods, especially when large numbers of subjects need to be monitored. The pill is non-reusable and lasted in the body for about 18 to 30 hours before passing safely [141].

On the other hand, Van Staaij *et al* [142] demonstrated that CBT measurement by infrared Tympanic Membrane (TM) thermometer has also been shown to accurately reflect CBT during hyperthermia in the clinical situation albeit in young children and is relatively inexpensive. Yamakoshi *et al* [143] demonstrated a feasible method to monitor real-time CBT via TM by developing a wearable infrared TM thermometer. Yamakoshi *et al* fabricated a custom ear mold to embed the infrared temperature sensor. Proper positioning of the ear mold is important for accurate TM temperature measurement as improper positioning leads to inaccurate measurement due to contamination of skin surface temperature from the surrounding ear canal. The ear mold aided to direct the sensor to the line of sight view of the TM within the ear canal.

The infrared temperature sensor used by Yamakoshi *et al* is commonly deployed in the commercially available handheld infrared TM thermometer and it contains only a single thermal infrared thermopile detector [144]. Commercial infrared TM thermometer can be easily found in clinics and hospitals for the sole purpose of non-invasive and fast CBT measurements. The thermometer has a single infrared thermopile detector positioned along the line of sight to the TM with the aid of a speculum [144]. The thermometer measures the average

thermal infrared emissions from the TM surface and calculates its equivalence in temperature. Non-proper positioning of the thermometer due to human error or anatomical constraints is a primary factor for inaccurate temperature measurement.

Extensive research has been conducted in Chapter 3 for the purpose of justifying the TM is reliable in indicating core body temperature (CBT). As highlighted in Chapter 3, the TM surface temperature is uneven, and evidences have shown that the highest temperature measurement point on the TM that correctly indicate CBT exists [104] [105]. Thus, by using the temperature sensor and method suggested by Yamakoshi *et al*, the measured TM temperature is the summed average of the overall TM surface temperature, which is inaccurate in indicating true CBT.

The shortfall of the system proposed by Yamakoshi *et al* has been thoroughly reviewed together with other similar systems by independent researchers [145–148]. This chapter attempt to address the shortfall by leveraging on research done in Chapter 3, and propose a novel wearable infrared TM temperature monitoring system utilizing infrared thermopile sensors array (TSA) and low power electronics. None of the systems reviewed ever utilize any method of temperature measurements pertaining to the human TM using TSA. It has been previously shown that TM temperature measurement for indicating CBT is feasible and it exhibits certain potential traits. Thus, this chapter presents the details pertaining to the design and development of VitalMON - a real-time mobile CBT monitoring and motion activity detection system for use by ordinary users and military personnel performing strenuous physical activities.

By adopting the TM for CBT measurement and with a re-usable temperature sensor, VitalMON is able to monitor in real-time the vital CBT change of a human body, and is capable of generating localized and remote alerts to report an impending heat related injury.

VitalMON is designed from ground-up based on a close collaboration with the Defense Science Organization (DSO). With documented cases of military personnel collapse and suffer from heat related injuries when undergoing strenuous physical field exercises and training, DSO aims to search for a reliable and accurate CBT monitoring solution in-order to monitor in real-time the CBTs of military personnel during field exercise and training, and to reduce or to prevent any occurrences of heat related injuries. To summarize, the primary aims of VitalMON are: (a) to accurately monitor users CBT, (b) to locally and remotely indicate the CBT status of the user and (c) to provide simple visual indicator, indicating the users current CBT range (Normal, Warning and Danger) so that the user or any person near the user is aware of what is happening. The requirements by DSO are straightforward and do not have any restriction on the VitalMON usage and deployment. Based on these requirements, VitalMON is classified as an AH device as it provides vital status (CBT) monitoring and reporting functions. Thus, VitalMON can also be used by other groups of users and not restricted to only military applications. Examples of non-military related applications are:

1. **Sports** - CBTs of Sports personnel undergoing rigorous field training can be continuously monitored to reduce the occurrences of heat related injuries. The application also applies to participants participating in stren-

uous sports events (e.g., long distance marathon).

2. **Personal Temperature Monitor** - Elderly people and people with certain health conditions can monitor their own CBT while performing physical exercises, so as not to unintentionally over exert themselves.

3. **Temperature Monitoring for the Patient with Critically Illness** - Existing VitalMON system can easily be adapted with some minor modification to provide continuous and accurate real-time CBT monitoring of critically ill patients, where medical treatments and procedures can be effectively administered.

4.2 System Architecture

In this section, VitalMON is designed from ground-up based on DSO requirements, and the military is the target user, specifically for military personnel performing strenuous physical activities and training. VitalMON is designed to be scalable, and capable of supporting a whole range of configurations from stand-alone and localized CBT monitoring within a small user group, to large scale pervasive CBT monitoring for multiple user groups. VitalMON consists of three major components: (a) Personal Vital Status Monitor (P-VSM) for ordinary military personnel, (b) Group Coordinator (GC) for military and medical officers, and (c) Backend Monitoring and Database System (BMDS).

Figure 4.1 depicts a functional block diagram of a P-VSM module. The P-VSM is a personalized wearable device which consists of two sub-modules, namely the Wireless Temperature Acquisition (WTA) unit and the Personal Data Logger/Temperature Monitor (PDL/TM) unit. The WTA is a miniature

wireless infrared thermometer to be worn in-the-ear and behind-the-ear of an ordinary military personnel. It comprises of a TSA that measures thermal infrared emission from the TM surface. A low power microcontroller unit (MCU) converts the measured infrared emission into a temperature equivalent and wirelessly transmits the temperature via the Bluetooth Low Energy (BLE) transceiver to the PDL/TM. A miniature 3V coin battery powers the WTA.

The PDL/TM module communicates with WTA via BLE to receive and process temperature data. The MCU within the module serves as a local processing unit with an added functionality to continuously track changes in the CBT of the military personnel. The PDL/TM uses an intuitive visible light indicator system as a local CBT status indicator. CBT status is signaled to other personnel within its visual vicinity in the form of a tri-color LED indicator (TLight) that mimics a typical road traffic light system. TLight is Green (Normal) if CBT is within the normal threshold, Yellow (Warning) if CBT is above the normal but still within the safe threshold, and Red (Alert) if CBT is within the unsafe threshold.

CBT is inferred from the TM temperature by performing the following steps proposed in Chapter 3. The PDL/TM monitors the inferred CBT and generates local and remote alert base on the pre-programmed CBT thresholds. There are two thresholds: *CBT_WARNING* configured at $39^{\circ}C$ and *CBT_CRITICAL* at $41^{\circ}C$. When the inferred $CBT < CBT_WARNING$, the tri-color LED indicator (TLight) on the PDL/TM is shown as blinking GREEN, when $CBT_WARNING \leq CBT < CBT_CRITICAL$, TLight is shown blinking YELLOW, and when $CBT \geq CBT_CRITICAL$, the TLight is shown solid RED. When the CBT is

within the range of *CBT_CRITICAL*, an additional loud audible alert can also be initiated as an additional measure to request for immediate medical attention. Physical activity will have ceased once the *CBT_CRITICAL* limit is reached.

The 39°C and 41°C thresholds are used during the development phase for calibration and functional tests of the PDL/TM within the lab environment involving an artificial heat source emulating an extremely fit individual known to have high CBT due to the person's ability to sustain high metabolic rate while performing strenuous physical activities [97] [149]. Based on the local context (in Singapore), 40°C is the *CBT_CRITICAL* threshold adopted by the Singapore Arm Forces. Thus, the thresholds are not fixed but largely depend on the context of interest.

PDL/TM can be programmed to automatically issue remote alert and to request for assistance through GSM (Global System for Mobile Communications) and ZIGBEE (ZBEE) wireless communications networks. Besides CBT monitoring, the PDL/TM is also motion and location aware with the inclusion of a tri-axial digital accelerometer (ACC) and a global positioning system (GPS) receiver module. This further enhances the overall P-VSM functionality with which any ordinary military personnel with a P-VSM can be remotely monitored for CBT with motion status and geographical location known, and in the event of injuries, critical assistance can be rendered on demand. A rechargeable Lithium-Ion battery powers the P-VSM, is more than sufficient for 24 hours' continual operation.

Figure 4.2 depicts a functional block diagram of a GC module. The GC is made up of a Device Coordinator (DC) unit and an Apple iPad or iPhone loaded

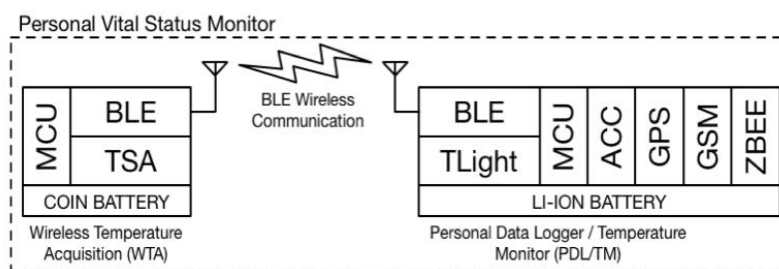


Figure 4.1: P-VSM functional block diagram.

with a custom monitoring application for an intuitive graphical user interface. The DC unit receives individual CBT, motion and geographical location data from each connected P-VSM of each ordinary military personnel. The iPad or iPhone serves as a graphical user interface for the field military officer or medical officer to observe the CBT trends, motion and location data of each ordinary military personnel. The iPad or iPhone also serves as an alerting device in an event of an emergency. There can be several GCs to monitor the same number of P-VSMs.

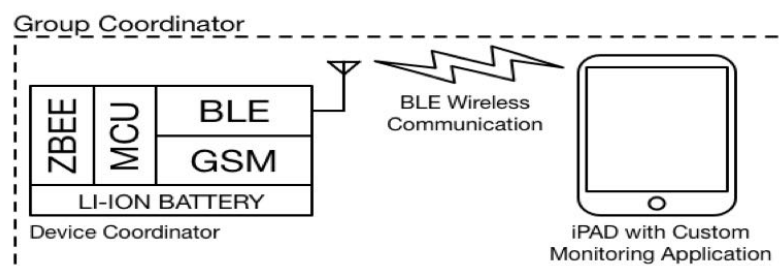


Figure 4.2: GC functional block diagram.

The BMDS serves to collect operational data for all the P-VSM deployed to the military personnel. BMDS implements an additional layer of health status and alert monitoring base on real-time data streamed by the active P-VSM of the ordinary military personnel. The BMDS usually reside at headquarter, and

real-time data from the active P-VSM are collected via the established GSM wireless communication network or via Internet cloud services.

4.2.1 Operational Advantages

The VitalMON wearable device monitors CBT of ordinary military personnel working in harsh environments or performing strenuous physical activities. VitalMON monitors in real-time the vital CBT change of the human body, and generates localized and remote alerts to report an impending heat related injury. VitalMON attaches CBT measurements with motion activity and geographical location information to ease of search and rescue operations. The wearable device also includes a Request-for-Assistance Switch, when manually activated by hand, it sends a SOS requesting for immediate assistance. VitalMON fully supports major wireless communication infrastructure including the GSM network, BLE and ZIGBEE wireless personal area network (PAN).

The WTA of the P-VSM performs contactless infrared temperature measurements using a 16×4 resolutions TSA. The sensors array measures 64 simultaneous temperature points at the TM surface and along the ear canal as opposed to a single thermopile sensor commonly used by a handheld tympanic thermometer [144]. The sensors array is capable of detecting multiple hotspots on the surface of the TM. Custom analysis firmware is developed to select temperature hotspot with highest value for valid TM temperature measurement. CBT is determined by applying custom inference algorithm developed in Chapter 3 to infer CBT from measured temperature at the TM.

4.2.2 Operational Configurations

VitalMON is scalable and it can be customized based on different operational needs. As stated earlier, VitalMON supports stand-alone and localized CBT monitoring within a small target group, as well as CBT monitoring for large scale pervasive and multiple groups.

Figure 4.3 depicts typical CBT monitoring within a small-localized group (military unit) of ordinary military personnel performing strenuous physical exercises together with a field military officer in-charge of the group and a medical officer on standby. Each group consists of a fixed number of personnel, and in most cases all the members within a military unit are involved during an exercise or training. VitalMON can easily support this group formation where each group (or military unit) is assigned a unique ZIGBEE wireless PAN, and the group members are within the ZIGBEE wireless PAN range. Each personnel is equipped with P-VSM (WTA + PDL/TM), while the officers are equipped with GCs. CBT, motion and GPS geographical location data of each personnel is periodically streamed via ZIGBEE network to the GCs. The GCs within the group will be able to monitor locally the CBT of all the personnel. A copy of the data is also sent via the GSM network or Internet cloud services to the BMDS. At any instance during the exercise, the field and medical officers, and the BMDS can be alerted of any potential heat related emergencies, and the affected personnel can be attended to immediately, thus preventing any serious heat related injuries. Each group PAN is uniquely assigned. In scenarios where multiple groups are performing field exercises or training, group leaders will only monitor personnel in their own respective groups.

Chapter 4. Core Body Temperature Sensing: VitalMON, a Minimally Invasive System for Mobile Monitoring

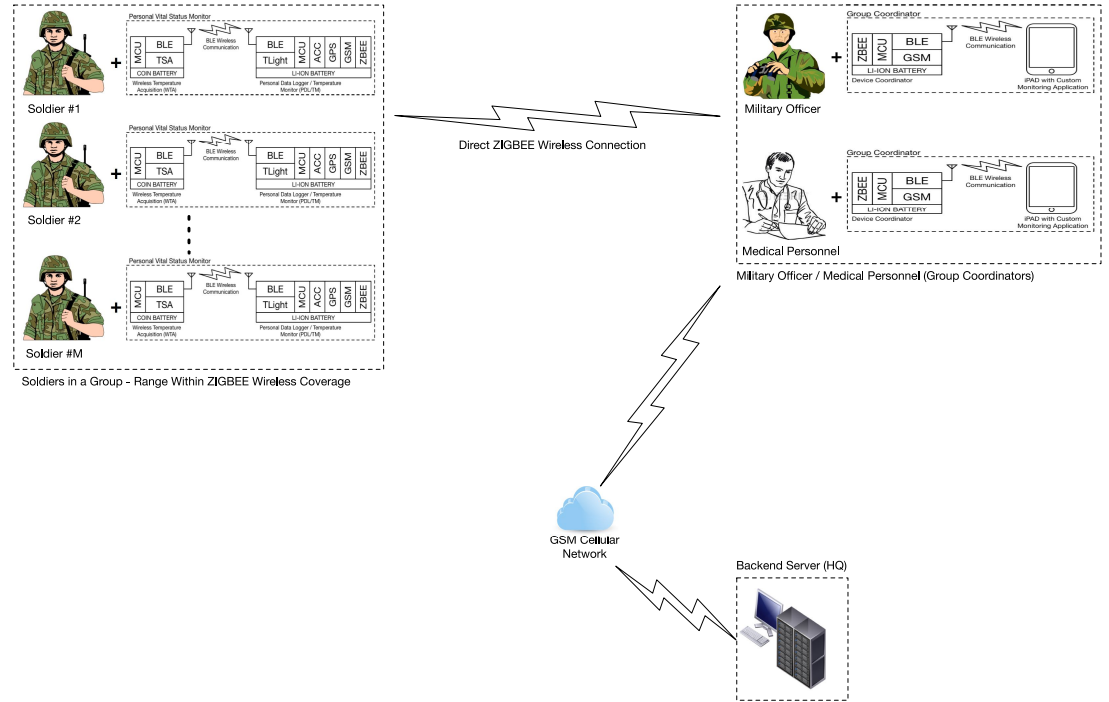


Figure 4.3: VitalMON in small group deployment at a localized area.

Figure 4.4 depicts an area deployment of VitalMON, wherein ordinary military personnel equipped with P-VSM performing strenuous exercises can be either in local or pervasive categories. Personnel in the local category is within the ZIGBEE PAN communication range with the GCs. Personnel in the pervasive category is located beyond the ZIGBEE communication range with the GCs. In this scenario, the local category still uses ZIGBEE as a primary way of communication with the GCs. The pervasive category uses GSM wireless communication network or cloud services via Internet as the primary method of communication with the GCs. The GPS location information from the P-VSM of the pervasive category is able to assist officers in locating personnel in need of urgent medical attention.

Figure 4.5 depicts another scenario where ordinary military personnel in multiple groups (military units) under the pervasive category are scattered over a

Chapter 4. Core Body Temperature Sensing: VitalMON, a Minimally Invasive System for Mobile Monitoring

wide geographical area during a large scale exercise. Each deployed P-VSM can only use the GSM communication network or cloud services via Internet in-order to communicate with assigned GCs. VitalMON is robust and fully customizable for various operational scenarios, and it includes support for existing well-established wireless communication networks. Depending on the operational requirements, VitalMON system can be configured to transmit data via one or more wireless communication networks within its range, thus eliminating the needs of providing its own custom communication infrastructure.

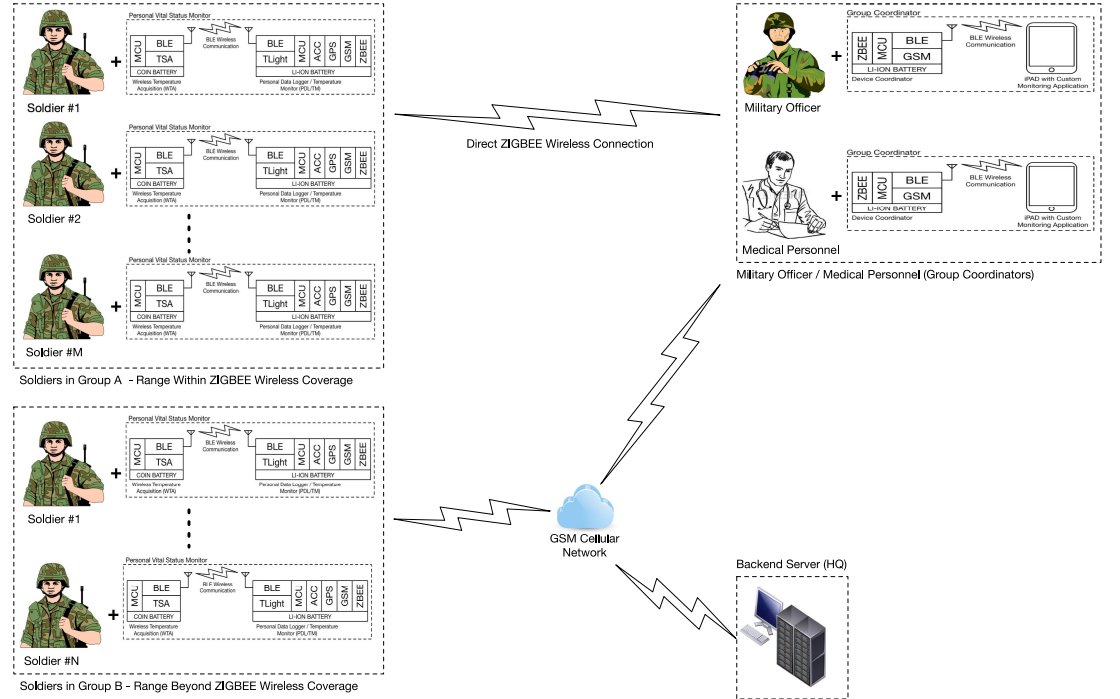


Figure 4.4: VitalMON in multiple groups deployments (local and pervasive categories).

4.3 Hardware Design

VitalMON consists of several application specific low-power autonomous embedded controller hardware, wirelessly linked to each other to form the intended

Chapter 4. Core Body Temperature Sensing: VitalMON, a Minimally Invasive System for Mobile Monitoring

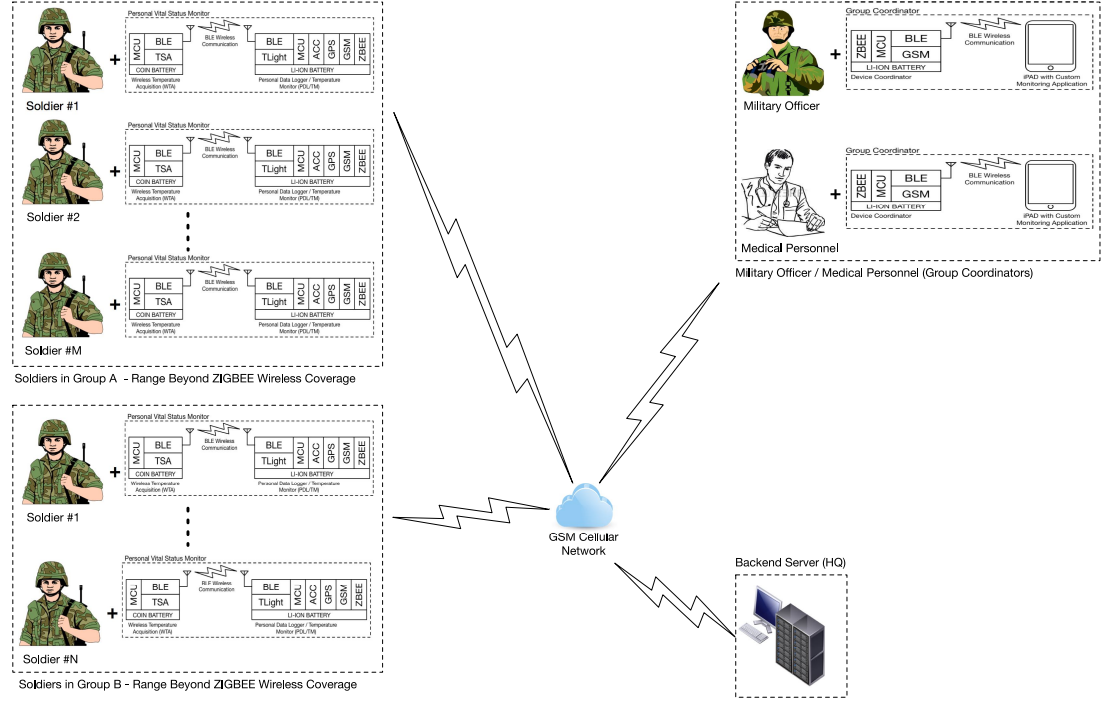


Figure 4.5: VitalMON in multiple groups deployments under the pervasive category.

real-time CBT monitoring system. VitalMON is designed as a wearable device, thus important design considerations will have to be in term of size and power consumption on top of the standard design considerations for an embedded system.

4.3.1 P-VSM Hardware

The P-VSM is a networked embedded system consisting of a WTA and PDL/TM autonomous modules. Each module has its own sets of defined functionalities, operates autonomously, and wirelessly communicates via BLE. Each module requires different firmware to function correctly. Refer to Appendix B for the details of the firmware developments.

The WTA hardware is designed with a Renesas RL78 based 16-bit low power Microcontroller Unit (MCU) [150], and clocked at 1MHz to facilitate low power

operations with $\leq 400\mu A$ in standby current. The MCU connects and communicates to the TSA via a standard Inter-Integrated Circuit (I2C) communication bus. The WTA also provides regulated 2.6V power source to the TSA so as to ensure operational stability. Thermal infrared radiation data acquired from the TSA is converted to temperature by the MCU and transferred via RS232 serial communication interface to the BLE controller. The BLE controller provides a wireless RS232 serial link to the PDL/TM to enable direct transfer of temperature data. The User Interface facilitates visual information pertaining to WTA operation modes and error status. The switch-mode type Power Controller module provides a stable 3V primary power source to the WTA from an attached miniature coin cell battery. Figure 4.6 depicts the detailed hardware block diagram of the WTA hardware.

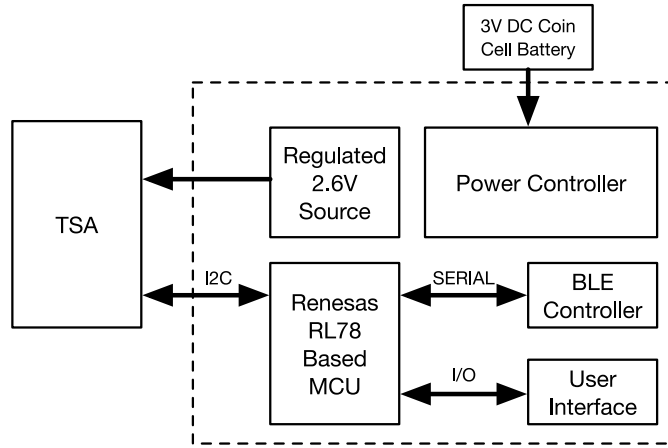


Figure 4.6: WTA block diagram.

The WTA is designed with a TSA for non-contact temperature measurement. The TSA is selected in many ways to be different from any of those standard single infrared detector used by the off-the-shelves infrared tympanic thermometers. A MLX90620 16×4 infrared TSA [67] [68] [71] [151] [152] manufactured

by Melexis is selected for this purpose. The TSA has a $60^\circ \times 10^\circ$ optical field-of-view (FOV) from an attached infrared lens, and digitally interfaced to a 16-bit low power MCU via an I2C bus. Figure 4.7 (a) depicts a cross sectional area of a human ear with a conceptualization of a WTA unit that is similar to a typical in-the-ear hearing aid which consists of a custom ear mold constructed with hypo-allergic material encapsulating the TSA, and a behind-the-ear low-power electronics module. The TSA is enclosed in a custom plastic ear mold, and is positioned within the human ear canal with a direct line-of-sight view of the TM in-order to pick-up the thermal infrared (heat) emission from the TM surface. The TSA is connected via short and shielded electrical wires to the behind-the-ear electronics module that contains BLE and Control Electronics hardware for control and communication purposes. Figure 4.7 (b) is an actual constructed WTA prototype with the TSA embedded within a clinical plastic ear speculum replacing the custom ear mold. The prototype is constructed to demonstrate its intended functionality; hence the speculum is used to replace the costly and customized plastic ear mold. The speculum provides the same function as the ear mold in securing the TSA in a proper position in-order ensure a direct line-of-sight view of the TM.

Figure 4.8 depicts the TSA square thermal pixel arrangement where each on-chip individual pixel is a thermopile infrared detector. By placing the TSA in a line-of-sight exposure to the TM surface along the ear canal wall, the thermal infrared emission from the TM and the surrounding canal wall can be captured and measured, and the highest temperature point can be determined based on the infrared emission. The area of interest (AOI) from the 16×4 pixels thermal image

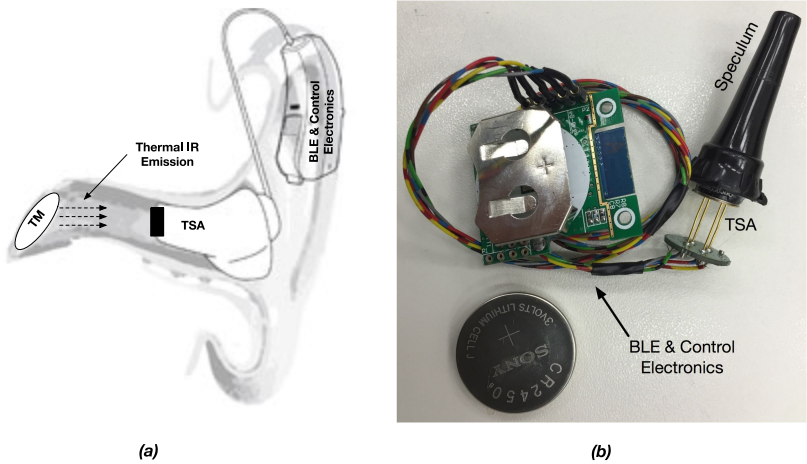


Figure 4.7: (a) Conceptual design and fitting of a WTA for ordinary military personnel, and (b) Actual WTA prototype with a clinical ear speculum.

with $60^{\circ} \times 10^{\circ}$ FOV implemented with an embedded infrared lens represents the actual location of the TM as seen by the TSA. In an ideal line-of-sight positioning of the TSA, the AOI will be right at the center of the thermal image. In most cases, the anatomy of the ear canal differs for each human subject. Thus, the design of the ear mold is critical to ensure proper positioning of the TSA in the ear canal.

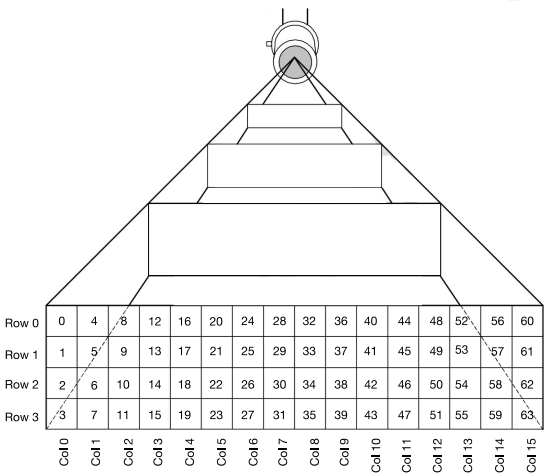


Figure 4.8: TSA Thermal Pixel Configuration.

The TSA measures levels of thermal infrared emissions. Each of the square

pixels on the array is an individual infrared thermopile detector connected to a 16-bit analogue to digital converter. Each raw data represents an infrared emission level. The longer the distance between a heat emitting object and the TSA, the less accurate result can be expected from the surface infrared emission measurement of the object. This issue does not affect the overall WTA performance due to the short line-of-sight distance between the TSA and the TM.

A WTA prototype is constructed where the TSA is embedded into a clinical plastic speculum with its sensing window pointed at the distal opening of the speculum. The speculum measuring 3.6cm in overall length and 0.4cm in diameter at the distal opening is used in-place of a custom ear mold. A block diagram summarizing the WTA with a TSA embedded in a speculum together with its interface electronics board is depicted in Figure 4.9. The TSA has an original FOV of $60^\circ \times 10^\circ$ for 16×4 pixels implemented with an embedded infrared lens. However, embedding of the TSA into the clinical speculum resulted in a much-reduced FOV of $10^\circ \times 10^\circ$. The main reason behind the original FOV reduction is due to the speculum's distal opening diameter of 0.4 cm blocking some of the views of the TSA. As such, the effective TSA resolution also reduced to 4×4 pixels representing the effective FOV at the distal end.

Using a smaller size clinical speculum of the same length will result in a loose fit of the speculum within the ear canal. In this scenario, the distal end of the speculum is still being positioned at the line of sight to the TM. However, due to the distal end of the speculum being reduced in diameter, the effective FOV will also be further reduced, hence reducing the effective resolution of the TSA.

Thus, the 16×4 pixels TSA might not be able to cover the whole TM surface. In a worst case scenario, the TSA behaves very much like the single pixel sensor commonly found in those off-the-shelves infrared ear thermometers.

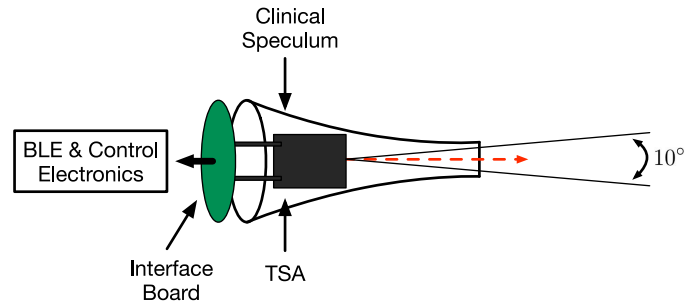
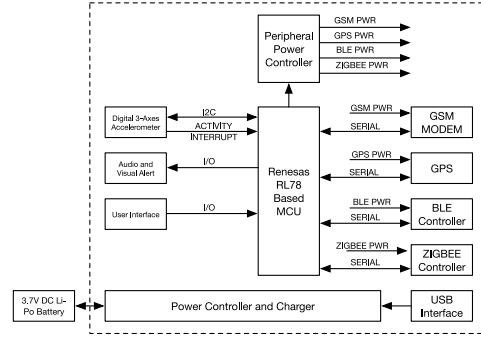


Figure 4.9: TSA embedded in disposable plastic speculum with 10° effective FOV forming the WTA module prototype.

The PDL/TM hardware is designed with a similar Renesas RL78 based MCU. The MCU interfaces to more peripherals hence requires higher clock rate of 32MHz to improve in its overall processing efficiency. The attached peripherals are the GSM Modem, GPS module, BLE controller, ZIGBEE controller, 3-Axes Digital Accelerometer, Lithium-Ion (Li-Ion) Battery Power Controller and Charger, Audio and Visual Alert and User Interface. Each of the peripheral's power supply is individually controlled by the MCU via the Peripheral Power Controller and is only turned on when required. This approach presents a simple and yet effective methodology for controlling the device's overall power consumption by allowing only the active peripherals to be turned on, while turning off idle peripherals (selective load shedding), thus eliminating the quiescent currents consumed by the idle peripherals. The PDL/TM is powered by a 3.7 Volts, 2.2AH rechargeable Li-Ion battery that is able to ensure continuous operational time duration of at least 24 hours. Figure 4.10(a) depicts the hardware block diagram of a PDL/TM, and Figure 4.10(b) depicts a completed hardware

prototype.



(a) Block diagram



(b) Prototype

Figure 4.10: PDL/TM: (a) Block diagram (b) Prototype

The GSM Modem provides a wide area communication link via the GSM communication network; the GPS module provides current GPS coordinates of the PDL/TM; the BLE controller wirelessly connects to the paired WTA module; the ZIGBEE controller provides local area communication link via ZIGBEE wireless mesh network; the Accelerometer detects various forms of human motion activities; the Power Controller and Charger provide stable 3.3V supply to all on-board components and to charge the 3.7V Li-Ion battery; the Audio and Visual Alert provides audible notifications and alerts, and it also serves as a tri-color TLight status indicator; and finally the User Interface provides simple push-button based control to the PDL/TM.

4.3.2 GC Hardware

The GC Hardware is made up of a DC hardware module and an iPad pre-loaded with a custom User Interface (UI). The DC hardware module shares a similar hardware functions as PDL/TM but with less attached peripherals. The attached peripherals are the GSM Modem, BLE controller, ZIGBEE controller

and Li-Ion battery Power Controller and Charger. Figure 4.11(a) depicts the DC hardware block diagram. Based on a similar approach in controlling power consumption as in PDL/TM hardware, the power supply to each attached peripheral is independently controlled by the MCU, and only turned on when required. The DC is also powered by a 3.7 Volts, 2.2AH rechargeable Lithium-Ion battery which delivers similar operational lifespan as PDL/TM.

The GSM Modem provides wide area communication link via GSM communication network; the BLE Controller connects the DC to an iPad or iPhone; the ZIGBEE Controller establishes a unique and secured local wireless ZIGBEE mesh network; and forms connections to the PDL/TM within its wireless coverage; and User Interface provides simple push-button based control to the DC. Figure 4.11(b) depicts a GC which consists of a DC prototype and an iPad custom user interface application.

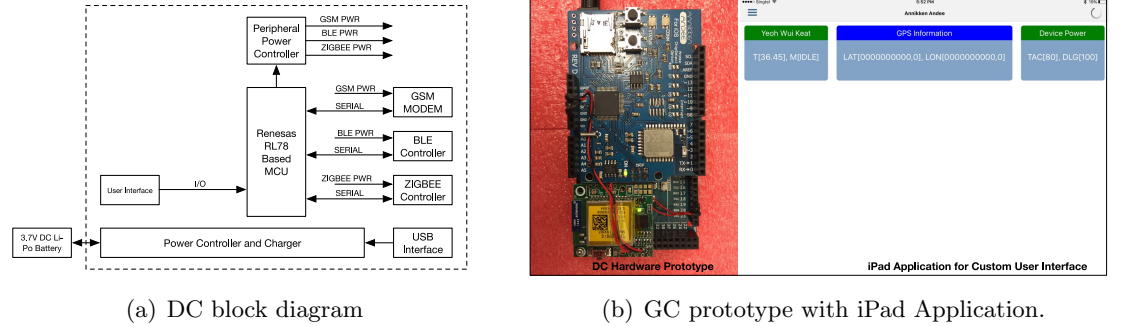


Figure 4.11: GC: (a) DC block diagram (b) GC prototype

4.4 Thermal Infrared based TM Temperature Measurement with P-VSM

It has been established that the TM has an uneven surface temperature distribution. Temperature at the hottest spot on the TM must be used in-order

to infer an accurate CBT [104] [105]. The TM is a valid thermal infrared source as its surface emits heat. The most elegant way to engage the hottest spot will be via thermal infrared imaging. By using an infrared detector with sufficient resolution, the temperature at the hottest spot can be easily determined. A typical handheld infrared tympanic thermometer can only measure the average surface temperature and is unable to discriminate the highest temperature spot on the TM [144].

As discussed earlier, the P-VSM is a personalized wearable device, which consists of two sub-modules. In this section, the WTA sub-module will be discussed in detail as it embodies an infrared detector, which is important for accurate CBT measurement. The PDL/TM sub-module will also be briefly discussed as it houses the CBT measurement algorithm developed in Chapter 3 and alert systems.

4.4.1 Optical line-of-sight view of the TM for accurate temperature measurement via thermal infrared emission

The accuracy of the TM temperature measurement relies on the direct line-of-sight view between the TM and the infrared detector. The direct line-of-sight view of the TM can be achieved by using a custom ear mold that perfectly fits the ear canal with its distal end pointing at the TM. A custom ear mold will fit perfectly to a specific user's ear canal, is comfortable to use and is non-transferable due to hygiene reasons. Alternatively, the ear canal can be straightened with an aid of a clinical ear speculum of an appropriate size and length. A clinical ear speculum is used by medical practitioners for visual ear examinations, and it is also commonly used in off-the-shelves infrared ear thermometers. Ear speculums

vary in sizes and lengths and they are tailored for specific usages. A clinical ear speculum chosen for this project has a length of 3.6cm and distal end diameter of 0.4cm, and the ear canal is automatically straightened when the speculum is fully inserted into the canal. Similar in functionality to a custom ear mold, the plastic speculum secures the TSA in a proper position for a direct line of sight view of the TM. The available sizes of plastic speculums are limited and the sizes may not properly fit all the volunteers ear canals. Each volunteer may experience varying level of discomfort due to the speculum being inserted deep into the ear canal. For development purpose, using an off-the-shelf plastic speculum is the only feasible and economical alternative. Volunteers from different gender and age groups are tasked to test the CBT measurement accuracies and other functionalities for only a short period of time. It will not be practical to fabricate custom ear molds for each of these volunteers. In an actual field deployment, customized TSA module which is much smaller in diameter, together with a personalized ear mold made from hypo-allergic material will be provided for each user. The ear mold design will introduce good fit and removes the inherent discomfort associated with the plastic speculums.

Figure 4.12 (a) - (d) depict the clinical speculum fitted tightly into an ear canal. The figures also depict how an ear canal is automatically straightened. The distal end of the clinical speculum is at the near proximity and with line-of-sight view to the TM. A simple geometrical analysis shows that the degree of freedom is rather limited when the clinical speculum is fitted tightly into an ear canal. Reference x-axis and y-axis lines are defined to indicate the position of rotation angle of the clinical speculum. θ is positive if rotation is clockwise

and negative if rotation is counter-clockwise. The red dotted arrow depicts the center of line-of-sight view from the distal end of the speculum. The FOV area of coverage of the clinical speculum is depicted with a dotted red rectangle box.

Figure 4.12 (a) depicts the speculum positioned with $\theta = 0^\circ$ and its distal end touching the ear canal surface. Due to the deep penetration of the speculum, its distal end is along the line of sight towards the TM and there is no contamination from the ear canal surface. Figures 4.12 (b), (c) and (d) depict line of sight views of the TM at $\theta = 2^\circ$, 4° and 6° respectively covering the whole TM surface. Due to the clinical speculum being deeply inserted into the ear canal, the allowable value of θ is limited between 0° and 6° (inclusive of both). User will experience varying amount of pain if θ is at 0° and 6° , and outside this range. This is due to the distal end of the speculum pressed against the inner ear canal wall tissue (near to the TM). The limited value of θ directly ensures proper coverage of the line-of-sight view of the TM without any direct contamination from the surrounding ear canal wall. The clinical speculum might not be comfortable for the user, but it ensures proper line of sight view of the TM.

A short length speculum that is approximately 2.3cm in length and with a diameter of 0.7cm at its distal end is commonly used in commercial infrared ear thermometer. The short length speculum limits the deep insertion into the ear canal and improves the usage comfort. A short length speculum can be positioned comfortably at the outer ear with its distal end inserted into the shallow opening of the ear canal, hence avoiding any form of physical contact to the distal end of the ear canal wall in proximity to the TM. The shallow penetration into the ear canal ensures comfort of use. However, this approach

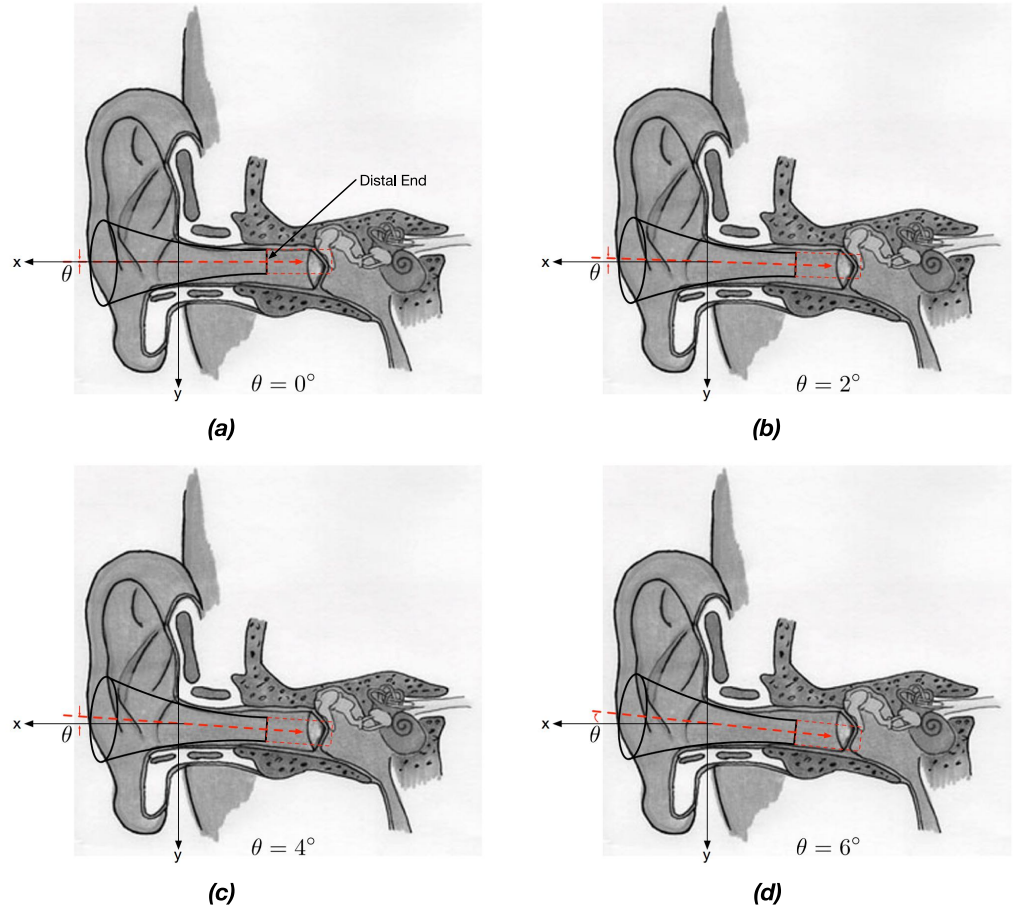


Figure 4.12: Clinical speculum with distal end exposed to the TM within an automatically straightened ear canal.

does not automatically straighten the ear canal, hence resulting in erroneous measurement (if the ear canal is not properly straightened). Figure 4.13 (a) - (d) depict typical scenarios when a short length speculum is inserted into an un-straightened ear canal. Figure 4.13 (a) depicts the speculum positioned at $\theta = 0^\circ$ which indicates the line-of-sight view of only the canal wall without the TM coverage. Figure 4.13 (b) depicts the speculum positioned at $\theta = -10^\circ$ which indicates the partial line-of-sight coverage of the TM with an obvious ear canal wall contamination at the bottom area. Figure 4.13 (c) depicts the speculum positioned at $\theta = -15^\circ$ which indicates the partial line-of-sight coverage of the

TM without any known ear canal wall contamination. Figure 4.13 (d) depicts the speculum positioned at $\theta = -20^\circ$ which indicates another line-of-sight view of only the ear canal wall without the TM coverage. Speculum positioned at $\theta = -15^\circ$ is determined to be optimal for measuring temperature of the partially exposed TM without ear canal wall contamination. Other values of θ result in TM temperature measurements with ear canal wall contamination or purely measuring only the ear canal wall temperature.

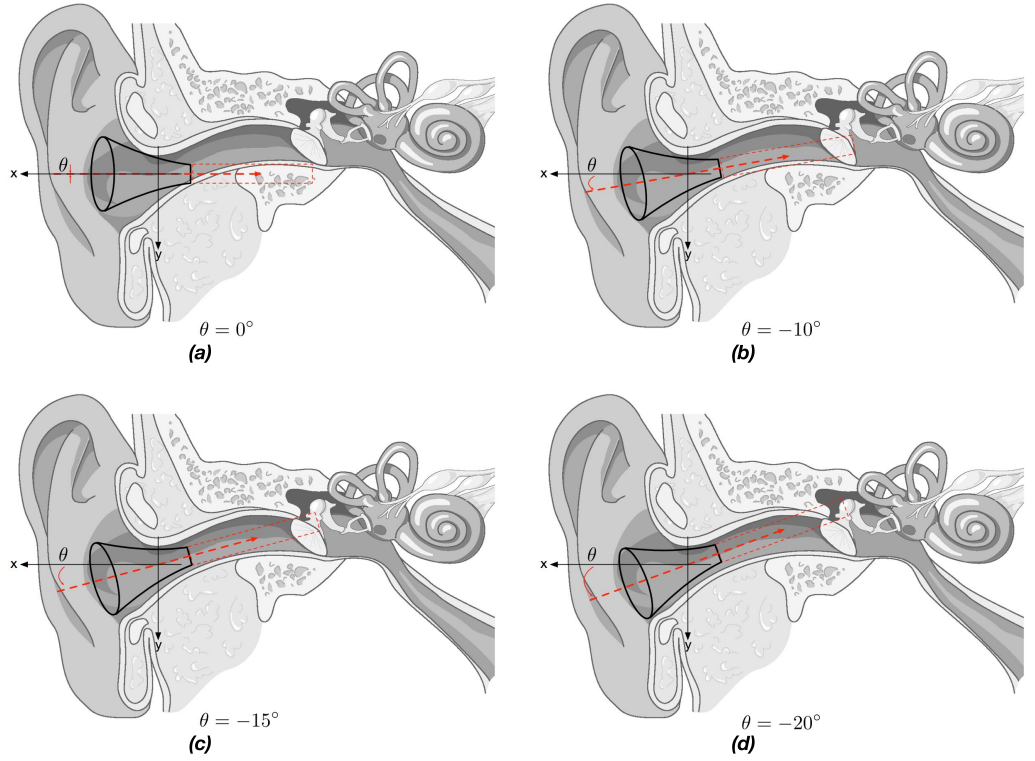


Figure 4.13: Short length speculum with distal end partially exposed to the TM within an un-straightened ear canal.

An ear canal can be straightened manually (by hand) by gently pulling the top of the ear lobe towards the back of the head. Figure 4.14 (a) - (f) depict the short length speculum fitted into an ear canal that has been straightened in this manner. The line-of-sight views at the distal end of the short length

speculum for Figure 4.14 (a) - (d) are the same as those in Figure 4.12 (a) - (d), with proper views of the TM without any contamination from the ear canal surface. However, at $\theta > 6^\circ$ as depicted in Figure 4.14 (e) and (f), the line-of-sight view of the TM is clearly being contaminated with the ear canal wall. $\theta = 6^\circ$ is determined to be the rotation limit of a clinical speculum, however with the short length speculum, due to its loose-fit nature at the ear canal, θ can be effectively increased beyond 6° . It has been shown that at $\theta > 6^\circ$, the line-of-sight view of the TM is clearly being contaminated with the ear canal wall.

The short length speculum is very prone to improper positioning along the ear canal that affects the line-of-sight view of the TM, hence is not adopted for this project. This problem is quite common for most off-the-shelf infrared ear thermometer that ultimately affects the TM temperature measurement accuracy. Thus, the easiest and optimal way for providing good line-of-sight view of the TM is by using a clinical ear speculum albeit the associated pain and discomfort. A custom ear mold mimics the performance of a clinical ear speculum in providing tight fitting as well as proper positioning within the ear canal for proper line-of-sight view of the TM without the inherent discomfort and pain.

It has been shown that the clinical and short length speculums can only provide limited FOV of the overall TM surface. The speculums must be rotated in-order to cover other areas on the TM surface, and depending on the type of speculums used, the rotational angle might cause ear canal contamination. As such, any single infrared sensor positioned at the distal end of the speculum might not be effective in measuring the proper TM temperature if the rotational

angle is not correct for the speculum to cover the optimal spot as highlighted in [104] [105]. A form of corrective infrared lens must be deployed at the distal end in-order to increase the FOV of sensor to cover the overall TM surface.

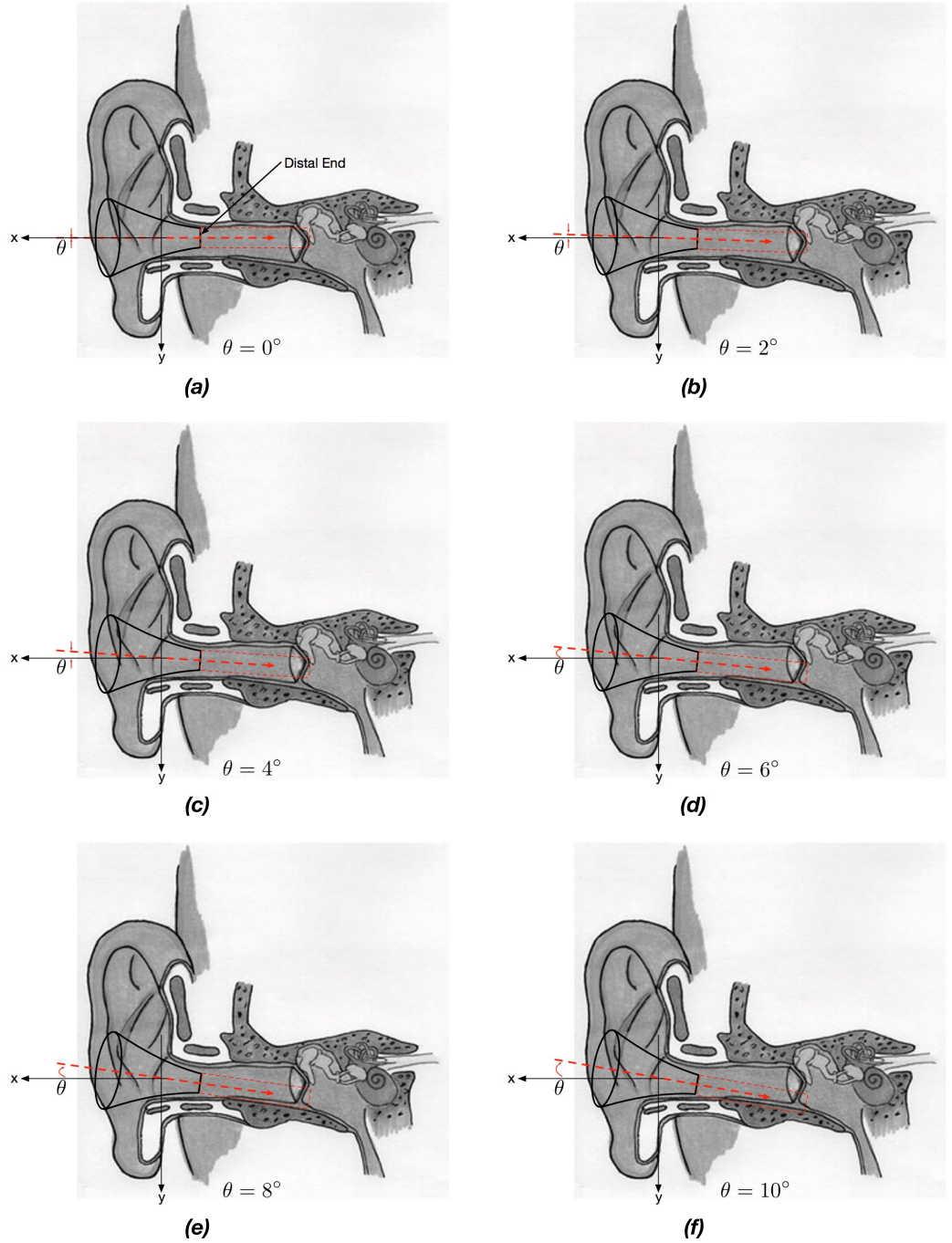


Figure 4.14: Short length speculum with distal end exposed to the TM within a straightened ear canal.

Figure 4.15 depicts a conceptual method showing a WTA prototype being tightly fitted into an ear canal. It has been previously shown that the ear speculums can only partially view the TM surface area. The effective FOV of $10^\circ \times 10^\circ$ from the embedded infrared lens is able to increase the view coverage that sufficiently covers the overall TM surface. Thus, this is an added advantage of using a TSA as opposed to a single infrared sensor without embedded lens.

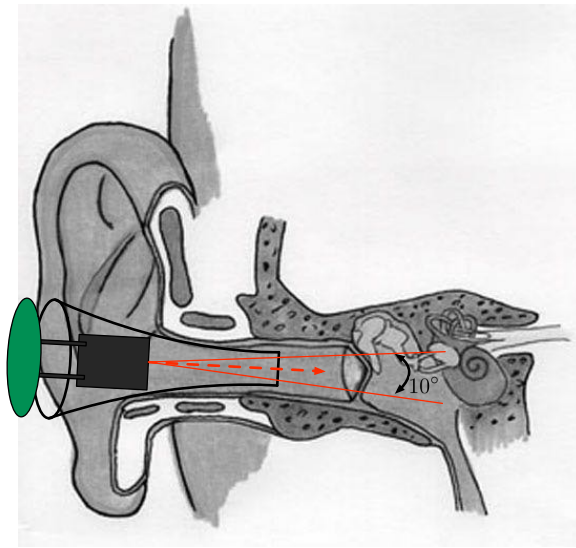


Figure 4.15: WTA prototype tightly fitted into an ear canal.

4.5 Feasibility Study of WTA for Measuring TM Temperature

5 healthy adult volunteers between 30 - 40 years of age were engaged in a feasibility study to test the effectiveness of the WTA prototype where the TSA was embedded into a clinical ear speculum for real-time measurement of the TM temperatures. The study was carried out within an enclosed air-conditioned room with a stable room temperature of 24°C . A TSA was embedded into each

of the 5 speculums intended for use by the volunteers. By using an otoscope as a guide, the speculums were fitted very deeply and firmly into all the volunteers' left ear canals where clear line-of-sight views of the TMs from the TSAs were provided. In the study, with the aid of the speculums, the left ear canals of the volunteers were observed to be automatically straightened. Due to tight fitting, the distal ends of the speculums have very limited degree of freedoms for any form of internal movements. Thus, regardless of any limited small movements to the speculums, the distal ends were still properly aligned to the line of sight views of the TMs. It was also noted that each of the ear canal wall at the distal end of the speculum in proximity to the TM was extremely sensitive to touch and pressure, thus the volunteers wearing tight fitting speculums experienced substantial pains and discomforts. The WTA prototypes with clinical ear speculums deployed in the study may not be comfortable but they ensured good line of sights to the TMs.

Figure 4.16 - 4.20 depict 5 sets of 16 x 4 low resolutions thermal images constructed from temperature data acquired from the views at the clinical speculums positioned securely in 5 volunteers' ear canals. In Figure 4.16 - 4.20, the areas of the thermal images enclosed within the dotted rectangles areas are consistently showing the thermal images of the exposed TMs of the volunteers. The affected pixels are consistently from locations (in brackets) 28 to 43 for an effective FOV of $10^{\circ} \times 10^{\circ}$. Consistently, the hottest points captured on 5 thermal images are on the TMs of the volunteers. The areas outside the dotted line rectangles areas are the ear canal walls and show lower infrared emissions than the TMs, and these results are consistent with the human skin surface temperature that is

always lower than the CBT. The hottest pixels are consistently being measured at pixel location 34, 37 or 38 of the thermal images. The prototypes reliably show performance consistency for the ability to detect temperature hotspots on the TMs of the volunteers.

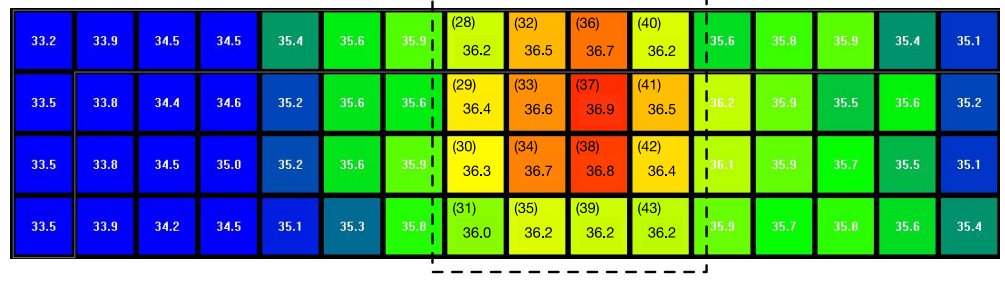


Figure 4.16: Constructed thermal image at the view from a speculum of Volunteer 1 (Thermal data at time t).

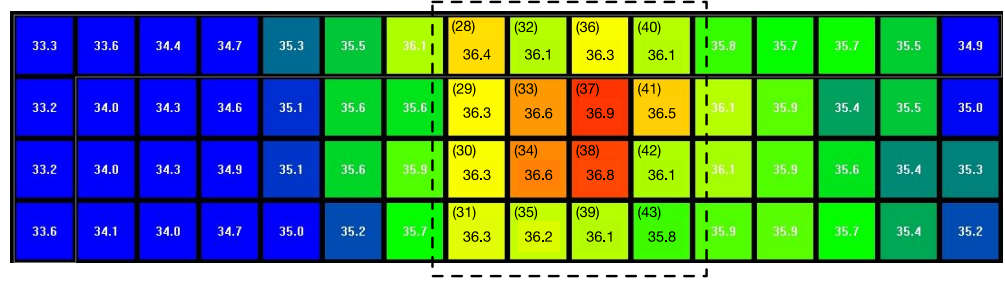


Figure 4.17: Constructed thermal image at the view from a speculum of Volunteer 2 (Thermal data at time t).

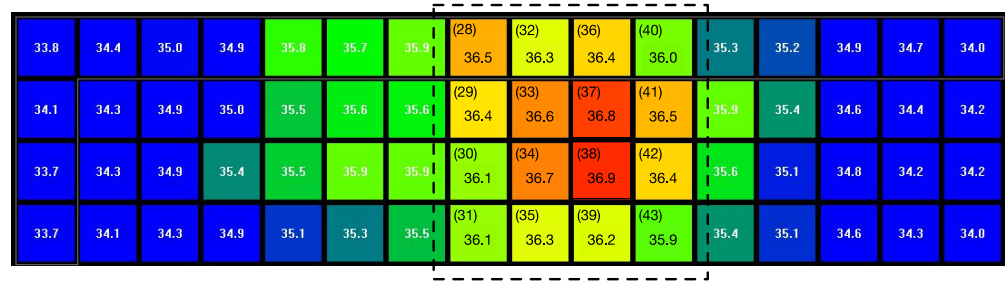


Figure 4.18: Constructed thermal image at the view from a speculum of Volunteer 3 (Thermal data at time t).

An effective AOI is defined as a small area on the thermal image that represents an actual line of sight thermal view of the TM. The rest of the area on the

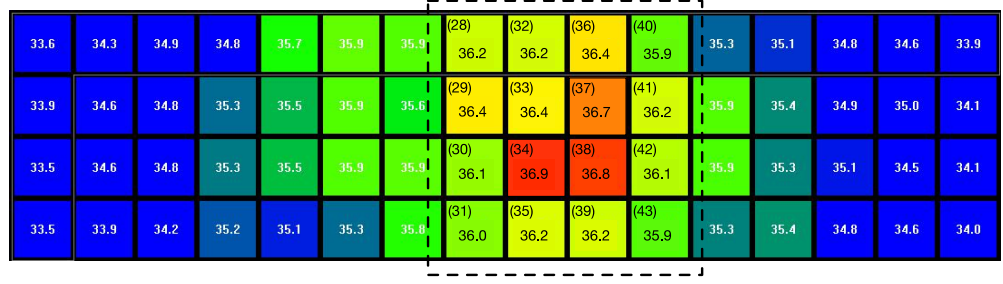


Figure 4.19: Constructed thermal image at the view from a speculum of Volunteer 4 (Thermal data at time t).

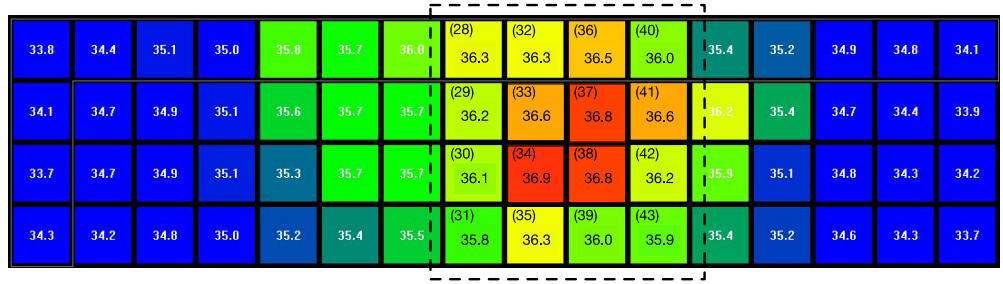


Figure 4.20: Constructed thermal image at the view from a speculum of Volunteer 5 (Thermal data at time t).

image represents the tissue surface of the ear canal. With the known AOI of the TM, the rest of the pixel data outside the AOI is no longer important. Thus, a 16 x 4 pixels custom TM-MASK representing the AOI of the TM can effectively mask out (remove or ignore) the unwanted pixels and leave the effective thermal pixels representing the TM intact, hence resulting in a smaller set of raw infrared data for processing. In the feasibility study, the AOIs of the 5 volunteers' left TMs were determined by constructing the thermal images depicted in Figure 4.16 - 4.20, from the sets of processed temperature data from all the 64 pixels downloaded from the WTAs in operations. A custom rectangle TM-MASK (in dotted black rectangle) for each volunteer is defined where pixels beyond the dotted rectangle area are ignored. By applying the masks, TMs temperature measurements from infrared emissions can be efficiently conducted.

In the feasibility study, the temperature and infrared emissions from the left TMs of the volunteers were measured at every 1 hour interval for total of 8 hours. The TM temperature of each volunteer was carefully measured by using a Braun ThermoScan 5 clinical infrared ear thermometer, and the respective thermal infrared emissions were measured by using a WTA prototype discussed earlier. The temperature data from the ThermoScan 5 were used for accuracy benchmark against the temperature data calculated from the thermal infrared emissions measurements from the WTA. The measurements involved manual re-insertion and re-positioning of the ThermoScan 5 and the WTA along the ear canal. The ThermoScan 5 was positioned with care to ensure proper line of sight view to the TM. The line of sight view of the TM as seen by the WTA may vary slightly at each re-positioning.

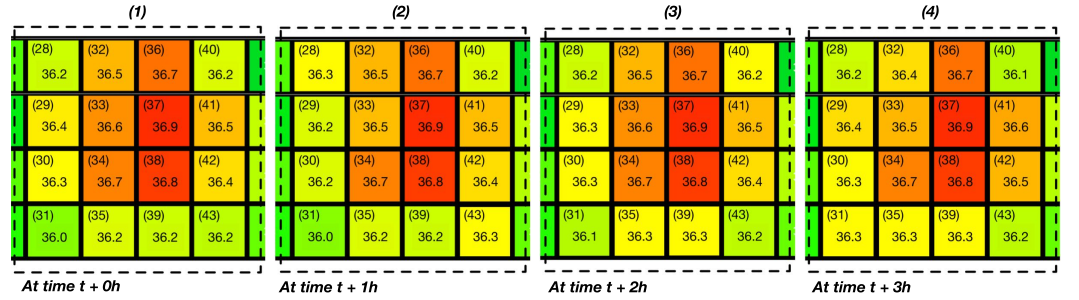
The resultant TM thermal images for volunteer 1 to 5 were constructed as depicted in Figure 4.21(a) - 4.25(a) for the first 4 hours and in Figure 4.21(b) - 4.25(b) for the last 4 hours. In all of the 5 figures, the dotted rectangle areas contain the volunteers' TMs temperature map with thermal pixel location and temperature labels. The first half (first 4 hours) of the measurements were conducted without the effects of head cooling. During the second half (last 4 hours) of the measurements, forced convection head cooling was introduced by using small direct current (DC) electric fans blowing 120 Cubic Feet per Minute (CFM) of cool ambient air directed toward the left face of each volunteers from a distance of 20 cm away.

The hot pixel location is defined as the identified thermal pixel with the highest temperature value, can be observed in Figure 4.21(a) - 4.25(a) and in

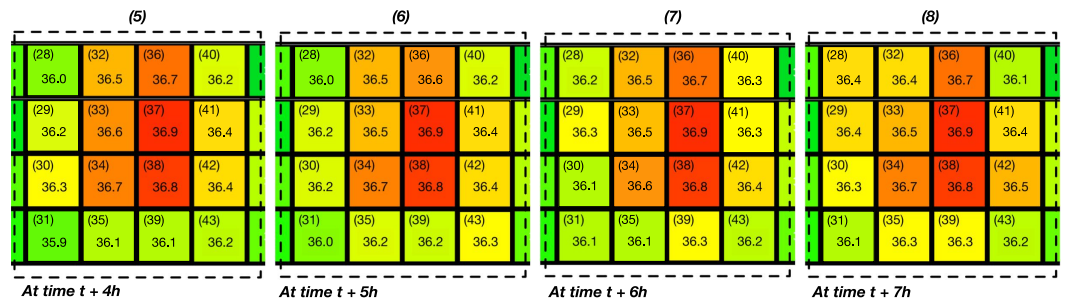
Figure 4.21(b) - 4.25(b) to alternate between pixels at the 3 locations 34, 37 and 38 for all the volunteers. It is interesting to note that for each volunteer, the corresponding hot pixel only appears in 1 of these 3 pixels locations. The TM areas measured by pixels at the 3 locations can be attributed to the highest temperature spot as previously reported by Brinnel and Cabanac [104] and Sato *et al* [105]. At every instance when the speculum was re-fitted with care on each of the volunteer's ear canal, small positioning error was observed where the hot pixel may be shifted between the 3 locations. The hotspot temperature (highest temperature) measurement was consistent at $36.9^{\circ}C$. Head cooling introduced certain level of fluctuations to the overall surface temperature of the TM as observed in the TM temperature map of each volunteer in Figure 4.21(b) - 4.25(b). However, no apparent effects were observed at the hotspots on all the TMs when measured with the WTA prototype. The hot pixels locations and highest temperature for the 5 volunteers remained stable at $36.9^{\circ}C$.

Table 4.1 - 4.5 depict the measured temperature (\bar{T}_{tm}) of the volunteers' TMs by using the Braun ThermoScan 5 infrared ear thermometer, with reference to the highest TM temperature (\hat{T}_{tm}) calculated from WTA in Figure 4.21(a) - 4.25(a) and in Figure 4.21(b) - 4.25(b). The ThermoScan 5 measured an average TM temperature range of $36.7^{\circ}C$ to $37^{\circ}C$ during the first half (4 hours) of the measurements that were conducted without the effects of head cooling. During the second half (last 4 hours) of the measurements with head cooling, ThermoScan 5 measured an average TM temperature range of $36.5^{\circ}C$ to $36.7^{\circ}C$. The measured temperatures data during head cooling were noticeable to be lower than the temperature data without head cooling. When compared to the TM

temperature measured by the ThermoScan 5 with the highest TM temperature obtained from the WTA, the temperature reading from the ThermoScan 5 showed some level of fluctuations, whereas the highest temperature obtained from the WTA remained stable at 36.9°C throughout, with the hot pixel locations shifted between pixel location 34, 37 and 38. The feasibility study showed the feasibility of continuous CBT monitoring via the TM. The thermal images in Figure 4.21(a) - 4.25(a) and in Figure 4.21(b) - 4.25(b) depict the highest temperature hotspot on the TM can be easily determined from a WTA. A properly positioned clinical ear speculum ensures adequate view of the TM, resulted in proper measurement of the highest temperature on the TM surface.



(a) Without head cooling

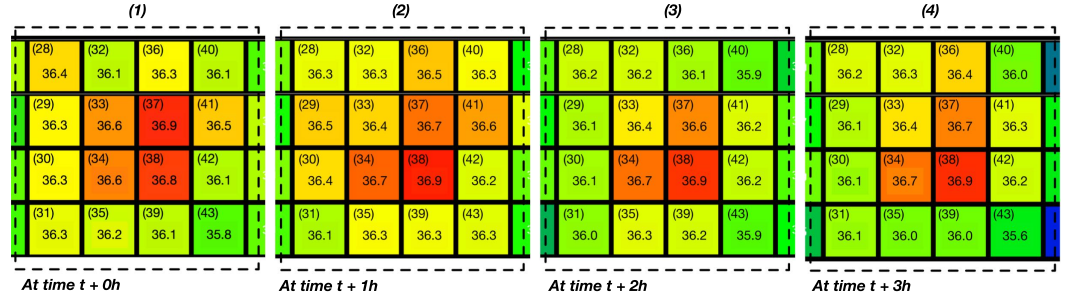


(b) With head cooling

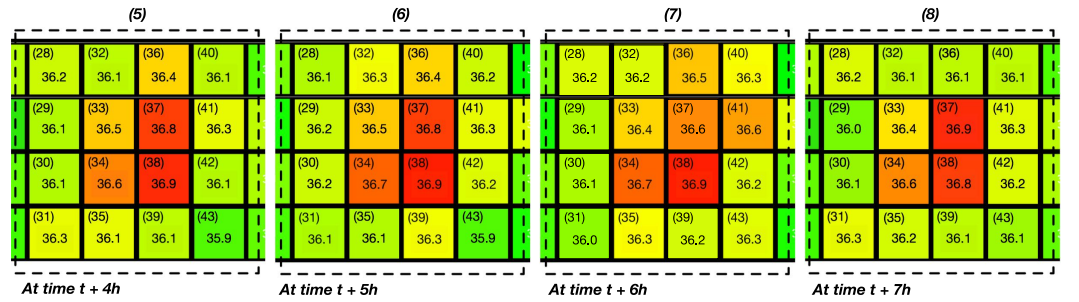
Figure 4.21: View of 8 TM thermal images from a speculum attached to an ear, each image was recorded at 1h interval for Volunteer 1: (a) without head cooling, (b) with head cooling.

Table 4.1: Volunteer 1 - TM temperature measured from WTA and Braun ThermoScan 5

Time	WTA		ThermoScan 5
	Hot Pixel Location	\hat{T}_{tm}	\bar{T}_{tm}
<i>Without Head Cooling</i>		(°C)	(°C)
$t + 0h$	37	36.9	36.7
$t + 1h$	37	36.9	37.0
$t + 2h$	37	36.9	36.9
$t + 3h$	37	36.9	36.8
<i>With Head Cooling</i>			
$t + 4h$	37	36.9	36.6
$t + 5h$	37	36.9	36.6
$t + 6h$	37	36.9	36.5
$t + 7h$	37	36.9	36.7



(a) Without head cooling

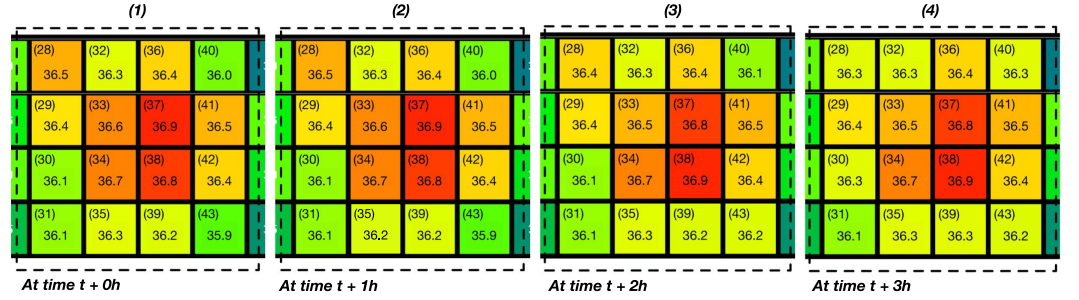


(b) With head cooling

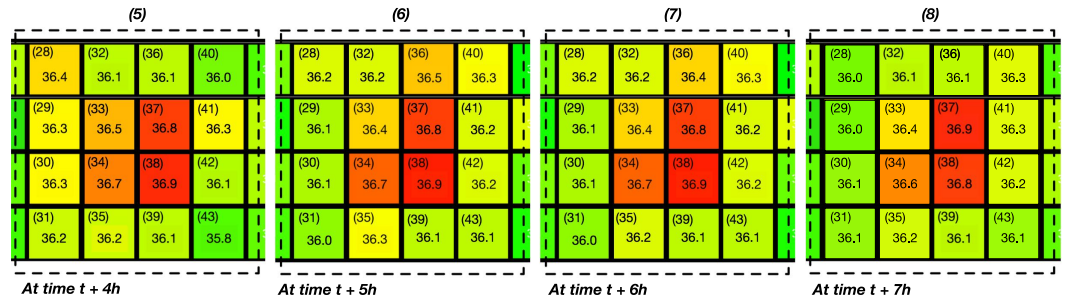
Figure 4.22: View of 8 TM thermal images from a speculum attached to an ear, each image was recorded at 1h interval for Volunteer 2: (a) without head cooling), (b) with head cooling.

Table 4.2: Volunteer 2 - TM temperature measured from WTA and Braun ThermoScan 5

Time	WTA		ThermoScan 5
	Hot Pixel Location	\hat{T}_{tm}	\bar{T}_{tm}
<i>Without Head Cooling</i>		($^{\circ}C$)	($^{\circ}C$)
$t + 0h$	37	36.9	36.9
$t + 1h$	38	36.9	36.8
$t + 2h$	38	36.9	37.0
$t + 3h$	38	36.9	36.9
<i>With Head Cooling</i>			
$t + 4h$	38	36.9	36.7
$t + 5h$	38	36.9	36.5
$t + 6h$	38	36.9	36.6
$t + 7h$	37	36.9	36.6



(a) Without head cooling

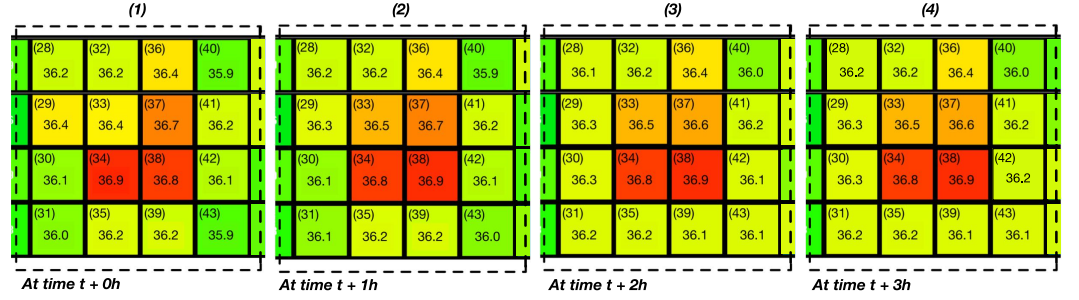


(b) With head cooling

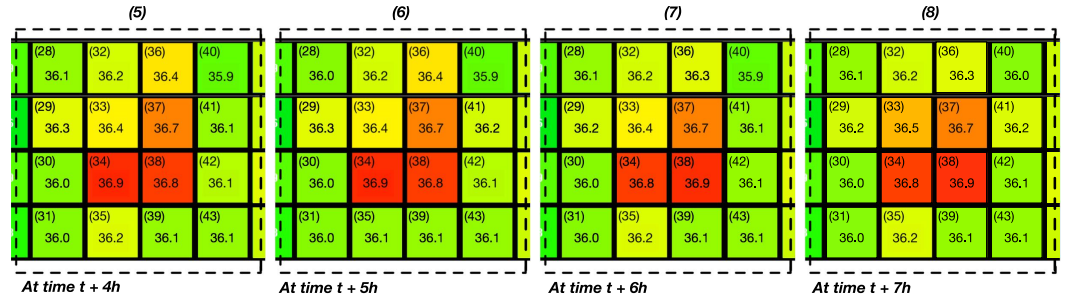
Figure 4.23: View of 8 TM thermal images from a speculum attached to an ear, each image was recorded at 1h interval for Volunteer 3: (a) without head cooling), (b) with head cooling.

Table 4.3: Volunteer 3 - TM temperature measured from WTA and Braun ThermoScan 5

Time	WTA		ThermoScan 5
	Hot Pixel Location	\hat{T}_{tm}	\bar{T}_{tm}
<i>Without Head Cooling</i>		($^{\circ}C$)	($^{\circ}C$)
$t + 0h$	37	36.9	36.7
$t + 1h$	37	36.9	36.8
$t + 2h$	38	36.9	36.8
$t + 3h$	38	36.9	37.0
<i>With Head Cooling</i>			
$t + 4h$	38	36.9	36.7
$t + 5h$	38	36.9	36.6
$t + 6h$	38	36.9	36.6
$t + 7h$	37	36.9	36.5



(a) Without head cooling

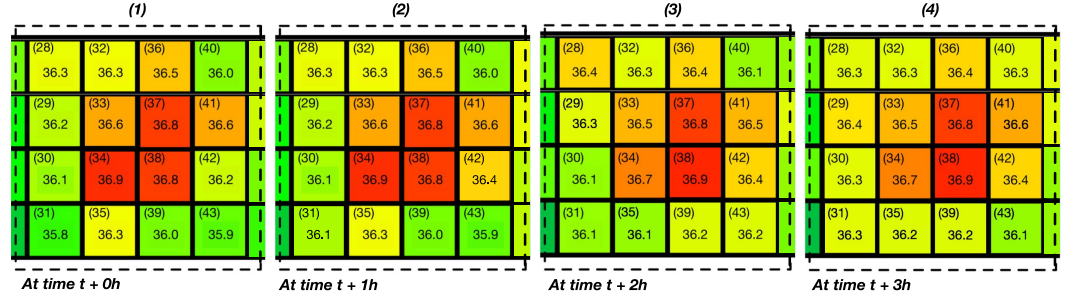


(b) With head cooling

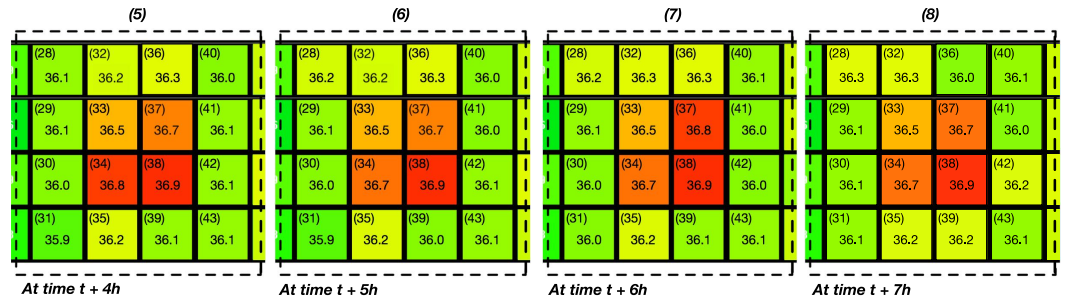
Figure 4.24: View of 8 TM thermal images from a speculum attached to an ear, each image was recorded at 1h interval for Volunteer 4: (a) without head cooling), (b) with head cooling.

Table 4.4: Volunteer 4 - TM temperature measured from WTA and Braun ThermoScan 5

Time	WTA		ThermoScan 5
	Hot Pixel Location	\hat{T}_{tm}	\bar{T}_{tm}
<i>Without Head Cooling</i>		($^{\circ}C$)	($^{\circ}C$)
$t + 0h$	34	36.9	36.9
$t + 1h$	38	36.9	36.7
$t + 2h$	38	36.9	36.8
$t + 3h$	38	36.9	36.8
<i>With Head Cooling</i>			
$t + 4h$	34	36.9	36.6
$t + 5h$	34	36.9	36.6
$t + 6h$	38	36.9	36.5
$t + 7h$	38	36.9	36.7



(a) Without head cooling



(b) With head cooling

Figure 4.25: View of 8 TM thermal images from a speculum attached to an ear, each image was recorded at 1h interval for Volunteer 5: (a) without head cooling, (b) with head cooling.

Table 4.5: Volunteer 5 - TM temperature measured from WTA and Braun ThermoScan 5

Time	WTA		ThermoScan 5
	Hot Pixel Location	\hat{T}_{tm}	\bar{T}_{tm}
<i>Without Head Cooling</i>		($^{\circ}C$)	($^{\circ}C$)
$t + 0h$	34	36.9	36.8
$t + 1h$	34	36.9	36.8
$t + 2h$	38	36.9	37.0
$t + 3h$	38	36.9	36.8
<i>With Head Cooling</i>			
$t + 4h$	38	36.9	36.7
$t + 5h$	38	36.9	36.7
$t + 6h$	38	36.9	36.7
$t + 7h$	38	36.9	36.6

4.6 User Data Privacy and Security Considerations

VitalMON uses BLE, ZIGBEE PAN and GSM mobile communication networks for data transfer operations. Each VitalMON user is required to wear the WTA and carry a PDL/TM. Each WTA has a Media Access Control (MAC) address used as a unique identifier (ID) and is wirelessly paired to a designated PDL/TM via BLE. The WTA data transfer to its paired PDL/TM is encrypted [153–155] to prevent any form of passive and active man-in-the-middle (MITM) eavesdropping attacks [155–157]. Encryption makes the data unintelligible to all but the successfully paired BLE devices forming a communication link.

At the PDL/TM, a User Data Packet (UDP) is assembled comprising of TM Temperature data from the WTA, and motion and geographical location (GPS) data from the PDL/TM. The UDP is uniquely tagged with WTA MAC ID as a form of user identity. The fully assembled UDP is transmitted via a ZIGBEE

PAN to the designated GC. The PAN is encrypted [154] [155] to prevent any unauthorized network access, and has to be established prior to any successful data transfer by the PDL/TM.

The GC contains the information of each registered user name together with the assigned WTA MAC ID in its local database. The GC uses the WTA MAC ID from the UDP it received and check against its local database in-order to display user name, CBT, motion and geographical location information on the graphical user interface screen. The remote BMDS received UDPs from PDL/TMs via the GSM mobile communication network.

VitalMON users are informed of the documented methods VitalMON handle their personalized UDPs and the underlying data encryptions efforts to ensure their personalized data remain safe, private and secured. User are also informed that the VitalMON does not collect or store any other form of user information data.

4.7 Ethical Issue

The ethical issue of using VitalMON system is with regards to the motion and geographical location tracking functions that may result in an invasion of privacy issue. VitalMON implements a strict data collection guideline discussed earlier, and the guideline prevents this issue from occurring. VitalMON users are made aware of the data collection method and signed consents must be provided by the users in-order to allow VitalMON deployments.

Motion and geographical position tracking functions are possible due to the availability of motion and geographical location information from the UDP. Vi-

talMON users are informed that apart from CBT monitoring, they are also being monitored for motion and geographical location information. Each user has full control over the decision to disable the motion and position tracking functions if the user is uncomfortable of being monitored.

4.8 Summary

The prototype hardware design and related algorithm developments for VitalMON has been successfully developed and completed and its performance rigorously calibrated. VitalMON has been trialed on 5 volunteers, and the results have indicated that VitalMON is accurate in indicating CBT from the TM. VitalMON is a scalable and robust architecture for implementation of continuous real-time CBT monitoring based on the surface temperature of the TM of sports and military personnel, and other user groups. The primary purpose of VitalMON is to reduce heat related injuries during strenuous physical activities, when compared to the expensive and non-reusable temperature pills, VitalMON is cost effective as it employed commercial off-the-shelves electronics components and is fully reusable.

Chapter 5

e-Care: A Non-Intrusive Activity Monitoring for the Elderly

5.1 Introduction

Elderly people living alone is prone to accidental falls. In many instance, a simple fall can turn life threatening if help does not arrive in-time. The incidence of age induced chronic illnesses is also on the rise among this vulnerable segment of the society. Disease such as stroke affects the mortality rate of the elderly people living alone. With the onset of a stroke, and without any caregiver in vicinity, chances of survival are low. Between 2007 and 2011, in Singapore, at least 50 elderly people have been found dead in their own homes from causes related falls and illnesses [7] [8].

With the rapid technological advancements, various small and non-intrusive

remote monitoring solutions have been proposed and developed with the objectives to solve or mitigate problems encountered by elderly people living alone, and ultimately to save lives by providing them timely assistance. In Singapore, the government takes initiative in making elderly friendly public housing for the elderly people so as to facilitate in place [158]. In 2013, a pilot project called Elderly Monitoring System (EMS) was deployed to 500 public housing flats occupied by lone elderly residents. These in-home monitoring and alert system monitors round the clock activity levels of each resident in a non-intrusive way, and triggers an alert to a designated caregiver in the event of anomalies [158]. With the initial success of the pilot runs, several similar systems [159] [160] were also proposed and underwent trials by different competing solutions providers aimed to solve or mitigate the same set of problems defined earlier.

5.2 Problem Formulation and Proposed Solution

The solutions proposed and demonstrated by [158–160] capitalized on detecting and analyzing motion activity patterns of elderly people living alone. Motion activity detection is one of the commonly use methods to ascertain the well-being of the lone elderly people [161]. Motion activity data from the sensor is collected and processed either locally or remotely. The data is processed and subject to analysis to detect changes in daily activity of the elderly people. As a result, it is possible to recognize patterns in daily motion activity and to generate alerts if deviations occur [162].

Peetoom *et al* [56] conducted a systematic and detailed investigation on currently available literatures on monitoring technologies to detect activities of daily

life or significant events for elderly people. Their research highlighted the monitoring technology using passive infrared (PIR) motion sensors being the most favorable with total of 61 known research articles to date. In all the articles, various hardware implementations and algorithms aimed at improving PIR motion sensing accuracy and efficiency were presented, and none of them ever achieve 100% accuracy in motion activity detection of an elderly person, with error in detection ranging from 1.1% to 25%.

PIR motion sensor has the advantage of being non-intrusive, and invasion of privacy is not an issue as it is not a video image sensor. In most setups, sensors are placed on walls or ceilings in the home of an elderly people and they detect the presence of an elderly people entering or moving in a room through changes in the surrounding ambient temperature. The idea and method of using the sensor is not new, Celler *et al* [57] in 1995 used PIR motion sensors and demonstrated a home monitoring sensor and communication technology for the elderly people.

PIR motion sensor is sensitive to temperature and has a defined effective target detection range. [163] [164]. A subject that moves into the sensor's field of view (FOV) within its detection range causes a sudden change in the ambient temperature surrounding the subject and the temperature difference is detected by the sensor. If the subject stays stationary within the FOV for a long period of time, the ambient temperature reaches an equilibrium, and with no temperature change, no motion activity. This method of detection is simple and elegant, but has drawbacks. The most prominent drawback will be the un-intended change or sudden change in the ambient temperature with the sensor's FOV.

This phenomenon is common if the sensor's FOV is directed near to a glass window where sunlight shines through. The heat from the infrared radiation causes the ambient temperature to change, and results in being detected as a valid motion activity. Thus, a PIR motion sensor works well if it is installed away from the sunlight, especially during the night time. This is also the primary reason a PIR motion detector is usually activated during night time or deployed within an enclosed room or hallway with no sunlight [165] [166].

A typical PIR motion sensor is unable detect a stationary or extremely slow moving body. It is possible to increase the sensitivity of the sensor to detect extremely slow moving body, but at the expense of frequent false detections as any small changes in ambient temperature will be registered as a valid motion (e.g., Sudden change in amount of sunlight in the room, or cooling of nearby walls in the evening) [165] [167]. Research are still actively ongoing in various attempts to improve the detection accuracy of a PIR motion sensor, and complex algorithms have been proposed and introduced, resulting in the adoption of higher throughput processing elements (faster MCU) and complex electronics, hence increasing the overall costs. This cycle will continue to the point where the detection system is no longer cost effective in production and in deployment.

This chapter is set to refine the human motion activity detection in a non-intrusive way. By using a PIR motion sensor to detect general (or course) motion activity of an elderly people, together with a 16×4 infrared thermopile sensors array (TSA) [67] [68] [71] [151] [152] (introduced in Chapter 4) for confirming the presence of the elderly people via human body thermal signature detection, motion activity with confirmed human presence is possible, resulting in a highly

accurate activity detection of an elderly people with minimal false alarms. This chapter presents e-Care motion activity monitoring and alert notification for elderly people living with improved motion activity detection.

5.3 e-Care Operating Concept

e-Care is an innovative, low cost and scalable home/community-based round the clock motion activity monitoring and alert system for the vulnerable elderly people living alone. It aims to transform eldercare into a collaborative effort mainly involving people who know and care about them. e-Care can be used to request for help in the event of an emergency and monitors simple activities such as walking and casual movements. This system is simple and low cost, yet still capable of alerting caregivers at life-critical moments. e-Care's modular and scalable architecture allows various customization in accordance to the various needs of the elderly people. It is designed to be cost effective by utilizing commonly available off-the-shelves components, commercially available ZIGBEE personal area network (PAN), and existing mobile network or broadband internet infrastructures.

e-Care monitoring hardware consists of a Base Station and the following wireless peripheral modules: (a) Thermal-Motion (TMotion) sensor module, (b) PIR Door (PIRD) sensor module (c) Wireless alert switch (AlertSW) module, and (d) Wireless alert cancel switch (AlertCL) module. Refer to Appendix C for the details on the e-Care hardware and firmware developments.

5.3.1 e-Care Base Station

e-Care Base Station is the main communication and processing endpoint that must be included in each home fitted with e-Care monitoring system. The Base Station contains processing element that is of high reliability performing main processing logic and algorithm to carry out motion activity monitoring and alerting operations. It setups and maintains a ZIGBEE PAN within the house, and communicates with all the modules that constituted e-Care system. It receives: (a) motion and thermal information from TMotion sensor modules, (b) deactivation of monitoring command from PIRD module, (c) alert request from AlertSW modules, and (d) alert cancel request from AlertCL module. The Base Station processes all the received information based on its onboard pre-programmed algorithm, and if required, it will communicate with caregivers or with a remote server.

The Base Station can operate in Simple or Infrastructure mode. Simple mode requires the Base Station to communicate directly to the designated caregivers via Short Messaging Services (SMS) using the GSM mobile network. This is the simplest method of deploying e-Care system, and is targeted at small community where the number of elderly people staying alone is small. Infrastructure mode requires the Base Station to communicate via the Internet with a remote e-Care application server. The server hosts a custom application program that processes all the communications from Base Stations from lone elderly people homes, and alerts the designated caregivers registered with the server, either via Internet messaging applications (e.g., WhatsApps) or via SMS. Infrastructure mode targets at organizations managing welfares of large group of elderly people

staying alone.

The Base Station monitors motion activity of an elderly person, it detects motion activity and target temperature by receiving information from a TMotion sensor module when its PIR sensor detects motion activity and the TSA measures target human body temperature and simple body posture via thermal mapping. The temperature information is used to track the known location of the elderly person within the house or apartment. When only motion activity is detected and temperature readout is absent, it is likely that the elderly person has not moved into the FOV of the TSA on the TMotion sensor, thus the detection is purely motion based. In this scenario, the Base Station only monitors motion activity and it can only guess the last known location of the elderly person within the house. If there is no new motion information update from the last known location, and no update from other locations, the Base Station motion inactivity timer will timeout and alerts will be sent to caregivers. A default inactivity timeout duration (customized according to the average elderly person's movement behavior and may not be accurate) is required in this scenario, and the elderly person's lack of detected motion can be interpreted as an emergency, as it is not common for an elderly person to stay stationary until timeout occurs. Any new motion detection will reset the inactivity timer so as to prevent a timeout.

When the TSA detects a valid human temperature, this means that the elderly person has moved into the FOV of the TSA. In this scenario, the location of the elderly person within the house is known from the temperature information, together with the simple posture of the elderly person (i.e., sitting/standing up or lying down). Knowing the posture helps in setting of the inactivity timeout

duration, a sitting/standing up posture uses the default inactivity timeout duration, while a lying down posture warrants a longer inactivity timeout duration. This longer inactivity timeout covers the assumption that the elderly person is lying down taking a nap, and the longer timeout value is again estimated from the daily activity of the elderly person and may takes several iterations before an accurate value is determined. This simple posture detection is done by analyzing temperature measurements from the TSA and complements the PIR sensor, where motion activity detection is now smarter with elderly person location and posture known to the Base Station and inactivity timeout value can be adjusted automatically. The PIR sensor still detects motion and any new motion detection will still reset the inactivity timer so as to prevent a timeout.

5.3.2 Thermal-Motion Sensor Module

TMotion sensor modules for motion activity monitoring are installed at strategic places within an elderly person's house or apartment such as in the living room, bedroom, kitchen and toilet. TMotion modules contains a PIR motion sensor for motion detection and a TSA for human thermal signature detection. The PIR sensor has a FOV of 90° , while the TSA has a narrower FOV of $60^\circ \times 10^\circ$. Both sensors have calibrated sensing distance of 2m - 2.5m radius. The PIR motion sensor continuously scans for motion activity. Once a motion activity is detected (when an elderly person moves into the FOV), the TSA checks within own its FOV if the target is indeed a valid human by detecting and analyzing the registered thermal signature. If an elderly person (valid human) is detected, the TMotion module notifies the Base Station via the established wireless ZIGBEE PAN, and updates the Base Station with motion

activity data and the highest temperature readout of the elderly person. TMotion module analyze the 16×4 pixels temperature layout of the elderly person in-order detect the posture type and notifies the Base Station. At present, TMotion module is able to accurately detect lying down posture and differentiate it from other postures (i.e., sitting/standing). In the event the elderly person leaves the monitored area, TMotion updates the Base Station that the area is vacant.

5.3.3 PIR Door (PIRD) Sensor Module

PIRD sensor module is installed near the main door so as to deactivate activity monitoring when the elderly person leaves the house. PIRD is activated when an elderly person move into the FOV of sensor and signals the Base Station to stop activity monitoring for a defined short period of time. Activity monitoring will re-start when any of the TMotion sensor module is activated when the elderly person returns. This module is important as it disables the motion activity monitoring system when monitoring is not needed, and eliminates unwanted false inactivity alert.

5.3.4 Wireless Alert Switch and Wireless Alert Cancel Switch Modules

AlertSW modules for requesting help in the event of an emergency are also installed at the same places as the TMotion Sensors modules. AlertSW consumes no current when not activated, and it is designed to be powered by an off-the-shelf CR123A 3V Lithium battery that theoretically will last according to the battery shelf life (3 years). When AlertSW is activated by pressing the RED push-button, it notifies the Base Station to broadcast an alert message requesting for help to

the designated caregivers via the GSM mobile network or via the internet.

AlertCL module is used to cancel the Base Station's request for help in the event any of the AlertSW is accidentally activated. The module is installed at a convenient and easy to reach location within the house. Similar to the AlertSW module, AlertCL consumes no current when not activated, and it is designed to be powered by the same CR123A 3V Lithium battery. When AlertCL is activated by pressing the GREEN push-button, it notifies the Base Station to broadcast an alert cancel message notifying the designated caregivers via the GSM mobile network or via the Internet.

5.3.5 Deployment Modes

Figure 5.1 depicts an example of e-Care system in Simple Mode deploys in a lone elderly person's studio apartment. Figure 5.2 depicts a floorplan on how e-Care is deployed in the apartment. There are total of 1 Base Station (#B01), 11 TMotion sensor modules (#T01 - #T11), 4 AlertSW modules(#R01 - #R04), 1 PIRD Sensor module (#D01) and 1 AlertCL module (#G01) deployed. Since the elderly person will spend most time at the living/sleep area, a total of 7 TMotion sensor modules are installed in this area in-order to ensure maximum coverage. The system is programmed to alert two designated caregivers via SMS. Caregivers information is programmed into the Base Station, and it's the Base Station duty to communicate with the caregivers in the event of an emergency.

Figure 5.3 depicts an example multiple e-Care systems in Infrastructure Mode deployed in the studio apartments of the lone elderly people. The systems ride on the available home broadband Internet connection of the apartments or mobile broadband internet (when home Internet is not available), and communicate with

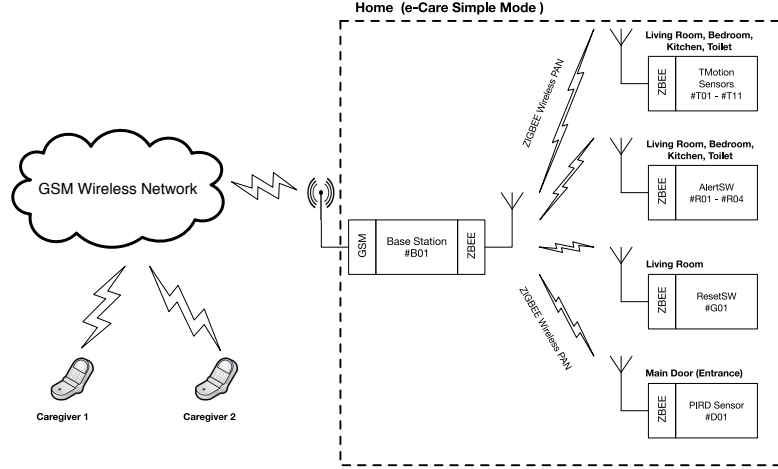


Figure 5.1: e-Care system in Simple Mode for a lone elderly person with 2 caregivers.

a remote application and database server. Caregivers information are maintained by the remote server. In the event of an emergency, the affected Base Station communicates with the remote server, and the remote server notifies designated caregivers registered in the database, either via Internet messaging or via SMS.

Figure 5.2 and 5.3 depict the highly scalable design of e-Care system. The system can be adapted to a small community with a small groups of lone elderly people living alone, or used by an organization that manage the wellbeing of the large numbers of lone elderly people living alone in a large community.

5.4 Feasibility Study on Posture Detection and Fore-head Surface Temperature Measurement with TSA

5.4.1 Study Procedure and Setup

The TSA contains 16×4 pixels arranged in a rectangle format, with a FOV of $60^\circ \times 10^\circ$. An experiment was conducted to verify the idea of using a TSA to detect simple human postures by calculating the number of pixels with high

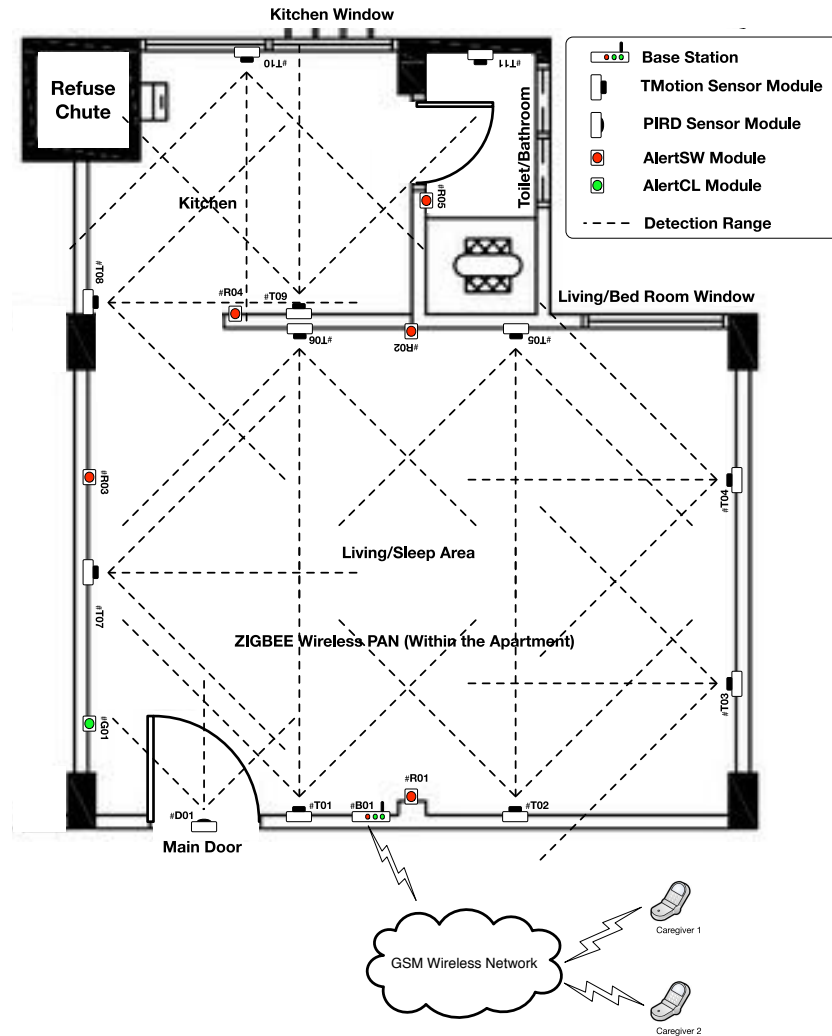


Figure 5.2: e-Care system (Simple Mode) deployed in a studio apartment.

temperature. Figure 5.4 depicts the experiment set up. The experiment is set up using a TSA mounted on top of a pole angled at 45° facing downwards. The length of the pole is 2.5m. The TSA is facing a wooden platform at 2.5m away with a dimension of (W x H x L) $0.83m \times 0.46m \times 1.8m$. Volunteers are asked to sit and lie down on top of the wooden platform, and to stand in front of the platform. The experiment was conducted in a room with ambient temperature fixed at 23°C .

Five volunteers were engaged to demonstrate standing, sitting, and lying

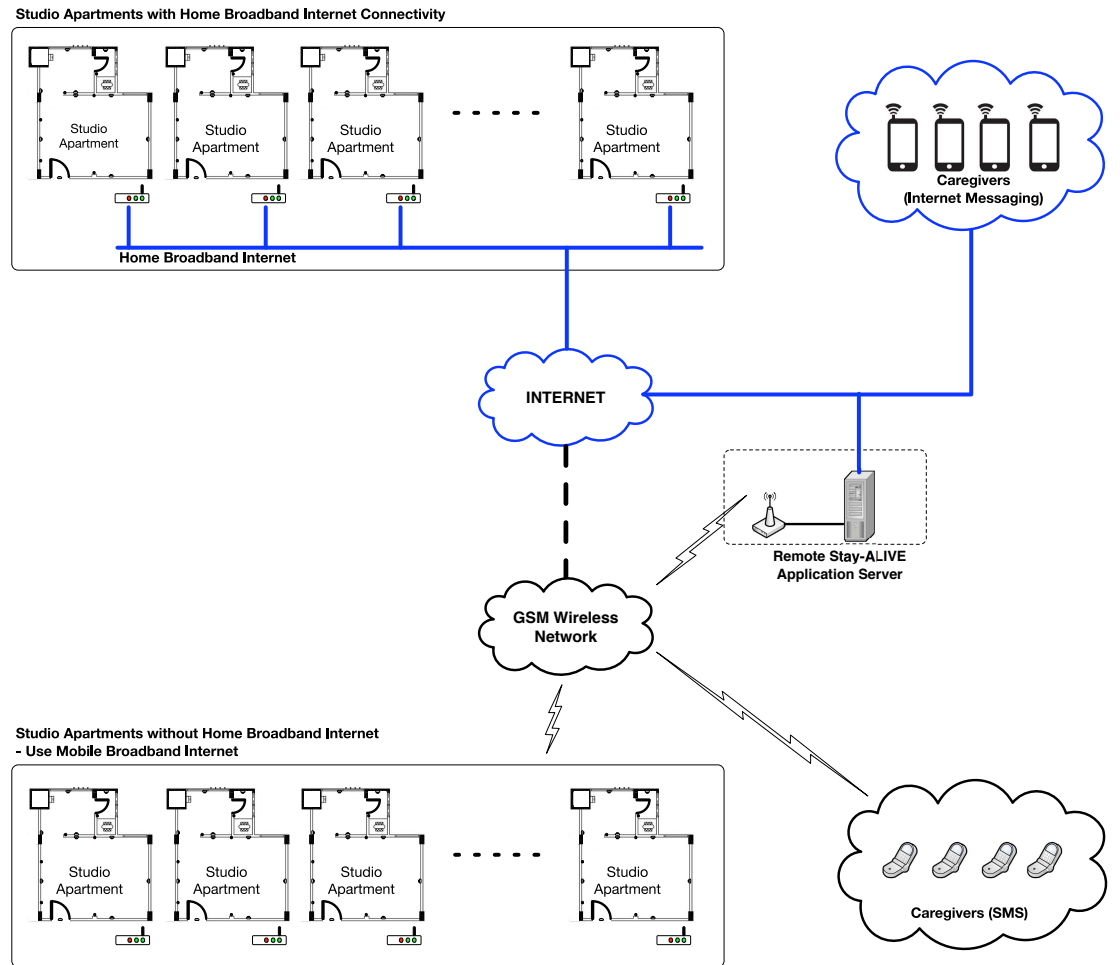


Figure 5.3: e-Care systems (Infrastructure Mode) deployed in multiple studio apartments and central managed by an organization.

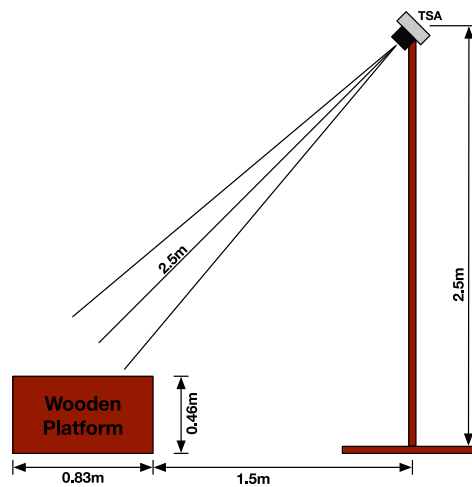


Figure 5.4: Experiment Setup - Simple Human Posture Detection with TSA

down postures in front of the TSA. The 16×4 low resolution raw thermal images were captured and processed. Each raw image subtracts away a background image of the experiment area. After subtraction, the new images only contain pixel information featuring the volunteers. Further processing was done by applying a fixed thresholding function on the new images, where temperature of each pixel within each image was compared against a defined temperature threshold. For each pixel where its temperature was smaller than the threshold, is assigned with a new low (fixed) temperature value. Thus, any unwanted noise within the new thermal images were effectively masked or attenuated. The processed new images contain only the effective temperature difference showing the effective area occupied by the volunteers posed in various postures.

Forehead skin surface temperature were measured from the volunteers when they were required to lie down on the wooden platform. The measurements were performed by using a contact thermometer and by using the same mounted TSA.

5.4.2 Results and Discussion

5.4.2.1 Posture Detection

Figure 5.5 to 5.9 depict the processed thermal images of the volunteers (a) standing in front of, and (b) sitting on the wooden platform. Figure 5.10 to 5.14 depict the thermal images of the volunteers lying down on the wooden platform. For each thermal image in Figure 5.5 to 5.9, the pixels indicating higher temperature values are grouped together in a small area within the thermal image consistently indicating a heat generating body of the volunteer in standing or sitting position. The total number effective pixels required to represent a person

standing up is in the range of 6 to 12 and sitting down is in the range of 6 to 10.

For each of the thermal image in Figure 5.10 to 5.14, the pixels with higher temperature values represent the volunteer lying down. The total number effective pixels required to represent a volunteer lying down is in the range of 21 to 29, more than double the requirement for sitting down and standing up.

This simple experiment shows that the TSA is poor to distinguish the standing and sitting postures as the total number of pixels required to represent each posture are almost equivalent. The TSA is able to detect lying down posture from standing and sitting posture due to more than double the amount of pixels are required to represent a lying down posture of an elderly person. Thus, this experiment confirms that the TSA is good at detecting an elderly person lying down or sitting/standing just by calculating the number of pixels with higher temperature values.

5.4.2.2 Forehead Surface Temperature Measurement

Human skin surface temperature is different from core body temperature (CBT). The CBT remains fixed to a constant value, while the skin surface temperature differs. Temperature measurements experiment at various parts of the human body has been conducted by Regan *et al* [168] and again by Huizenga *et al* [169]. Both shared the same conclusion that skin surface temperature differs according to the area of the body, and the human forehead surface has the highest temperature due to the proximity of the temporal artery. When a human enters the TSA FOV, the highest surface temperature measured by the TSA is from the forehead area that is always exposed. The rest of the body parts exhibit lower surface temperatures and portions covered with fabric exhibit

much lower and inconsistent surface temperatures. In this situation, it is safe to assume that the highest temperature (within the valid human skin surface temperature range) obtained from the TSA is from the forehead. Observations are made from a series of thermal images from Figure 5.10 to 5.14 depicting volunteers lying down within the FOV of a TSA. Each figure depicts highest temperature spot represented by darker pixel colors which coincides with each volunteer head (forehead). Thus, a TSA can be used to check for a valid human present by measuring the highest temperature of the subject (forehead surface temperature) and compares against a known sets of temperature thresholds.

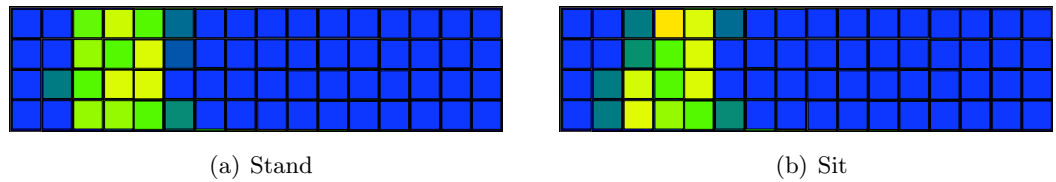


Figure 5.5: Thermal image of Volunteer 1

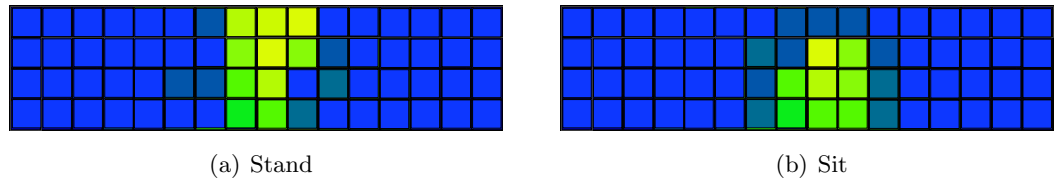


Figure 5.6: Thermal image of Volunteer 2

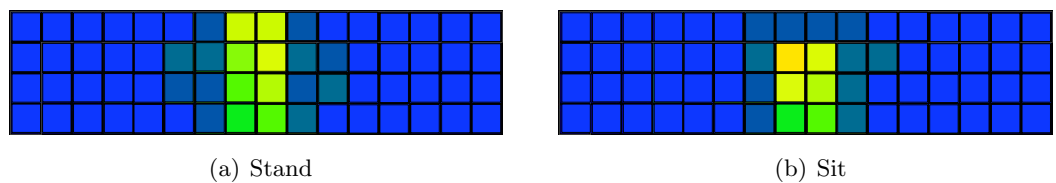


Figure 5.7: Thermal image of Volunteer 3

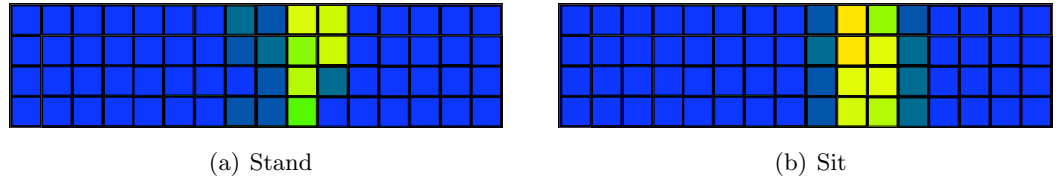


Figure 5.8: Thermal image of Volunteer 4

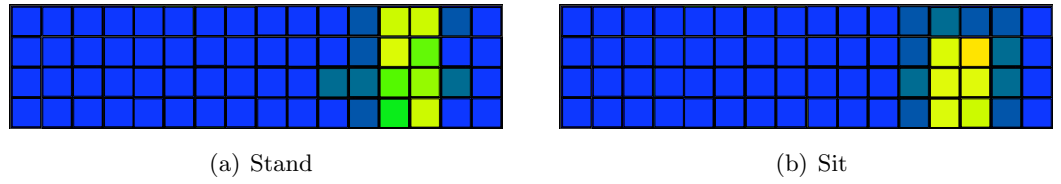


Figure 5.9: Thermal image of Volunteer 5

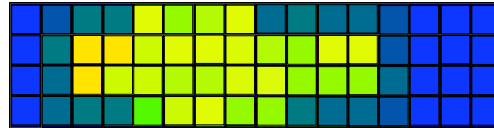


Figure 5.10: Thermal image of Volunteer 1 lying down



Figure 5.11: Thermal image of Volunteer 2 lying down

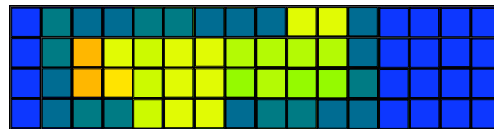


Figure 5.12: Thermal image of Volunteer 3 lying down



Figure 5.13: Thermal image of Volunteer 4 lying down

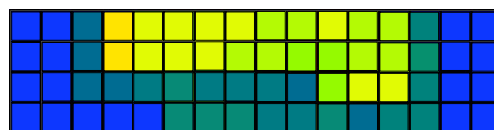


Figure 5.14: Thermal image of Volunteer 5 lying down

5.5 e-Care Trial, Result and Discussion

e-Care systems have been tested in selected homes of lone elderly people. Several conditions must be met before an elderly person is selected for the trial:

- ≥ 65 years of age and lives alone in a studio apartment.
- Must sleep at own apartment for the period of the trial.
- Have access to caregivers who are family members or friends.
- Able body, healthy and without any known chronic and mental illness.
- Allows motion activity data to be collected during the trial period.

5.5.1 Parameter Setup for Base Station

The trial was conducted on 4 lone elderly people households (E1 - E4) meeting the requirements, located in various parts of Singapore, for a period of 30 days. Two caregivers were assigned to each household. During the first 10 days, motion inactivities and temperature measurements data were collected with inactivity and alert monitoring feature disabled. The data was analyzed to determine the custom motion inactivity and valid forehead skin temperature thresholds for each elderly person. The daily wake up and sleep time (24 hours HHMM format), and measured forehead skin temperature ($^{\circ}C$) were also manually recorded by each elderly person in a separate worksheet provided. Each elderly person was provided with a digital forehead thermometer in order to assist them in daily forehead temperature measurement. Table 5.1 and 5.2 depict the summary of the motion activity and temperature data of the lone elderly people. Each table records wake up time (WT), sleep time (ST), daily maximum inactivity duration (IT), daily maximum lying down duration (LT), TSA measured daily

maximum forehead temperature (TS), and daily measured forehead skin surface temperature (MT). The measurement units are in minute and $^{\circ}C$ respectively.

The IT and LT were measured everyday from the wake time (WT) until sleep time (ST). It was noted that the 4 elderly persons did not take naps everyday (observed as 0 in the LT columns of the tables). Another observation was, the IT values for each elderly person can transit from small values to a comparatively large values. The comparatively large values were double checked with the respective elderly persons, and were attributed by the elderly persons dozing off while in sitting positions. Comparisons were made between TS and MT values of the four elderly persons. The TS values did not reflect the actual forehead skin temperature (MT) due to the TSA being positioned a distance away from each elderly person, and the exact distance values are not known. It is well-known that distance between the TSA and the object affects the temperature measurement accuracy [71] [151]. It was observed that each elderly person has a certain forehead temperature threshold that can be used for a simple valid human present detection by comparing a TSA measured temperature against the threshold.

The e-Care Base Stations were programmed with custom timing and forehead surface temperature thresholds depicted in Table 5.3 after completed 10 days of data collection and analysis. The individual sleep time threshold (ST_{th}) and wake up time threshold (WT_{th}) were programmed based on individual elderly person's input.

The individual inactivity duration threshold (IT_{th}) and lying down duration threshold (LT_{th}) were calculated from each elderly person's maximum IT and

Table 5.1: Elderly person E1 - E2 Wakeup (WT), Sleep (ST), Inactivity (IT), Lying Position (LT) durations, TSA Temperature (TS) and Measured Temperature (MT).

Day	E1						E2					
	WT	ST	IT	LT	TS	MT	WT	ST	IT	LT	TS	MT
1	0700	2300	7	61	28.6	35.7	0630	2200	16	0	30.1	36.0
2	0700	2300	22	55	27.5	35.7	0630	2200	8	63	29.1	35.5
3	0700	2300	18	62	28.1	35.4	0630	2200	4	57	29.6	35.5
4	0700	2300	8	59	29.2	35.6	0630	2200	15	0	28.9	35.7
5	0700	2300	7	64	27.6	35.7	0630	2200	18	60	28.3	35.5
6	0700	2300	9	0	29.4	35.5	0630	2200	6	62	29.7	36.0
7	0700	2300	16	0	28.8	35.7	0630	2200	8	53	28.8	36.1
8	0700	2300	20	60	28.7	35.7	0630	2200	17	0	28.6	36.0
9	0700	2300	19	61	28.1	35.5	0630	2200	9	62	29.5	35.8
10	0700	2300	7	50	27.8	35.7	0630	2200	17	53	30.0	35.8

Table 5.2: Elderly person E3 - E4 Wakeup (WT), Sleep (ST), Inactivity (IT), Lying Position (LT) durations, TSA Temperature (TS) and Measured Temperature (MT).

Day	E3						E4					
	WT	ST	IT	LT	TS	MT	WT	ST	IT	LT	TS	MT
1	0730	2200	18	0	27.5	35.8	0700	2200	6	61	27.9	35.7
2	0730	2200	8	0	30.1	36.1	0700	2200	9	0	28.2	35.7
3	0730	2200	6	49	29.6	35.7	0700	2200	8	0	28.8	35.9
4	0730	2200	7	52	29.0	35.9	0700	2200	15	0	29.3	36.0
5	0730	2200	18	0	28.7	35.8	0700	2200	17	62	29.7	35.8
6	0730	2200	8	0	28.4	35.9	0700	2200	8	0	28.7	35.7
7	0730	2200	16	0	29.1	35.7	0700	2200	15	0	29.1	35.7
8	0730	2200	7	52	28.3	35.8	0700	2200	9	57	29.8	36.0
9	0730	2200	8	50	28.2	36.0	0700	2200	19	64	28.2	36.1
10	0730	2200	17	55	29.0	35.6	0700	2200	17	0	27.9	35.8

LT duration values (IT_{max} and LT_{max}) in their respective data columns in Table

5.1 and 5.2 with extra inactivity tolerances (Δ_{IT} and Δ_{LT}) respectively included.

The Δ_{IT} and Δ_{LT} values for each elderly person were calculated by finding the standard deviations of the non-zero IT and LT values in Table 5.1 and 5.2. The

IT_{th} and LT_{th} were calculates as: $IT_{th} = IT_{max} + \Delta_{IT}$ and $LT_{th} = LT_{max} + \Delta_{LT}$,

resulting in $IT_{th} > IT_{max}$ and $LT_{th} > LT_{max}$. These measures were added to

eliminate unwanted IT and LT in activities alerts triggering when the detected inactivities were equal to the maximum durations values recorded.

In order to confirm the presence of the elderly persons within their apartments, their forehead surface temperature were measured by the TSA and compared against temperature thresholds. The human forehead surface temperature threshold TS_{th} for each elderly person was calculated from the minimum TS value (TS_{min}) in their respective data column in Table 5.1 and 5.2 with extra temperature tolerance (Δ_{TS}) included. The Δ_{TS} for each elderly person was calculated by finding the standard deviation of the non-zero TS values in Table 5.1 and 5.2. The TS_{th} was calculates as: $TS_{th} = TS_{min} - \Delta_{TS}$, resulting in $TS_{th} < TS_{min}$. This approach of calculating TS was to reduce the false human absence detection.

Table 5.3: Elderly person E1 - E4 Wakeup (WT_{th}), Sleep (ST_{th}), Inactivity (IT_{th}), Lying Position (LT_{th}) and TSA Temperature(TS_{th}) threshold values.

Elderly Person	Parameters				
	WT_{th}	ST_{th}	IT_{th}	LT_{th}	TS_{th}
E1	0700	2300	28.2	68.5	26.8
E2	0630	2200	23.3	67.3	27.7
E3	0730	2200	23.2	57.3	26.8
E4	0700	2200	23.7	66.9	27.2

5.5.2 Motion Inactivity Monitoring and Lying Down Posture Sensing

In the subsequent 20 days, the inactivity and alert monitoring features were activated with inactivity monitoring from the wake up (WT) time until sleep time (ST). Table 5.4 and 5.5 depict the summary of motion inactivity monitoring

results. There was an unwanted motion inactivity alert triggered in the elderly person E3 home on day 20 of the trial. Elderly person E3 dozed off in a sitting position while watching a television program, and the PIR motion sensor failed to detect any motion activity until the inactivity timeout occurs (highlighted in **bold** in Table 5.5). Since elderly person E3 did not lie down while dozing off, the TSA detects the dozing off position as a normal sitting posture, and the Base Station will not adjust the inactivity timeout to be longer. This resulted in an unwanted false alert, and alert messages were sent via SMS to the designated caregivers. Caregivers called to verify and confirmed elderly person E3 is fine.

5.5.3 Forehead Surface Temperature Measurement

The forehead surface temperature measurement for human presence detection worked well based on the pre-defined TS_{th} values for each elderly. All the recorded temperature values in Table 5.4 and 5.5 were well above the TS_{th} values. Thus, throughout the length of the trial, the elderly persons were properly detected as being presence in their apartments, by monitoring the forehead surface temperature using the TSA. This temperature monitoring procedure can be further enhance upon in the future by incorporating algorithm to estimate core body temperature.

5.6 User Data Privacy and Security Considerations

e-Care system uses ZIGBEE PAN for its sensor modules to communicate with a Base Station and GSM mobile communication network or the Internet for emergency request for assistance. e-Care system installed in each elderly person's

Table 5.4: Elderly person E1 - E2 Wakeup (*WT*), Sleep (*ST*), Inactivity (*IT*), Lying Position (*LT*) durations, and TSA Temperature(*TS*).

Day	E1					E2				
	<i>WT</i>	<i>ST</i>	<i>IT</i>	<i>LT</i>	<i>TS</i>	<i>WT</i>	<i>ST</i>	<i>IT</i>	<i>LT</i>	<i>TS</i>
11	0700	2300	8	49	29.5	0630	2200	16	0	29.2
12	0700	2300	7	0	27.8	0630	2200	7	57	30.0
13	0700	2300	19	0	27.6	0630	2200	9	62	28.9
14	0700	2300	9	62	28.6	0630	2200	15	58	28.4
15	0700	2300	7	53	29.4	0630	2200	17	0	29.7
16	0700	2300	18	60	29.6	0630	2200	5	0	30.1
17	0700	2300	8	0	29.3	0630	2200	8	60	29.4
18	0700	2300	7	62	29.5	0630	2200	16	40	28.2
19	0700	2300	8	0	29.8	0630	2200	8	0	28.6
20	0700	2300	12	0	29.2	0630	2200	9	61	29.1
21	0700	2300	20	61	27.9	0630	2200	7	0	30.0
22	0700	2300	7	55	29.6	0630	2200	7	0	28.9
23	0700	2300	9	40	29.7	0630	2200	8	0	30.1
24	0700	2300	7	0	29.7	0630	2200	11	56	29.4
25	0700	2300	8	0	27.6	0630	2200	19	0	29.7
26	0700	2300	7	59	29.6	0630	2200	4	62	29.5
27	0700	2300	22	50	28.2	0630	2200	9	60	28.8
28	0700	2300	8	0	29.7	0630	2200	9	65	29.3
29	0700	2300	6	55	29.7	0630	2200	8	0	29.3
30	0700	2300	9	61	29.1	0630	2200	17	0	29.1

home has a unique PAN and a Base Station associated with it. Sensor modules install in each home must be configured to access the unique PAN to enable communication with the home's Base Station. The PAN is encrypted [154] [155] to prevent any unauthorized network access, and has to be established prior to any successful data transfer to the Base Station.

e-Care TMotion sensor module detects for motion signal from the PIR sensor and acquires the human body temperature data from the TSA. When a valid PIR motion signal detected, the TSA data is processes locally to determine the human forehead temperature and human posture information, and the TSA data is discarded after processing. The processed temperature and posture information is assembled into a simple Temperature-Posture Data Packet (TPP) and

Table 5.5: Elderly person E3 - E4 Wakeup (*WT*), Sleep (*ST*), Inactivity (*IT*), Lying Position (*LT*) durations, and TSA Temperature(*TS*).

Day	E3					E4				
	<i>WT</i>	<i>ST</i>	<i>IT</i>	<i>LT</i>	<i>TS</i>	<i>WT</i>	<i>ST</i>	<i>IT</i>	<i>LT</i>	<i>TS</i>
11	0730	2200	19	0	29.2	0700	2200	9	0	29.9
12	0730	2200	6	0	29.9	0700	2200	11	0	28.1
13	0730	2200	8	0	27.7	0700	2200	5	64	29.7
14	0730	2200	10	49	29.1	0700	2200	15	0	27.7
15	0730	2200	6	0	29.6	0700	2200	8	0	28.3
16	0730	2200	7	0	28.3	0700	2200	7	0	27.8
17	0730	2200	18	53	29.6	0700	2200	10	0	29.4
18	0730	2200	5	0	30.1	0700	2200	9	0	28.3
19	0730	2200	16	0	29.9	0700	2200	8	0	27.8
20	0730	2200	23.2	0	29.7	0700	2200	20	57	29.7
21	0730	2200	7	50	30.0	0700	2200	8	43	29.9
22	0730	2200	7	41	29.2	0700	2200	7	0	28.1
23	0730	2200	8	0	30.0	0700	2200	8	0	29.3
24	0730	2200	8	35	27.9	0700	2200	17	0	29.9
25	0730	2200	6	0	29.4	0700	2200	6	63	27.8
26	0730	2200	10	0	29.6	0700	2200	4	0	28.7
27	0730	2200	19	38	28.1	0700	2200	16	0	28.5
28	0730	2200	7	0	27.8	0700	2200	8	0	28.7
29	0730	2200	8	0	29.8	0700	2200	18	0	29.3
30	0730	2200	8	0	30.1	0700	2200	9	37	29.7

is transmitted to the Base Station for further processing. TPP does not contain any other types of user information besides the temperature and posture information.

At the Base Station, the received TPPs are processed locally by using the developed motion activity detection algorithm. Processed TPPs are not stored and immediately discarded. In the event of an emergency situation, the Base Station directly informs the designated caregivers either by SMS via the GSM mobile communication network or by Internet messaging (for e-Care operating in Simple Mode). For e-Care operating in Infrastructure Mode, the Base Station notifies the remote server about the emergency situation, and the server in-turn informs the designated caregivers stored in its database.

In both Simple and Infrastructure Modes of operations, e-Care users have full controls over their choice of caregivers, and have the ability to disable the system. Caregivers contact information are stored locally in the Base Station or at the remote server. e-Care users and caregivers are informed of the documented methods e-Care handle their TPPs and contact information and the underlying data encryption effort to ensure their personalized data remain safe, private and secured.

5.7 Ethical Issue

The ethical issue of deploying an e-Care system is with regards to the round the clock motion activity detection that may results in an invasion of privacy issue. e-Care implements a strict data collection guideline discussed earlier, and the guideline prevents this issue from occurring. e-Care users are made aware of the data collection method and sign consents must be provided by the users in-order to allow e-Care deployments.

Motion activity detection function is possible due to the availability of temperature and posture information from TPP. e-Care users are informed that they are only being monitored for motion activity derived from the TPPs data. Each user has a full control over the choice of caregivers, and has the ability to disable the system if the user is uncomfortable of being monitored round the clock.

5.8 Summary

e-Care system has been successfully developed. Its functionalities has been tested and verified in a feasibility trial involving lone elderly people living by

themselves. Due to the small number of lone elderly people available and willing to participate in the trial, e-Care operates in Simple mode where remote application and database server is not required. The task of alerting caregivers is handled by the Base Station. The Base Station is designed with off-the-shelves components so as to keep its production cost low.

The combination of PIR motion sensor and TSA, together with low power embedded controller hardware of the TMotion module result in an enhanced motion activity with human presence detection. The detection method is unique as it is able to detect the presence of a live human subject via a known thermal signature even if the person is motionless or with minimal movement for a long period of time. The TSA allows simple human posture detection where a sleeping or lying down posture is accurately detected which enables the inactivity timeout timer value on the Base Station to be automatically lengthen so as to prevent any unwanted false inactivity alert. The TMotion module is scalable and modules can be easily added in order to improve on the coverage and detection accuracy.

Chapter 6

pVoice: Assistive Device for a Class of Speech Impaired Elderly with Vocal Cord Paralysis

6.1 Introduction

The production of a clear and audible human speech is contingent on three main components; a reservoir of air in the lungs, an intact functioning larynx, and a normal physical form and function of the oropharynx converting voice into intelligible speech [170–173]. Human speech is impaired when any of these three components are not in satisfactorily functional conditions. In particular, phonatory disturbances can be caused by diseases of the larynx. Some of these diseases can be corrected either medically or surgically to restore voice [174] and

therefore speech. More persistent conditions include vocal cord paralysis [175] due to advance aging, recurrent laryngeal nerve injury or tumor infiltration. While the patient continues to be able to generate his/her own voice and speech, they can be significantly degraded in quality.

Loss of ability to phonate can be overcome with various approaches depending on the severity. In mild phonatory impairment, the patient may not feel the need to improve the voice or to seek behavioral therapy. In moderate impairment, the patients may use assistive devices such as a microphone and an audio amplifier. These devices, in the conventional forms, are not ideal for portable usage with their physical sizes, and the clarity of the processed speech remains poor with only a direct amplification of the signals detected. The most severe impairment occurs when the larynx has to be removed entirely in a procedure called total laryngectomy [176]. The patient will lose the ability to generate phonation in speech.

This chapter aims to produce an assistive device, henceforth called pVoice, to assist patients and senior citizens with moderate speech dysfunction arising from vocal cord paralysis. The device will be capable of audio processing, not only in terms of amplification but also selective and customized speech enhancement such as speech envelope detection, noise suppression, frequency bands equalization and formants enhancement, thus assisting these patients who have problems communicating in the usual manner. It is intended to offer both augmentative and corrective speech functions to patients with vocal cord paralysis who can still speak albeit poorly and who are difficult to be understood.

The aim is to produce the device in a light, portable and low power con-

suming form to assist these patients without overwhelming them with physical restraints and inconvenience. By utilizing a portable low power microcontroller unit (MCU) and digital signal processing (DSP) techniques to sense and process speech-induced vibrations [177] acquired from the throat surface, the speech can be enhanced both in loudness, clarity and multi-tone quality. The processed voice signal is projected via a low power magnetic speaker.

pVoice is a wearable device that is able to be used as a standalone independent unit, or as part of an e-Care system (developed in Chapter 5) with indoor/outdoor motion activity monitoring and alerting functions for an elderly person. It also has built-in functions such as manual alert request and accelerometer based fall detection. A built-in Bluetooth low energy (BLE) transceiver allows seamless interface to a wireless throat microphone or a smartphone. In an outdoor setting, the smartphone connection allows pVoice to function as a motion activity monitoring and alert wearable device for an elderly person. pVoice sends SMS messages using the connected smartphone during an emergency situation to notify caregivers. A built-in global positioning satellite (GPS) receiver allows the SMS messages to include geographical position information so as to facilitate the caregivers in finding the location of the elderly person. In an indoor setting, the built-in ZIGBEE unit allows pVoice to communicate with an e-Care Base Station. In an elderly person's home installed with e-Care system, pVoice is a wearable device tasked to monitor motion activity for a valid fall occurrence and manual alert request while performing its primary task. In the event of an emergency, pVoice communicates with the e-Care Base Station via the ZIGBEE wireless personal access network (PAN) to raise an alert.

6.2 Overview

An overview of pVoice main function is provided in Figure 6.1. Its development comprises of a synergy of hardware selection and configurations, and design of digital signal processing algorithms. pVoice is a wearable embedded hardware, designed for low power signal processing application. Figure 6.2 depicts the key system functional block diagram of pVoice, showing the three key functional blocks of an Audio Analogue Front-end (AFE), a Digital Signal Processor (DSP) and an Audio Output Driver. The Audio AFE interfaces to an audio input device in the form of an external throat microphone (laryngophone), and it conditions the speech-induced vibration signals from the throat surface with the appropriate pre-amplification gain which is adjusted automatically to prevent signal clipping. The Output Driver is an amplifier providing driving capability for operating a low power loud speaker. The DSP is the signal processing element between the two and constitutes a major component of the pVoice hardware implementation. These hardware components will be elaborated in detail in Appendix D.

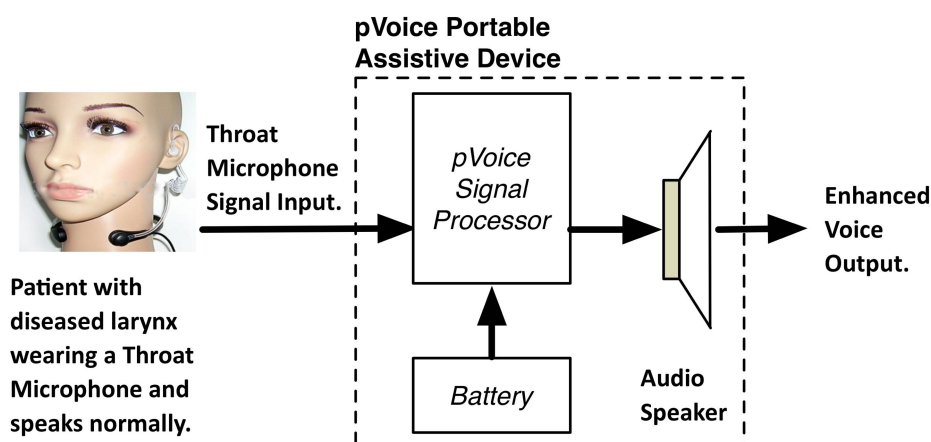


Figure 6.1: pVoice Main Working Principle

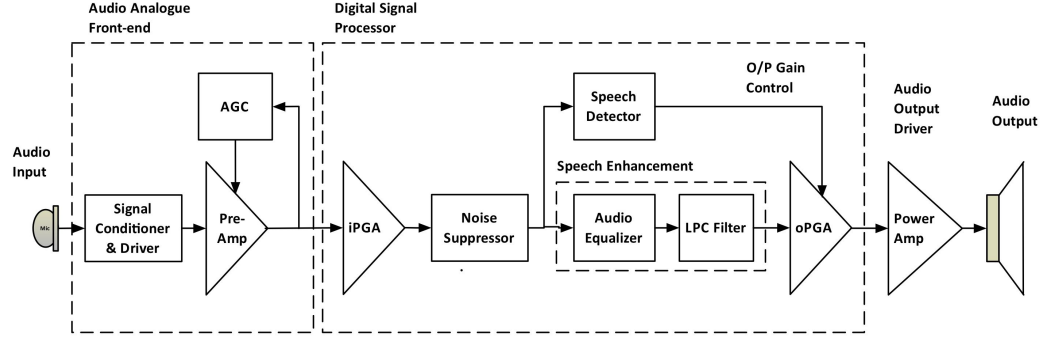


Figure 6.2: pVoice Main Functional Block Diagram

6.3 DSP Voice Enhancement Algorithms

Various candidate algorithms for voice processing and speech enhancement were considered for use in pVoice. Hardwick *et al* [178] proposed the Dual Excitation (DE) speech model for speech processing and enhancement which was shown to be superior in performance compared to the spectral subtraction system. Another independent development by Shamsoddini *et al* [179] also achieved good performance when using directional and harmonicity cues during the processing of the sampled speech signals. Both algorithms yield excellent results from sampled speech when air is the medium for acoustic transmission.

However, pVoice samples speech-induced vibrations $x(t)$ from the throat surface and thus, these two algorithms are not suitable. To meet the specific requirements of pVoice, an alternate voice enhancement algorithm is proposed and developed, comprising of a suite of low level algorithms as shown in Figure 6.3, which includes: (a) Noise Suppressor, (b) Speech Detector and Voice Activation, and (c) Speech Enhancement.

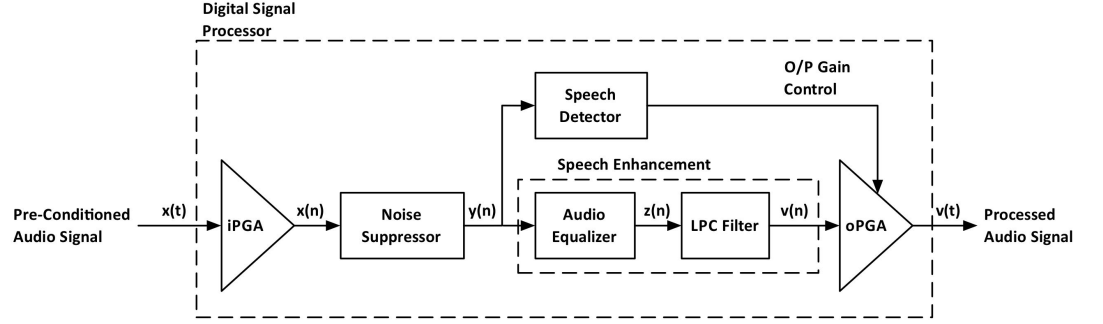


Figure 6.3: pVoice DSP Functional Blocks

6.3.1 Noise Suppressor

A throat microphone mounted in direct contact to the throat surface picks up the speech-induced vibration signals, and is not sensitive to the surrounding and unwanted sound sources. This setup has effectively suppressed most unwanted noise sources. The main source of noise infiltrating into pVoice is the noise generated from undue movements of the contact microphone against the throat surface. An active noise cancellation (ANC) method is required to suppress this noise source. Windrow et al. [180] and Burgess [181] independently proposed a Filtered-X Least Mean Square (FXLMS) algorithm for ANC. Eriksson [182] successfully demonstrated a single-channel ANC system based on FXLMS which is an adaptive feed-forward system that synthesizes its own reference signal.

The pVoice implementation of noise suppression (NS) algorithm for ANC function is based on the FXLMS structure by Eriksson. The algorithm suppresses the effects of noise in the sampled vibration signal $x(n)$ while it adaptively detects and sieve out true voice activities $y(n)$. Figure 6.4 depicts the NS algorithm block diagram in z-domain. $y(n)$ denotes the algorithm's residual function that also represents the true voice activities. S is a transfer function representing the secondary path effects that are inherent for ANC [183]. S constitutes of

propagation delays and phase shifts along the signal path due to various signal processing elements, and unwanted acoustic coupling effects. S is unknown and is estimated by an additional finite impulse response (FIR) filter \hat{S} , that is used in part to calculate and generates noise reference signal $r(n)$. $y(n)$ is defined in Eqn. (6.1) where n is the discrete sample time index, $x(n) = [x(n) \ x(n-1) \ \dots \ x(n-L+1)]^T$ is the sampled vibration signal vector, $s(n)$ is the impulse response of the secondary path, $w(n) = [w_0(n) \ w_1(n) \ \dots \ w_{L-1}(n)]^T$ is the coefficients vector for W and $r(n) = [r(n) \ r(n-1) \ \dots \ r(n-L+1)]^T$ is the reference signal vector, and L is the filter order. $*$ denotes linear convolution. In most practical cases, S can be modeled as a pure delay, hence $S \approx \hat{S} = Z^{-\Delta}$. Thus, Eqn. (6.1) can be simplified to (6.2) where Δ is the discrete unit time delay.

$$y(n) = x(n) - s(n) * [w^T(n)r(n)] \quad (6.1)$$

$$y(n) = x(n) - w^T(n - \Delta)r(n - \Delta) \quad (6.2)$$

The key objective of the NS algorithm is to adapt coefficients $w(n)$ in W , so that $y(n)$ is minimized [183]. The built-in LMS function updates filter coefficients in W based on the square of the residual $y(n)$ according to the objective function defined in Eqn. (6.3). The LMS function minimizes $y^2(n)$ using the steepest descent algorithm, which updates $w(n)$ in W in the negative gradient direction with step size μ . The gradient is a vector pointing in the direction of the change in filter coefficients that will cause the greatest increase in $y(n)$. Since the goal is to minimize $y^2(n)$, Eqn. (6.3) updates the filter coefficients in the direction opposite to the gradient. The constant μ weights the extent of gradient information used to update each coefficient. A large value of μ leads to faster convergence, but

while talking, the sampled speech signal $x(n)$ is contaminated with noise signal from the unwanted rubbing action. The NS algorithm applied on $x(n)$ is observed to be effective as the resultant $y(n)$ is observed with noise reduction of 8 – 12 dB.

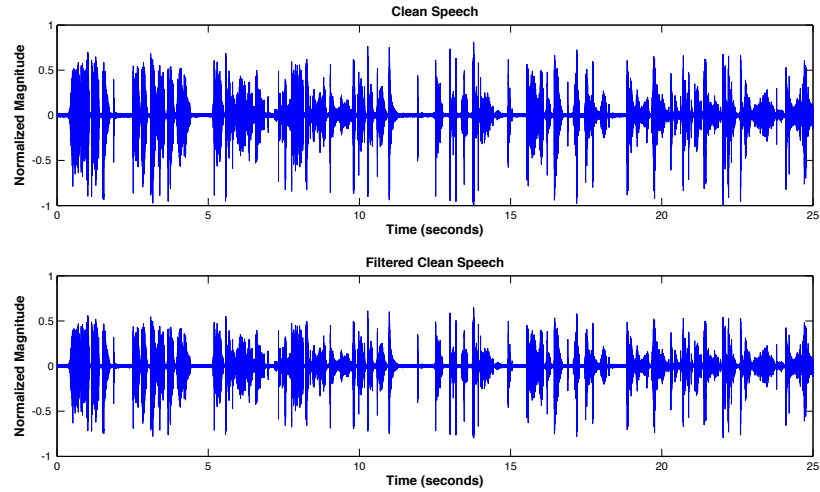


Figure 6.5: Unfiltered and filtered clean speech signals plots

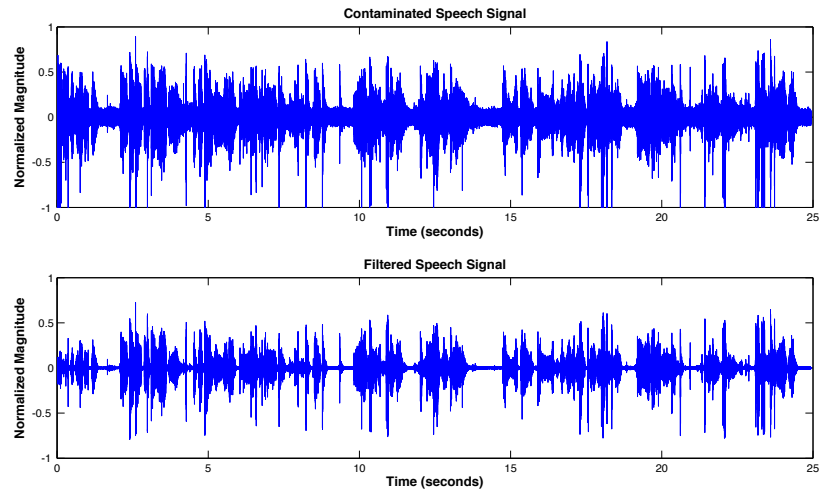


Figure 6.6: Unfiltered and filtered contaminated speech signals plots

6.3.2 Speech Detection and Voice Activation

The Speech Detection and Voice Activation algorithm retrieves the speech envelope from the signals received. The algorithm is developed with the main objective to conserve battery power by shutting down the audio output driver when no speech activity is detected. The throat microphone is sensitive only to speech-induced vibrations. Hence, the algorithm design is relatively simple, straightforward and it requires less computational efforts compared to the works by Harsha *et al* [186] and Chin *et al* [187].

Continuous blocks of 20 ms of voice samples are processed by first converting each block to the frequency domain using Fast Fourier Transform (FFT). The average normalized spectrum power per block is then calculated and compared with a pre-programmed threshold. A valid speech activity corresponds to the spectrum power value above a pre-programmed threshold. A power value within the threshold will put the output driver in the sleep mode.

6.3.3 Speech Enhancement

The throat surface offers a lower bandwidth for transmitting an audio signal compared to open-air acoustic transmission [188]. This in turn means that higher frequency voice components will be inevitably attenuated. Thus, a direct reproduction of the vibration signal sampled using the throat microphone sounds unpleasant to the listener. An algorithm for speech enhancement to improve the speech quality is designed for pVoice which consists of an audio equalizer (AE) and a Linear Predictive Coding (LPC) Filter [189]. LPC represents human speech as a linear model for speech production where the glottis and vocal tract

are totally uncoupled.

The AE is adjusted to provide frequency-specific gains to the processed digital audio signal $y(n)$. With this method, the suppressed voice components signal levels at higher frequencies can be improved by pre-emphasizing the amplitude attenuation. Figure 6.7 depicts the audio equalizer implementation for eight frequency bands: 31, 62, 125, 250, 500, 1000, 2000, 4000 Hz, and a Q-factor of 1.4 for all bands. Each equalizer frequency band is defined by a FIR bandpass filter given in Eqn. (6.4).

$$z_j(n) = \sum_{k=0}^{N-1} b_j(k).y(n-k) \quad (6.4)$$

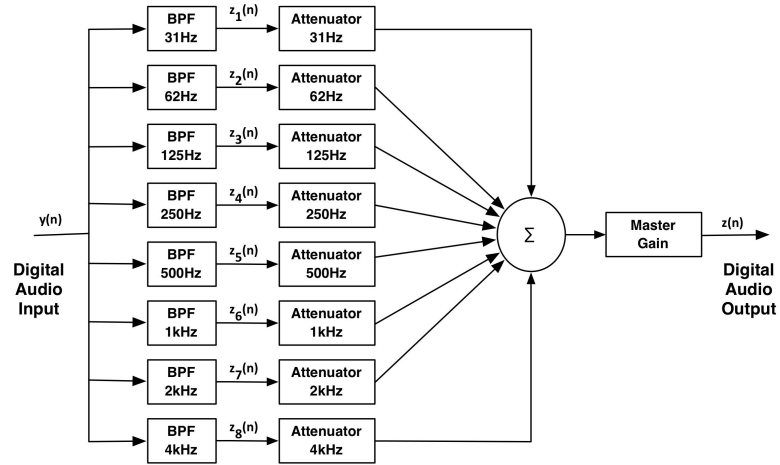


Figure 6.7: pVoice Digital Equalizer Implementation

The band equalized speech signal is further processed by a LPC filter to enable the production of a natural sounding speech. LPC models human vocal tract characteristic as a digital filter with a set of linear prediction (LP) coefficients which are the filter's polynomials [190–193]. A similar approach of speech enhancement has been demonstrated by Rizwan *et al* [194] to improve esophageal speech.

Figure 6.8 depicts a detailed block diagram of the LPC filter implementation. In the block diagram, the equalized speech signal $z(n)$ is channeled through a pre-emphasize filter with gain coefficient $\alpha_{pre-amp}$ to obtain $z_p(n)$. Pre-emphasis is carried out to boost the high frequency components. It is required due to the spectral roll-off of around 6dB/Octave. The LPC Analyzer analyzes $z_p(n)$ in order to extract the excitation (or residual) signal $\hat{z}(n)$, and LP coefficients $a(p)$. The coefficients represent the estimated vocal tract parameters [189] [191] [192]. $\hat{z}(n)$ is determined from Eqn. (6.5) where P is the order of the LPC filter. $a(p)$ are calculated by minimizing the mean square error (MSE) [189] of $\hat{z}(n)$.

$$\hat{z}(n) = z_p(n) - \sum_{p=1}^P a(p) \cdot z_p(n-p) \quad (6.5)$$

$a(p)$ are channeled into the Line Spectral Frequencies (LSF) Enhancer where line spectral frequencies $f_a(p)$ are obtained from $a(p)$ by applying the LP-LSF converter base on method proposed in [195]. Formants [196] are resonant components in the speech contributing directly to speech intelligibility [197]. LSF Enhancer provides formants enhancement by modifying $f_a(p)$ to $\hat{f}_a(p)$ base on coefficient α . The enhancement of formants peaks and spectral valleys can significantly improves quality of synthesized speech [198]. Independent works by Raitio *et al* [199] and Mizuno *et al* [200] evaluated various formants enhancement methods for LPC including the LSF, power spectrum based enhancement methods and waveform-based synthesis. pVoice leverages on LSF for formants enhancements. LSF-based formants enhancement modifies LSFs positions by shifting them closer to each other for spectral sharpening [201].

The LSF positions are modified according to Eqn. (6.6) [199], [202]. $\hat{f}_a(p)$

and $f_a(p)$ are the modified and original LSF respectively. α is the formant enhancement control coefficient, in the range of $0 \leq \alpha \leq 1$. By changing the value of α , the distances between LSFs vary, hence affecting the synthesized speech quality in term of audibility and sharpness. By allowing α to be configurable, pVoice ensures that the synthesized voice is audible, offering reasonable clarity to the listeners, and flexibility to tune the output closer to the patient's true voice.

$$\begin{aligned} \hat{f}_a(p) = & f_a(p-1) + c(p-1) \\ & + \frac{c^2(p-1)}{c^2(p-1) + c^2(p)} ((f_a(p+1) \\ & - f_a(p-1)) - (c(p) + c(p-1))) \end{aligned} \quad (6.6)$$

Where:

$$c(p) = \alpha(f_a(p+1) - f_a(p))$$

$\hat{f}_a(p)$ is re-converted to $\hat{a}(p)$ by applying the LSF-LP converter [195] that produce modified LP coefficients with improved vocal characteristics. LPC Synthesizer re-synthesizes an improved speech signal $\hat{v}(n)$ from $\hat{z}(n)$ and $\hat{a}(p)$. Eqn. (6.7) depicts the LPC Synthesizer. $v(n)$ is obtained after $\hat{v}(n)$ is channeled through a de-emphasize filter with gain coefficient α_{de-amp} . The de-emphasize process is necessary to correct the high frequency components back to normal level. LPC filter length $P = 11$ for $F_s = 8\text{kHz}$ is estimated by [203] where $P \approx (F_s/1000) + 3$ that includes certain number of redundancies.

$$\hat{v}(n) = \hat{z}(n) + \sum_{p=1}^P \hat{a}(p) \cdot \hat{v}(n-p) \quad (6.7)$$

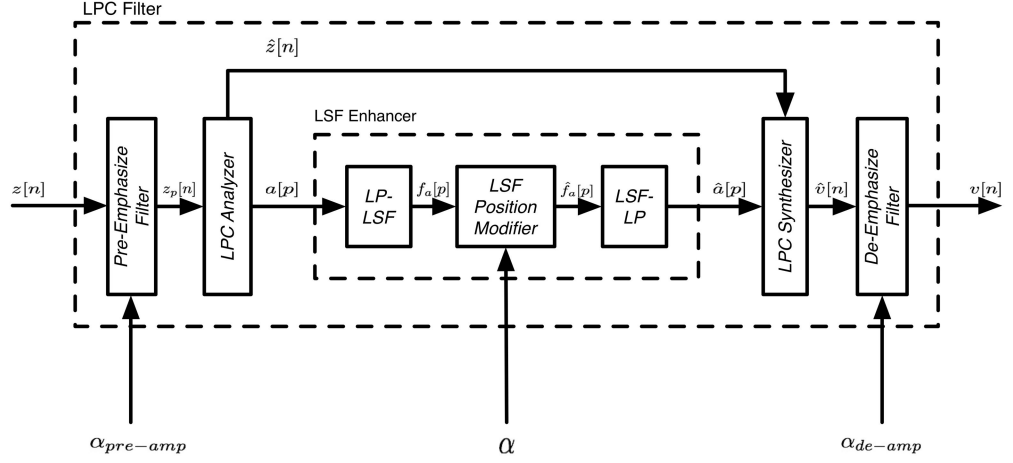


Figure 6.8: pVoice LPC Filter Implementation

6.4 Tests and Results

pVoice is intended to serve as a portable, low cost and low power consuming assistive device. The assembled prototype depicted in Figure 6.9 measuring 61mm x 88mm x 22mm and weights about 60g. The components and assembly cost US\$130.00 in total. It can operate continuously for 8 - 10 hours with a full charge of the internal 3.7V 1450 mAH LiPo rechargeable battery. Figure 6.10 depicts how pVoice is to be correctly worn by a user. The ergonomic exterior of pVoice ensures ease of handing by the user. The constituent hardware modules of pVoice were tested to be functioning to the modular specifications using instruments in the engineering laboratory for signal calibration and analysis. The periphery parts of the voice enhancement algorithm, such as noise suppression, speech detection and voice activation, were also directly verified to conform to

the requirements by the authors. These tests do not require the participation of the patients.



Figure 6.9: pVoice prototype with an attached Throat Microphone

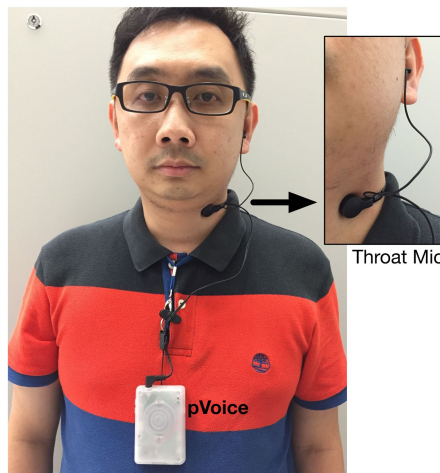


Figure 6.10: pVoice prototype worn by a user

The final speech quality enhancement will be evaluated on patients belonging to the target class. A large scale controlled clinical trial is currently being conducted, but pre-clinical verifications were done on two patients with vocal cord paralysis; a middle-aged male patient suffering from Unilateral Vocal Cord Paralysis (UVCP) due to a large thyroid cancer that invaded the nerves responsible for left vocal cord movement (Patient 1) and a 49 years old male patient suffering from Thyroarytenoid Muscle Paralysis (TMP) due to bacterial infection

(Patient 2).

Both patients were asked to read out loud the following sentences: *"Man's first boat. Long ago man found that it was easier to travel on water than on land. They needed a clear path or road when they traveled on land."* The time duration to read the whole sentences varied depending on each patient's condition. The raw and pVoice processed speech signals of the two patients were logged for analysis.

The pre-emphasize filter and de-emphasize filters in the LPC filter block were empirically adjusted with $\alpha_{pre-emp} = 0.98$ and $\alpha_{de-emp} = 0.9$ respectively. The α of the LSF Enhancer were empirically determined to be 0.28, 0.32, 0.34 and 0.36, to be used to generate the correspondingly enhanced speech signals from UVCP and TMP patients.

For benchmarking purpose, a speech synthesizer was used to synthesize a reference speech signal based on the pre-defined text sentences. The reference speech signal did not contain any noise and was not signal processed by the pVoice. Figure 6.11 is the spectrogram of the reference speech signal that depicts dense frequency components of comparatively high spectral energies throughout the human voice frequency bandwidth. Spectrograms of patients' raw and enhanced speech signals are shown from Figure 6.12 to Figure 6.21. The patients' raw speech signals' spectrograms depicted in Figure 6.12 and Figure 6.17, when compare to the reference, clearly indicate the absence of frequency components that constitute a pleasant sounding speech. The spectrograms also show the levels of speech degradation in patients with UVCP and TMP. The patients' voices are weak, hoarse and raspy, and they manifest evidence of upper range

harmonics loss. Such a voice affects the overall speech clarity and these undesirable characteristics appear in the spectrograms in the form of considerable spectral energies distributed randomly at the higher frequencies (seen as uneven distributions of darker color dots along the higher frequency scale). A weak voice is characterized by the presence of lower spectral energies at the lower frequencies (seen as lighter color lines along the lower frequency scale) [204]. A healthy voice should exhibit considerable consistent spectral energies lines throughout the human voice frequency bandwidth (darker color lines) [204].

The primary aim of pVoice speech enhancement is to improve the patient's speech clarity. With the LSF-based speech enhancement, spectrograms of the enhanced speech signals show characteristics pointing to improvements in speech clarity. A change in the color densities can be seen along the high frequency scale. The reduction in spectral energies distributed randomly at the higher frequencies is clearly evident as α increases, hence illustrating the reduction of the effects associated with a hoarse and raspy voice.

Listening assessments were done by five independent volunteers chosen at random and who are not part of the study and they are not aware of the technical details and the patients conditions. A generally unanimous feedback was obtained from them of the enhancement in speech clarity achieved with pVoice. The two key assessment criterion formulated and the assessment results will be briefly explained in the following subsections.

6.4.1 Assessment of Amplification and Clarity

This assessment is specific to amplification and clarity of processed speech signals. The amplification measurement is based on a sliding scale of zero to

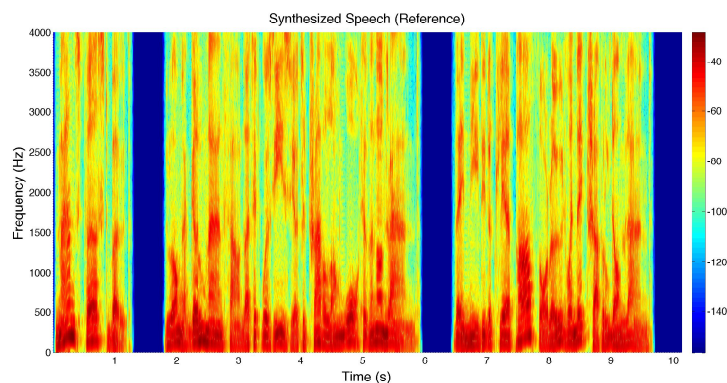


Figure 6.11: Spectrogram - Reference Speech Signal

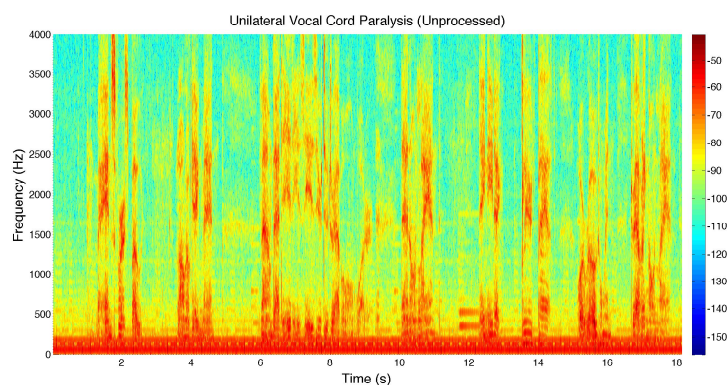


Figure 6.12: Spectrogram - UVCP (Raw)

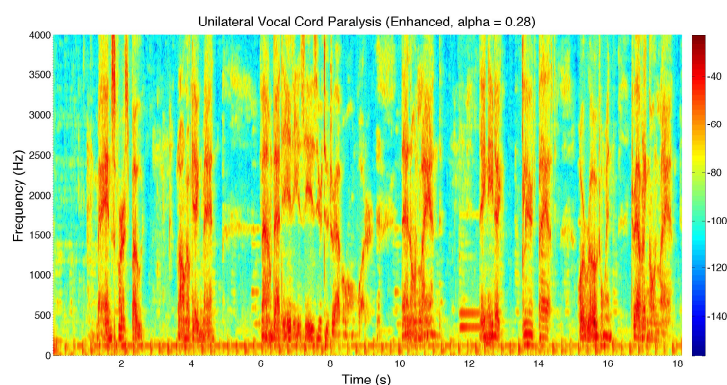


Figure 6.13: Spectrogram - UVCP (Enhanced, $\alpha = 0.28$)

ten, with zero being no sound heard, five being sound is normal level and ten being sound is very loud. The assessors were instructed to concentrate only on the amplification quality. Scores of five and above were taken to be indicators that the device has produced sufficient amplification.

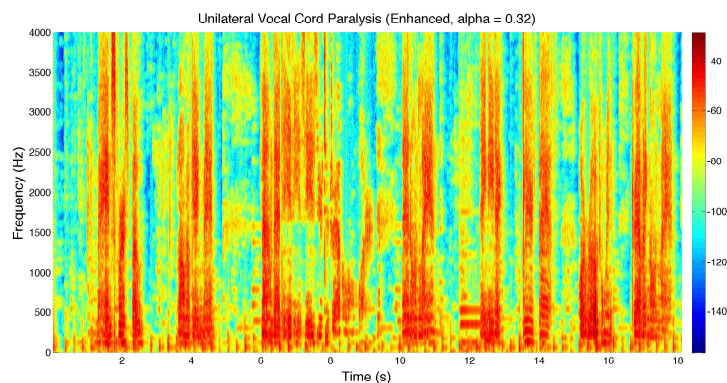


Figure 6.14: Spectrogram - UVCP (Enhanced, $\alpha = 0.32$)

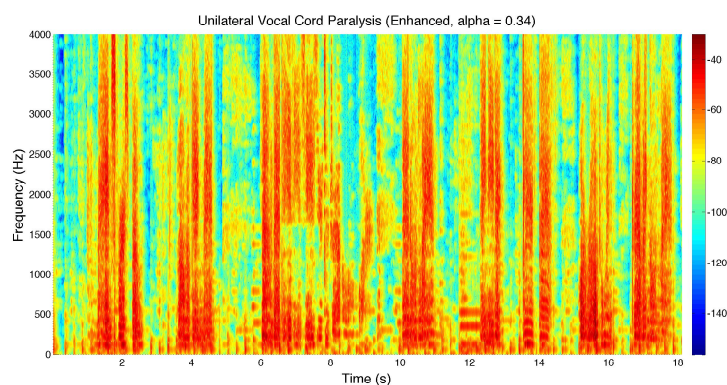


Figure 6.15: Spectrogram - UVCP (Enhanced, $\alpha = 0.34$)

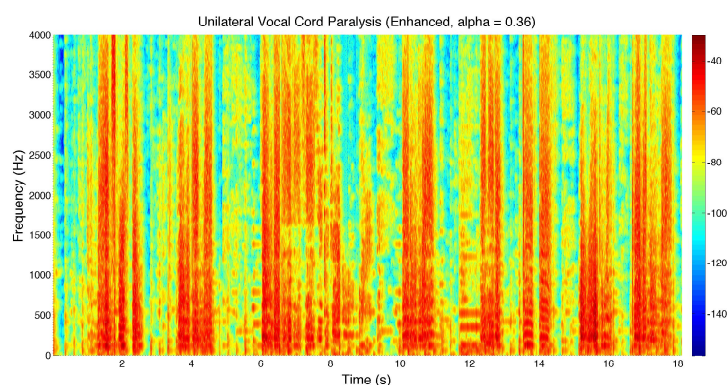


Figure 6.16: Spectrogram - UVCP (Enhanced, $\alpha = 0.36$)

The clarity measurement is based on the same sliding scale of zero to ten, with zero being speech is unintelligible, five being acceptable in clarity and ten being normal. The assessors were instructed to concentrate only on the speech clarity. Scores of five and above were taken to be indicators that the device has

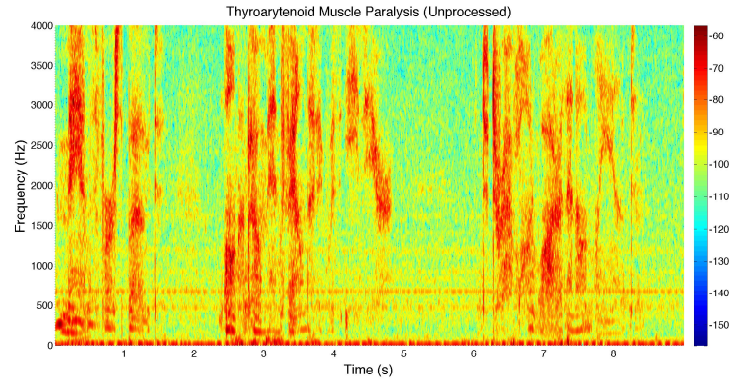


Figure 6.17: Spectrogram - TMP (Raw)

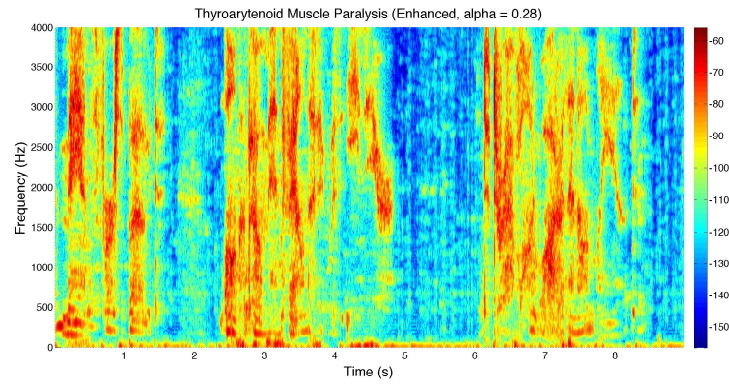


Figure 6.18: Spectrogram - TMP (Enhanced, $\alpha = 0.28$)

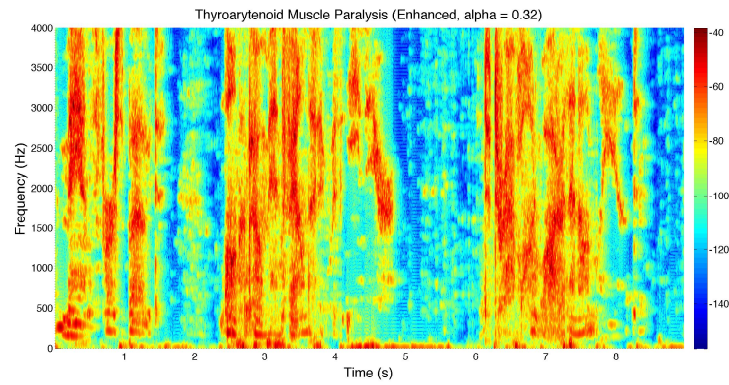


Figure 6.19: Spectrogram - TMP (Enhanced, $\alpha = 0.32$)

produced speech with acceptable clarity.

Assessors were also asked to provide a subjective feedback on the combined amplification and clarity of the processed speech signals based on how well they can discern the words in the sentences and the meaning of the sentences. They

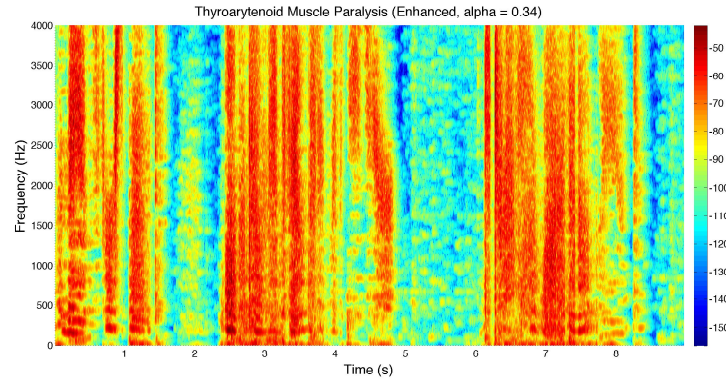


Figure 6.20: Spectrogram - TMP (Enhanced, $\alpha = 0.34$)

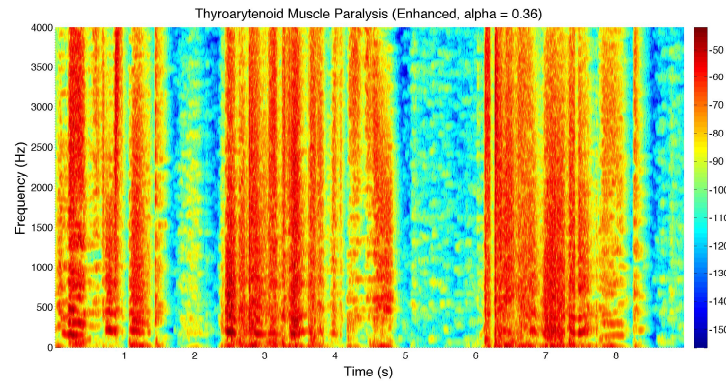


Figure 6.21: Spectrogram - TMP (Enhanced, $\alpha = 0.36$)

also wrote down the sentences the way they heard them. An objective indicator can then be derived based on the number of correct words from the original sentences they reproduced.

Table 6.1 shows the assessment in terms of amplification only. All the assessors were able to hear the processed speeches well. Table 6.2 shows the outcomes of the evaluation from the assessors on the clarity of the processed speech signals based on their judgement. The results show the speech enhancement corresponding to $\alpha = 0$ (raw speech) and $\alpha = 0.28, 0.32, 0.34, 0.36$ (enhanced speech). Based on the average scores computed in Table 6.2, an improved in clarity can be observed as α increases. But while a larger α can lead to a sharper speech quality, it is noted that it may induce speech distortion. Relative to the raw speeches of

the patients, it is observed that the clearest improvement (without distortion) to the synthesized speech amplification and clarity is achieved with $\alpha = 0.32$ for Patient 1 and $\alpha = 0.34$ for Patient 2. Beyond these values, sharpness is achieved at the expense of distortion.

Table 6.3 shows the accuracies of the assessors in reproduction of the sentences comprising of the 29 words. Based on the average scores computed in the table, the accuracy improves as α increases. However, at $\alpha = 0.36$ for Patient 2, the induced distortion resulted in a drop in the accuracy of reproduction.

Table 6.1: Assessment of Amplification

	Assessors' Score					Average Score
	1	2	3	4	5	
Patient 1	5	6	6	5	5	5.4
Patient 2	6	6	5	5	6	5.6

Table 6.2: Assessment of Clarity

	α	Assessors' Score					Average Score
		1	2	3	4	5	
Patient 1	0	3	2	3	2	2	2.4
	0.28	3	2	4	3	3	3
	0.32	4	4	5	4	4	4.2
	0.34	5	5	6	5	4	5
	0.36	7	6	6	6	5	6
Patient 2	0	3	2	3	3	2	2.6
	0.28	4	4	3	4	3	3.6
	0.32	4	4	4	4	4	4.6
	0.34	7	7	6	6	6	6.4
	0.36	8	8	7	7	7	7.4

Table 6.3: Pronunciation Accuracy of Listened Speech

		Assessors' Score (%)					Average Score
	α	1	2	3	4	5	(%)
Patient 1							
	0	79	69	79	79	79	77
	0.28	79	69	83	79	79	78
	0.32	79	69	83	79	79	78
	0.34	90	93	97	83	83	89
	0.36	90	93	97	83	83	89
Patient 2							
	0	79	79	79	72	79	78
	0.28	86	90	86	86	86	87
	0.32	93	93	93	83	93	93
	0.34	93	93	93	93	93	93
	0.36	93	83	86	93	83	88

6.4.2 Assessment of Multi-tone Quality

pVoice was also evaluated in terms of how the device can maintain the integrity of the multiple tones of the speech. The measurement of adequate tonal integrity is based on the clarity of the tones present in the processed speeches to the five assessors. Tone is defined in this study as pitch. The patient should have varying tone in the speech. The tonal quality measurement is made by assessing the sentences read by the patient. The assessment of tonal quality is based on a sliding scale of zero to five, with zero being no tone heard, one being a single tone heard, five being speech has normal tone. The assessors are instructed to concentrate only on the tonal quality. Scores of three and above are taken to be indicators that the device has produced sufficient tonal quality.

Table 6.4 shows the assessment results in terms of multi-tone quality of the processed speeches from the two patients. The results show the level of enhancement resulting from $\alpha = 0$ (raw speech) and $\alpha = 0.28, 0.32, 0.34, 0.36$ (enhanced speech). Based on the average scores computed in Table 6.4, improvement in

multi-tone quality is observed as α increases. The improvement achieved is clear with $\alpha \geq 0.32$ for Patient 1 and $\alpha \geq 0.34$ for Patient 2. With $\alpha = 0.34, 0.36$, near to normal multi-tone qualities for both patients are observed.

Table 6.4: Assessment of Multi-tone Quality

		Assessors' Score					
α		1	2	3	4	5	Average Score
<hr/>							
Patient 1							
	0	2	2	2	2	2	2
	0.28	3	4	2	2	3	2.8
	0.32	4	3	3	3	4	3.4
	0.34	4	4	4	3	4	3.8
	0.36	4	3	4	4	4	3.8
Patient 2							
	0	2	2	2	2	2	2
	0.28	3	2	2	3	2	2.4
	0.32	3	3	4	4	4	3.6
	0.34	4	4	4	4	4	4
	0.36	4	4	4	4	4	4
<hr/>							

6.5 User Data Privacy and Security Considerations

pVoice deployed as a standalone independent voice enhancement device does not collect any form of user information. There is no immediate concerns over data privacy and security issues as the device only samples voice induced vibration signal from the throat surface. The vibration signal is locally processed and enhanced using a developed algorithm. The enhance signal is being amplified as an audible speech.

pVoice deployed as part of e-Care system (developed in Chapter 5) uses BLE, ZIGBEE PAN and GSM mobile communication network for emergency request for assistance. When pVoice is used indoor together with the e-Care sensor modules and a Base Station, pVoice data privacy and security considerations are

the same as those listed in e-Care (in Chapter 5). The additional sensing feature introduced by pVoice is the human fall detection. In the indoor setting, pVoice uses its built-in accelerometer to monitor user motion's activity for valid a fall occurrence. In the event of a valid fall, pVoice notifies the e-Care Base Station using the encrypted PAN [154] [155], and the Base Station in-turn informs the designated caregivers with methods defined in Chapter 5.

In the outdoor setting, pVoice uses the built-in accelerometer and GPS receiver to track user's motion activity and geographical location information. pVoice is wirelessly paired to the user's smartphone via BLE. The data transfer to the smartphone is encrypted [153–155] to prevent any unwanted data privacy and security issues. pVoice uses its accelerometer to monitor user's motion activity for fall occurrence. In the event of a valid fall, pVoice uses the paired smartphone to send SMS request for assistance messages to the designated caregivers. User's current geographical location information is also included in the SMS messages.

In both indoor and outdoor settings, pVoice uses its accelerometer to track user's motion activity. Geographical location is also monitored in an outdoor setting. This information is not time stamped and stored locally or remotely so as to prevent any privacy and security related issues. Similar to e-Care Base Station, pVoice users have full controls over their choice of caregivers, and have the ability to disable the system. Caregivers contact information are stored locally in the e-Care Base Station and on the pVoice. Users and caregivers are informed of the documented methods e-Care and pVoice handle their acquired data and the underlying data encryption effort to ensure their personalized data

remain safe, private and secured.

6.6 Ethical Issue

The ethical issue of using a pVoice is with regards the built-in accelerometer and GPS receiver that enable motion and geographical location tracking, that may result in an invasion of privacy issue. pVoice implements a strict data collection guideline discussed earlier, and the guideline prevents this issue from occurring. Users are made aware of the data collection method and must sign consents before pVoice can be used.

Users using pVoice in the outdoor setting are informed that they are being monitored only for occurrence of fall. When a valid fall is detected, geographical location information is acquired from the GPS receiver and sent together as part of the SMS alert messages to the designated caregivers. Each user has full control over the choice of caregivers, and has the ability to disable the system if the user is uncomfortable of being monitored.

6.7 Summary

This chapter has presented the design and development of pVoice as an assistive healthcare device for a class of speech-impaired patients with vocal cord paralysis who can speak albeit poorly and who are difficult to be understood. The hardware selection and configuration, and the design of DSP algorithms collectively resulted in a portable, compact and low power consuming wearable device which picks up speech-induced vibrations at the throat surface and processes them to result in a speech which is improved in loudness, clarity and

multi-tone quality. In particular, the speech enhancement algorithms allow configuration to approach the patient's true voice. The performance of pVoice was assessed positively from controlled pre-clinical tests on a small sample of patients with vocal cord paralysis. A larger scale clinical trial is currently being conducted.

Chapter 7

Conclusions

Rapidly aging population poses challenge to countries like Singapore in terms of optimizing their healthcare delivery system to the mass. As the percentage of the population in need of healthcare rapidly increases, healthcare providers in these countries are already finding it a challenge to cater their resources to such high demand. Assistive healthcare, a method of remote healthcare monitoring and resource management by making use of remote sensing and communications technologies advancements, is indeed the way forward. With the reach of mobile telecommunication and Internet to almost all corners of the world, it is a viable option to implement, that can help to reduce the increasing conventional healthcare expenses as well as assist in optimal utilization of the limited available healthcare resources.

A lot of research has been conducted on the feasibility of implementing assistive healthcare systems, especially for the monitoring of senior citizens, and to provide timely medical interventions by healthcare professionals when required. As discussed in Chapter 1, the first ever documented assistive health care technol-

ogy was demonstrated in 1995 [57]. Various different implementations of assistive healthcare systems exist, and many are still under active developments, mobile and Internet communications technologies are the catalysts to further increase the momentum and more advanced solutions were introduced afterwards.

The works presented in this thesis focused on designing and developing assistive healthcare solutions with specific emphasis on vital status monitoring, motion activity monitoring and alert management, and portable voice assist for effective communication. Experiments were conducted to validate the various algorithms as well as other functions and the results proved the efficiency of the system as well as its capability to ensure its usefulness under various environments.

7.1 Main Contributions

In Chapter 2, design and formulation of an assistive healthcare framework with the identified common core components was presented. The framework defines the various requirements for a practical implementation of assistive healthcare systems. In-order to demonstrate on the practicality of implementation, three assistive healthcare device were proposed and developed.

The framework presented in Chapter 2 formed the foundation to develop the three assistive healthcare devices. The first device to be developed is a vital sign monitor that serves the purpose for real-time monitoring of core body temperature, which is useful in early detection of heat related illnesses on sports and military personnel performing strenuous physical activities. In Chapter 3, detailed study to re-visit the tympanic membrane vicinity as core body temperature

measurement site was conducted. The research proposed the middle ear cavity as a potentially new site for accurate core temperature monitoring, as the new site demonstrated good correlations to the alternative core body temperature monitoring sites (tympanic membrane, esophagus and rectum). Chapter 3 also covered a detailed development of an accurate temperature model for the middle ear cavity. The temperature model is demonstrated to be able to accurately infer middle ear cavity temperature from a known tympanic membrane temperature. Experiment to verify the accuracy was conducted on a live sedated primate. The developed temperature model was further improved in order to infer core body temperature from other known sites apart from the middle ear cavity. A Gain-Scheduled lookup table was introduced to improve on the accuracy of the temperature model.

Chapter 4 detailed the development of VitalMON - minimally invasive system of mobile monitoring of core body temperature. The assistive healthcare device is developed from scratch to monitor real-time core body temperature via the surface of the tympanic membrane. A customize ear mold is required this purpose. The development uses an infrared thermopile sensors array to measure infrared emissions from the surface of the tympanic membrane, and highest temperature spot is extracted from the sensors. The highest temperature spot is used to for core body temperature measurement based on algorithm developed in Chapter 3. The assistive health care device has been successfully developed and demonstrated its intended usage.

Chapter 5 highlighted the development of e-Care - a non-intrusive activity monitoring for the lone elders living by themselves. This was the second type of

assistive healthcare device developed by using the common framework defined in Chapter 2. The hardware developed in this chapter demonstrated an improved method of motion activity monitoring of a lone elder staying at home by improving on the Passive Infrared (PIR) sensor based motion activity monitoring with the addition of human body temperature detection and simple postures detection. The improvement required a thermopile sensors array to be used side by side with a PIR sensor.

Chapter 6 highlighted the development of pVoice, an assistive wearable device for a class of speech impaired patients with vocal cord paralysis. This was the third hardware developed based on the assistive healthcare framework. The hardware developed improved on the speech and communication of patient or an elder with weak vocal cord due to disease or advance aging. The hardware is a small wearable device that picked up weak sound signal from the surface of the throat and processed it with a custom algorithm, and projected it out as an improved and audible voice. The hardware has been trailed in National University Hospital, Ear Nose and Throat clinic with favorable results. Further trials will be required in-order to further improve on the voice enhancement algorithm.

7.2 Limitations and Suggestions for Future Work

Based on the prior research as well as the experience acquired while working on this thesis, the following deserves further consideration and investigation to improve the completed assistive healthcare systems.

7.2.1 VitalMON

In Chapter 4, The VitalMON system has only been tested with limited users. Although the test results were very good and were helpful in validating all the implemented features and algorithms, it is essential to conduct a trial run for large number of users in wide geographical locations such as those in the developing countries whereby home based users are being monitored by distantly located healthcare professionals and caregivers. Such a trial is necessary to detect potential short comings and to improve on it, so that the developed systems can be ready for field deployment.

The Wireless Temperature Acquisition (WTA) module requires further engineering effort in miniaturizing it to the point that the final size is comparable to a size of a typical behind-the-ear type of electronics hearing aid. The protective case of the Thermopile Sensors Array (TSA) used by the WTA should be customized to further reduce its overall diameter so as to make it easier to be encapsulated by a personalized ear mold. Personalized ear mold is to be fabricated for each user so as to provide an improved comfort level.

The current PDL/TM electronics hardware only supports 2G mobile phone communication network that provides Short Message Service (SMS) and General Packet Radio Service (GPRS) based internet connection. 2G network is currently being phased out, the PDL/TM hardware should be modified to include native supports for 3G and 4G mobile phone networks so as to be able to adopt the broadband high speed internet connectivity as its primary form of communication. Supports for other competing wireless technologies developed for Internet of Things (IoT) should also be added as an option to cater

for deployments in different geographical terrains. Proprietary interface to the Iridium Satellite Communication Network should be also developed to enable the VitalMON system to be deployed without any geographical constraints.

The circuit boards can be made smaller by utilizing smaller components and multi-layer printed circuit board. Industrial design should be carried out to design ergonomic enclosures for all the VitalMON modules so as to provide good user handling experience.

7.2.2 e-Care

In Chapter 5, The e-Care system has only been tested with limited users. Although the results of the tests were very promising and helpful in validating all the implemented features and algorithms, it is essential to conduct trials for large number of users in wide geographical locations whereby home based elderly people are being monitored by distantly located healthcare professionals and caregivers. The trials are necessary to detect hidden problems and to serve as an opportunity to collect usage experience data. The data can be used to further improve on the system to a level suitable for commercial deployments.

The developed e-Care hardware does not incorporate a distance measurement sensor in order to measure the distance between the TSA and the target. This shortfall resulted in non-accurate temperature calculation of the TSA when used to measure target temperature. The accuracy of the TSA depends on the distance from the target, thus with this additional hardware module, distance information can be determined and used together with the TSA measurement to accurately determine target temperature. The PIR sensor can be potentially replaced with a 25GHz pulsed Doppler radar for improved human motion de-

tection and distance measurement. The radar module is also sensitive enough to detect human fall activity. Thus, e-Care can be further improved with an additional role as a reliable fall activity detector.

At present, the e-Care system can only measures forehead surface temperature, and does not estimates CBT from it. In order to enhance the existing forehead temperature measurement system, further work should be conducted to study and develop an algorithm to estimate CBT from forehead temperature. This enhancement will improve the e-Care system to incorporate a fever detection function for the purpose of early detection of disease or chronic health condition that may requires medical intervention.

The current e-Care Base Station contains interface support for 2G mobile phone communication network and 2G network is in the process being phased out. The Base Station hardware should be modified accordingly to provide interface supports for 3G and 4G mobile phone communication network. The Base Station circuit board size can be further reduced by using smaller electronics components and multi-layer printed circuit board. All the modules of e-Care require ergonomic enclosures so as to render proper protection and to improve on handling experience.

7.2.3 pVoice

pVoice is a wearable device and in the early development stage, pVoice has been designed to incorporate product ergonomics of look and feel. The prototype functions satisfactorily. There are still some product improvements that are worth looking into so as to raise the user's usage experience. The existing low power magnetic acoustic speaker's sound quality can be further improved by

replacing the speaker with a miniature piezo-electric based speaker that offers higher fidelity speech reproduction. The continuous usage time can be improved by replacing the existing Lithium-Ion (Li-Ion) battery with a lighter and much higher capacity Lithium Polymer Ion battery. The current battery charging circuit should be modified to incorporate fast charging function that effectively cuts down the existing charging time.

The present plastic enclosure is of water splash resistance design. Further improvements to the casing design is required to make pVoice into a fully water resistance product suitable for all types of environments and weather conditions.

7.3 Ethical Issues

In Chapters 3 - 6, ethical issues have been identified that required attention to resolve. Chapter 3 contains ethical issue with regards animal testing and humane treatments of animal test subjects. The needs to engage a live animal for the proposed experiments has been justified that no other alternative methods were available to carry out the proposed experiments, and it was neither safe nor ethical to engage a human. Approvals from both the National University of Singapore Institutional Review Board and Institutional Animal Care and Use Committee have been sought prior to the conduct of the proposed experiments involving a live primate. The experiments followed the National Advisory Committee for Laboratory Animal Research (NACLAR) guidelines so as to ensure proper and humane treatments of the primate. Appropriate medical treatments and sufficiently long rest duration was enforced on the primate in-order to allow it to fully recover before being subjected to another round of experiment of the

same nature.

Chapter 4 - 6 contain ethical issues relating to the invasion of privacy and unauthorized data access. The three chapters are pertaining to the developments of the three types of assistive healthcare devices. Each device contains some built-in hardware features that can be potentially abused for unauthorized human activity monitoring, spying and geographical location tracking. The firmware designs for the affected assistive healthcare device have been properly reviewed to include strict data access and processing procedures in-order to prevent the privacy and data access issues from occurring. Users data privacy protection were further enhanced by implementing data encryptions on the three assistive healthcare devices in-order to prevent any form unauthorized data access.

Potential end-users of the assistive healthcare devices were thoroughly briefed on the devices data collection and processing procedures, and written consents were required from the users prior to operating the devices.

7.4 Summary

This thesis presented a practical assistive healthcare framework, and the design and, development and demonstration of three practical assistive healthcare devices based on the proposed framework. The proposed solutions have been demonstrated to perform satisfactorily under various conditions imposed by trial users. It is important to have such a solution in the current situation, where the rapidly aging population is a real concern and access to proper healthcare is unevenly distributed with limited resource settings. This dissertation is a small

step in enabling the communities to have access to such facilities and believed to be in the right direction for optimizing the healthcare resources with innovative use of technology tools while making use of the existing infrastructure.

Bibliography

- [1] Nikita Konstantina S, Lin James C, Fotiadis Dimitrios, and Arredondo Maria T. Editorial: special issue on mobile and wireless technologies for healthcare delivery. *IEEE Transactions on Biomedical Engineering*, 59(11):3083–3089, 2012.
- [2] United Nations. World population ageing. Online, December 2013. ST/ESA/SER.A/348.
- [3] L Normie. Technology for ageing in place. *IFA (International Federation on Ageing) Global ageing*, 7(2):45–53, 2011.
- [4] Aubrey DNJ De Grey. Life span extension research and public debate: societal considerations. *Studies in Ethics, Law, and Technology*, 1, 2007.
- [5] SingStat. Population trends 2015. Online, September 2015.
- [6] Tai Janice and Kay Lim Leslie. Seniors living alone may rise to 83,000 by 2030. Online, April 2012.
- [7] Tai Janice. Old and home alone in singapore. Online, August 2015.
- [8] Tan Theresa. More singaporeans living alone; trend seen rising. Online, March 2014.
- [9] Ann Horgas and Gregory Abowd. The impact of technology on living environments for older adults. 2004.
- [10] Gillian Parker, Padma Bhakta, Savita Katbamna, Caroline Lovett, Suzy Paisley, Stuart Parker, Kay Phelps, Richard Baker, Carol Jagger, James Lindesay, et al. Best place of care for older people after acute and during subacute illness: a systematic review. *Journal of Health Services, Research & Policy*, 5(3):176–189, 2000.
- [11] Frank G Miskelly. Assistive technology in elderly care. *Age and ageing*, 30(6):455–458, 2001.
- [12] Martha E Pollack. Intelligent technology for an aging population: The use of ai to assist elders with cognitive impairment. *AI Magazine*, 26(2):9, 2005.
- [13] Anthea Tinker and Peter Lansley. Introducing assistive technology into the existing homes of older people: feasibility, acceptability, costs and outcomes. *Journal of Telemedicine and Telecare*, 11(suppl 1):1–3, 2005.

- [14] Harkness Lorrie. Assistive technology: An essential component of health care reform. Online, 2011.
- [15] Alan Walker. Active ageing in employment: Its meaning and potential. *Asia-Pacific Review*, 13(1):78–93, 2006.
- [16] Basma M Mohammad El-Basioni, Sherine Mohamed Abd El-Kader, and Hussein S Eissa. Independent living for persons with disabilities and elderly people using smart home technology. *International Journal of Application or Innovation in Engineering & Management (IJAIEEM)*, 2014.
- [17] Dana P Goldman, Paul G Shekelle, Jayanta Bhattacharya, Michael Hurd, and Geoffrey F Joyce. Health status and medical treatment of the future elderly. 2004.
- [18] Shyamal Patel, Hyung Park, Paolo Bonato, Leighton Chan, and Mary Rodgers. A review of wearable sensors and systems with application in rehabilitation. *Journal of neuroengineering and rehabilitation*, 9(1):1, 2012.
- [19] Xiao Tan, Xianxiang Chen, Xinyu Hu, Ren Ren, Bing Zhou, Zhen Fang, and Shanhong Xia. Emd-based electrocardiogram delineation for a wearable low-power ecg monitoring device. *Canadian Journal of Electrical and Computer Engineering*, 37(4):212–221, 2014 Fall.
- [20] Elisa Spano, Stefano Di Pascoli, and Giuseppe Iannaccone. Low-power wearable ecg monitoring system for multiple-patient remote monitoring. 2015.
- [21] Phillip A Shaltis, Andrew Reisner, and H Harry Asada. Wearable, cuff-less ppg-based blood pressure monitor with novel height sensor. In *Engineering in Medicine and Biology Society, 2006. EMBS06. 28th Annual International Conference of the IEEE*, pages 908–911. IEEE, 2006.
- [22] H Harry Asada, Phillip Shaltis, Andrew Reisner, Sokwoo Rhee, and Reginald C Hutchinson. Mobile monitoring with wearable photoplethysmographic biosensors. *Engineering in Medicine and Biology Magazine, IEEE*, 22(3):28–40, 2003.
- [23] Phil Corbishley and Esther Rodriguez-Villegas. Breathing detection: towards a miniaturized, wearable, battery-operated monitoring system. *Biomedical Engineering, IEEE Transactions on*, 55(1):196–204, 2008.
- [24] Miikka Ermes, Juha Parkka, Jani Mantyjarvi, and Ilkka Korhonen. Detection of daily activities and sports with wearable sensors in controlled and uncontrolled conditions. *Information Technology in Biomedicine, IEEE Transactions on*, 12(1):20–26, 2008.
- [25] James AC Patterson, Douglas G McIlwraith, and Guang-Zhong Yang. A flexible, low noise reflective ppg sensor platform for ear-worn heart rate monitoring. pages 286–291, 2009.
- [26] Yong-Sheng Yan and Yuan-Ting Zhang. An efficient motion-resistant method for wearable pulse oximeter. *Information Technology in Biomedicine, IEEE Transactions on*, 12(3):399–405, 2008.

- [27] Levi Benjamin Wood and H Harry Asada. Low variance adaptive filter for cancelling motion artifact in wearable photoplethysmogram sensor signals. In *Engineering in Medicine and Biology Society, 2007. EMBS 2007. 29th Annual International Conference of the IEEE*, pages 652–655. IEEE, 2007.
- [28] Antonio Lanatà, Enzo Pasquale Scilingo, Elena Nardini, Giannicola Loriga, Rita Paradiso, and Danilo De-Rossi. Comparative evaluation of susceptibility to motion artifact in different wearable systems for monitoring respiratory rate. *Information Technology in Biomedicine, IEEE Transactions on*, 14(2):378–386, 2010.
- [29] R Soniyapriyadarshini. Case study on smart wearable sensors and systems with application in rehabilitation. *International Journal of Scientific & Engineering Research*, 4(5), 2013.
- [30] Toshio Nakano, Emi Koyama, Toshiyuki Nakamura, Takeo Ito, Koji Tamura, and Masaaki Yaginuma. Use of an infrared sensor system to take long term bedside measurements of rest activity patterns in the elderly with dementia. *Psychiatry and clinical neurosciences*, 56(3):287–288, 2002.
- [31] E Campo and M Chan. Detecting abnormal behaviour by real-time monitoring of patients. In *Proceedings of the AAAI-02 Workshop Automation as Caregiver*, pages 8–12, 2002.
- [32] Kyoko Makimoto, Eun Ah Lee, Younhee Kang, Miyae Yamakawa, Nobuyuki Ashida, and Kyung Rim Shin. Temporal patterns of movements in institutionalized elderly with dementia during 12 consecutive days of observation in seoul, korea. *American journal of Alzheimer’s disease and other dementias*, 2008.
- [33] Motoki Miura, Sadanori Ito, Ryoza Takatsuka, and Susumu Kunifuji. Aware group home enhanced by rfid technology. In *International Conference on Knowledge-Based and Intelligent Information and Engineering Systems*, pages 847–854. Springer, 2008.
- [34] Toshio Hori, Yoshifumi Nishida, Hiroshi Aizawa, Shin’ichi Murakami, and Hiroshi Mizoguchi. Sensor network for supporting elderly care home. In *Sensors, 2004. Proceedings of IEEE*, pages 575–578. IEEE, 2004.
- [35] Yvonne Schikhof and Ingrid Mulder. *Under watch and ward at night: design and evaluation of a remote monitoring system for dementia care*. Springer, 2008.
- [36] Anthony Wood, Gilles Virone, Thao Doan, Quihua Cao, Leo Selavo, Yafeng Wu, L Fang, Zhimin He, Shan Lin, and Jack Stankovic. Alarmnet: Wireless sensor networks for assisted-living and residential monitoring. *University of Virginia Computer Science Department Technical Report*, 2, 2006.
- [37] Michael J McGrath and Cliodhna N Scanail. Body-worn, ambient, and consumer sensing for health applications. In *Sensor Technologies*, pages 181–216. Springer, 2013.

- [38] Daniele Giansanti, Giovanni Maccioni, and Sandra Morelli. An experience of health technology assessment in new models of care for subjects with parkinsons disease by means of a new wearable device. *TELEMEDICINE and e-HEALTH*, 14(5):467–472, 2008.
- [39] Edward S Sazonov, George Fulk, Nadezhda Sazonova, and Stephanie Schuckers. Automatic recognition of postures and activities in stroke patients. In *Engineering in Medicine and Biology Society, 2009. EMBC 2009. Annual International Conference of the IEEE*, pages 2200–2203. IEEE, 2009.
- [40] Omer Aziz, L Atallah, B Lo, M ElHelw, L Wang, Guang-Zhong Yang, and A Darzi. A pervasive body sensor network for measuring postoperative recovery at home. *Surgical innovation*, 14(2):83–90, 2007.
- [41] Oliver Amft and Gerhard Tröster. Recognition of dietary activity events using on-body sensors. *Artificial intelligence in medicine*, 42(2):121–136, 2008.
- [42] Oliver Amft, Martin Kusserow, and G Troster. Bite weight prediction from acoustic recognition of chewing. *Biomedical Engineering, IEEE Transactions on*, 56(6):1663–1672, 2009.
- [43] Maria Grazia Benedetti, Annalisa Di Gioia, Linda Conti, Lisa Berti, Degli Linda Esposti, Giulietta Tarrini, Nazario Melchionda, and Sandro Giannini. Physical activity monitoring in obese people in the real life environment. *Journal of neuroengineering and rehabilitation*, 6(1):1, 2009.
- [44] Edward S Sazonov, Stephanie AC Schuckers, Paulo Lopez-Meyer, Oleksandr Makeyev, Edward L Melanson, Michael R Neuman, and James O Hill. Toward objective monitoring of ingestive behavior in free-living population. *Obesity*, 17(10):1971–1975, 2009.
- [45] Anthony Dalton, Shyamal Patel, AC Roy, Matt Welsh, Trudy Pang, Steven Schachter, Gearóid ÓLaighin, and Paolo Bonato. Detecting epileptic seizures using wearable sensor technologies. *Book Detecting epileptic seizures using wearable sensor technologies*, pages 73–74, 2010.
- [46] Uri Kramer, Svetlana Kipervasser, Arie Shlitner, and Ruben Kuzniecky. A novel portable seizure detection alarm system: preliminary results. *Journal of Clinical Neurophysiology*, 28(1):36–38, 2011.
- [47] Surabhi Patel, Chiara Mancinelli, Anthony Dalton, Ben Patritti, Trudy Pang, Steven Schachter, and Paolo Bonato. Detecting epileptic seizures using wearable sensors. In *Bioengineering Conference, 2009 IEEE 35th Annual Northeast*, pages 1–2. IEEE, 2009.
- [48] Ming-Zher Poh, Tobias Loddenkemper, Nicholas C Swenson, Shubhi Goyal, Joseph R Madsen, and Rosalind W Picard. Continuous monitoring of electrodermal activity during epileptic seizures using a wearable sensor. In *Engineering in Medicine and Biology Society (EMBC), 2010 Annual International Conference of the IEEE*, pages 4415–4418. IEEE, 2010.

- [49] Louise McCallum and Dan Higgins. Measuring body temperature. *Nursing times*, 108(45):20–22, 2011.
- [50] Michael F Bergeron, Melissa D Laird, Elaina L Marinik, Joel S Brenner, and Jennifer L Waller. Repeated-bout exercise in the heat in young athletes: physiological strain and perceptual responses. *Journal of Applied Physiology*, 106(2):476–485, 2009.
- [51] Brian Smalley, Robin M Janke, and David Cole. Exertional heat illness in air force basic military trainees. *Military medicine*, 168(4):298, 2003.
- [52] FJ Maxton, L Justin, and D Gillies. Estimating core temperature in infants and children after cardiac surgery: a comparison of six methods. *J Adv Nurs*, 45(2):214–222, 2004.
- [53] J Shin, J Kim, K Song, and Y Kwak. Core temperature measurement in therapeutic hypothermia according to different phases: comparison of bladder, rectal, and tympanic versus pulmonary artery methods. *Resuscitation*, 84(6):810–817, 2013.
- [54] S Sarkar, SM Donn, I Bhagat, RE Dechert, and JD Barks. Esophageal and rectal temperatures as estimates of core temperature during therapeutic whole-body hypothermia. *The Journal of pediatrics*, 162(1):208–210, 2013.
- [55] OR Eyelade, AE Orimadegun, OA Akinyemi, OO Tongo, and OO Akinyinka. Esophageal, tympanic, rectal, and skin temperatures in children undergoing surgery with general anesthesia. *J Perianesth Nurs*, 26(3):151–159, 2011.
- [56] Kirsten KB Peetoom, Monique AS Lexis, Manuela Joore, Carmen D Dirksen, and Luc P De Witte. Literature review on monitoring technologies and their outcomes in independently living elderly people. *Disability and Rehabilitation: Assistive Technology*, 10(4):271–294, 2015.
- [57] BG Celler, W Earnshaw, ED Ilsar, L Betbeder-Matibet, MF Harris, R Clark, T Hesketh, and NH Lovell. Remote monitoring of health status of the elderly at home. a multidisciplinary project on aging at the university of new south wales. *International journal of bio-medical computing*, 40(2):147–155, 1995.
- [58] Nancy R Milloy. Management of adult speech disorders ii. In *Breakdown of Speech*, pages 123–141. Springer, 1991.
- [59] Hanjun Liu and Manwa L Ng. Electrolarynx in voice rehabilitation. *Auris Nasus Larynx*, 34(3):327–332, 2007.
- [60] Wootton Richard. *Telehealth in the developing world*. IDRC, 2009.
- [61] ICT Data and Statistics Division. Ict facts and figures. Online, May 2015.
- [62] Renesas. R178/g13 renesas mcu datasheet. Online, March 2016.
- [63] Microchip. Microchip dspic33epxxx datasheet. Online, March 2012.

- [64] Sewook Jung, Alexander Chang, and Mario Gerla. Comparisons of zigbee personal area network (pan) interconnection methods. In *2007 4th International Symposium on Wireless Communication Systems*, pages 337–341. IEEE, 2007.
- [65] Dae-Man Han and Jae-Hyun Lim. Smart home energy management system using ieee 802.15. 4 and zigbee. *IEEE Transactions on Consumer Electronics*, 56(3):1403–1410, 2010.
- [66] Telegesis. Etrx35x zigbee modules product manual. Online, June 2015.
- [67] Melexis. Melexis mlx90620 16x4 ir array datasheet. Online, June 2012.
- [68] Sujay Narayana, R Venkatesha Prasad, Vijay S Rao, Tamma V Prabhakar, Sripad S Kowshik, and Madhuri Sheethala Iyer. Pir sensors: characterization and novel localization technique. In *Proceedings of the 14th International Conference on Information Processing in Sensor Networks*, pages 142–153. ACM, 2015.
- [69] WH Chen and HP Ma. A fall detection system based on infrared array sensors with tracking capability for the elderly at home. *2015 17th International Conference on E-health Networking, Application Services (HealthCom)*, 2015.
- [70] Sinan Kockara, Tansel Halic, Cody Hudson, Alex Loney, and Aaron Crawford. Portable malignant lesion detection with low cost mobile infrared thermography. *Innovations in Technology Conference (InnoTek), 2014 IEEE*, pages 1–5, 2014.
- [71] M Vesely, A Cieszczyk, and Y Zhao. Low cost infrared array as a thermal comfort sensor. *CISBAT 2015 Future*, 2015.
- [72] Michael Vollmer and Klaus-Peter Mollmann. *Infrared thermal imaging: fundamentals, research and applications*. John Wiley & Sons, 2010.
- [73] Parallax. Parallax pir sensor (555-28027) datasheet. Online, March 2014.
- [74] Tamara L Hayes, Francena Abendroth, Andre Adami, Misha Pavel, Tracy A Zitzelberger, and Jeffrey A Kaye. Unobtrusive assessment of activity patterns associated with mild cognitive impairment. *Alzheimer's & Dementia*, 4(6):395–405, 2008.
- [75] Beth Logan, Jennifer Healey, Matthai Philipose, Emmanuel Munguia Tapia, and Stephen Intille. A long-term evaluation of sensing modalities for activity recognition. In *International conference on Ubiquitous computing*, pages 483–500. Springer, 2007.
- [76] Dimitrios Lymberopoulos, Thiago Teixeira, and Andreas Savvides. Macroscopic human behavior interpretation using distributed imager and other sensors. *Proceedings of the IEEE*, 96(10):1657–1677, 2008.
- [77] Vince Stanford. Using pervasive computing to deliver elder care. *IEEE Pervasive computing*, 1:10–13, 2002.

- [78] Ning Jia. Fall detection application by using 3-axis accelerometer adxl345. *Analog Devices, Application Note*, 1023, 2012.
- [79] Yuan Xi, Chen Dong, Tian Xiang, and LV Jing. Three-axis digital accelerometer adxl345 and its application in sins design [j]. *Electronic Design Engineering*, 3:058, 2010.
- [80] Analog Devices. Adxl345 3-axis digital accelerometer datasheet. Online, June 2015.
- [81] Majd Alwan, Prabhu Jude Rajendran, Steve Kell, David Mack, Siddharth Dalal, Matt Wolfe, and Robin Felder. A smart and passive floor-vibration based fall detector for elderly. *2006 2nd International Conference on Information & Communication Technologies*, 1:1003–1007, 2006.
- [82] Mary Presciutti, Mary Kay Bader, and Millie Hepburn. Shivering management during therapeutic temperature modulation: nurses’ perspective. *Critical care nurse*, 32(1):33–42, 2012.
- [83] Daniel I Sessler. Temperature monitoring and perioperative thermoregulation. *Anesthesiology*, 109(2):318, 2008.
- [84] K Lattavo, J Britt, and M Dobal. Agreement between measures of pulmonary artery and tympanic temperatures. *Res Nurs Health*, 18(4):365–370, 1995.
- [85] Barbara J Holtzclaw. Monitoring body temperature. *AACN Advanced Critical Care*, 4(1):44–55, 1993.
- [86] Danica Krizanac, Peter Stratil, David Hoerburger, Christoph Testori, Christian Wallmueller, Andreas Schober, Moritz Haugk, Maria Haller, Wilhelm Behringer, and Harald Herkner. Femoro-iliacal artery versus pulmonary artery core temperature measurement during therapeutic hypothermia: an observational study. *Resuscitation*, 84(6):805–809, 2013.
- [87] P Fulbrook. Core body temperature measurement: a comparison of axilla, tympanic membrane and pulmonary artery blood temperature. *Intensive and Critical Care Nursing*, 13(5):266–272, 1997.
- [88] WI Cranston, J Gerbrandy, and ES Snell. Oral, rectal and oesophageal temperatures and some factors affecting them in man. *The Journal of physiology*, 126(2):347–358, 1954.
- [89] JL Robinson, RF Seal, DW Spady, and MR Joffres. Comparison of esophageal, rectal, axillary, bladder, tympanic, and pulmonary artery temperatures in children. *The Journal of pediatrics*, 133(4):553–556, 1998.
- [90] J Robinson, J Charlton, R Seal, D Spady, and MR Joffres. Oesophageal, rectal, axillary, tympanic and pulmonary artery temperatures during cardiac surgery. *Canadian journal of anaesthesia*, 45(4):317–323, 1998.

- [91] R Huggins, N Glaviano, N Negishi, DJ Casa, and J Hertel. Comparison of rectal and aural core body temperature thermometry in hyperthermic, exercising individuals: a meta-analysis. *Journal of athletic training*, 47(3):329–338, 2012.
- [92] T Akata, K Yamaura, T Kandabashi, S Sadamatsu, and S Takahashi. Changes in body temperature during profound hypothermic cardiopulmonary bypass in adult patients undergoing aortic arch reconstruction. *Journal of anesthesia*, 18(2):73–81, 2004.
- [93] RN Roth, VP Verdile, LJ Grollman, and DA Stone. Agreement between rectal and tympanic membrane temperatures in marathon runners. *Annals of emergency medicine*, 28(4):414–417, 1996.
- [94] Christopher Byrne and Chin Leong Lim. The ingestible telemetric body core temperature sensor: a review of validity and exercise applications. *British journal of sports medicine*, 41(3):126–133, 2007.
- [95] Chris Easton, Barry W. Fudge, and Yannis P. Pitsiladis. Rectal, telemetry pill and tympanic membrane thermometry during exercise heat stress. *Journal of Thermal Biology*, 32(2):78–86, 2007.
- [96] LPJ Teunissen, A de Haan, JJ de Koning, and HAM Daanen. Telemetry pill versus rectal and esophageal temperature during extreme rates of exercise-induced core temperature change. *Physiological measurement*, 33(6):915, 2012.
- [97] C Byrne, JK Lee, SA Chew, CL Lim, and EY Tan. Continuous thermoregulatory responses to mass-participation distance running in heat. *Medicine and science in sports and exercise*, 38(5):803–810, 2006.
- [98] Catherine O’Brien, Reed W Hoyt, Mark J Buller, John W Castellani, and Andrew J Young. Telemetry pill measurement of core temperature in humans during active heating and cooling. *Medicine and science in sports and exercise*, 30:468–472, 1998.
- [99] TH Benzinger. On physical heat regulation and the sense of temperature in man. *Proceedings of the National Academy of Sciences of the United States of America*, 45(4):645, 1959.
- [100] TH Benzinger. Clinical temperature. new physiological basis. *JAMA*, 209(8):1200–1206, 1969.
- [101] Theodor H Benzinger. Heat regulation: homeostasis of central temperature in man. *Physiological Reviews*, 49(4):671–759, 1969.
- [102] TV McCaffrey, RD McCook, and RD Wurster. Effect of head skin temperature on tympanic and oral temperature in man. *Journal of Applied Physiology*, 39(1):114–118, 1975.
- [103] B Nielsen. Natural cooling of the brain during outdoor bicycling? *Pflügers Archiv*, 411(4):456–461, 1988.

- [104] Heiner Brinzel and Michel Cabanac. Tympanic temperature is a core temperature in humans. *Journal of Thermal Biology*, 14(1):47–53, 1989.
- [105] KT Sato, NL Kane, G Soos, CV Gisolfi, N Kondo, and K Sato. Reexamination of tympanic membrane temperature as a core temperature. *Journal of Applied Physiology*, 80(4):1233–1239, 1996.
- [106] Salah Mansour, Jacques Magnan, Hassan Haidar, Karen Nicolas, and Stéphane Louryan. *Comprehensive and Clinical Anatomy of the Middle Ear*. Springer, 2013.
- [107] Linda Brodsky, Patrick Brookhauser, David Chait, James Reilly, Ellen Deutsch, Stephen Cook, Milton Waner, Steven Shaha, and Eric Nauenberg. Office-based insertion of pressure equalization tubes: The role of laser-assisted tympanic membrane fenestration. *The Laryngoscope*, 109(12):2009–2014, 1999.
- [108] Erik James Shahoian. System and method for the simultaneous automated bilateral delivery of pressure equalization tubes. 2014.
- [109] Salah Mansour, Jacques Magnan, Hassan Haidar, Karen Nicolas, and Stéphane Louryan. *Comprehensive and Clinical Anatomy of the Middle Ear*. Springer, 2013.
- [110] Sam Van der Jeught, Joris JJ Dirckx, Johan RM Aerts, Adrian Bradu, Adrian Gh Podoleanu, and Jan AN Buytaert. Full-field thickness distribution of human tympanic membrane obtained with optical coherence tomography. *Journal of the Association for Research in Otolaryngology*, 14(4):483–494, 2013.
- [111] CV Gisolfi, K Sato, PT Wall, and F Sato. In vivo and in vitro characteristics of eccrine sweating in patas and rhesus monkeys. *Journal of Applied Physiology*, 53(2):425–431, 1982.
- [112] GS Johnson and RS Elizondo. Eccrine sweat gland in macaca mulatta: physiology, histochemistry, and distribution. *Journal of applied physiology*, 37(6):814–820, 1974.
- [113] GS Johnson and RS Elizondo. Thermoregulation in mwcscr: mulatta: a thermal balance study. *Journal of applied physiology*, 1979.
- [114] IR Oddershede and RS Elizondo. Body fluid and hematologic adjustments during resting heat acclimation in rhesus monkey. *Journal of Applied Physiology*, 49(3):431–437, 1980.
- [115] CC Barney and RS Elizondo. Prostaglandins and temperature regulation in the rhesus monkey. *Journal of Applied Physiology*, 50(6):1248–1254, 1981.
- [116] CV Gisolfi, PT Wall, and WR Mitchell. Thermoregulatory responses to central injections of excess calcium in monkeys. *American Journal of Physiology-Regulatory, Integrative and Comparative Physiology*, 245(1):R76–R82, 1983.

- [117] RD Myers, CV Gisolfi, and F Mora. Role of brain ca^{2+} in central control of body temperature during exercise in the monkey. *Journal of Applied Physiology*, 43(4):689–694, 1977.
- [118] Sune Bergstrom, Lars A Carlson, and James R Weeks. The prostaglandins: a family of biologically active lipids. *Pharmacological reviews*, 20(1):1–48, 1968.
- [119] Cristine L Heaps and Stefan H Constable. The metabolic and thermoregulatory responses of rhesus monkeys to combined exercise and environmental heat load. *DTIC Document*, 1993.
- [120] Stefan H Constable, Clifford J Sherry, and Thomas J Walters. An applied model for the evaluation of multiple physiological stressors. *Neuroscience & Biobehavioral Reviews*, 15(1):115–121, 1991.
- [121] José González-Alonso. Human thermoregulation and the cardiovascular system. *Experimental physiology*, 97(3):340–346, 2012.
- [122] GP Kenny and AD Flouris. 13 - the human thermoregulatory system and its response to thermal stress. pages 319–365. Woodhead Publishing, 2014.
- [123] AP Gagge. An effective temperature scale based on a simple model of human physiological regulatory response. *Ashrae Trans.*, 77:247–262, 1971.
- [124] Robert C Eberhart and Avraham Shitzer. *Heat Transfer in Medicine and Biology: Analysis and Applications*, volume 2. Springer Science Business Media, 2012.
- [125] Robert J Roselli and Kenneth R Diller. *Biotransport: principles and applications*. Springer Science Business Media, 2011.
- [126] M Necati Ozisik. *Heat conduction*. John Wiley Sons, 1993.
- [127] A. Pharo Gagge and Yasunobu Nishi. Heat exchange between human skin surface and thermal environment. In *Comprehensive Physiology*. John Wiley Sons, Inc., 2011.
- [128] Francis J. Ring E., Hartmann Jurgen, Ammer Kurt, Thomas Rod, L David, and Jeff W. Hand and. Chapter 7 - infrared and microwave medical thermometry. In Benjamin K. Tsai Zhuomin, M. Zhang and Machin Graham, editors, *Radiometric Temperature Measurements: II. Applications*, volume 43, pages 393–448. Academic Press, 2010.
- [129] AF Robertson and Daniel Gross. An electrical-analog method for transient heat-flow analysis. *Journal of Research of the National Bureau of Standards*, 61(2):105–115, 1958.
- [130] Q Chen, RH Fu, and YC Xu. Electrical circuit analogy for heat transfer analysis and optimization in heat exchanger networks. *Applied Energy*, 139:81–92, 2015.
- [131] Hisatake Sato. Moving average filter. 2001.

- [132] Hu Song, Jiang Xiao-Wei, and Yang Guang. Using of moving average filter in faint pulse signal detection [j]. *Computer & Digital Engineering*, 10:057, 2007.
- [133] Richard J Oliver, Paul M Embree, and Casper William Barnes. Variable-length moving-average filter. 2000.
- [134] SM am Shahruz and S Behtash. Design of controllers for linear parameter-varying systems by the gain scheduling technique. In *Decision and Control, 1990., Proceedings of the 29th IEEE Conference on*, pages 2490–2491. IEEE, 1990.
- [135] Douglas J Leith and William E Leithead. Survey of gain-scheduling analysis and design. *International journal of control*, 73(11):1001–1025, 2000.
- [136] Wilson J Rugh. Analytical framework for gain scheduling. In *American Control Conference*, pages 1688–1694, 1990.
- [137] Douglas A Lawrence and Wilson J Rugh. Gain scheduling dynamic linear controllers for a nonlinear plant. *Automatica*, 31(3):381–390, 1995.
- [138] Pierre Apkarian and Richard J Adams. Advanced gain-scheduling techniques for uncertain systems. *Control Systems Technology, IEEE Transactions on*, 6(1):21–32, 1998.
- [139] Michael B Maron, Jeames A Wagner, and SM Horvath. Thermoregulatory responses during competitive marathon running. *Journal of Applied Physiology*, 42(6):909–914, 1977.
- [140] Michael N Sawka, C Bruce Wenger, and Kent B Pandolf. Thermoregulatory responses to acute exercise heat stress and heat acclimation. *Comprehensive physiology*, 2011.
- [141] Colm Mc Caffrey, Olivier Chevalerias, Cian O Mathuna, and Karen Twomey. Swallowable-capsule technology. *Pervasive computing, IEEE*, 7(1):23–29, 2008.
- [142] Birgit K van Staaij, Maroeska M Rovers, Anne G Schilder, and Arno W Hoes. Accuracy and feasibility of daily infrared tympanic membrane temperature measurements in the identification of fever in children. *International journal of pediatric otorhinolaryngology*, 67(10):1091–1097, 2003.
- [143] T Yamakoshi, K Matsumura, P Rolfe, N Tanaka, Y Yamakoshi, and K Takahashi. A novel method to detect heat illness under severe conditions by monitoring tympanic temperature. *Aviation, space, and environmental medicine*, 84(7):692–700, 2013.
- [144] Jacob Fraden. The development of thermoscan® instant thermometer. *Clinical pediatrics*, 30(4 suppl):11–12, 1991.
- [145] Peter Hegen. Continuous measurements of core body temperature using body sensor networks. 2012.

- [146] Mirza Mansoor Baig and H GholamHosseini. Wireless remote patient monitoring in older adults. In *Engineering in Medicine and Biology Society (EMBC), 2013 35th Annual International Conference of the IEEE*, pages 2429–2432. IEEE, 2013.
- [147] Kanako Ono, Kotaro Yamasue, Osamu Tochikubo, Yasuo Terauchi, and Shunsaku Mizushima. Lifestyle monitoring with the use of an earphone-type thermometer, an ambulatory blood pressure monitoring and a new wristwatch-type pulsimeter with accelerometer. *Clinical and Experimental Hypertension*, 36(2):97–102, 2014.
- [148] Jose A Hidalgo, Alejandro Cajiao, Claudia M Hernández, Diego M López, and Víctor M Quintero. Visignet: a wireless body area network with cloud data storage for the telemonitoring of vital signs. *Health and Technology*, 5(2):115–126, 2015.
- [149] Jason KW Lee, Amanda QX Nio, Chin Leong Lim, Eunice YN Teo, and Christopher Byrne. Thermoregulation, pacing and fluid balance during mass participation distance running in a warm and humid environment. *European journal of Applied Physiology*, 109(5):887–898, 2010.
- [150] Alexander G Dean and James M Conrad. *Creating Fast, Responsive and Energy-Efficient Embedded Systems using the Renesas RL78 Microcontroller*. Micrium Press, 2012.
- [151] Luc W Adriaenssens and Stewart Findlater. Infrared sensor array based temperature monitoring systems for data centers and related methods. 2014.
- [152] S. Sruthi and M. Sasikala. A low cost thermal imaging system for medical diagnostic applications. In *Smart Technologies and Management for Computing, Communication, Controls, Energy and Materials (ICSTM), 2015 International Conference on*, pages 621–623, May 2015.
- [153] S Sandhya and KA Sumithra Devi. Analysis of bluetooth threats and v4.0 security features. *2012 International Conference on Computing, Communication and Applications*, pages 1–4, 2012.
- [154] JS Lee, YW Su, and CC Shen. A comparative study of wireless protocols: Bluetooth, uwb, zigbee, and wi-fi. *Industrial Electronics Society, 2007. IECON 2007. 33rd Annual Conference of the IEEE*, pages 46–51, 2007.
- [155] Lei Wang, Guang-Zhong Yang, Jin Huang, Jinyong Zhang, Li Yu, Zedong Nie, and David RS Cumming. A wireless biomedical signal interface system-on-chip for body sensor networks. *Biomedical Circuits and Systems, IEEE Transactions on*, 4(2):112–117, 2010.
- [156] Keijo MJ Haataja and Konstantin Hypponen. Man-in-the-middle attacks on bluetooth: a comparative analysis, a novel attack, and countermeasures. *Communications, Control and Signal Processing, 2008. ISCCSP 2008. 3rd International Symposium on*, pages 1096–1102, 2008.

- [157] Keijo Haataja and Pekka Toivanen. Practical man-in-the-middle attacks against bluetooth secure simple pairing. *2008 4th International Conference on Wireless Communications, Networking and Mobile Computing*, pages 1–5, 2008.
- [158] Tan Hwee Pink. Integrated approach to ageing in place. Online, January 2016.
- [159] Yeo Sam Jo. Hdb elderly alert system well-received in test-bed. Online, March 2015.
- [160] Lim Benjamin. Putting her mind at ease. Online, April 2014.
- [161] Andrew Sixsmith, Nick Hine, Ian Neild, Nick Clarke, Steve Brown, and Paul Garner. Monitoring the well-being of older people. *Topics in Geriatric Rehabilitation*, 23(1):9–23, 2007.
- [162] Anthony P Glascock and David M Kutzik. The impact of behavioral monitoring technology on the provision of health care in the home. *J. UCS*, 12(1):59–79, 2006.
- [163] Jacob Fraden. *Handbook of modern sensors: physics, designs, and applications*. Springer Science & Business Media, 2004.
- [164] M Moghavvemi and Lu Chin Seng. Pyroelectric infrared sensor for intruder detection. In *TENCON 2004. 2004 IEEE Region 10 Conference*, volume 500, pages 656–659. IEEE, 2004.
- [165] Byunghun Song, Haksoo Choi, and Hyung Su Lee. Surveillance tracking system using passive infrared motion sensors in wireless sensor network. In *2008 International Conference on Information Networking*, pages 1–5. IEEE, 2008.
- [166] X Guo, DK Tiller, GP Henze, and CE Waters. The performance of occupancy-based lighting control systems: A review. *Lighting Research and Technology*, 42(4):415–431, 2010.
- [167] Yanbo Zhao and Zhaohui Ye. A low cost gsm/gprs based wireless home security system. *IEEE Transactions on Consumer Electronics*, 54(2):567–572, 2008.
- [168] JM Regan, DJ Macfarlane, and NAS Taylor. An evaluation of the role of skin temperature during heat adaptation. *Acta physiologica scandinavica*, 158(4):365–375, 1996.
- [169] Charlie Huizenga, Hui Zhang, Edward Arens, and Danni Wang. Skin and core temperature response to partial-and whole-body heating and cooling. *Journal of Thermal Biology*, 29(7):549–558, 2004.
- [170] Philip Lieberman. The evolution of human speech. *Current Anthropology*, 48(1):39–66, 2007.
- [171] D O’Shaughnessy. Speech production and acoustic phonetics. pages 35–107, 2009.

- [172] J Deller, J Hansen, and J Proakis. Fundamentals of speech science. pages 99–150, 2009.
- [173] Brendan T Finucane, Ban CH Tsui, and Albert H Santora. Anatomy of the airway principles of airway management. pages 1–25. Springer, 2010.
- [174] Patrick J Doyle, Edwin C Everts, and Robert E Brummett. Treatment of recurrent laryngeal nerve injury. *Archives of Surgery*, 96(4):517–520, 1968.
- [175] Lucian Sulica, Anthony Cultrara, and Andrew Blitzer. Vocal fold paralysis: Causes, outcomes, and clinical aspects. In *Vocal fold paralysis*, pages 33–54. Springer, 2006.
- [176] Victor R Preedy and Ronald Ross Watson. *Handbook of disease burdens and quality of life measures*. Springer New York, 2010.
- [177] Mark Nolan, Brian Madden, and Edward Burke. Accelerometer based measurement for the mapping of neck surface vibrations during vocalized speech. In *Engineering in Medicine and Biology Society, 2009. EMBC 2009. Annual International Conference of the IEEE*, pages 4453–4456. IEEE, 2009.
- [178] John Hardwick, Chang D Yoo, and Jae S Lim. Speech enhancement using the dual excitation speech model. In *Acoustics, Speech, and Signal Processing, 1993. ICASSP-93., 1993 IEEE International Conference on*, volume 2, pages 367–370. IEEE, 1993.
- [179] A Shamsoddini and PN Denbigh. Enhancement of speech by suppression of interference. In *Signal Processing, 1996., 3rd International Conference on*, volume 1, pages 753–756. IEEE, 1996.
- [180] Bernard Widrow and Michel Bilello. Adaptive inverse control. In *Intelligent Control, 1993., Proceedings of the 1993 IEEE International Symposium on*, pages 1–6. IEEE, 1993.
- [181] John C Burgess. Active adaptive sound control in a duct: A computer simulation. *The Journal of the Acoustical Society of America*, 70(3):715–726, 1981.
- [182] LJ Eriksson. Recursive algorithms for active noise control. In *Proc. Int. Symp. Active Control of Sound Vibration*, pages 137–146, 1991.
- [183] Sen M Kuo and Dennis R Morgan. Active noise control: a tutorial review. *Proceedings of the IEEE*, 87(6):943–973, 1999.
- [184] Jacob Benesty, Yiteng Arden Huang, and Jingdong Chen. Wiener and adaptive filters. In *Handbook of Speech Processing*, pages 103–120. Springer, 2008.
- [185] Juan Manuel Górriz, Javier Ramírez, S Cruces-Alvarez, Carlos G Puntonet, Elmar W Lang, and Deniz Erdogmus. A novel lms algorithm applied to adaptive noise cancellation. *Signal Processing Letters, IEEE*, 16(1):34–37, 2009.

- [186] BV Harsha. A noise robust speech activity detection algorithm. In *Intelligent Multimedia, Video and Speech Processing, 2004. Proceedings of 2004 International Symposium on*, pages 322–325. IEEE, 2004.
- [187] Siew Wen Chin, Kah Phooi Seng, Li-Minn Ang, and King Hann Lim. Improved voice activity detection for speech recognition system. In *Computer Symposium (ICS), 2010 International*, pages 518–523. IEEE, 2010.
- [188] Engin Erzin. Improving throat microphone speech recognition by joint analysis of throat and acoustic microphone recordings. *Audio, Speech, and Language Processing, IEEE Transactions on*, 17(7):1316–1324, 2009.
- [189] Douglas O’Shaughnessy. Linear predictive coding. *Potentials, IEEE*, 7(1):29–32, 1988.
- [190] Robert Vich, Jiri Pribil, and Z Smekan. New cepstral zero-pole vocal tract models for tts synthesis. In *EUROCON’2001, Trends in Communications, International Conference on.*, volume 2, pages 459–462. IEEE, 2001.
- [191] Paul Milenkovic. Glottal inverse filtering by joint estimation of an ar system with a linear input model. *Acoustics, Speech and Signal Processing, IEEE Transactions on*, 34(1):28–42, 1986.
- [192] Paavo Alku and Unto K Laine. A new glottal lpc method for voice coding and inverse filtering. In *Circuits and Systems, 1989., IEEE International Symposium on*, pages 1831–1834. IEEE, 1989.
- [193] Ying Cui and Kunio Takaya. Recognition of phonemes in a continuous speech stream by means of parcor parameter in lpc vocoder. In *Electrical and Computer Engineering, 2007. CCECE 2007. Canadian Conference on*, pages 1606–1609. IEEE, 2007.
- [194] Rizwan Ishaq and Begona Garcia Zapiain. Adaptive gain equalizer for improvement of esophageal speech. In *Signal Processing and Information Technology (ISSPIT), 2012 IEEE International Symposium on*, pages 000153–000157. IEEE, 2012.
- [195] Yao Tianren, Xiang Juanjuan, and Lu Wei. The computation of line spectral frequency using the second chebyshev polynomials. In *Signal Processing, 2002 6th International Conference on*, volume 1, pages 190–192. IEEE, 2002.
- [196] Ahmad Ali, Safiullah Bhatti, and Muhammad Sleem Mian. Formants based analysis for speech recognition. In *Engineering of Intelligent Systems, 2006 IEEE International Conference on*, pages 1–3. IEEE, 2006.
- [197] Qin Yan and Saeed Vaseghi. Analysis, modelling and synthesis of formants of british, american and australian accents. In *Acoustics, Speech, and Signal Processing, 2003. Proceedings.(ICASSP’03). 2003 IEEE International Conference on*, volume 1, pages I–712. IEEE, 2003.
- [198] Chao Huang, Yingchun Huang, Frank Soong, and Jianlai Zhou. Weighted likelihood ratio (wlr) hidden markov model for noisy speech recognition. In

- Acoustics, Speech and Signal Processing, 2006. ICASSP 2006 Proceedings. 2006 IEEE International Conference on*, volume 1, pages I–I. IEEE, 2006.
- [199] Tuomo Raitio, Antti Suni, Hannu Pulakka, Martti Vainio, and Paavo Alku. Comparison of formant enhancement methods for hmm-based speech synthesis. In *SSW*, pages 334–339, 2010.
 - [200] Hideyuki Mizuno, Masanobu Abe, and Tomohisa Hirokawa. Waveform-based speech synthesis approach with a formant frequency modification. In *Acoustics, Speech, and Signal Processing, 1993. ICASSP-93., 1993 IEEE International Conference on*, volume 2, pages 195–198. IEEE, 1993.
 - [201] Robert W Morris and Mark A Clements. Modification of formants in the line spectrum domain. *Signal Processing Letters, IEEE*, 9(1):19–21, 2002.
 - [202] Yinqiu Gao and Zhen Yang. Pitch modification based on syllable units for voice morphing system. In *Network and Parallel Computing Workshops, 2007. NPC Workshops. IFIP International Conference on*, pages 135–139. IEEE, 2007.
 - [203] Jacob Benesty, M Mohan Sondhi, and Yiteng Huang. *Springer handbook of speech processing*. Springer Science & Business Media, 2007.
 - [204] Janina K Casper and Rebecca Leonard. *Understanding voice problems: A physiological perspective for diagnosis and treatment*. Lippincott Williams & Wilkins, 2006.
 - [205] Simon Ang and Alejandro Oliva. *Power-switching converters*. CRC press, 2005.
 - [206] Gabriel Rincon-Mora. *Analog IC design with low-dropout regulators (LDOs)*. McGraw-Hill, Inc., 2009.
 - [207] Young-Giu Jung, Mun-Sung Han, Kyung-Yong Chung, and Sang Jo Lee. A valid frequency range analysis of throat signal for voice command system. In *Information Science and Applications (ICISA), 2011 International Conference on*, pages 1–5. IEEE, 2011.
 - [208] Hauke Kruger, Thomas Lotter, and Peter Vary. A versatile dsp-system for student-projects on embedded real-time audio signal processing. In *Acoustics, Speech, and Signal Processing, 2004. Proceedings.(ICASSP'04). IEEE International Conference on*, volume 5, pages V–1033. IEEE, 2004.
 - [209] Mark Kahrs, GW Elko, SJ Elliot, S Makino, JM Kates, M Bosi, and JO Smith. The past, present and future of audio signal processing. *IEEE Signal Processing Magazine*, 5(14):30–57, 1997.
 - [210] Simon Cimin Li, Vincent Chia-Chang Lin, Krissanapong Nandhasri, and Jitkasame Ngarmnil. New high-efficiency 2.5 v/0.45 w rwdm class-d audio amplifier for portable consumer electronics. *Circuits and Systems I: Regular Papers, IEEE Transactions on*, 52(9):1767–1774, 2005.

- [211] Sungwan Bokuwan and Taworn Benjanarasuth. Code generation of fractional filters for dspic microcontrollers. In *TENCON 2011-2011 IEEE Region 10 Conference*, pages 1275–1279. IEEE, 2011.
- [212] Yuichi Sasaki, Chiharu Miyazaki, Naoto Oka, and Yoshihiko Konishi. Experimental evaluation of isolation effect on printed circuit board with gapped power plane. In *Electromagnetic Compatibility, 2007. EMC 2007. IEEE International Symposium on*, pages 1–4. IEEE, 2007.
- [213] Wei Cui, Jun Fan, Yong Ren, Hao Shi, James L Drewniak, and Richard E DuBroff. Dc power-bus noise isolation with power-plane segmentation. *Electromagnetic Compatibility, IEEE Transactions on*, 45(2):436–443, 2003.

Appendix A: Modeling of Dynamics Between Middle Ear Cavity and Tympanic Membrane Temperatures

Middle ear temperature (T_{me}) is demonstrated in Section 3.4.2 to be very responsive to changes in core body temperature (CBT). It is able to pick up small changes which are not evident in the temperatures at the rectum and esophagus, and it is more robust to changes in ambient conditions relative to the tympanic membrane temperature (T_{tm}). This approach is especially useful for the monitoring CBT for early signs of heat related injuries [121] which has to be continuously done in an efficient and non-invasive manner, with high accuracy. Driven by these motivations, the aim is to derive a dynamic Middle Ear Heat Balance (MEHB) model describing heat flows in the middle ear (ME) cavity vicinity.

The Two-Node model (TNM) by Gagge *et al* [122] [123] is used to provide

the baseline relationship to represent heat transfers localized to the vicinity of the ME. The generic equation is given in Eqn. (A.1), where Q_b is the rate of change of the heat content of that point in terms of heat flow rate per unit area (heat flux); M_b is the rate of metabolic energy expenditure per unit area; W_b is the rate of external work per unit area (+ for work against external forces, - for eccentric or negative work); R_b is the rate of radiant heat exchange per unit area; C_b is the rate of convective heat exchange per unit area; D_b is rate of conductive heat exchange per unit area; and E_b is the rate of evaporative heat exchange per unit area.

$$Q_b = M_b - (\pm W_b) \pm (R_b + C_b + D_b) - E_b \quad (\text{A.1})$$

The areas of interest of the dynamical model here is the TM, interacting essentially with the environment within the ear canal on one side and the ME cavity on the other. The TM is thin and concave in nature [109], and it is located at the distal end of the external auditory canal, forming a thin barrier separating the auditory canal from the ME cavity. The TM outer surface facing the canal is exposed to the ambient air while the inner surface facing the ME cavity is part of the cavity wall. Since the TM is extremely thin, heat from the surface is mostly lost to the ambient environment via convection and radiation due to the relatively larger interacting contact area compared to the edge of the TM that is attached to canal wall. Thus, the conduction heat loss to the canal wall is negligible.

The TM is shielded from the ambient air turbulence as it is sited at the distal end of the canal, if temperature measurements are indeed taken at the

TM (Chapter 3). The TNM can be reduced with the specific situations at the TM. First, $M_b \approx 0$ since there is negligible heat generation by the thin TM tissue; $W_b = 0$ at this passive point; $E_b = 0$ with no sweat glands in this area; $D_b \approx 0$ with negligible conductive heat exchange.

Thus, at the interface with the ambient environment, Eqn. (A.1) can be reduced to Eqn. (A.2) with only the dominant convection and radiant heat terms. In Eqn. (A.2), q_{am} refers to the heat flow rate from the TM to the ambient environment; T_{tm} and T_{am} are the TM and ambient temperatures in Kelvin. The convection heat transfer term can be represented as $h_{ca}A_{tm}(T_{tm}-T_{am})$ [124] [125] [126] [127] where h_{ca} is the heat transfer coefficient and A_{tm} is the effective area of the TM.

$$q_{am} = h_{ca}A_{tm}(T_{tm} - T_{am}) + \Delta_{am} \quad (\text{A.2})$$

The radiant term is represented by $\Delta_{am} = \sigma\epsilon_{ra}A_{tm}(T_{tm}^4 - T_{am}^4)$ [126] [127] in Eqn. (A.3) to account for the heat transfer through thermal radiation from the surface of the TM, where $\sigma\epsilon_{ra}$ is the TM surface radiant heat transfer coefficient; $\sigma = 5.6704 \times 10^{-8} J/(s \cdot m^2 \cdot K^4)$ is the Stefan-Boltzmann constant and ϵ_{ra} is the surface emissivity constant of the TM.

$$\Delta_{am} = \sigma\epsilon_{ra}A_{tm}(T_{tm}^4 - T_{am}^4) \quad (\text{A.3})$$

Δ_{am} can be re-written as $h_{ra}A_{tm}(T_{tm} - T_{am})$ depicted in Eqn. (A.4) with h_{ra} defined in Eqn. (A.5) as a temperatures (T_{tm} and T_{am}) dependent coefficient.

$$\Delta_{am} = h_{ra}A_{tm}(T_{tm} - T_{am}) \quad (\text{A.4})$$

$$h_{ra} = \sigma \epsilon_{ra} (T_{tm} + T_{am})(T_{tm}^2 + T_{am}^2) \quad (\text{A.5})$$

The relative strength of the radiant term is expected to be small due to the absence of a physical receiving surface perpendicular to the TM to facilitate the radiant heat exchange [126], resulting in a small and uneven radiant heat transferred to the surface of the ear canal in the vicinity of the TM [126] [128]. In the analysis of the results subsequently in Section 3.6, this component will be calibrated from the data collected to verify the significance of its contribution.

Next, the other side of the interface with the ME cavity, serving as the primary heat source to the TM, will be similarly examined. The inner surface of the TM constitutes a wall of the ME cavity. The ME cavity is an enclosed area with an air pocket, and the heat circulation from this area to the TM is dominated primarily by convection and radiation processes. However, within the cavity, heat transfer through conduction is more significant than at the other side due to the two conductive channels: (a) via the edge of the TM where it joins the side walls of the ME [109], (b) via the malleus bone which engages the inner surface of the TM [109]. Heat transfer via radiation may also be present since the walls of the cavity are potential radiation sources, and the TM is the potential receiving surface [109] [126]. Thus, effective heat flows q_{tm} from within the ME cavity to the TM is given in Eqn. (A.6). T_{me} is the temperature of the ME cavity (in Kelvin). h_{ct} represents the lumped convective and conductive heat transfer coefficient for the heat transfer from an effective area A_{me} of the ME cavity to the TM. ϵ_{rt} is the surface emissivity constant of the ME cavity. The ME cavity is able to store heat energy and it can be thought of as a thermal capacitor denoted by C_{me} (heat storage element). There is thus another flow from the heat stored

in this energy bank which is represented by $C_{me} \cdot \frac{d}{dt}(T_{me} - T_{tm})$.

$$q_{tm} = h_{ct}A_{me}(T_{me} - T_{tm}) + C_{me} \cdot \frac{d}{dt}(T_{me} - T_{tm}) + \Delta_{tm} \quad (\text{A.6})$$

Similar to Eqn (A.2), the radiant term Δ_{tm} depicted in Eqn. (A.7) captures the heat transfer through thermal radiation from the wall of the ME cavity. Δ_{tm} can be similarly re-written as $h_{rt}A_{me}(T_{me} - T_{tm})$ as depicted in Eqn. (A.8) with h_{rt} defined in Eqn. (A.9). The relative strength of the radiant term will similarly be calibrated from the results subsequently in Section 3.6.

$$\Delta_{tm} = \sigma\epsilon_{rt}A_{me}(T_{me}^4 - T_{tm}^4) \quad (\text{A.7})$$

$$\Delta_{tm} = h_{rt}A_{me}(T_{me} - T_{tm}) \quad (\text{A.8})$$

$$h_{rt} = \sigma\epsilon_{rt}(T_{me} + T_{tm})(T_{me}^2 + T_{tm}^2) \quad (\text{A.9})$$

To get the dynamic equation relating T_{me} to T_{tm} and T_{am} , the principle of energy conservation is used as in Eqn (A.10).

$$q_{tm} - q_{am} = C_{tm} \cdot \frac{d}{dt}T_{tm} \quad (\text{A.10})$$

Expand Eqn (A.10) into Eqn (A.11):

$$h_{ct}A_{me}(T_{me} - T_{tm}) + C_{me} \cdot \frac{d}{dt}(T_{me} - T_{tm}) + \Delta_{tm} - h_{ca}A_{tm}(T_{tm} - T_{am}) - \Delta_{am} = C_{tm} \cdot \frac{d}{dt}T_{tm} \quad (\text{A.11})$$

Divide Eqn (A.11) with $(h_{ct}A_{me})$ and rearrange into Eqn (A.12):

$$(T_{me}-T_{tm})+\frac{C_{me}}{h_{ct}A_{me}}\cdot\frac{d}{dt}(T_{me}-T_{tm})-\frac{C_{tm}}{h_{ct}A_{me}}\cdot\frac{d}{dt}T_{tm}-\frac{h_{ca}A_{tm}}{h_{ct}A_{me}}(T_{tm}-T_{am})=\frac{\Delta_{am}-\Delta_{tm}}{h_{ct}A_{me}} \quad (\text{A.12})$$

Define a lump radiant term $\Delta = \frac{\Delta_{am}-\Delta_{tm}}{h_{ct}A_{me}}$ and substitute Δ into Eqn (A.12)

to get Eqn (A.13):

$$(T_{me}-T_{tm})+\frac{C_{me}}{h_{ct}A_{me}}\cdot\frac{d}{dt}(T_{me}-T_{tm})-\frac{C_{tm}}{h_{ct}A_{me}}\cdot\frac{d}{dt}T_{tm}-\frac{h_{ca}A_{tm}}{h_{ct}A_{me}}(T_{tm}-T_{am})=\Delta \quad (\text{A.13})$$

Finally, rearrange Eqn (A.13) into Eqn (A.14):

$$\Rightarrow T_{me} = (1+\frac{h_{ca}A_{tm}}{h_{ct}A_{me}})T_{tm} - (\frac{h_{ca}A_{tm}}{h_{ct}A_{me}})T_{am} + (\frac{C_{tm}+C_{me}}{h_{ct}A_{me}})(\frac{d}{dt}T_{tm}) - C_{me}(\frac{d}{dt}T_{me}) + \Delta, \quad (\text{A.14})$$

Expand $\Delta = \frac{\Delta_{am}-\Delta_{tm}}{h_{ct}A_{me}}$ into Eqn (A.15):

$$\Delta = \frac{\sigma\epsilon_{ra}A_{tm}}{h_{ct}A_{me}}(T_{tm}^4 - T_{am}^4) - \frac{\sigma\epsilon_{rt}}{h_{ct}}(T_{me}^4 - T_{tm}^4) \quad (\text{A.15})$$

Finally, simplify Eqn (A.15) and rearrange into Eqn (A.16):

$$\Rightarrow \Delta = -(\frac{\sigma\epsilon_{rt}}{h_{ct}})T_{me}^4 + (\frac{\sigma\epsilon_{rt}A_{me} + \sigma\epsilon_{ra}A_{tm}}{h_{ct}A_{me}})T_{tm}^4 - (\frac{\sigma\epsilon_{ra}A_{tm}}{h_{ct}A_{me}})T_{am}^4. \quad (\text{A.16})$$

Eqn (A.14) is the MEHB model equation with Eqn (A.16) representing the radiant term.

Appendix B: VitalMON

P-VSM Firmware Design and Implementation

P-VSM consists of two autonomous modules: (a) WTA, and (b) PDL/TM. Each autonomous module requires custom firmware design in order to implement its defined functionality.

B.1 WTA firmware design

The WTA uses a 16-bit fixed-point low power MCU that execute a custom firmware. The firmware embodied structured instructions and computational algorithms that defined the functions of a WTA. Figure B1 depicts the simplified state diagram representing the various operations executed in a sequence of state. There are 6 top-level operational states: *Initialization()*, *Shutdown()*, *CheckBattery()*, *MeasureTemperature()*, *TransmitTemperature()*, and *Sleep()*.

The *Initialization()* state implements low level initialization instructions in order to properly configure the required built-in peripherals and memory re-

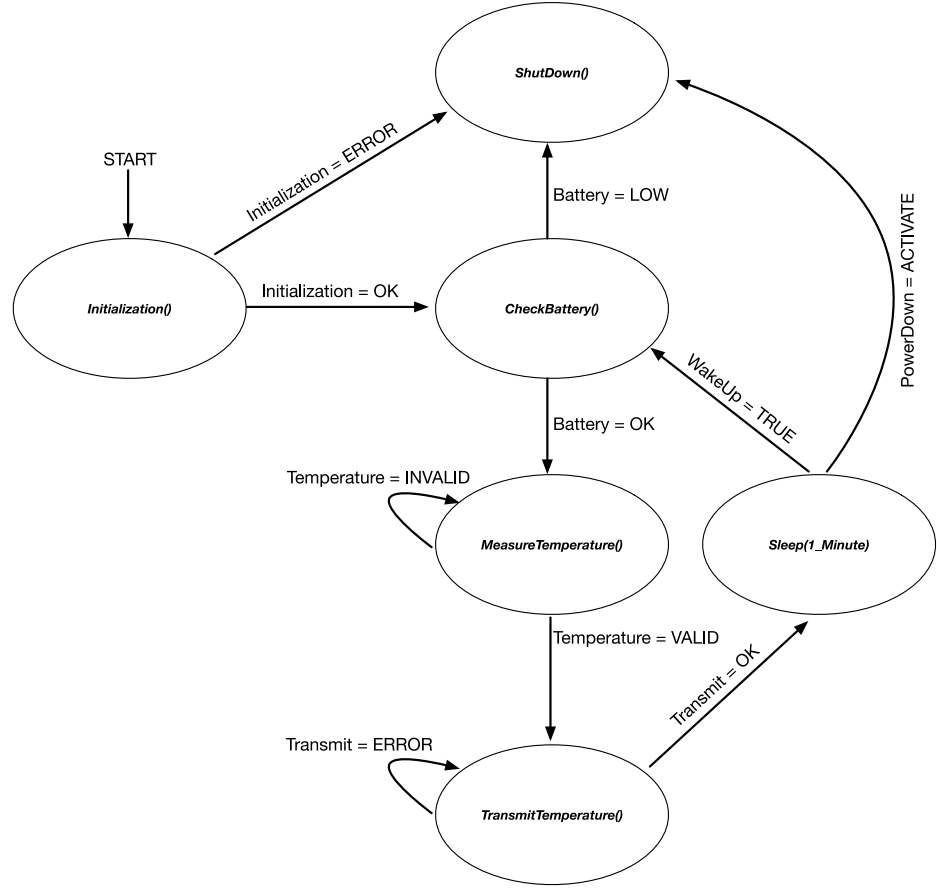


Figure B1: WTA firmware operational states.

sources of the MCU. The *ShutDown()* state powers off the MCU and all hardware connected to it, effectively powering off the whole WTA hardware. The *Check-Battery()* state inspects the health condition of the 3V battery which provides power to the WTA. The *TransmitTemperature()* state controls the Bluetooth Low Energy hardware on the WTA, and transmit the processed temperature data to the PDL/TM sub-module. The *Sleep()* state puts the WTA into a 1 minute MCU idle mode that effectively reduces the overall current consumption, and only wakes up after the 1 minute interval timer expires.

The *MeasureTemperature()* state implements algorithms to measure TM temperature by: (a) converting measured thermal infrared value to equivalent tem-

perature, (b) to determine the hot pixel location and its corresponding hotspot value, and (c) to define a new *TM-MASK* from current hot pixel location for new TM temperature measurement. Figure B2 depicts the pseudo-code of *MeasureTemperature()* state. The *fetchIrPixelsData()* function fetches all the 64 pixels thermal infrared emission data and stores into *IrPixelArray* data array in MCUs memory before any data processing can be performed. Two very important algorithms utilized within the state are the *GetArrayTemperature()* and *ConstructNewMask()*.

```

MeasureTemperature()
  if (WTA_JustPoweredUp == TRUE)
    TM-MASK = Default-TM-MASK
    OldHotPixelLocation = DefaultHotPixelLocation
    HotPixelLocation = DefaultHotPixelLocation
    WTA_JustPoweredUp = FALSE
  end

  IrPixelArray = FetchIrPixelsData()
  [HotPixelLocation, MaxTemperature] = GetArrayTemperature(TM-MASK, IrPixelArray)

  if(OldHotPixelLocation != HotPixelLocation)
    TM-MASK = ConstructNewMask(HotPixelLocation, Default-TM-MASK)
    OldHotPixelLocation = HotPixelLocation
  end
end

```

Figure B2: Pseudo-code for *MeasureTemperature()* state.

The *GetArrayTemperature()* algorithm returns hotspot temperature and its related hot pixel location base on the *IrPixelArray* and *TM-MASK* as inputs. It has been shown in Section 4.5, that only a small subset of the 64-pixels infrared emission data is relevant to the TM. Thus, valuable MCUs processing cycles will be consumed unnecessarily if all the 64-pixels data are sequentially processed. In order to efficiently process only the effective TM pixels data, an adaptive *TM-MASK* is applied to the pixels data stored in *IrPixelArray* in order to eliminate the unwanted ear canals pixels while retaining the TMs pixels. With this method, the MCU is able to use less of the processing cycle to process only the effective

TM pixels to calculate the temperature values, and valuable battery power can be conserved.

The *ConstructNewMask()* algorithm adaptively re-construct a new *TM-MASK* for the next measurement on the TM if a change in the hot pixel location is detected. The new *TM-MASK* ensures the hot pixel is always located at the defined center area of the mask.

B.1.1 *GetArrayTemperature()* - Infrared to temperature conversion and hot pixel location identification algorithm

TM temperature thermal pixels are extracted by applying *TM-MASK* on *Ir-PixelArray* and stored in *TM_IR* array within the MCU. A series of mathematical formulae [67] provided by Melexis are applied to each pixel value stored in the *TM_IR* in-order to convert each pixel to temperature equivalent, and to concurrently apply a custom computational algorithm in-order to determine from among the pixels, the highest temperature value and location. Thus, at the end of the overall infrared to temperature conversion, the highest temperature with the actual pixel location (hot pixel) is also determined.

Figure B3 depicts a summary of processes for TSA pixels masking, infrared to temperature conversion and a computation to determine maximum TM temperature. The sequence of steps are: (1) 64 pixels TSA is effectively reduced to an equivalent 16 pixels array by applying an adaptive *TM-MASK* of size 16, hence $p = 16$ which is the size of the required *TM_IR* array. (2) The valid TM pixels are populated into *TM_IR*. (3) Infrared to temperature conversion algorithm and highest temperature search algorithm are concurrently applied in an iterative manner, where only 16 iterations are required from the full 64 iterations.

Thus, a valid *TM-MASK* effectively reduces the computational time by at least 75% for $p = 16$. Maximum TM temperature (*MaxTemperature*) and location of hot pixel (*HotPixelLocation*) are returned once execution is completed.

B.1.2 *ConstructNewMask()* - *TM-MASK* adjustment algorithm

A *TM-MASK* representing the effective pixel area of a TM is designed to be adaptive depending on the last known hot pixel position. The default *TM-MASK* has effective pixels area that is pre-determined during setting up and personalizing of WTA for a specific user. This default *TM-MASK* is first used for measurement of infrared emissions of the TM every time upon WTA powering up. The new *TM-MASK* for use in the next measurement is adjusted from the default mask based on the last known location of the hot pixel. The algorithm uses the last known hot pixel location to define a four pixels size square area with the hot pixel located in the fourth quadrant of the square. The square area is defined as hot pixel area. The hot pixel area is expanded to the size of the default *TM-MASK* in-order to form a new *TM-MASK* at the new location. Figure B4 (a) depicts the *ConstructNewMask()* algorithm forming a new *TM-MASK* with the last known hot pixel at location 38. The new *TM-MASK* effectively reduces the processing of pixels data from 64 to 16. Figure B4 (a) shows the hot pixel to be more or less at or near to the center of the TSA when the WTA is positioned in the ear canal. In the event of small-unwarranted movement of the WTA while still inserted in the ear canal, the hot pixel location may shift. Figure B4 (b) - (d) depict some possible scenarios of the shifted hot pixel locations and the resulted new *TM-MASKs*. The algorithm checks the validity of the masks four boundaries. If any of the boundaries falls into an invalid area, a new boundary

is defined. Thus, depending on the last known hot pixel location, the new *TM-MASK* size may be the same or smaller than the default *TM-MASK* size. MCU processing time can be further reduced if the new *TM-MASK* size is indeed smaller than the default, which is shown to be dependent on the positioning of the WTA in the ear canal.

B.2 PDL/TM firmware design for CBT calculation

The PDL/TM is a data-logger that logs in real-time via BLE wireless communication the highest TM temperature measured from the WTA. CBT is inferred from the TM temperature by performing the following steps proposed in Chapter 3. The PDL/TM monitors the inferred CBT and generates local and remote alert base on the pre-programmed CBT thresholds. The remote alert is based on the PDL/TM built-in support for wireless ZIGBEE and GSM infrastructure. When CBT is within the range of the *CBT_WARNING*, a reminder message is transmitted via ZIGBEE to the officers who are equipped with GCs within the ZIGBEE communication range, and via GSM if they are out of range. When CBT is within the range of the *CBT_CRITICAL*, a repeated alert message is transmitted at a fixed interval (programmable in firmware) via the same wireless communication channel. Figure B5 depicts the top level state machine representing a summary of the basic processes implemented in the PDL/TM firmware architecture.

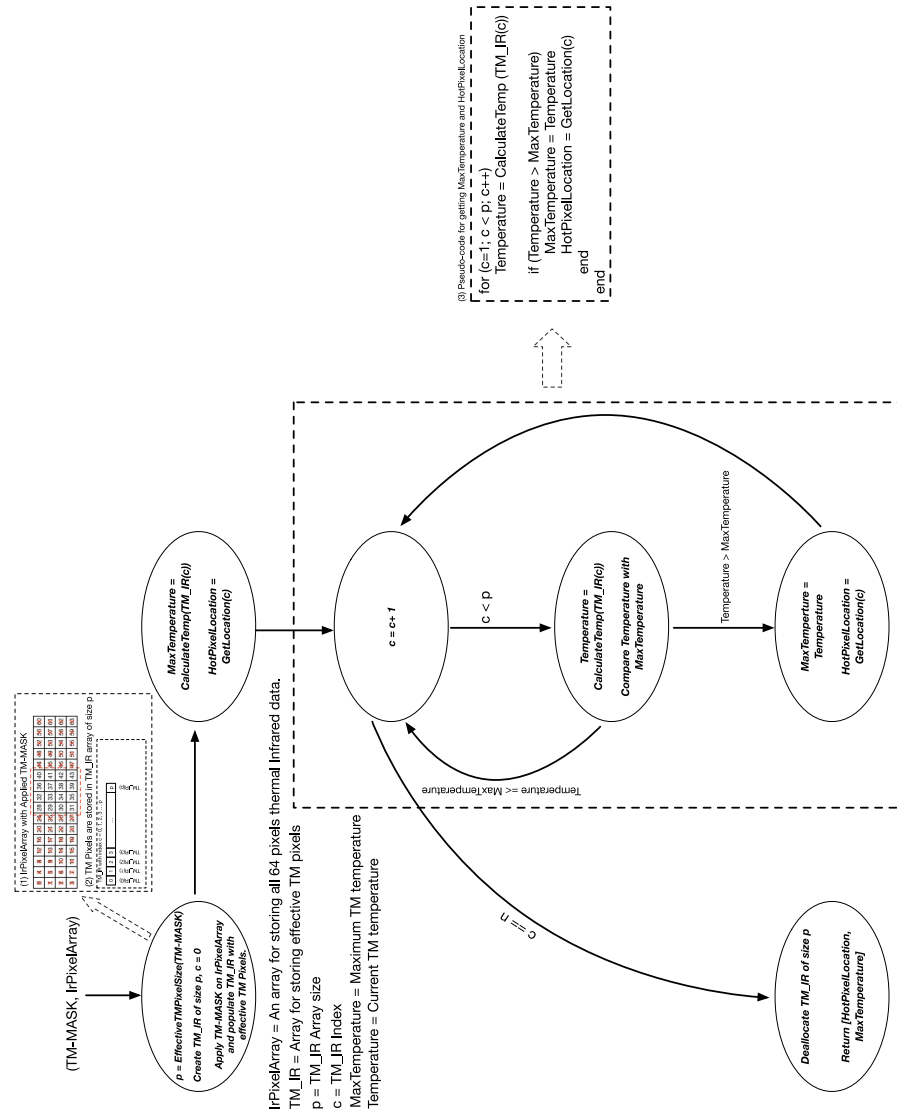


Figure B3: Summary of processes for pixels masking, pixels conversion to temperatures and computational algorithm to determine maximum TM temperature.

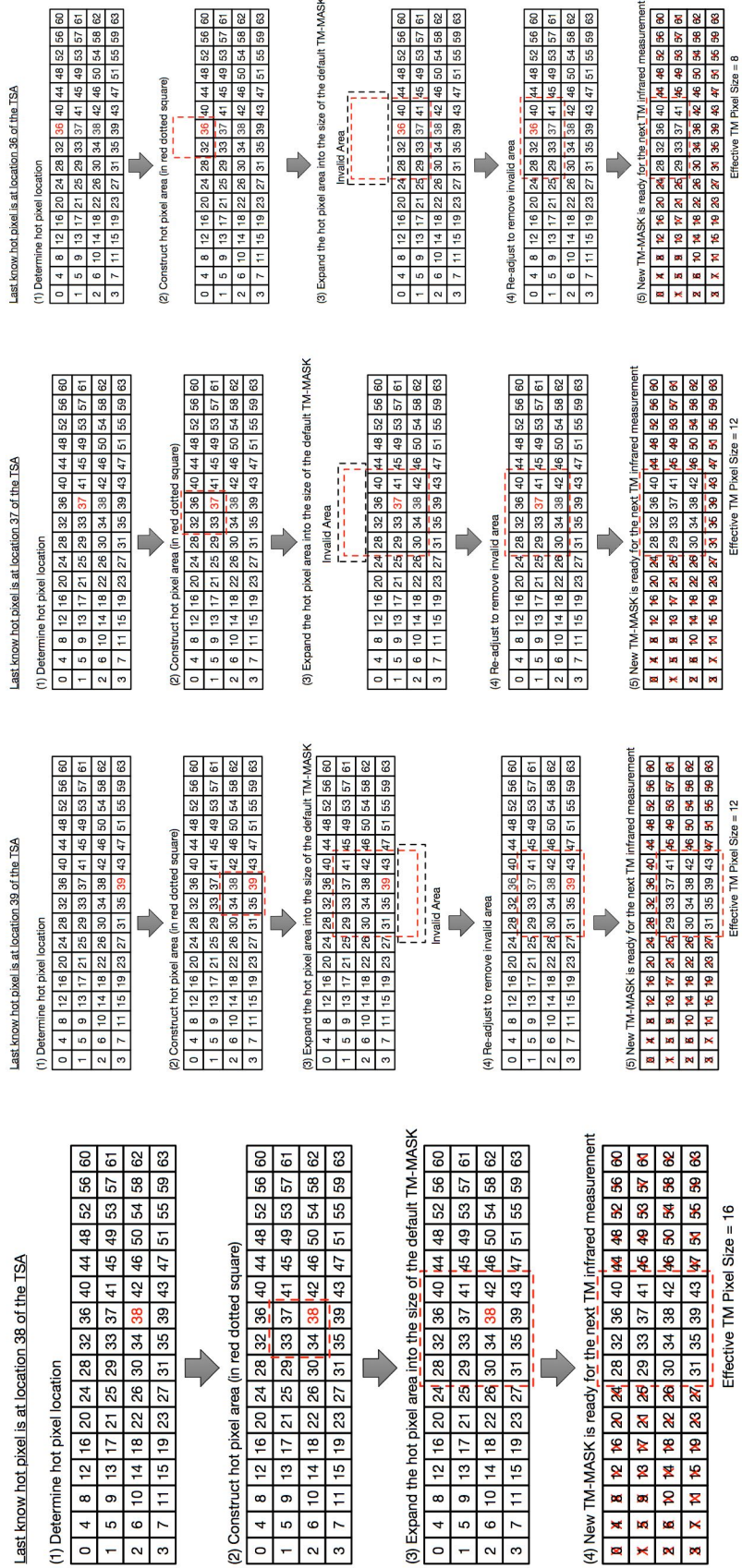


Figure B4: TM-MASKs from possible hot pixel locations.

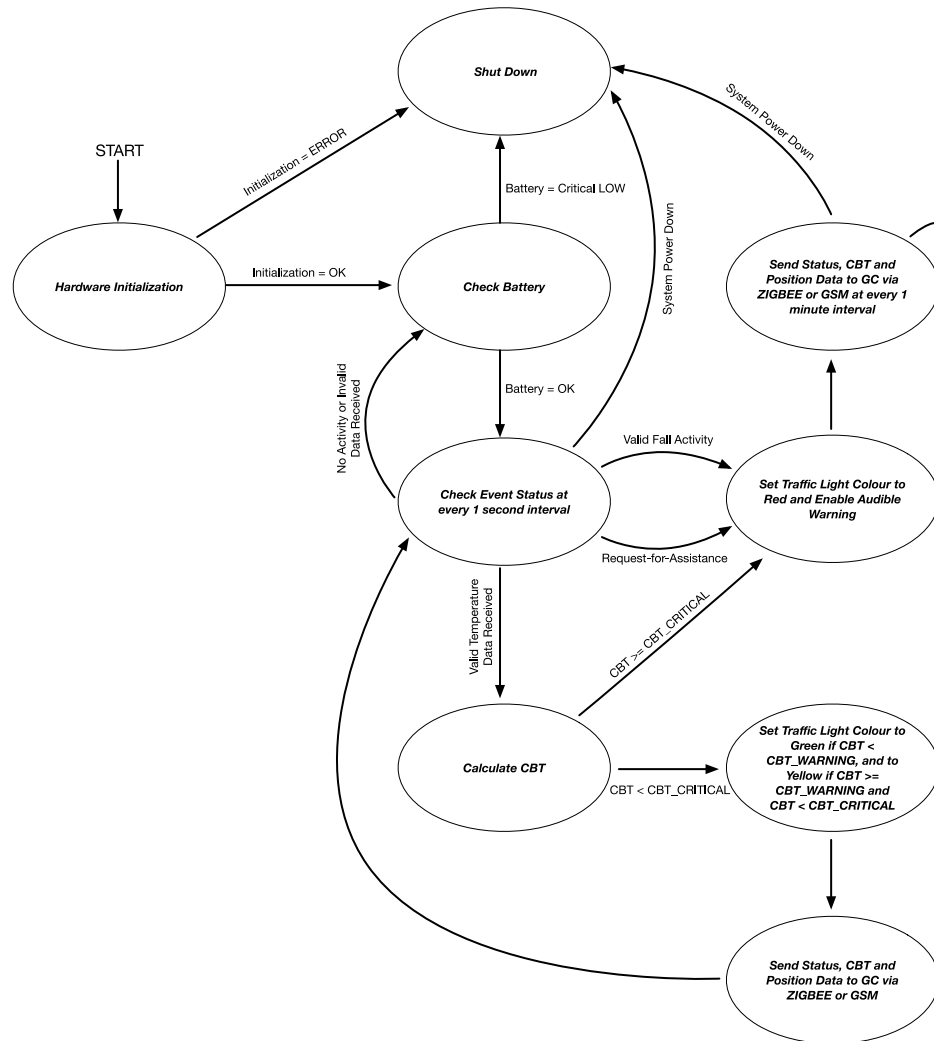


Figure B5: Summary of processes for PDL/TM firmware.

Appendix C: e-Care Hardware and Firmware Developments

C.1 Hardware Design

C.1.1 e-Care Base Station

Figure C1 depicts the hardware operational blocks of a e-Care Base Station. The Base Station consists of: (a) GSM/Internet Messaging unit (GSM/IM), (b) Renesas R5F100GLAFB Microcontroller unit (BS-MCU) [62], (c) ZIGBEE wireless communication unit (ZBEE), (d) Real-Time Clock with backup battery (RTC) unit, (e) Local Alert unit (LA), (f) Simple User Interface (UI), and (g) Switch-mode power control unit (SW-PCN).

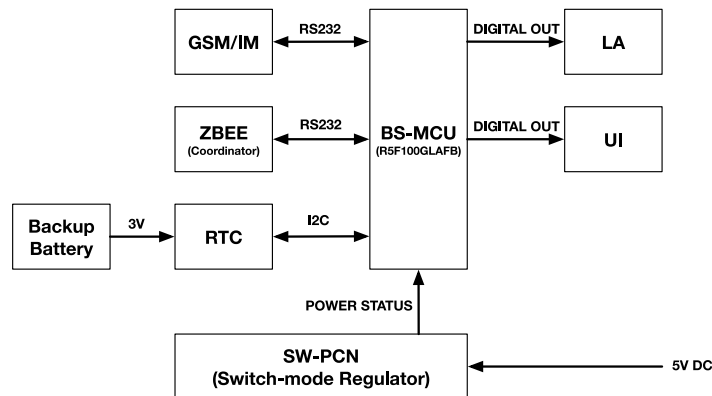


Figure C1: e-Care Base Station System Block Diagram

GSM/IM unit is used to communicate with caregivers or remote server. The unit is a miniature off-the-shelf GSM modem or Internet access point, and communicates with BS-MCU via RS232 serial communication interface. The ZBEE unit is implemented by using a Telegesis ETRX357 ZIGBEE radio module, and its role is a PAN Coordinator [66] tasked to setup and maintains a wireless mesh PAN used for internal e-Care wireless messaging among various hardware modules. ZBEE communicates with the BS-MCU via RS232. The RTC keeps an accurate date and time information for internal time reference, and day and night motion activity monitoring operation. Motion activity monitoring algorithm requires the accurate time information as motion inactivity timeout parameter differs for day and night. The RTC communicates with the BS-MCU via I2C serial interface. The LA generates loud audible and visual alert in the event of an emergency to request for help from anyone nearby. The UI displays current operational status of the Base Station. The SW-PCN unit contains switch-mode power circuitry that provides regulated 3.3VDC power supply to power up the Base Station. Switch-mode type of regulated power supply is more efficient than its linear counterpart as it is capable of achieving $\geq 90\%$ output efficiency while supplying high current [205] at the expense of physical circuit's size, it is selected to supply power to the multiple functional units within the Base Station, and most importantly a stable supply to the GSM/IM unit as the unit consumes high current while establishing network connectivity (GSM mobile network or Internet) and transmitting messages. The BS-MCU is the central processing unit that implements the motion activity monitoring algorithm and the required control logics. The BS-MCU is a reliable automotive grade 16-bit R5F100GLAFB

Renesas microcontroller [62] running at 32MHz, with 512KB Flash Memory and 32KB RAM, to ensure sufficient processing bandwidth for reliable and unattended operation.

Figure C2(a) depicts the completed hardware design of the Base Station, and Figure C2(b) depicts the boxed up prototype. The Base Station draws 80mA of peak current during operation.

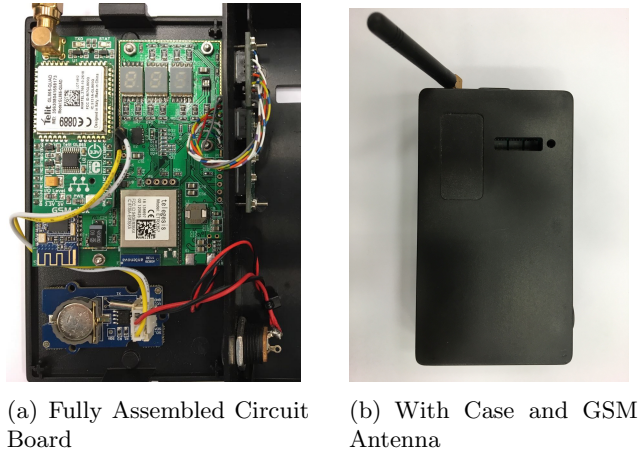


Figure C2: e-Care Base Station Hardware

C.1.2 TMotion and PIRD Sensors Modules

Figure C3 depicts the hardware operational blocks of an e-Care TMotion sensor module. The module consists of: (a) TSA, (b) PIR motion sensor, (c) Renesas R5F100BEANA [62] low pin count microcontroller unit (SM-MCU), (d) ZIGBEE wireless communication unit (ZBEE) and (e) Linear power control unit (LN-PCN).

The TSA is used to measure thermal infrared radiation of the target. It performs 16×4 simultaneous target temperature measurement and determines the corresponding temperature map of the target. The TSA detects infra-red radiation wavelength in the $2\mu\text{m}$ - $22\mu\text{m}$ range. This is the wavelength of radiant

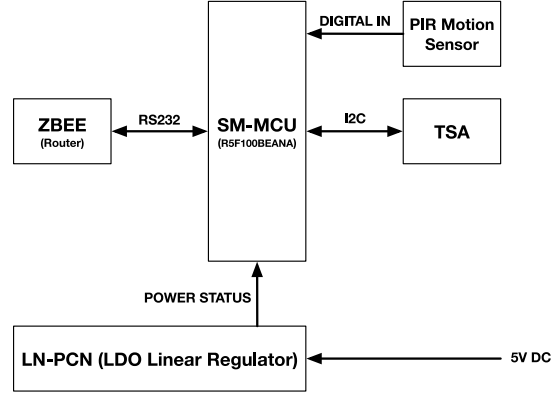


Figure C3: e-Care TMotion System Block Diagram

heat and human body emits heat [72]. It communicates with the SM-MCU via I2C interface. The PIR motion sensor detects motion from changes in ambient temperature, and it provides a single-bit logic output to one of the SM-MCU digital input interface where a logic '1' indicates valid motion detection and a logic '0' indicates otherwise. ZBEE is based on Telegesis ETRX357 ZIGBEE radio module, the same unit used in the Base Station and its role is a PAN Router [66] and is used to expand the PAN coverage. It is tasked to find the best route to the destination over which to transfer a message. A Router performs all functions similar to a Coordinator except the establishing of a network. ZBEE communicates with SM-MCU via RS232. Due to space and size constrain, the LN-PCN contains a linear low dropout (LDO) regulator [206] that supplies regulated 2.6V power supply to the TSA and 3.3VDC power supply to the rest of the circuit within the TMotion sensor module. LDO regulator is chosen due to its small size as compared to its switch-mode counterpart, and has comparable in output efficiency ($\geq 90\%$) when used to supply current to low power circuit. However, the output efficiency drops if higher power is drawn due to heat generated by the LDO regulator. The TMotion circuit is of very low power design where the

maximum operating current drawn is $\leq 8mA$ at 3.3V, hence LN-PCN high efficiency output is not an issue. The SM-MCU is based on a highly reliable low pin count automotive grade 16-bit R5F100BEANA Renesas microcontroller [62] running at 16MHz, with 64KB Flash Memory and 4KB RAM, sufficient to control and process the TSA temperature data, PIR motion detector and ZBEE communications.

Figure C4(a) depicts the completed hardware design of the TMotion sensor module, and Figure C4(b) depicts the properly boxed up prototype. The TMotion sensor module draws $\leq 8mA$ of current during operation, and $\leq 400\mu A$ during standby.

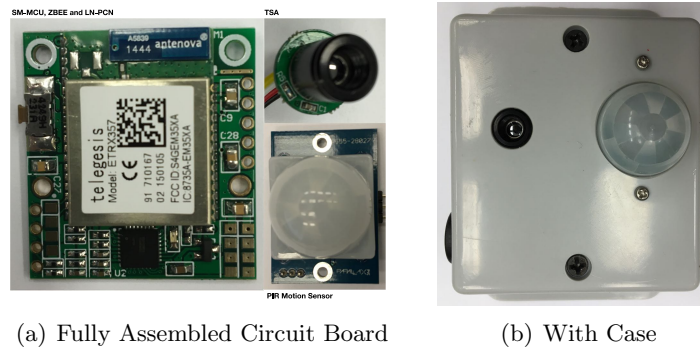


Figure C4: e-Care TMotion Sensor Hardware

Figure C5 depicts the hardware operational blocks of a e-Care PIRD sensor module. The module consists of: (a) PIR motion sensor, (b) Renesas R5F100BEANA [62] low pin count microcontroller unit (SM-MCU), (c) ZIG-BEE wireless communication unit (ZBEE) and (d) Linear power control unit (LN-PCN).

The PIRD block diagram is similar to the TMotion sensor block diagram. The main difference is the absence of the TSA unit. In term of functionality, all the internal units inherit the same hardware functions as the TMotion sensor.

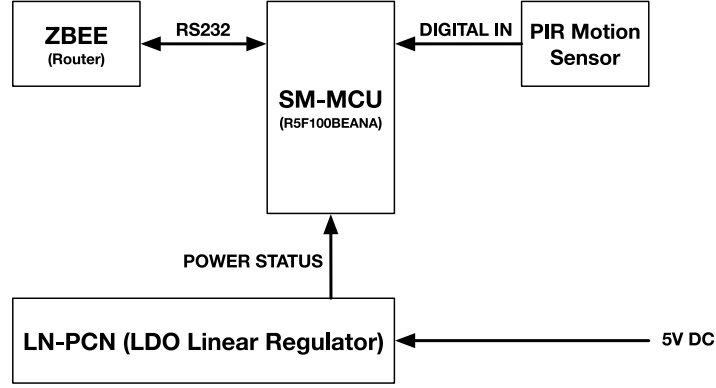


Figure C5: e-Care PIRD System Block Diagram

Figure C6(a) depicts the completed hardware design of the PIRD sensor module, and Figure C6(b) depicts the boxed up prototype. The PIRD sensor module draws $\leq 5mA$ of current during operation, and $\leq 400\mu A$ during standby.

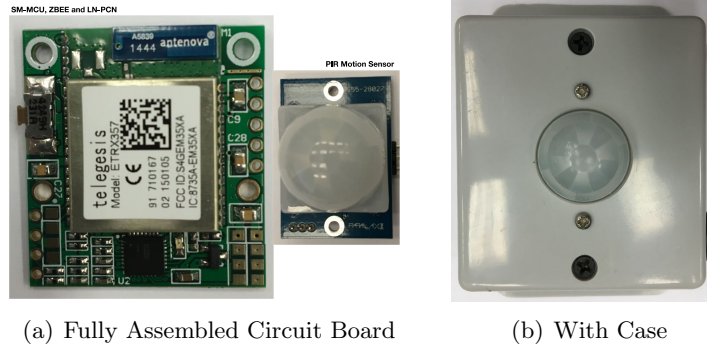


Figure C6: e-Care PIRD Sensor Hardware

C.1.3 AlertSW and AlertCL Modules

Figure C7 depicts the hardware operational blocks of a e-Care AlertSW and AlertCL modules. Each module consists of: (a) Mechanical push-button switch (RED for AlertSW and GREEN for AlertCL), (b) Renesas R5F100BEANA [62] low pin count microcontroller unit (SM-MCU), (c) ZIGBEE wireless communication unit (ZBEE) and (d) Battery power control unit (BT-PCN).

The AlertSW/AlertCL block diagram is similar to the TMotion sensor block

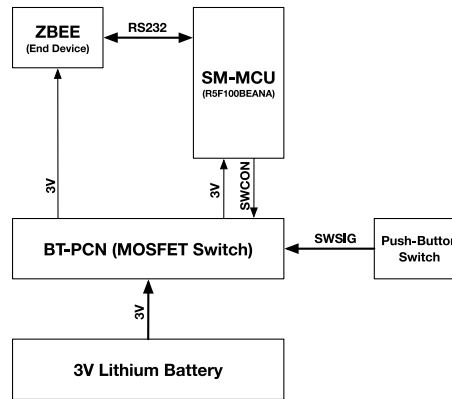
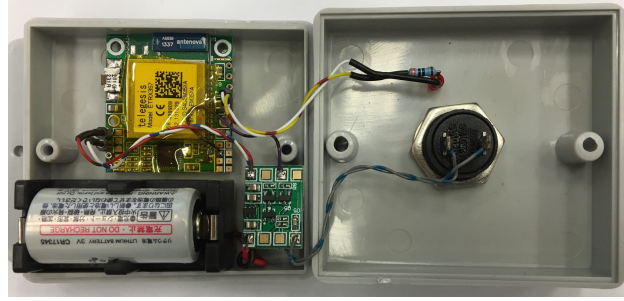


Figure C7: e-Care AlertSW/AlertCL System Block Diagram

diagram, using the same SM-MCU and ZBEE units. The main differences are the absence of the TSA and PIR motion sensor, and a mechanical push-button switch is installed in place and directly controls the BT-PCN unit. The BT-PCN provides stable power to the AlertSW/AlertCL module from a 3V 1AH CR123A Lithium battery. When the switch is pressed, SWSIG signal on BT-PCN is asserted and the solid-state MOSFET switch connects the battery to power up the AlertSW/AlertCL module. Upon powering up, SM-MCU asserts SWCON signal on the BT-PCN with one of its digital output port in-order to ensure the battery power is not cut-off when the switch is released. The SM-MCU communicates with ZBEE to transmit relevant message to the Base Station. It controls the BT-PCN to cut-off battery power to the AlertSW/AlertCL module once message transmission is completed. Due to battery power consideration, the ZBEE unit is configured as a PAN End Device.

Figure C8(a) depicts the completed hardware design of the AlertSW/AlertCL module with a Lithium battery attached. Figure C8(b) and C8(c) depict the boxed up prototype of AlertSW (Red push-button switch) and AlertCL (Green push-button switch) modules respectively. The AlertSW/AlertCL module draws

$\leq 4mA$ of current during 3 seconds of operation, and does not draws current if the push-button switch is not pressed.



(a) Fully Assembled Circuit Board with Battery



(b) AlertSW



(c) AlertCL

Figure C8: e-Care AlertSW/AlertCL Hardware

C.2 Firmware Design

There are total four sets of firmwares (Base Station, TMotion Sensor, PIRD Sensor and AlertSW/AlertCL) to be designed for e-Care system. Each firmware is modeled as a state machine in-order to identify the number of known states, and to define proper program execution flow. The final steps will be to convert the finalized state machines into C-programming language codes for each of the modules within the e-Care system.

C.2.1 Base Station

Figure C9 depicts the top level state diagram representing the Base Station firmware. The firmware is divided into three parts: (a) Interrupt Services (Back ground Tasks), (b) Global Buffers and (c) Monitoring Service (Foreground Task). The Interrupt Services are the background tasks responsible for providing low level control, timing and communication functions to the Monitoring Service. The Interrupt Services consist of *BS_TickGenerator()*, *BS_IdleCtControl()*, *BS_StopActMonitor()*, *BS_UserInterface()*, *BS_RTCControl()*, *BS_ZIGBEE()* and *BS_SMS()*. The global buffers are memory variables that serve as message or data sinking and sourcing containers for the Interrupt Services to send or retrieve information to or from the Monitoring Service, and vice-versa. There are total of 12 memory variables defined as global buffers. The Monitoring Service implements an algorithm to monitor motion activity monitoring and to manage alerts.

C.2.1.1 Interrupt Services

BS_TickGenerator() generates 20ms time reference tick signal (*Tick20*) for used in generating time delays and more importantly for the *BS_IdleCtControl()* to perform countdown of Motion Inactivity Timer (*IdleCt*) for detected motion inactivity event. The function uses the BS-MCU 16-bit hardware timer configured to generate a periodic 20ms interrupt.

BS_IdleCtControl() controls the Motion Inactivity Timer (*IdleCt*) and decrements the timer at every 100ms for detected motion inactivity event. The function decrements *IdleCt* only if *IdleCt* > 0 and activity monitoring variables *Stop*

and *Monitor* are respectively reset and set. The *Stop* variable is set when the PIRD sensor is activated (the elderly leaves the house). *Monitor* variable is reset by default during start of operation, and is set when motion is detected, and is again reset during an alert or when an alert is cancelled.

BS_StopActMonitoring() temporarily halts motion activity monitoring for a defined period of time. The duration is defined by Stop Monitor Timer (*StopCt*). The function delays motion activity monitoring by decrementing *StopCt* for every 100ms interval until *StopCt* reaches 0. Motion activity monitoring continues thereafter. The function is activated only when *Stop* variable is set.

BS_UserInterface() displays Base Station operating modes. There are 3 modes of operation: (a) Normal - when Base Station is not in any form of alert, (b) Alert0 - when Base Station detects motion inactivity timeout, and (c) Alert1 - when Base Station detects manual request for help (AlertSW is activated).

BS_RTCControl() monitors time for day and night monitoring operation. The function monitors the elderly estimated wake up and sleep time, and programs the motion inactivity time thresholds for *IdleTH* and *LongTH* variables with timeouts values that suit the current time of the day. When TMotion sensor detects activity via its PIR sensor, *IdleTH* value is used, and if the TSA measures a valid human body temperature and detects a lying down posture, *LongTH* is used instead. *IdleTH* value is usually shorter than *LongTH*, and it is the default motion inactivity time threshold for all situations with the exception when TSA detects a lying down posture.

BS_ZIGBEE() monitors and extracts valid communication messages from wireless modules via ZIGBEE PAN. The valid messages are stored in the Message

Ring Buffer (*MesgBuf*).

BS_SMS() monitors and extracts valid communication messages from received SMS messages. The valid messages are stored in *MesgBuf*.

C.2.1.2 Monitoring Service

The Base Station Monitoring Service implements the motion activity/inactivity monitoring and alert management algorithm. The service is represented as a state machine depicted in Figure C9 with 5 defined states: (a) *BS Check IdleCt*, (b) *BS Check MesgBuf*, (c) *BS Save TSA Temperature*, (d) *BS Discard TSA Temperature*, and (e) *BS Alert*.

The *BS Check IdleCt* state always check if motion inactivity timer *IdleCt* > 0 . If *IdleCt* = 0, then an inactivity alert event will occur. The *BS Check MesgBuf* state receives messages from all the wireless peripheral modules (TMotion sensor, PIRD sensor, AlertSW and AlertCL). SMS messaging is also incorporated into the service where caregivers can clear alert condition remotely. The list of registered messages associated with the peripheral modules are:

- TMotion: PIRACT - when motion activity detection is detected by PIR motion sensor.
- TMotion: TSATMP - when TSA detects valid human body temperature, message contains target temperature and detected body posture information, and when an TSA loses the target, TSATMP contains null (invalid) target temperature and no posture information.
- PIRD: DBLMON - when PIRD sensor is activated (Temporary stops motion activity monitoring).
- AlertSW: SWIRED - when AlertSW is activated (Alert, request for help).

- AlertCL: SWIGRN - when AlertSW is activated (Alert cancel).
- SMS: SMSCLR - when clearing alert is conducted via SMS remotely by the caregivers.

The *BS Check MesgBuf* state updates the following variables within the global buffers: (a) *IdleCt* with *IdleTH* or *LongTH*, (b) *Mode* with *Normal*, *Alert0* or *Alert1*, (c) *Monitor* with TRUE (1) or FALSE (0), and (d) *Stop* with TRUE (1) or FALSE (0). The *Save TSA Temperature* state records valid human body temperature detected by the TSA into *TargetTMP* variable, and update *LDP* variable accordingly based on detected posture (0 - sitting/standing, 1 - lying down). The *Discard TSA Temperature* state discards temperature data stored in *TargetTMP* variable and removes posture data. The *Alert* state processes two types of alert: (a) Alert0 by *IdleCt*= 0, and (b) Alert1 by AlertSW being activated). The state sends out alert messages requesting help to pre-defined caregivers.

C.2.2 TMotion Sensor

Figure C10 depicts the top level state diagram representing the TMotion sensor module firmware. Similar to the Base Station, the TMotion firmware is simpler in design and also divided into three parts: (a)Interrupt Services (Back ground Tasks), (b) Global Buffers and (c) Detection Service (Foreground Task). The Interrupt Services are the background tasks responsible for providing low level control and timing functions to the Detection Service. The Interrupt Services consist of *TM_TickGenerator()* and *TM_TSAMCtControl()*. There are 7 memory variables defined as global buffers. The Detection Service implements an algorithm to detect motion activity detection, monitors human temperature

and detect posture.

The TMotion module Interrupt Services has a much simpler structure as it contains only 2 services. *TM_TickGenerator()* generates 100ms time reference tick signal (*Tick100*) for used by the *TM_TSAMCtControl()* to generate periodic delay for use in sending TSA messages. The function uses the SM-MCU 16-bit hardware timer configured to generate a periodic 100ms interrupt. There are 7 memory variables define as global buffers, they are: (a) *Tick100* - 100ms time reference signal variable, (b) *TSAMCt* - variable for implementing countdown delay timer for control of periodic sending of TSA messages, (c) *TmesgTH* - delay threshold for *TSAMCt*, (d) *SndMaMesg* - variable (or flag) for indicating completed in sending of motion activity message to Base Station, (e) *HTempTH* - threshold for valid human temperature measurement, (f) *HValid* - variable (or flag) indication valid human temperature detection, and (g) *TSABackgnd* - memory reference representing a stored 16×4 background temperature of the area monitored by the TSA. *TSABackgnd* is used mainly to detect human posture.

The Tmotion module Detection Service implements the motion activity detection, monitoring of human temperture and posture detection algorithm. The service is represented as a state machine depicted in Figure C10 with 6 defined states: (a) *Check TM PIR Motion Activity*, (b) *Save TSA Background*, (c) *Measure Target Temperature*, (d) *Detect Posture*, (e) *Send MA Message*, and (f) *Send TSA Message*.

The *Check TM PIR Motion Activity* state monitors for PIR sensor motion activity. *Save TSA Background* state saves background temperature of the area

monitored by the TSA when no motion activity is detected. *Measure Target Temperature* state measures target temperature using TSA and compares with *HTempTH* in order to determine if the target is a human, and sets *HValid* if valid human is detected. *Detect Posture* state uses *TSABackgnd* together with current 16×4 temperature data to detect current posture of the target. The posture detection algorithm will be elaborated in detail in the Section 5.4. *Send MA Message* state transmits PIRACT message via ZIGBEE PAN to Base Station if valid motion activity is detected. *Send MA Message* transmits TSATMP message via ZIGBEE PAN to Base Station if valid human temperature is detected.

C.2.3 PIRD Sensor

Figure C11 depicts the top level state diagram representing the PIRD sensor module firmware. The firmware implementation is simple with only 2 states: (a) *Check PIRD Motion*, and (b) *Send PIRD Message*. The *Check PIRD Motion* state continuously checks for motion activation by the PIR sensor. Motion activation shows that an elderly is near to the main entrance of the house either going out of, or coming into the house. *Send PIRD Message* state transmits DBLMON message via ZIGBEE PAN to the Base Station when a valid motion is confirmed, and the state sets *SndPIRDMesg* variable (or flag) upon complete of transmission.

C.2.4 AlertSW and AlertCL

Figure C12 depicts the top level state diagram representing the AlertSW/AlertCL module firmware. The firmware implementation is simple with only 2 states: (a) *Check Push-Button Switch*, and (b) *Send SW Message*. The *Check Push-Button*

Switch state continuously checks for push-button switch activation (pressed by an elderly). Switch activation indicates that an elderly requests for help (press AlertSW) or cancels a help request (press AlertCL). *Send SW Message* state transmits SWIRED (for AlertSW) or SWIGRN (for AlertCL) message via ZIG-BEE PAN to the Base Station when the switch is pressed, and the state sets *SndSWMesg* variable (or flag) upon complete of transmission.

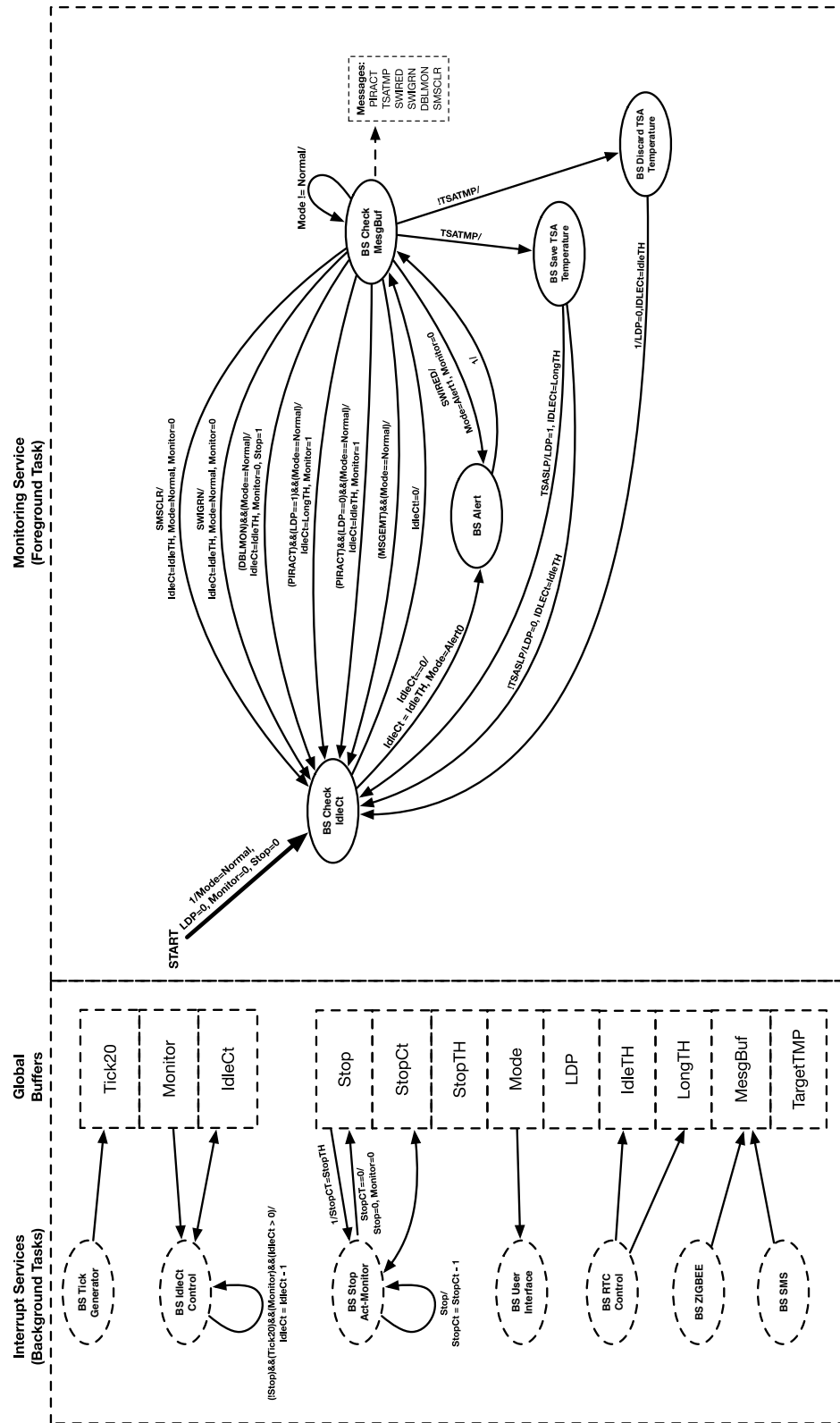


Figure C9: Base Station firmware represented in a top-level state diagram.

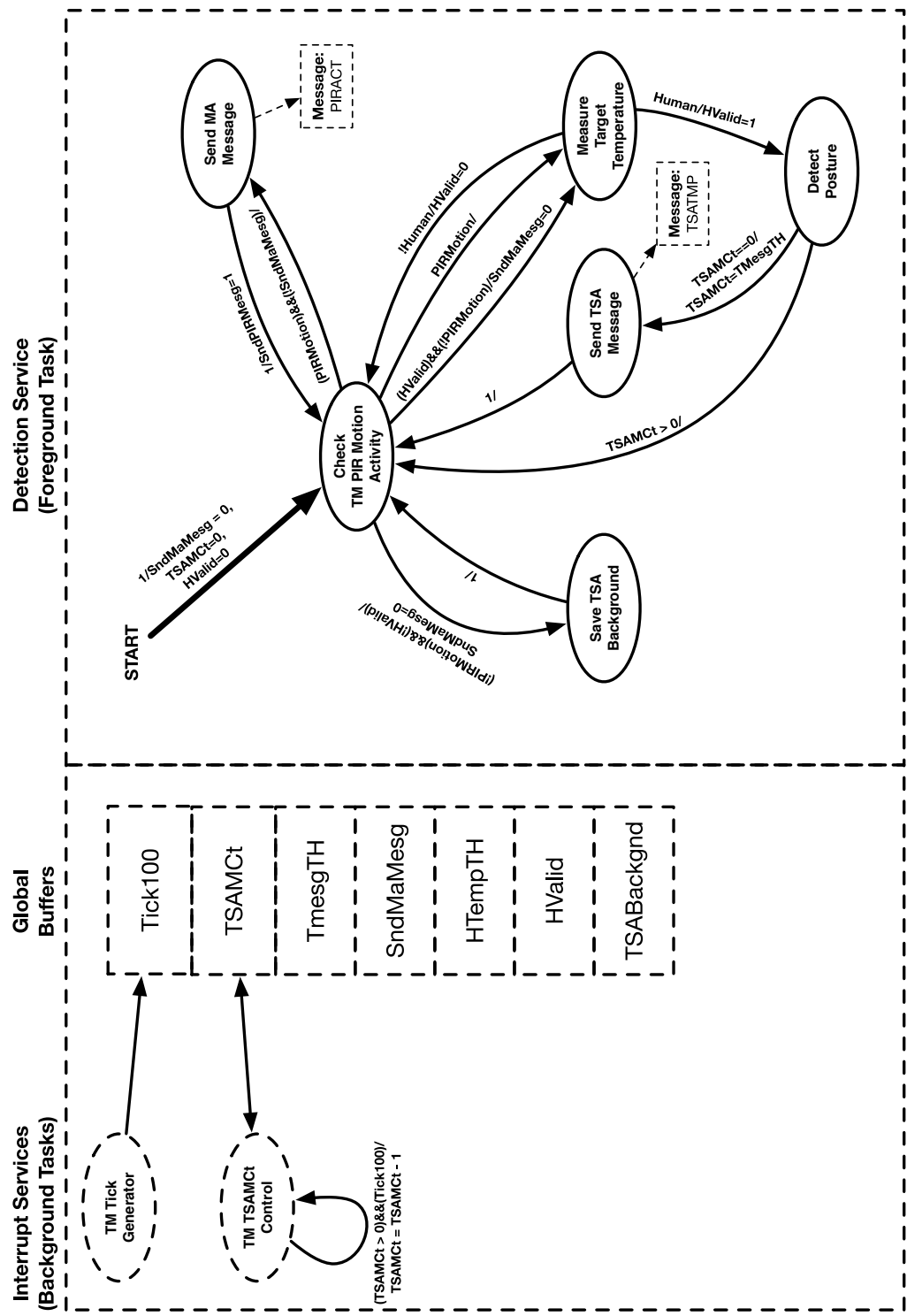


Figure C10: Thermal-Motion sensor module firmware represented in a top-level state diagram.

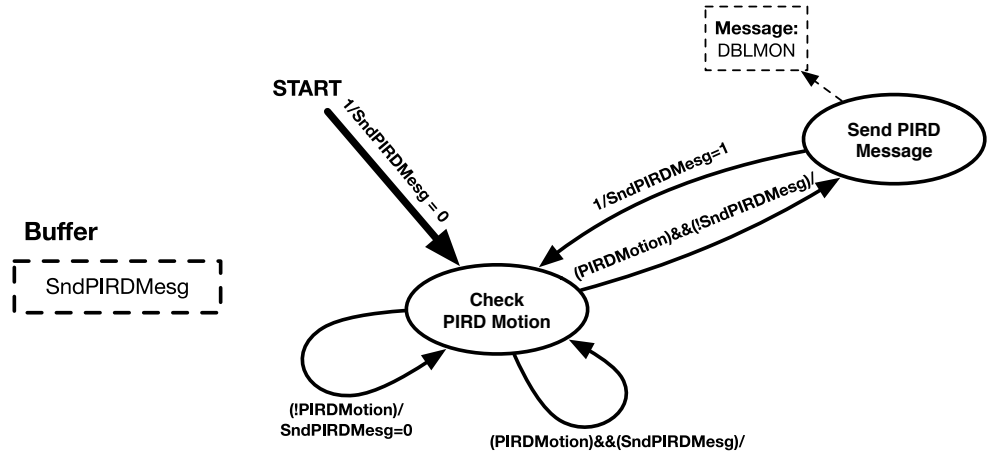


Figure C11: PIR Door sensor module firmware represented in a simple state diagram.

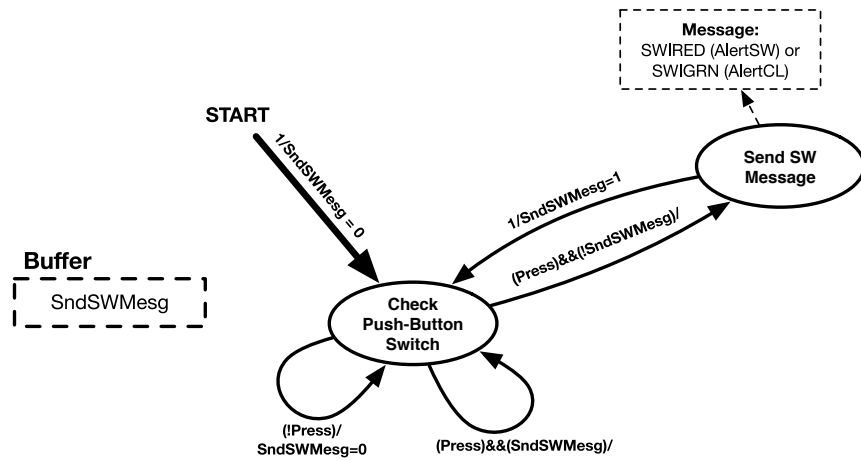


Figure C12: AlertSW/AlertCL module firmware represented in a simple state diagram.

Appendix D: pVoice Hardware Design

An overall block diagram with the constituent hardware modules of pVoice is shown in Figure D1.

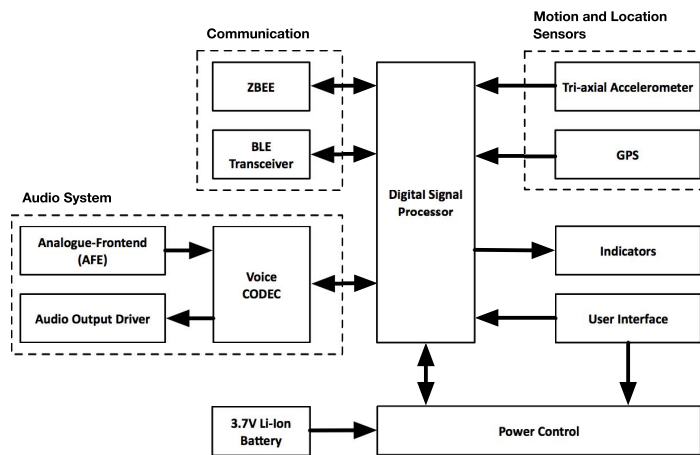


Figure D1: pVoice Hardware Block Diagram

D.1 Audio System

The Audio System block internally consists of an AFE, a 16-bit Voice CODEC and an Audio Output Driver:

1. The AFE interfaces to an external throat microphone (laryngophone).

Jung *et al* [207] analyzed speech and throat vibration signals and showed the vibration signal at the throat surface contained frequencies in the range from 200Hz to 2kHz, and frequencies beyond 2kHz were suppressed. Thus, the vibration signal is a low-passed filtered standard speech signal. The microphone measures vibration signal at the throat surface and input to an audio pre-amplifier with Automatic Gain Control (AGC). The amplifier can yield a gain from 20 to 40 dB over the frequency range from 200Hz to 4kHz. Outside of this frequency range, the signal is attenuated by 6dB/Oct, thereby reducing the low and high frequency noise components [208], [209].

2. A 16-bit voice CODEC is used for audio signal conversion. The audio signal is continuously sampled at $F_s = 8\text{KHz}$. Signal gain and attenuation can be programmed with a 1.5dB step resolution.
3. The Audio Output Driver drives an external 1W magnetic speaker at 91dB Sound Pressure Level (SPL). A bridge-tied load (BTL) output audio power amplifier is designed for this purpose which minimizes the external components count, and provides a high-quality audio reproduction. The amplifier is able to deliver continuous power to the speaker with less than 1% Total Harmonic Distortion (THD) while operating from a single +3.7V Lithium-Ion battery [210].

D.2 Communication

The Communication block consists of a wireless Bluetooth Low Energy (BLE) transceiver and a ZIGBEE wireless communication unit (ZBEE):

1. A BLE transceiver is featured in the design to allow seamless interface to a wireless throat microphone or a smartphone. The smartphone connection allows pVoice to function as a motion activity monitoring and alert wearable device for an elderly. pVoice sends SMS from the connected smartphone during an emergency situation to notify caregivers.
2. A ZIGBEE unit is included to allow pVoice to communicate to an e-Care Base Station (developed in Chapter 5). In an elderly home installed with e-Care system, pVoice is a wearable device tasked to monitor motion activity/inactivity and alert request while performing its primary task. In the event of an emergency, pVoice communicates with the Base Station via the ZIGBEE wireless network to raise an alert.

D.3 Motion and Location Sensors

The Motion and Location Sensors block consists of a digital Tri-axial Accelerometer and a global positioning system (GPS):

1. The Tri-axial Accelerometer is included to detect motion activity when pVoice is used as a motion activity monitoring and alert wearable device.
2. The GPS provides location based information when pVoice is used outdoor. The information is included in the SMS to notify caregivers during an emergency situation.

D.4 Digital Signal Processor

A 16-bit fixed-point DSP operating at 70 MIPS serves as the processing engine. The DSP is a single-chip embedded controller with built-in peripherals that seamlessly integrates the control attributes of a microcontroller unit(MCU) with the computational and throughput capabilities of a classical DSP [211]. The programming model follows that of a standard MCU, hence offering a robust and easy to use approach with little knowledge of DSP required as prerequisites.

D.5 Indicators

The Indicators are the coloured LEDs that display system status such as Bluetooth enable/disable, charging in-progress/completed, and system ready/fault. The LEDs used are of low-power and high efficient type.

D.6 User Interface

The User Interface is a set of soft-touch push-buttons that are used to control power on/off, volume up/down, Bluetooth connect/dis-connect and pitch select features.

D.7 Power Control

The Power Control consists of a Lithium-Ion battery charging circuit and Low-Dropout (LDO) regulators for powering the various peripherals. pVoice hardware consists of isolated analogue and digital circuits sections. Hence, there are two dedicated LDO regulators to supply power to these two sections of

pVoice. Experiments conducted by Sasaki *et al* [212] and Wei *et al* [213] demonstrated the benefits of having such isolations.

Author's Publications

Journal Papers

Wui Keat, Yeoh, Kok Kiong, Tan, and Kwok Seng, Loh, “pVoice, an Assistive Device for a Class of Speech Impaired Patients with Vocal Cord Paralysis”, *Submitted for publication in Elsevier Journal of Sound and Vibration*.

Wui Keat, Yeoh and Kok Kiong, Tan, “e-Care, a Non-Intrusive Activity Monitoring for the Elderly”, *Submitted for publication in IEEE Sensors Journal*.

Wui Keat, Yeoh, Jason Kai Wei, Lee and Kok Kiong, Tan, “A Minimally Invasive System for Mobile Monitoring of Core Body Temperature”, *Submitted for publication in IEEE Sensors Journal*.

Kok Kiong, Tan, Wui Keat, Yeoh, Hsueh Yee, Lim, Chee Wee, Gan, Wenyu, Liang and Jason Kai Wei, Lee, “Re-visiting the Tympanic Membrane Vicinity as Core Body Temperature Measurement Site”, *Submitted for publication in PLOS ONE Journal*.

Kok Kiong, Tan, Wui Keat, Yeoh, Hsueh Yee, Lim, Chee Wee, Gan, and Jason Kai Wei, Lee, “Heat Balance Model for Indication of Middle Ear Temperature from Tympanic Membrane Temperature”, *Submitted for publication in Elsevier*

Journal of Thermal Biology.

Kok Kiong, Tan, Wui Keat, Yeoh, Hsueh Yee, Lim, Chee Wee, Gan, and Jason Kai Wei, Lee, "Heat Balance Model with Gain-Scheduling for Indication of Temperatures at Critical Sites", *Submitted for publication in Elsevier Journal of Thermal Biology.*

Conference Papers

Wui Keat, Yeoh, Qingshuo, Zhou, Kok Kiong, Tan, "Control of Medical Device with Arduino", *In Inventive Research Organization International Conference on Computation and Communication Technologies (ICCCT 2016)*, Kuala Lumpur, June. 14-15, pp. 43-55, 2016.

Wui Keat, Yeoh, Kok Kiong, Tan, "VitalMON Minimally Invasive System of Mobile Monitoring of Core Body Temperature", *In Inventive Research Organization International Conference on Computation and Communication Technologies (ICCCT 2016)*, Kuala Lumpur, June. 14-15, pp. 56-74, 2016.

Wui Keat, Yeoh, Jason Kai Wei, Lee, Hsueh Yee, Lim, Chee Wee, Gan, Wenyu, Liang and Kok Kiong, Tan, "Re-visiting the Tympanic Membrane Vicinity as Core Body Temperature Measurement Site", *In Academic Fora International Conference on Society of Medical, Medicine and Health Sciences (MMHS 2016)*, Kuala Lumpur, June. 16-17, pp. 13, 2016.

Wui Keat, Yeoh, Kok Kiong, Tan, and Kwok Seng, Loh, "Development of pVoice, for a Class of Speech Impaired Patients with Vocal Cord Paralysis", *In Academic*

Fora International Conference on Society of Medical, Medicine and Health Sciences (MMHS 2016), Kuala Lumpur, June. 16-17, pp. 14, 2016.